Investigation on stability and efficiency improvement of modified Cd-chalcogenide nanostructures for photoelectrochemical H$_2$ generation

A Dissertation

Submitted by

Alka Pareek

in partial fulfilment of the requirements for the award of the degree of

Doctor of Philosophy

in

Materials Engineering

School of Engineering Sciences and Technology
University of Hyderabad

September 2015

Dedicated

To

My

Beloved Guruji

&

Family

Declaration

I, **Alka Pareek,** hereby declare that this dissertation work entitled *"***Investigation on stability and efficiency improvement of modified Cd-chalcogenide nanostructures for photoelectrochemical H$_2$ generation***"*, submitted in partial fulfilment for the award of **Doctor of Philosophy** (in Materials Engineering) in the School of Engineering Sciences and Technology (SEST), University of Hyderabad is a bonafide work which was carried out by me under the supervision of **Dr. Pradip Paik and Dr. Pramod H. Borse,** which is also free from plagiarism. I also declare that this thesis has not been submitted previously in part or in full to this University or any other University or Institution for the award of any degree or diploma.

A report on plagiarism statistics from the University Librarian is enclosed.

Alka Pareek

Reg. No.: 11ETPM07

School of Engineering Sciences and Technology

Certificate

This is to certify that this thesis work entitled **"Investigation on stability and efficiency improvement of modified Cd-chalcogenide nanostructures for photoelectrochemical H$_2$ generation"**, submitted by **Alka Pareek** bearing Reg. No. **11ETPM07** in partial fulfilment of the requirements for the award of the degree of **Doctor of Philosophy** in **Materials Engineering**, is a bonafide work that has been carried out by her under my supervision. Dr. Pramod H. Borse (ARCI) have also supervised the above mentioned thesis work with me. This thesis has not been submitted previously in part or in full to this or any other University or Institution for the award of any other degree or diploma.

Thesis Supervisor

Dr. Pradip Paik

Assistant Professor

School of Engineering Sciences and Technology

University of Hyderabad

Approved by

Prof. Rajender Singh

Dean

School of Engineering Sciences and Technology

University of Hyderabad

ACKNOWLEDGEMENTS

I wish to express my deep sense of gratitude and indebtedness to my guide Dr. Pramod H. Borse Scientist "F" at ARCI, for his guidance in all the experiments and discussions. He has always supported me in good and tough times. I am greatly indebted to my supervisor Dr. Pradip Paik, Asst. Professor at University of Hyderabad, for his incredible support during valuable discussions. I sincerely thank Dr. T. N. Rao for his constant moral support and valuable guidance during my stay at ARCI. I would like to express my sincere gratitude towards Dr. G. Sundararajan, Director, Dr. S. V. Joshi *Ex*-Additional Director, and Dr. G. Padmanabham, Associate Director, ARCI, for providing me an opportunity to work as a senior research fellow at ARCI and for granting me the permission to register for Ph. D. at University of Hyderabad. I sincerely thank my doctoral committee (DC) members and Dr. Dibakar Das, Associate Professor, University of Hyderabad for his valuable suggestions during DRC meetings. I like to thank all the faculty members of SEST, UoH, who taught me during the course work.

I sincerely thank Dr. Neha Hebalkar, Dr. Papiya Biswas, Dr. B. V. Sarada, Mr. K. Ramesh Reddy, Mr. G. V. R Reddy, Mr. L. Venkatesh, Mr. M. Ramakrishna from ARCI and Durga Prasad (UoH) for their great help in the characterization of the samples. I am very thankful to my lab mates and colleagues in ARCI and UoH, who has helped me during experiments and discussions. I sincerely thank Santhosh, Koushi and Chandrapal for their help during thesis submission. I would like to thank Dr. Rekha Dom for her help during initial year of my Ph.D in ARCI.

Research Publications from this Dissertation

1. A. Pareek, R. Dom, P. H. Borse, Fabrication of large area nanorod structured CdS photoanode for solar H_2 generation using spray pyrolysis technique- Published- *International Journal of Hydrogen energy*, 2012, **36,** 1

2. A. Pareek, N. Y. Hebalkar, P. H. Borse, Fabrication of highly efficient and stable nano-modified photoanode for solar H_2 generation-Published-*RSC advances,* 2013, **3,** 19905

3. A. Pareek, R. Purbia, P. Paik, N. Y. Hebalkar, H. G. Kim, P. H. Borse, Stabilizing effect in nano-titania functionalized CdS photoanode for sustained hydrogen generation. Published-*International Journal of Hydrogen energy*, 2014, **39**, 4170

4. A. Pareek, P. Paik, P. H. Borse, Characterization of nano-titania modified CdS /polysulphide electrolyte interface by utilizing electrochemical impedance spectroscopy- Published *Electroanalysis*, 2014, **26,** 2403

5. A. Pareek, P. Paik, P. H. Borse, Niobia Modification of CdS photoanode for Efficient and Stable Photoelectrochemical cell-*Langmuir*, 2014, **30**, 15540

Proceedings

1. A. Pareek, P. Paik, P. H. Borse, Photoelectrochemical characterization of coupled metal-semiconductor nanoparticles on nanostructured CdS thin films

Fifth ISEAC Triennial International Conference on Advances and Recent Trends in Electrochemistry (ELAC-2013), p 372-375, 2013

2. A. Pareek, P. Paik, P. H. Borse, Electrochemical characterization of Ag-loaded nano-titania modified CdS /polysulphide electrolyte interface

Published for Proceedings in ICEE- 2014, ISBN- 978-93-81212-96-7

3. A. Pareek, P. Paik, P. H. Borse, Role of Transition Metal-Hydroxide (M-OHx, M=Mn, Fe, Ni, Co) *Co*-catalyst Loading : Efficiency and Stability of CdS Photoanode

Published in MRS proceedings 2015 spring meeting, Volume 1776 / 2015

Manuscripts uploaded

1. A. Pareek, P. Paik, P. H. Borse, Sustained impulsive performance of CdS photoanode *via* robust M: Ni, *Co* –based nano *co*-catalysts: *Dalton transactions*

2. A. Pareek, P. Paik, P. H. Borse, Photoelectrochemistry of nanostructured CdS photoanodes: High efficiency improvement from nano-architectures: Chemistry of Materials

Manuscripts under preparation

3. A. Pareek, P. Paik, P. H. Borse, MoS_2-MoO_3 nanostructures decorated CdS photoanode for efficient and sustained hydrogen generation

4. A. Pareek, P. Paik, P. H. Borse, Poly(pyrrole) coated CdS photoanodes for efficient photoelectrochemical water splitting of water

5. A. Pareek, P. Paik, P. H. Borse, Improving the photoelectrochemical performance of CdS photoanode by coating polyaniline

Conferences

1. **International Conference on nano science and technology (ICONSAT-2012)**

   Poster: Nanostructuring of cadmium sulphide thin film for energy application

2. **11th ISEAC International Discussion Meet on Electrochemistry and its Applications (ELAC- 2013)**

   Poster: Photoelectrochemical characterization of coupled metal- semiconductor nanoparticles on nanostructured CdS thin films

3. **International Union of Materials Research Society (IUMRS-ICA 2013)**

   Oral: Stability improvement of CdS photoanode by control over adsorbed titania nanoparticle phase

4. **International discussion meet on electrochemistry and its applications, Discussion meet-2014 (ISEAC DM -2014)**

   Oral: Characterization of nano-titania modified CdS /polysulphide electrolyte interface by utilizing electrochemical impedance spectroscopy

   Achieved best oral presentation award

5. **International conference on Environment and Energy (ICEE-2014)**

   Oral: Electrochemical characterization of Ag-loaded nano-titania modified CdS /polysulphide electrolyte interface.

   Achieved best oral presentation award

6. **Materials Research Society (MRS 2015 Spring Meeting, San Francisco, US)**

   Poster: Role of Transition Metal-Hydroxide (M-OHx, M=Mn, Fe, Ni, Co) Co-catalyst Loading: Efficiency and Stability of CdS Photoanode

List of Figures

x

List of Tables

Abbreviations

Å	Angstrom
A	Ampere
au	Arbitrary unit
B.E.	Binding energy
C	Capacitance
C_0	Bulk concentration of species
$CdCl_2$	Cadmium chloride
CdS	Cadmium sulfide
CE	Current efficiency
$Co(NO_3)_2$	Cobalt nitrate
CV	Cyclic voltammetry
E	Electrode potential
E_0	Standard Electrode potential
E_D	Anodic dissolution potential
E_F	Fermi level
EC	Conduction band edge
EDX or EDS	Energy dispersive X-ray spectroscopy
E_{FB}	Flat-band potential
E_g	Bandgap
EIS	Electrode-Insulator- Semiconductor structure
ESS	Electrolyte-Semiconductor-Semiconductor structure
EV	Valence band edge
F	Faraday's constant
FESEM	Field emission scanning electron microscope
FF	Fill factor
Ga_2Se_3	Gallium selenide
GIXRD	Grazing incidence X-ray diffraction
HER	Hydrogen evolution reaction
HRTEM	High-resolution transmission electron microscope
hrs.	Hours
InP	Indium phosphide
I_{SC}	Short circuit current
ITO	Indium doped tin-oxide
JCPDS	Joint Committee on Powder Diffraction Standards

J_L	Photocurrent
J_{sc}	Short circuit current density
k_B	Boltzmann's constant
m_e^*	Electron effective mass
m_h^*	Hole effective mass
MIS	Metal-insulator-semiconductor
Mo	Molybdenum
mol	Moles
MoO_3	Molybdenum Oxide
MoS_2	Molybdenum sulpphide
min	Minutes
MS	Mott-Schottky
ms	milli-second
M-*OH*	Metal hydroxide
M-*O*	Metal oxide
NaOH	Sodium hydroxide
Nb_2O_5	Niobium (V) Oxide
NiO	Nickel oxide
$Ni(OH)_2$	Nickel hydroxide
$Ni(NO_3)_2$	Nickel nitrate
NH_3	Ammonia
NHE	Normal hydrogen electrode
$(NH)_2CS$	Thiourea
$(NH_4)_2MoO_4$	Ammonium molybdate
$NH_2OH.HCl$	Ammonium hydroxyl hydrochloride
NP	Nanoparticle
NPC	Niobia peroxo complex
NPT	Nanoparticles of TiO_2
PEC	Photoelectrochemical
PED	Pulse electrodeposition
P_{in}	Incident power
q	Charge
R_s	Series resistance
R_{SH}	Shunt resistance
SAED	Selected area electron diffraction
SCE	Saturated calomel electrode
Si	Silicon

SEM	Scanning electron microscopy
QDSSC	Quantum dot sensitized solar cells
T	Temperature
t	Time
TCO	Transparent conducting oxide
TEM	Transmission electron microscopy
TG	Thioglycerol
$TiCl_4$	Titanium tetrachloride
UV-Vis	Ultraviolet-visible
V	Voltage
V_B	Band bending
V_{oc}	Open circuit voltage
W	Width of depletion layer
XPS	X-ray photoelectron spectroscopy
XRD	X-ray diffraction
XRF	X-ray fluorescence
Z	Impedance
α	Absorption coefficient
ε	Dielectric constant
ε_0	Permittivity of free space
η	Efficiency
λ	Wavelength
ν	Frequency
e^-	Electron
h^+	hole

Contents

ABSTRACT

Photoelectrochemical cell is an advanced technology for generation of hydrogen energy from solar light and water. CdS is one of the most studied photoanodic material for this application. Due to its low band gap and well-suited band edge positions, it is one of the most preferred among other competent semiconductors. However, CdS is associated with a problem of undesirable decomposition of photoanode upon photo-irradiation in an electrolyte. Holes (h^+) produced in the valence band upon irradiation migrate to the surface of the photoanode material and oxidize it. This instability in aqueous media is major cause of concern to visualize this material as an ideal photoanode for PEC cell. In the present dissertation, we have carried tremendous efforts to stabilize CdS photoanode for sustained photoelectrochemical water splitting system. To accomplish this task we have modified the surface of CdS with different systems.

The work in this dissertation is divided into four broad categories: (I) Prior to modification of CdS photoanodes it was necessary to obtain a standard efficient CdS photoanode. The CdS photoanodes used in this study were deposited by spray pyrolysis technique. To achieve efficient CdS photoanodes, different optimization of deposition parameters *viz.* temperature, deposition time, flow rate, substrate area *etc.* was carried out. Optimized efficient film was regarded as standard CdS photoanode and was further modified with different systems for stabilization of CdS photoanode. (2) Stable Metal oxide coating that protects the surface of CdS; for metal oxide coatings-TiO_2 and Nb_2O_5 nanoparticles were synthesized by chemical method and linked on CdS surface by using linking agent. The structural, optical and

photoelectrochemical characterization was carried out. For stability measurements, prolong PEC measurements were recorded (3) Cost effective and earth abundant *co*-catalysts loading on CdS surface; economical *co*-catalysts *viz.* $Ni(OH)_2$, $Co(OH)_2$, Co_3O_4, NiO and MoS_2-MoO_3, were identified and used for modification of CdS surface by chemical impregnation method. The *co*-catalysts reduce the overpotential for gas evolution and lead to higher H_2 gas evolution; (4) Passivation of CdS surface by conducting polymers; the polymers *viz.* polypyrrole and polyaniline were electrodeposited on the surface of CdS in acidic media. These conducting polymers improve the charge transfer process at the interface and avoid direct exposure of CdS surface with electrolyte.

Chapter -1

INTRODUCTION

There are tremendous efforts to realize the idea of converting solar energy directly into chemical energy by use of photoelectrochemical (PEC) technology. The most important feature of this technology is to coordinate the energetics of electrochemical reaction with solar spectrum. Therefore, photoelectrochemistry of semiconducting material plays a vital role in this field. Exploring an efficient and stable semiconductor material for such purpose is an essential prospect. CdS is most studied system among others that shows perfect band gap and bandedge position that is desirable in ideal material, to act as a photoanode in PEC cell. However, it lacks the required stability in aqueous media. This chapter summarizes the mechanistic approach of photocorrosion process indepth. The different parameters affecting the photocorrosion process are discussed. The strategies that could be utilized to curb the photocorrosion process are also highlighted.

1.1 An overview of photoelectrochemistry

Ever-growing and huge energy demand of human being is becoming main challenge with respect to future energy need. An important fact is that 90 % of global energy is obtained from depleting carbon-based fossil fuels, which has been contributing to global warming. To address these energy and environmental concerns, one needs an ideal energy source generated from renewable

resource. In spite of ideal expectations, only 2 % of global energy consumption is contributed by renewable energy sources. Sun is an ultimate renewable source of energy, which bombards earth with about 120,000 terawatt of radiant power [1]. Of this huge energy, 36, 000 terawatt is absorbed by earth mass, which remains unutilized and thus need to be converted and stored into useful form. Practically, only 0.02 % of this energy is sufficient to fulfil the present energy requirements, which are currently met by fossil fuels and nuclear energy. There are many options to channelize this energy into usable form. Hydrogen, the most abundant element on earth is envisioned as ideal energy carrier for storage as well as renewable energy source. It has low density, high thermal conductivity and strong chemical reducing properties, which makes it apt for so many applications [2]. Among several renewable routes to produce hydrogen, PEC hydrogen method serves as most clean and natural way [1]. Accordingly, conversion of solar radiation into H_2 energy through water splitting is an important technology. This engraving technology has motivated a surge of development in solar active semiconducting nanostructures for photocatalytic and PEC technologies. These wet photovoltaic cells are advantageous over dry photovoltaic cells due to ease of formation and better contact between solid/liquid junction as well as low economy. A thorough understanding of physics of solid/liquid junction (semiconductor/electrolyte) *i.e.* semiconductor properties, Fermi level of semiconductor and redox couple of electrolyte, is key to attain an ideal photoelectrode to this technology. The basic knowledge of photoelectrochemistry was realized with the discovery of photovoltaic effect, which was first observed by Becquerel in 1839 [3]. It was postulated that the current was produced by chemical reaction not due to heating effect. Soon after that, the phenomenon of generation of electrical current by illumination of electrode in an electrolyte was named as "*Becquerel effect*". After this discovery, there were no efforts in the above field for next 100

years until 1954, when an extensive study was carried out on Ge based PEC cells [4]. The photoelectrochemistry of elemental semiconductors started much earlier in 1954 by Brattain with the studies on germanium semiconductor [4]. Gobrecht *et al.* investigated photovoltaic effect of metal and elemental semiconductor-electrolyte systems in 1954 [5]. In 1960s, Richard William studied the photovoltaic effect for the first time with a number of compound semiconductors like CdS, CdSe, CuI, ZnO, ZnS, ZnTe, GaAs. He reported two types of reactions taking place at electrode/electrolyte interface (1) degradation of electrode material (photoanodic dissolution) and (2) oxidation and reduction processes at two different electrodes [6]. Gerischer, Morrison, Memming and others in early seventies made significant contribution in 1970s to lay down the basic understanding of charge transfer kinetics at electrode/electrolyte interface [7-9]. The extensive work carried out until 1970s was fundamental in nature. The solar water splitting based hydrogen generation was initiated in the year 1968 by Boddy [10] who reportedly had shown hydrogen evolution by the illumination of *n-type* rutile single crystalline TiO_2 photoanode. Although this work couldn't seek much attention and was superseded by most renowned work of Fujishima and Honda [11] who demonstrated generation of hydrogen by water splitting reaction using *n-type* rutile TiO_2. Lot of efforts have been manifested in search of suitable photoanode material. All the materials were accessed to understand their photoanodic capability with respect to their efficiency and stability. Eventually until 1998, 12.24 % and over 18 % of efficiency has been achieved for p/n type GaAs-/GAInP$_2$ and multijunction photoanode, *respectively*, which are near to half of their theoretical efficiencies [12-13]. In spite of being most efficient, these photoanodes still lack the sustainable hydrogen generation due to their predominant photocorrosion problem. This is in contrast to most stable TiO_2 that exhibits a poor efficiency. Hence exploiting efficient candidates by making them photostable is highly desirable. There are

different ways; these were employed until now to attain an efficient and stable photoanode in a PEC cell *viz.*: (1) to improve the performance of already existing material by coating with appropriate *co*-catalyst or nanostructuring (2) to device new materials with suitable band gap, chemical stability and those are economic in nature [14]. It is well understood that PEC cell portrays an economic alternative to the solid-state solar cells and thus it is envisioned as an excellent solution for future energy crisis. To embark upon this issue it is thus necessary to identify most suitable and ideal semiconductor for the PEC cell technology.

1.2 Fundamentals of photoelectrochemical water splitting

In order to understand this technology it is important to understand the underlying physiochemical aspects, from the perspectives of photoelectrochemistry. We briefly discuss the PEC aspect in the following section. PEC cell is the simplest device consisting of a conducting counter electrode and semiconducting working electrode immersed in an electrolyte, which upon photon irradiation facilitates the electrochemical water splitting and generates H_2 and O_2 due to redox reactions. Figure 1.2.1 (a) shows the schematic presentation of 3-electrode PEC cell, where reference electrode is additional electrode that is otherwise not observed in two-electrode PEC cell. The electrode material being an important entity, its physico-chemical properties determine the feasibility of electrode to be used as photoelectrode [15]. Figure 1.2.1 (b) shows the schematic display of band edge positions and band gap of various semiconductors to decide if redox levels are suited to exhibit water splitting by the semiconductor. Let us consider the energetics of an ideal semiconductor used in PEC cell. Thermodynamically, when an ideal semiconductor is immersed in an electrolyte, a semiconductor/electrode junction is formed as shown in Figure 1.2.2 (a).
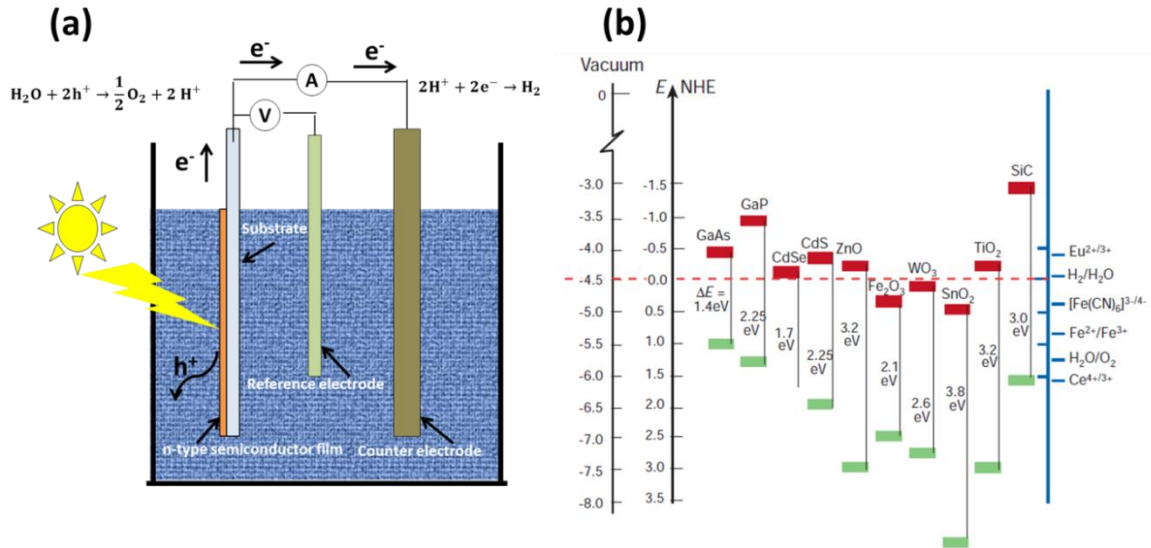
Figure 1.2.1 (a) Schematic presentation of working of PEC cell and **(b)** bandedge positions of most studied *n-type* semiconductors (Ref 2).

This acquires a thermodynamic equilibrium at interface, thereby to match the Fermi level of semiconductor with the chemical potential of electrolyte. This induces transport of charges (e^--h^+) thereby yielding depletion layer (in a similar way to *p-n* junction) and *Helmholtz layer* across the interface as clearly indicated in Figure 1.2.2 (a). The mechanism of equilibration varies in the case of *n-type* and *p-type* semiconductors. For an *n-type* semiconductors, Fermi level lies near the conduction band edge, whereas for *p-type* semiconductors, it lies near valence band edge. Figure 1.2.2 is discussed with respect to *n-type* electrode material.

The depletion layer creates a potential gradient and causes upward bending of conduction band as shown in Figure 1.2.2 (a). The space charge layer inhibits the further transfer of charges at the interface due to induced electric field that is correlated to the potential barrier. The width of the space charge layer (depletion width) is given by equation (1.1) [16]:
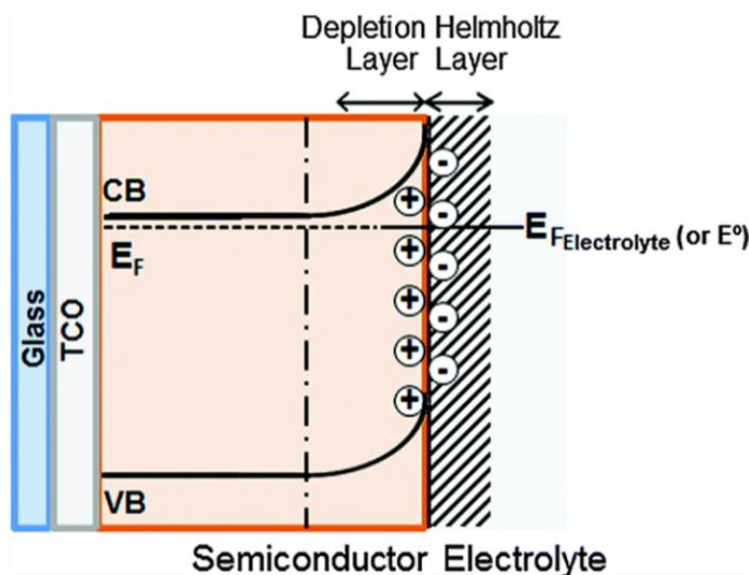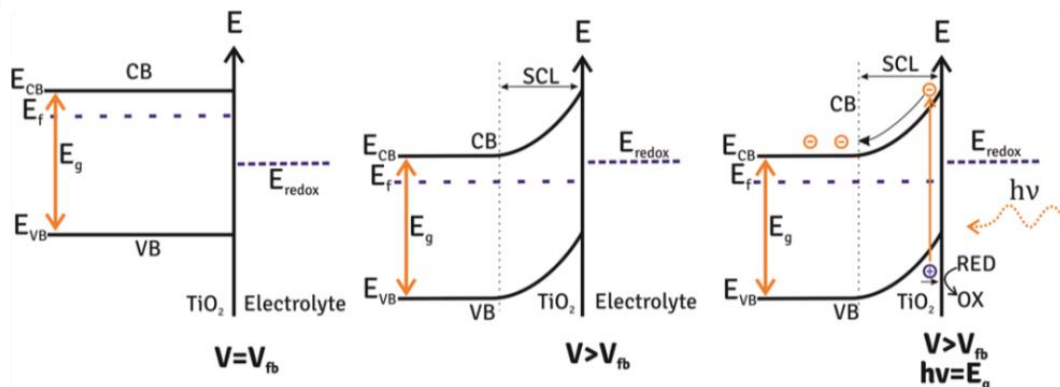
Figure 1.2.2 (a) Formation of a Schottky barrier (junction) in an *n*-semiconductor photoanode at the interface with aqueous electron donor/electrolyte solution (Lopes *et al.*, Phys. Chem. Chem. Phys.*, 2014, 16, 16515) and **(b)** Energy band diagram for a *n-type* semiconductor when the potential (V) is applied *(Bassegato et al., doi.org/10.5772/58333).*

$$W = (\frac{2\varepsilon\varepsilon_0 V_B}{qN})^{1/2} \dots\dots\dots\dots\dots\dots (1.1)$$

Where, V_B is the amount of band bending in the depletion layer, N is the charge carrier density in the semiconductor, q is the electronic charge, ε is the dielectric constant of the semiconductor, and ε_0 is the permittivity of free space. In semiconductors *depletion layer* width ranges from 100

Å to several microns. *Helmholtz layer* is induced due to the presence of ions in the electrolyte that are adsorbed on the electrode surface. The charge of these ions is opposite to that of charge induced in the electrode and potential drop across this layer depends upon ion equilibration rate at the interface. The width of Helmholtz layer is generally of few angstroms. The gradient of electric field at Helmholtz layer affects the band bending across the semiconductor/electrolyte interface [17]. If it was not there, band bending would only be difference in Fermi level of semiconductor and redox potential of electrolyte. Further, upon illumination of such semiconductor, there is separation of electron and holes that occurs in the band-bending region at electrode/electrolyte interface thus resulting in a photovoltage. The photovoltage between the illuminated semiconductor and counter electrode is known as "open circuit potential". When the circuit is closed, there is a net flow of current, which is regarded as short circuit current. In PEC cells, *n-type* semiconductors the majority charge carriers (electrons) leads to cathodic reduction process where as minority charge carriers (holes) carries out anodic oxidation process. The holes are transported through the electrolyte to oxidize water and electrons are swept to counter electrode *via* external circuit to reduce water molecule [18].

On the application of bias in PEC cell, there is shift in the Fermi level position of semiconductor above the H^+/H_2 potential. This phenomenon facilitates the electron transfer to H^+ ions in the electrolyte, which ultimately generates H_2 gas. The applied bias at which there is no band bending exists or there is zero net space charge layer at interface (Figure 1.2.2 (b)), is known as flat band potential (**U_{FB}**). Hence, band bending at the interface is given by equation (1.2) [19]:

$$V_B = E_F - U_{FB} \ldots\ldots\ldots (1.2)$$

Where, E_F is the electrode potential (Fermi level) of the semiconductor.

When the applied bias is more than the flat band potential, the band bending increases and illumination, further widens it, as shown in Figure 1.2.2 (b). Flat band potential is a crucial parameter to characterize the semiconductor electrode. It provides insight with respect to the carrier density, effective mass and the conduction band edge (*n-type* materials) and valence band edge positions (*p-type* materials) [16] of the semiconductor.

A simple PEC set up as can be seen in the Figure 1.2.1 (a). The holes at the surface of the semiconductor combine with the water molecules to release the oxygen gas, as given by equation (1.3) [20]:

$$H_2O + 2h^+ \rightarrow \frac{1}{2}O_2 + 2\,H^+ \quad \Delta E^o_{ox} = -1.229 \; V/NHE \; ....\; (1.3)$$
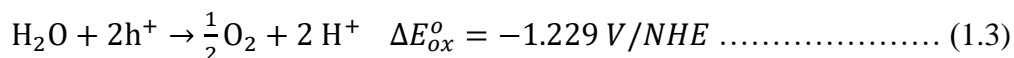
Whereas electrons at counter electrode reduce the H^+ ions and generate the hydrogen gas, as evident by equation (1.4):

$$2H^+ + 2e^- \rightarrow H_2 \quad \Delta E^o_{red} = +0.00 \; V/NHE....................\; (1.4)$$
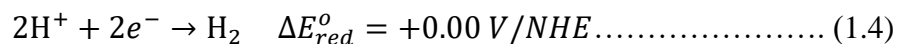
Therefore, over all reaction is given by equation (1.5):

$$H_2O \; (l) \xrightarrow{E=h\vartheta} H_2(g) + \frac{1}{2}O_2 \; (g)....................................\; (1.5)$$
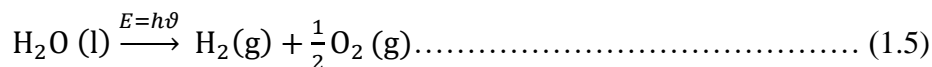
At 298 K, the electrochemical cell voltage ΔE of -1.229 V is equivalent to the Gibbs free energy change of +237 kJ/mol. This demonstrates that reaction involved in the water splitting is

thermodynamically uphill. This is unlike photocatalytic degradation reaction where Gibbs free energy change is negative.

This section has given a basic understanding of the mechanistic reactions associated with the PEC cell. As discussed in *section 1.1*, it clearly implies that there is no ideal material for PEC electrodes to perform the task of water splitting under solar radiation. Since long past, PEC research community has been investigating materials with respect to metal oxide, semiconductor, organic molecules *etc.* The studies indicate that oxides exhibits too large band gap to absorb the solar light photons, being insulators, while semiconductors such as GaAs, CdSe, CdS and GaP exhibit high difficulty in sustained water splitting under visible light for longer time [21]. In present dissertation, we have directly focussed on such efficient but less photostable material systems. It is necessary to understand properties pertaining to these systems those are responsible to display undesirable photo-instability. In order to exploit the high efficiency, it is necessary to tackle the issues related to photostability thus it is considered in this dissertation. In this work, we have selected CdS, as it is most economic system among Cd-chalcogenides.

It is a well-known fact that CdS is an *n-type* semiconductor with low band gap ($E_g = 2.44$ eV), which has a well suited band energetics for water splitting. Accordingly, CdS is most lucrative material for PEC application. Effectively, it implies that CdS is the most suited and efficient photoanode for PEC cell. This is clearly demonstrated by the availability of number of exhaustive reports in the past. Nevertheless, photostability of CdS remains main issue that needs attention and we have attempted to review the aspect related to photostability of CdS rather than efficiency of CdS photoanode in this work. This dissertation would thus throw light on important stability issues those need timely attention to solve the problem of photocorrosion in CdS.

1.3 Review of CdS stability: challenges and solutions

Photocorrosion a challenge

In past, plenty of research has been carried out to improve the PEC performance of CdS by varying its intrinsic properties through doping, surface modification and nanostructuring. However, there are still some shortcomings of CdS yet to be confronted. This includes anodic decomposition of CdS photoanode in aqueous electrolyte upon illumination, which is also known as "photocorrosion" [22]. In photocorrosion, the holes produced during illumination oxidize the semiconductor itself instead of facilitating oxygen evolution reaction. Consequently, the reaction degrades the photoanode thereby reduces the life of PEC cell, and hence the commercial viability of CdS based PEC technology remains a difficult and unachievable task. Thus, it is an important issue to tackle, if one has to exploit the efficient performance of this economic semiconductor. This problem related to Cd –chalcogenides is discussed in this section.

As already discussed in earlier section (*section 1.2*), when a semiconductor in a PEC cell, is illuminated the holes and electrons are produced. These photo-generated electrons and holes are generally characterized by strong oxidizing and reducing potentials, *respectively* [16]. Thus, in a more competitive mechanism they (e^-/h^+) are bound to oxidize or reduce the semiconductor itself, and cause degradation of the semiconductor. The occurrence of such mechanism is a serious obstacle towards the realization of practical PEC devices, since degradation of semiconducting electrode leads to shorter lifetime of electrode and thus the PEC cell. Utilization of the small band gap ($E_g < 2.4$ eV) semiconductors *viz.* CdS, Si, and GaAs as a photoanode in a PEC cell is limited by undesirable anodic dissolution or oxidative decomposition of these

semiconductors. The reactions occurring during such undesired mechanisms for the semiconductors can be stated as follows [23]:

1) **GaAs:** $GaAs + 6\,h^+ + 2H_2O \rightarrow Ga^{3+} + AsO_2^- + 4\,H^+$ ……. (1.6)

2) **GaP:** $GaP + 6h^+ + 3\,H_2O \rightarrow Ga^{3+} + H_2PO_3^- + 4H^+$ ……. (1.7)

3) **CdS:** $n\,CdS + 2n\,h^+ \rightarrow Cd^{2+} + S_n$ ………………………... (1.8)

4) **ZnO:** $2\,ZnO + 4h^+ \rightarrow 2Zn^{2+} + O_2$ …………………….... (1.9)
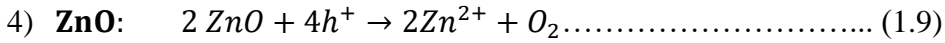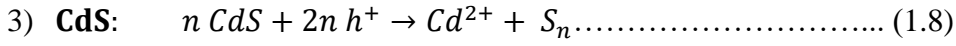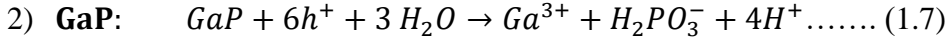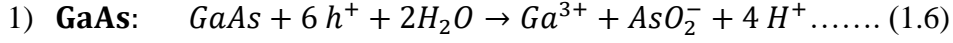
It is well accepted that the decreasing order of the stability of these systems can be graded as ZnO > CdS > GaP > GaAs. This indicates that ZnO is most stable and GaAs is least stable system. Among these, cadmium sulphide is most intensively studied small bandgap semiconductor for PEC cell but exhibit photostability. Meissner *et al.* studied complete mechanism of degradation of CdS in aqueous electrolyte. During photocorrosion process, oxidation of CdS under light illumination leads to sulphur formation on the CdS surface. In presence of oxygen, the sulphur undergoes further reduction. This can be easily understood by the following reactions [24]:

(a) $S^{\div}$ formation

$$CdS + h^+ \rightarrow Cd^{2+} + S_{ads}^{\div}$$ ……………….. (1.10)

(b) Sulphur formation

$$S_{ad}^{\div} + O_2 \rightarrow S_{ads}^{\circ}$$ …………………….. (1.11)

(c) Sulphite formation

$$S_{ads}^{\div} + O_2 \rightarrow SO_{2\,ads}^{\div}$$ ……...…………….. (1.12)

$$SO_{2\,ad}^{\div} + h^+ \rightarrow SO_{2\,ad}$$ ………………….. (1.13)

$$SO_{ad} + H_2O \rightarrow HSO_3^- + H^+$$ …………… (1.14)
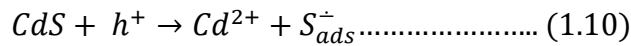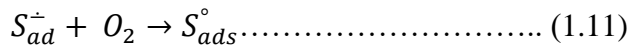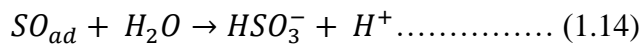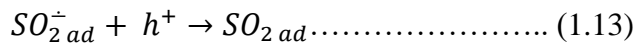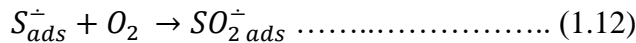
(d) Sulphate formation

$$HSO_3^- + H_2O + 2h^+ \rightarrow SO_4^{2-} + 3H^+ \ldots\ldots (1.15)$$
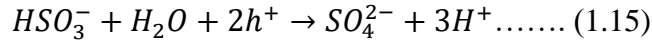
Thermodynamically, there is an oxidation potential associated with the decomposition of any semiconductor as shown in Figure 1.3.1 (c). Briefly, the underlying mechanism can be understood by considering Figure 1.2.2 (a). Let us consider the case of *n-type* material so as to have easy understanding and proper correlation with CdS (*n-type*). It is known that there is an electrochemical potential associated with any anodic decomposition reaction. This plays a decisive role with respect to its PEC performance and stability. In *n-type* semiconductors, the holes in the valence band are energetically capable of oxidizing the semiconductor instead of oxidation of redox couple. Apart from energy aspect, the stability of semiconductor does depend on the rate of transfer of holes to an electrolyte. "If the rate of transfer of holes to redox couple is higher than the semiconductor electrode the degradation of semiconductor will be minimized". Ideally, the above process *i.e.* the lower holes transfer rate to redox couple contributes to the photocorrosion process and thus it delimits the efficiency of PEC cell. The output power of a PEC cell depends on the band bending at the interface. The maximum band bending that can occur in a PEC cell depends on $(E_F - E_D°)$ [25], where $E_D°$ is anodic dissolution potential and E_F is the fermi level energy of the immersed semiconductor. If the redox potential of the selected electrolyte is more negative as compared to $E_D°$, then the band bending will be much less and the semiconductor will also be less efficient and unstable. Bard and Wrighton *et al.* predicted the criteria for photoanodic decomposition of semiconductors based on their rigorous and indepth studies [26]. In line with above concept, the criteria was based on oxidation and reduction potential of semiconductors and Fermi level of electrons and holes. Every *n-type* semiconductors has standard potential for anodic dissolution $(E_D°)$ which plays a key role in determining the

thermodynamic criteria of stability of *n-type* semiconductors in a PEC cell. If $E_D°$ is more negative than the valence band edge of electrode, the *n-type* semiconductor undergoes oxidative dissolution. Accordingly, in presence of a redox couple with a redox potential of E_{red}, when $E_D°<E_{red}$, the semiconductor is prone to degradation. Therefore for an *n-type* semiconductor with $E_D°<E_V$, then to attain stability for this electrode in a PEC cell, redox couple in the electrolyte should be chosen in the way that $E_{red}<E_D°$ as shown in Figure 1.3.1 (a). To be more precise electrode stability depends on the relative kinetics of the two possible types of reactions; 1) photocorrosion; it's a competition between thermodynamically possible semiconductor decomposition reactions (R_{cor}); and 2) thermodynamically possible desired redox reactions in the electrolyte (R_{oxi}) as summarized in Figure 1.3.1 (b) [27]. Let us consider the case when $R_{oxi>}$ R_{cor}. In TiO_2, the redox potential for the oxidation of water is more negative than the oxidation potential of TiO_2. This indicates that the water oxidation reaction is thermodynamically more preferable than degradation of TiO_2 (oxidation of TiO_2) and hence TiO_2 is a stable *n-type* semiconductor in a PEC cell. In another case situation is reverse ($R_{cor>}$ R_{oxi}), for some low band gap semiconductors (CdS, Si, GaP, GaAs), where the redox potential of the electrode decomposition is thermodynamically more favourable than the desired redox reaction (See Figure 1.3.1 (c) for various oxidation and reduction potential). This hypothesis is valid only until the thermodynamically favoured reactions are also kinetically favoured reaction. It has also been reported that the primary reason of this effect is existence of the surface states within the band gap of semiconductors [28]. These surface states permit the minority charges (holes) in *n-type* semiconductors to attain the highest redox level where iso-energetic holes transfer occurs. The issue of "*How stable is stable*?" for PEC electrodes is a debatable topic since long time [29]. If a

PEC cell works at its maximum power with photocurrent density that equals to or greater than 10 mA/cm^2 and shows no loss in output voltage for long period of time it is regarded as stable.
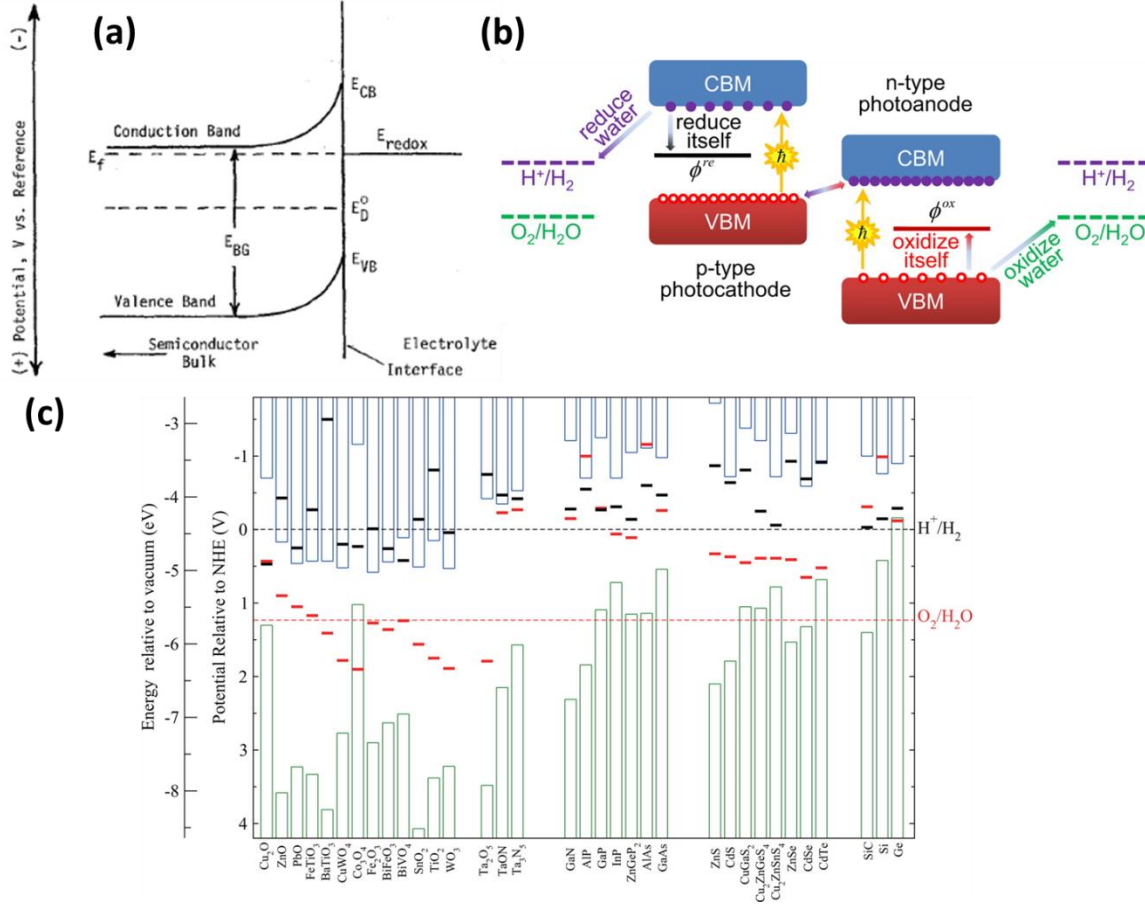
Figure 1.3.1 (a) Schematic diagram of semiconductor/electrolyte interface in a PEC cell for a condition when E_{red} is more negative than $E°_D$ (*Chen et al., Chem. Mater. 2012, 24, 3659)*, **(b)** Schematic plot of the band alignment of the *p-type* and *n-type* semiconductors relative to the water redox potentials in PEC cell where ϕ_{ox} and ϕ_{re}shows the oxidation potential and reduction potential of the photoanode in aqueous solution. **(c)** The water redox potentials $\phi(O_2/H_2O)$ and $\phi(H^+/H_2)$ (dashed lines), and the valence (green columns) and conduction(blue columns). The calculated oxidation potential ϕ_{ox} (red bars) and reduction potential ϕ_{re} (black bars) relative to the NHE and vacuum level for a series of semiconductors in solution at pH=0 (*Chen et al., Chem. Mater. 2012, 24, 3659)*.

There are very less efforts with respect to quantification of stability aspect in a PEC cell. However, for quantitative approach, one can describe that the number of coulombs of charge per square centimetre of electrode area those pass through the device can decide the stability of cell. In one such effort, Cahen and Mirosky (1985) reported a limit of 20 KCcm^{-2} at AM1.5 illumination for testing stability in laboratory [30]. Photocorrosion was the most studied topic during late 19th century among major PEC research groups.

Prospective strategic solution

Various strategies were employed to curb the photocorrosion process, which could be broadly divided into three categories (Figure 1.3.2) [31-32]: (1) Use of sacrificial reagent in electrolyte *viz.* S^{2-}, SO_3^{2-}, which scavenges extra holes giving rise to photocorrosion process; (2) Metal loading includes inert metals *viz.* Pt, Ru, RuO$_2$ over the surface of semiconductor, these metals acts as *co*-catalyst which increases the rate of oxygen evolution and hence consumes holes on the surface of semiconductor faster; (3) Protective coating passivates the surface of semiconductor *e.g.* coatings of wide band gap metal oxides, polymers those avoid direct contact of semiconductor with electrolyte.

Use of sacrificial reagents to control photocorrosion

There were tremendous efforts in the past on the attempts those were explicitly focussed on curbing photocorrosion by using first strategy *i.e.* sacrificial reagents; such efforts are chronologically reported in this section. The sacrificial reagents scavenge the holes on the semiconductor surface and avoid the photocorrosion reaction as mentioned in equation (1.16) [33]:

$$S^{2-} + 2\,h^+ \rightarrow S\ldots\ldots\ldots\ldots\ldots\ldots\ (1.16)$$

17

Fujishima *et al.* [26] reported on the use of iodide ions in the case of CdS photoanode constituted PEC cell but electrode decomposition was observed at considerable rate even at high concentrations of $I^{(-)}$. Then it was suggested that the anodic dissolution of CdS might be suppressed by the use of $Fe(CN)^{4-}$ which causes rapid annihilation of photogenerated holes. Gerischer and Gobrecht [34] studied the single-crystal *n*-CdS electrochemical photocells containing aqueous $Fe(CN)_6^{4-}$ and $S_2O_3^{2-}$. It was found that the latter redox couple gives smaller photo-potential due to the difference between the formal redox potential of the couple and the Fermi level of CdS. Minourva *et al.* studied the effect of several reducing agents on the anodic reactions those occur in competition to the water oxidation process when CdS photoanode is illuminated [35].
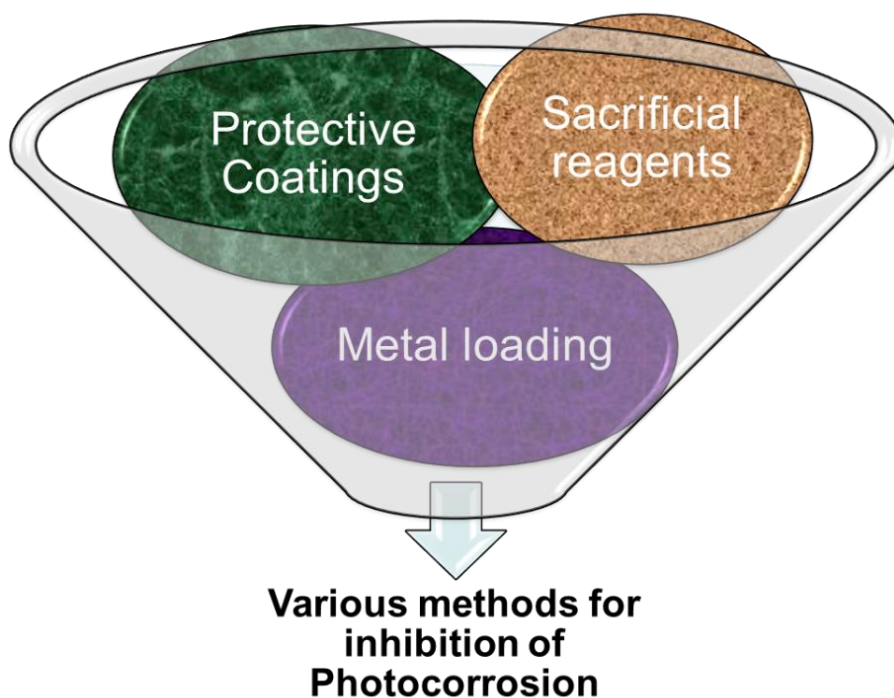
Figure 1.3.2 Different methods of curbing photocorrosion problem.

The reducing agents *viz.* S^{2-}, SO_3^{2-}- and $S_2O_3^{2-}$ ions were able to suppress the photocorrosion effectively and could shift flat band potential to the cathodic direction. It was demonstrated that these reducing agents interacts so strongly with CdS that the energy band structure at the electrode/electrolyte interface is changed and photocorrosion could be suppressed effectively. The effectiveness of reducing agents to suppress photocorrosion was in the order $S^{2-} > SO_3^{2-} > S_2O_3^{2-}$. Inoue *et al.* reported the effect of different reducing agent on surface dissolution of CdS photoanode [36]. Total eight reducing agents those having different redox potential viz. SO_3^{2-}, S^{2-}, $S_2O_3^{2-}$, $Fe(CN)_6^{4-}$, I^-, Fe^{2+}, Br^- and Cl^- were studied. It was found that the reducing agent whose redox potential is more negative, supressed the photocorrosion process more effectively. The percentage dissolution of Cd is lower for SO_3^{2-}, S^{2-} and $S_2O_3^{2-}$ at even very low concentration.

Following this, Hodes *et al.* investigated the effect of different factors on the stability of Cd chalcogenide/polysulphide in a PEC cell and summarized their conclusions as [37]: (1) CdSe and CdS show similar stability behaviour in a polysulphide electrolyte; (2) The stability of the semiconductor electrode increases as the grain size decreases or surface area increases; (3) the electrode stability increases in the order of its configuration, *i.e.* single crystal < sintered pellet < polycrystalline electrode < photo-etched polycrystalline electrode; (4) The composition of electrolyte is crucial to the stability. The maximum stabilizing effect is found to be dominant for ratio $[S^{2-}]/[S] \approx 0.5$; (5) Deactivation of the Cd chalcogenides induces loss in short circuit current (Isc); (e) electrode stability decreases as the photocurrent increases. Mesmaeker *et al.* studied the influence of cysteine solution on stability of CdS photoanodes [38]. It was demonstrated that as compared to NaOH electrolyte, the addition of cysteine increases the photo-oxidation current and

shifts the onset potential cathodically. Cysteine could not stabilize the CdS photoanodes completely but photocurrent enhanced remarkably.

Wilson *et al.* studied the photoanodic dissolution of CdS by rotating disc electrode [39]. They used EDTA as reducing agent to curb the photocorrosion process. The stability was found to be dependent on incident light intensity, the redox potential, concentration of the reducing agents and supporting electrolyte. It is important to note that though the stability of photoanode was independent of photon wavelength of light and applied bias. However, the light intensity and the concentration of reducing agent does effect the reaction kinetics thereby affect the electrode stability. The study indicates that the parameters indirectly reduce the rate of electron transfer by controlling the holes concentration at interface in the PEC cell. Further use of ferrocyanide electrolyte in this study indicated instability of CdS, which was attributed to the fact that redox potential of ferri/ferrocyanide pair is higher than dissolution potential of CdS at *p*H value lower than 4. Further, the use of supporting electrolyte (NaOH) indicated that it reduces the rate of photocorrosion reaction, as there is an improvement in the conductivity of charges (electron and holes) between electrode and electrolyte even at very low concentrations.

Licht *et al.* carried out numerical analysis for studying the effect of aqueous polysulphide solution on CdS photoanode in PEC cell [40]. They demonstrated that the instability of the polysulphide in electrolyte is responsible for gradual decrease in the performance of polysulphide based PEC cell. Lokhande *et al.* studied Al doped CdS thin films on stain less steel substrates by chemical bath deposition method [41]. The effect of heat and salts in electrolyte *viz.* NaCl, KCL was also discussed. It was found that CdS is most stable in NaOH+Na_2S+S electrolyte and Al doped films were stable only when salt were added in electrolyte.

Co-catalyst loading to curb photocorrosion

The use of *co*-catalysts on the surface of CdS (the second strategy) reduces the overpotential for the water oxidation reactions and hence holes are consumed for desirable gas evolution rather than anodic decomposition [42]. There are only few reports with inert metal modified CdS photoanodes that emphasises on stability of PEC cell. In 1981, Kalyansundaram *et al.* studied the photocorrosion of CdS colloidal by loading RuO_2 on the substrate [43]. It was observed that the flat band potential of CdS is located at -0.9 V (vs. SCE) which is sufficiently cathodic for water reduction, whereas valence band of CdS is at +1.5 eV. Consequently, the holes were trapped by RuO_2 on the surface of CdS and were used in evolution of O_2 from water. This indicates that RuO_2 loading on CdS surface enhances the driving force to facilitate the water oxidation, while inhibiting the photocorrosion. Meissner *et al.* also studied RuO_2 and Pt loaded CdS photoanodes [44, 45]. They observed hydrogen generation and an unexpected decrease in *p*H but no oxygen evolution was demonstrated. Rajeshwar *et al.* reported stability of CdS with Cl^- and Br^- in aqueous media [46]. The CdS was modified with polymer (pendant $Ru(bpy)_3)^{2+}$ coated with *co*-catalyst interlayer. The photocorrosion was found to be suppressed and photovoltage improved to 1.6 V.

Protective coating for inhibition of photocorrosion

Another alternative to inhibit the photocorrosion process in PEC cell is based on the third strategy *i.e.*, to modify the surface of the semiconductor in that carries out desired electrochemical reactions. In such cases, the surface of the semiconductor is passivated in such a way that the charge transfer properties (of the electrode) are not altered. The simplest ways to passivate the electrode is by deposition of thin film on the surface of semiconductor to prevent

the attack of the holes. A wide band gap semiconductor or a polymer film can be ideal for protecting the electrode surface. An important requirement for this coating is to have high optical transparency towards the complete solar spectrum, its chemical inertness and material that exhibits good electrical conductivity. The practical goal of the surface modification is not only to improve the stability but also to enhance the short circuit current and open circuit potential, and hence to attain a high conversion efficiency. The first demonstration of surface passivation of *n*-Si was reported by Wrighton *et al.* by using hydroxyl silanes [(1, l'-ferrocenediyl) dichlorosilane] in order to control the unwanted photocorrosion process [47]. The passivation yielded an improved stability as well as significant photo-conversion efficiency in the PEC cell. Noufi *et al.* reported polyaniline (PANI) coated semiconductors (Cd chalcogenides, Si, GaAs, GaP) by electrodeposition. An improved PEC performance and photostability were achieved for these modified films [48]. An improvement in the photocurrent was attributed to improved charge transfer kinetics due to the mediated polymer thin film. In 1981, the same group reported electrodeposition of polypyrrole (PPY) on Cd chalcogenides to reduce the photocorrosion [49]. In such case, the coating acts as a barrier to ion/solvent transport at the interfaces which otherwise would lead to degradation of the semiconductor. The major problem confronted by the polymer coating is its poor adhesion and thus its integrity with the semiconductor.

Mancini *et al.* worked on the thin polymer (Formvar, polyvinylacetal resin in dioxane) film on CdS surface [50]. They studied the rate of decrease in photocurrent as a function of polymer film thickness. The polymer film was deposited by drop cast method. The film had shown decay in photocurrent since the polymer film acts as barrier for transfer of holes. Zhang *et al.* investigated the PANI coated CdS photoanodes [51]. When PANI/CdS films were illuminated, the electrons from PANI were transferred to CdS, whereas holes in the valence band of CdS were transferred

to PANI. The fast rate of holes transfer and high separation efficiency of holes and electron improved the photocurrent and supressed photocorrosion to an extent. Lee *et al.* examined photocorrosion in CdS/CdSe sensitized QDSSC by depositing thin polymer layer of poly (ethylene oxide) (PEO) [52]. There was improvement in the stability of PEO/CdS as compared to the bare CdS sensitized photoanode but photocorrosion was not completely suppressed. Frank *et al.* reported PPY coated CdS photoanodes mediated by *co*-catalyst (RuO$_2$) [53]. The modified films have shown dramatic improvement in stability but only PPY without catalyst offers little prevention to photocorrosion.

Photocorrosion control: On parameters and mechanism

Heish *et al.* studied the important factors and mechanistic aspects of photocorrosion process of CdS [54]. According to the report, the dissolution of the CdS was insignificant in the absence of light even when oxygen was present at high concentration (1.4 x 10^{-4}, 13.1 ppm). The amount of dissolution of CdS in electrolyte during operation of PEC cell was found to be directly proportional to the intensity of light and it becomes constant after 700 W/cm^{-2}. The effect of electrolyte on *p*H was also studied and it was demonstrated that amount of dissolution of CdS was dominant at *p*H 6. The effect of *p*H is attributed to the formation of sulphur-oxidation product (SO$_4^{2-}$) on CdS surface (equation 1.15). Effect of existing or evolved O$_2$ concentration on the rate of photocorrosion reaction was studied; it was found that the substantial amount of Cd (II) dissolution occurs even at zero oxygen concentration. Although Henglein *et al.* reported that the pressure of O$_2$ could accelerate the photocorrosion of CdS [55]. The temperature of reaction also plays an important role in affecting the photocorrosion process. The rate of photocorrosion reaction initially increases with the temperature and then becomes constant. It is expected that the solubility of metal-sulphide would increase with increasing temperature. However, with

further increase in the temperature the CdS dissolution is constrained due to mass transfer as compared to surface dissolution reaction.

Meissner *et al.* also carried out an indepth fundamental study of the water splitting using CdS photoanode [43]. They demonstrated that oxygen is directly involved in the photocorrosion process of CdS photoanode, which leads to the formation of sulphate (SO_4^{2-}) (equation 1.15). The sulphate formation cleans CdS from elemental surface. Due to which flat band potential shifts to – 1.7 V (SCE) and valence band edge to -0.6 V (SCE) with the removal of sulphur from surface. This makes holes incapable of carrying out oxidation of water. In another study, Meissner *et al.* also analysed the effect of various parameters on photocorrosion [44]. They found that main chemical product of photocorrosion reaction is sulphur (equation 1.11), which shifts the flat band potential to anodic direction and causes potential drop across the Helmholtz double layer. The removal of sulphur was carried out by pre-polarizing electrode at -1.1 V (vs. SCE) in presence of oxygen. Due to which the flatband potential of CdS electrode shifted to -1.8 V (vs. SCE) in dark. When the electrode is illuminated, it yielded the surface state charging effect which lead to the formation of S^- (equation 1.6). This is an intermediate step in the formation of S^0 and SO_4^{2-} sulphate (equation 1.7 and 1.15). The S^{2-} on further reduction can form thiosulphate as intermediate step and then formation of sulphate takes place. The detection of thiosulphate on the CdS surface was done by Watani *et al.* by using in-situ infrared spectroscopy. From adsorption isotherm, they found that the thiosulphate group is strongly bound to the CdS surface while sulphate is weakly bound.

Noufi *et al.* investigated the S/Se substitution in CdSe/CdS photoelectrode by photoelectron spectroscopy [56]. The mechanism of S/Se substitution was discussed briefly and consequence of S/Se exchange on the electrode stability and the output power were mentioned. They found

that although cadmium chalcogenides are stable against photocorrosion in polysulphide electrolyte but through anion substitution with prolong operation working electrode can be deterioted. Tenne *et al.* suggested that photo-eching of Cd chalcogenides can improve the quantum efficiency as well as stability of electrode in polysulphide electrolyte [57]. They proposed a simple model to analyse the performance and stability of Cd chalcogenide photoanodes in PEC cell according to which any parameter that increases the efficiency of cell can enhance the stability of photoanode. Rincon *et al.* examined the stability of ZnO coated coupled CdS/CdSe electrodes in PEC cell [58]. After prolong PEC measurements changes in the surface structure, composition of ZnO coated and uncoated coupled electrodes and bare CdSe, were studied using X-ray diffraction and atomic force microscopy. The coupled electrodes have shown stability for the short operation time, which is attributed to an increase in the hexagonal character (strong binding, hexagonal structure is more stable than cubic), and smaller recombination rate of the photogenerated charges. However, for larger operation time the stability was lower as compared to CdSe due to band opening which increases the oxidation rate of the passivated electrodes. The ZnO (35 nm) coating could render stability to the coupled system for the shorter period of operation as ZnO itself is not a stable metal oxide in whole *p*H range.

Campet *et al.* published a research paper exclusively on the protection of photoanode against photocorrosion process by surface modification with metal oxide [59]. They discussed on the criteria for choosing different protective coatings over semiconductors: (1) Protection by a "non-conducting oxide coating" (electrolyte-insulator –semiconductor structure, EIS structure): three semiconductors were considered under this category *viz.* TiO_2 (3.2 eV), Al_2O_3 (4 eV) and Nb_2O_5 (3.4 eV). Since these are wide band gap semiconductors and valence band edge is well below to

the CdS, so the only method for charge transfer is *tunnelling effect*. However, charge transfer through tunnelling can only occur when the thickness of metal oxide doesn't exceed 20 Å, which is very challenging task; (2) Protection by "conducting oxide coating" (electrolyte-semiconductor-semiconductor, ESS structure): To study this effect ITO (90 % In_2O_3 + 10 % SnO_2) was suggested as suitable choice for conducting coating over semiconductor photoanodes. However, the space charge layer formed with this configuration at junction was about 30 Å thick that hindered an efficient carrier tunnelling across the ITO/electrode interface.

Kohl *et al.* investigated the *n-type* TiO_2 coating over different small band gap single crystal semiconductors (*n*-Si, *p*-Si, *n*-GaAs, *n*-GaP, *n*-InP and *n*-CdS) by chemical vapour deposition [60]. The high quality crack free TiO_2 coating stabilizes the electrode with almost no dissolution of semiconductor during the PEC reaction but due to higher thickness of TiO_2 over CdS, holes transfer was not possible at CdS/TiO_2 interface and hence performance of PEC cell diminished. Aliev *et al.* studied passivation of CdS photoanodes by TiO_2 films [61]. A stabilized and an improved photocurrent was shown for 70 min. We have demonstrated stability improvement of CdS photoanodes by utilization on nano-engineered TiO_2 and Nb_2O_5 modification [62, 63]. To facilitate the holes transfer process nanoparticles of metal oxide were used and nanoparticles were anchored on CdS surface *via* linking agent. Improved photocurrent as well as stability was demonstrated for around 10 hrs. for these nanoparticles modified CdS photoanodes. Stability was analysed using long term chronoampereometric curves and the stability factor was calculated by quantifying the slope of curve. Seoul *et al.* studied CdSe/CdS/ZnO system modified with $IrO_2.H_2O$ that provides stability upto 150 minutes and a photocurrent of 13.9 mA/cm^2 [64]. Yan *et al.* reported an ultrathin TiO_2 nanosheets coating over CdS nanoparticles [65]. The results exhibited an enhanced photocatalytic activity and stability. Yu *et al.* studied the stability of CdS

sensitized quantum dot solar cells (QDSSC) by coating of ultrathin (2 nm) TiO_2 layer by atomic layer deposition (ALD) [66]. ALD-TiO_2 layer improves the efficiency upto 1.41 % and stability for 20 min under full illumination.

1.4 Problem definition

The main goal of this chapter is to highlight the effects of photocorrosion on CdS performance, which is a challenging scientific problem in the field of PEC. Inherent instability issues related to CdS photoanodes in the PEC cell has been among most studied topic since the past decades and is being attended seriously. Many pioneer scientists have contributed their efforts towards this scientific problem. The work on stability of the CdS can be broadly categorized into three main strategies: (1) *Sacrificial reagents*: Sacrificial reagent term is given to the electron rich species, which acts as a holes scavenging agent in an electrolyte. These species combines with the excess holes participating in the photocorrosion process and hence help in suppressing it for example, Halides, EDTA, Fe $(CN)_6^{4-}$, S^{2-}, SO_3^{2-}; (2) *Metal loading*: Metal loading involves employing the inert metals as the catalytic material such as Pt, Ru and Au at the semiconductor-liquid interface which causes holes consumption at metal surface and hence reduces anodic oxidation or photocorrosion process. This method was not studied since it contained inert metals like Pt, Au *etc.* which are very costly and secondly the results obtained were not reproducible; (3) *Protective coatings*: It involves the passivation of photoanode with some stable material or polymer so that photoanode surface can be isolated from electrolyte. Campet *et al.* did in-depth and systematic studies on identifying the criteria for protective coatings [59]. For metal oxides since the valence band edge lies below unstable semiconductor so for holes to transfer only tunneling effect is needed. For tunnelng effect to be feasible the thickness of metal oxide over

unstable semicondutor should be less than 20 nm. Such study is carried out in this dissertation by modifying CdS surface using titania and niobia nanoparticles *via* linking agent. CdS photoanodes were stabilized for around 10 hrs. But still rigorous efforts are required to stabilize the CdS photoanodes and test if for longer than 100 hrs. as per the targets.

From the above discussion it is clear that stability of CdS is an important problem and rigorous efforts are required to address the issue. Based on the thorough literature survey we have tried to work on photocorrosion problem (in case of CdS photoanode) using three techniques *i.e.* metal oxide coating, *co*-catalyst loading and polymer coatings for the modification of CdS. The methods were modified using advanced nanotechnology techniques which helped in tackling the shortcomings of each method. On the basis of above mentioned problem, the objectives of the dissertation were defined and given below for the sake of completeness:

1.5 Objectives of Dissertation

(1) Deposition of CdS thin film and optimization of deposition parameters *viz.* flow rate, deposition temperature, time of deposition to obtain uniform adherent nanostructured CdS thin film for PEC hydrogen generation.

(2) Synthesis of metal oxide nanoparticles *viz.* TiO_2, Nb_2O_5 (size < 10 nm) by simple chemical method. Modification of CdS surface with as synthesized metal oxide nanoparticles *via* linking agents for stabilization of CdS photoanode. Different optimizations need to be carried out with respect to concentration and adsorption time of linking agent, phase and size of metal oxide nanoparticles so that we can get the best efficiency and stability for PEC cell.

(3) Identification and standardization of synthesis method for earth abundant and cost effective *co*-catalysts *viz.* MoS_2-MoO_3, $Co(OH)_2$, Co_3O_4, $Ni(OH)_2$, NiO by chemical precipitation method to use them for stability and efficiency improvement of CdS photoanodes. Modification of CdS photoanode with as synthesized *co*-catalysts by chemical impregnation method to achieve efficient and stable CdS photoanode for PEC cell.

(4) Deposition of conducting polymers *viz.* PPY and PANI on CdS surface by electro-polymerisation method for stabilization of CdS photoanodes against photocorrosion process. The optimization of process is required by varying the applied field, concentration of monomer and pH of precursor to obtain uniform and adherent coating.

Chapter -2

EXPERIMENTAL

This chapter deals with a detailed description of the materials used, experimental details, fabrication of PEC cell and characterization of the complete PEC cell. Accordingly, a main part related to the photoelectrode has been section wise explained. The details wherever necessary, are dealt independently and the other common procedure has been described accordingly. Effectively, throughout same CdS substrate was coated in all cases. The CdS modification has been described as per the method of use in *section 2.3* in the latter section below. Common method of electrode fabrication for its utilization in PEC cell is used and described in *section 2.4.2*. A brief overview of reactor design of PEC cell is given in following *section 2.4.1* for the sake of completeness, though it is not focus of this dissertation. The complete details of characterization are given in the *section 2.5*. Wherever the parameters details are important and desirable are accordingly given in the Results and discussion section (*Chapter-3*). Efficiency calculation for PEC cell is included in *section 2.6.*

2.1 Materials and Reagents

Details of the chemicals and reagents used in this work are as follows; $CdCl_2$ (Sigma Aldrich, 99.999%), $(NH)_2CS$ (Sigma Aldrich, 99.9 %), $TiCl_4$ (Sigma aldrich, 99.9 %), NH_3 (Sigma Aldrich, 99.99 %), $NH_4[NbO (C_2O_4)_2(H_2O)_2].nH_2O$ (CBMM, Brazil), H_2O_2 (Sigma Aldrich, 30

% w/w), Thioglycerol (Sigma Aldrich, $\geq$ 97%), Ni (NO$_3$)$_2$.6 H$_2$O (Sigma Aldrich, 99.99 %), Co(NO$_3$)$_2$.6 H$_2$O, NaOH (Qualigens, 97 %), (NH$_4$)$_2$MoO$_4$ (Sigma Aldrich, 99.98 %), NH$_2$OH.HCl (Sigma Aldrich, 99 %), pyrrole (Sigma Aldrich, 98 %), aniline (Sigma Aldrich, > 99.5 %). All of them are used without further purification.

2.2   Deposition of CdS thin films by spray pyrolysis method

Spray pyrolysis method is used to deposit the CdS films throughout the work carried out in this dissertation. Spray pyrolysis is a thin film deposition technique in which required compound salt solution (precursor) is sprayed on the hot substrate, where it decomposes and further constituents react to form a desired chemical compound. Chemical reactants are selected in such a way that the other by-products are volatile at that temperature. CdS thin films were deposited using spray pyrolysis deposition technique owing to its tremendous advantages over the other deposition processes, *viz.* scalability of process, ease of doping, moderate operation conditions as temperatures (100 ˚C - 500 ˚C) and cost-effectiveness with respect to equipment cost and energy consumed during deposition process. This method controllably yields the desired thickness, crystallinity, composition, possibility of multilayer deposition and possibility of its usability for variety of substrates.

In this technique the salts of desired compound (CdCl$_2$ and (NH$_2$)$_2$CS in present case) are sprayed onto hot the substrate to form the final product. The chemical reactants and temperature of the substrate are optimized in such a way that desired compound forms on the substrate while other volatile *by-products* evaporate out. The chemical reaction involved during the formation of CdS by spray pyrolysis method, which can be expressed by equation (2.1) [67]:

$$CdCl_2 + (NH_2)_2CS \rightarrow CdCl_2(NH_2)_2CS \rightarrow CdS \downarrow +2NH_4Cl \uparrow +CO_2 \uparrow \ldots\ldots\ldots\ldots\ldots\ldots(2.1)$$

Here, when an aqueous solution of $CdCl_2$ and $(NH_2)_2CS$ are mixed together, they form a water-soluble complex of $CdCl_2$ $(NH_2)_2CS$. The pyrolysis of this complex takes place when its aerosol is sprayed on the hot substrate, which upon decomposition (above 250 ℃) yields CdS on the substrate. Simultaneously the *by-products* of the reaction *i.e.* NH_4Cl and CO_2 evaporate out thereby completing the reaction. Finally, we obtain an adherent crystalline CdS thin films at 350 ℃ [39] and these films are further used for the surface modification by making use of different systems. Preciously equal amounts of solution of $CdCl_2$ (0.1M) and $(NH_2)_2CS$ (0.1M) were dissolved in double distilled water to achieve homogenous precursor. Fluorine doped tin oxide; FTO (Pilkington TCO-15) with resistivity 12 Ωcm was used as substrate. The distance between nozzle and substrate was maintained at 23 ± 2 cm throughout the experiment. Nanostructuring was carried out by varying the flow rate from 2 ml/min to 11 ml/min and deposition time from 1 min to 7 min. Temperature of the substrate was maintained at 350 ℃ throughout the experiments. However, all the CdS films used for this dissertation were fabricated keeping all the deposition parameters fixed and further they have been modified according to the requirement.

2.3 Synthesis of adsorbate nanoparticles by different techniques

In this section, synthesis procedure of TiO_2, Nb_2O_5, MoS_2-MoO_3, $Ni(OH)_2$, NiO, $Co(OH)_2$, Co_3O_4, PANI and PPY, have been discussed thoroughly. Each subsection explains the precise experimental conditions to synthesize different systems and method used for modification of CdS surface.

2.3.1 TiO$_2$ nanoparticles

TiO$_2$ nanoparticles were synthesized through *hydrolysis method* following the procedure explained in the literature [68, 69]. In this dissertation, TiO$_2$ nanoparticles are named as NPT (nanoparticle of TiO$_2$). Briefly, titanium tetrachloride was dissolved in distilled water at ice-cold temperature followed by the addition of ammonia solution. Thus, obtained mixture was stirred for an hour and refluxed for ~18 hrs. As received precipitate was collected by centrifugation, washed with distilled water to remove any un-reacted impurities, and then air-dried. The NPT (5 nm) were characterized and used for linking on the CdS surface by simple adsorption method.

2.3.2 Nb$_2$O$_5$ nanoparticles

Niobia nanoparticles were synthesized by *hydrothermal treatment* of niobia peroxo complex (NPC) in an aqueous solution [70]. The key point of this chemical synthesis includes retention of high surface area as well as acidic nature of nanoparticles, which is predominantly important for the catalytic properties. Hydrothermal treatment induces the crystallization process without the loss of superficial hydroxyl group and hence retains acidic sites and thus the surface area of the semiconductor. Growth of nanoparticles was studied by variation in the hydrothermal reaction time. In brief, 0.26 M of ammonium niobium oxalate powder was dissolved in deionised water (100 ml) to obtain a transparent solution. To this solution, H$_2$O$_2$ (30% in vol.) was added yielding a transparent yellow solution and thus indicating the formation of the NPC. Thus, obtained solution was transferred to 200 ml hydrothermal reactor, and further subjected to several hrs. (varied between 2-9 hrs.) of thermal treatment (120 °C). After the completion of the thermally induced chemical reaction, the mixture turned into colourless. Then the decomposed gases were allowed to carefully release from the autoclave to avoid any contact with skin or

eyes. Finally, received white product was thoroughly washed with ethanol-water mixture through centrifugation and repeated re-dispersion followed by air-drying.

TiO_2 and Nb_2O_5 nanoparticles were attached over CdS surface *via* linking agent. Optimum concentration of thioglycerol (TG) was used for complete adsorption of NPT and nanoparticles on the CdS photoanode surface. The concentration of TG is optimized by varying its volume ratio in the range 0.1-1.0. It was found that very low TG concentration (<0.1v/v) was insufficient to attach enough nanoparticles, whereas when higher concentration (>>0.1v/v) of TG was used it deteriorated the photoanode and the CdS films peeled off (Figure 2.3.1) from the FTO substrate. Our optimization shows that stable film and the best PEC performance can be achieved at TG concentration of 0.1 v/v%, which is used in present study.
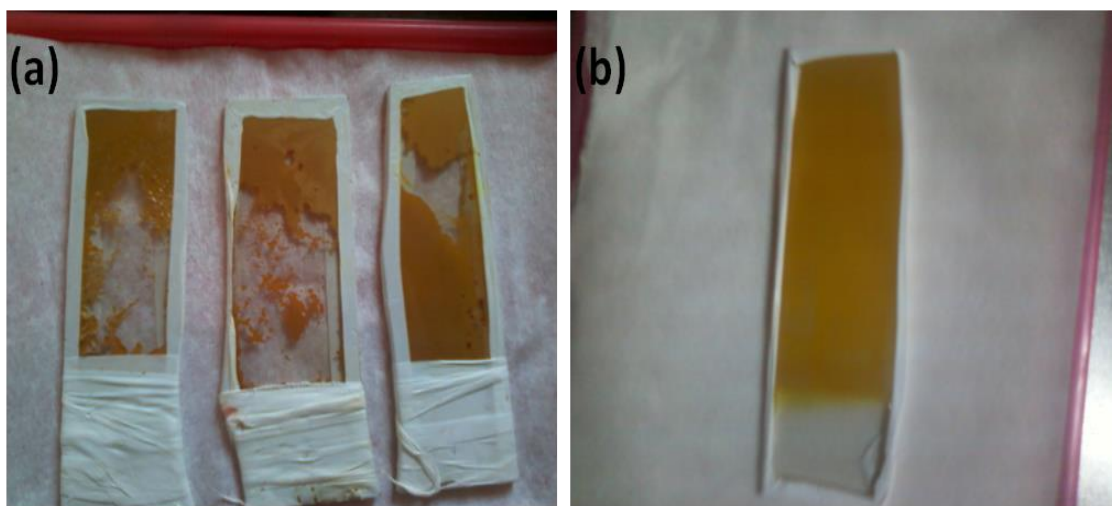
Figure 2.3.1 Image of the CdS thin films peeled off after treatment with (a) higher concentration of TG (>0.1 wt%) (b) Optimized concentration of TG (1:1 wt %).

2.3.3 $Ni(OH)_2$, NiO, $Co(OH)_2$ and Co_3O_4

The modification of CdS surface by *M*-OH (*M=Ni, Co*) nanoparticles were carried out by chemical impregnation method [71]. Accordingly the $Ni(OH)_2$ colloidal solution was prepared

by addition of NaOH in 0.1 M $Ni(NO_3)_2$ aqueous solution. This yielded light green colored colloid of $Ni(OH)_2$. In case of pink colored $Co(OH)_2$ colloid, similar procedure was followed, though $Co(NO_3)_2$ precursor was used instead. The optimal CdS films were immersed in these colloidal solutions for 1 hour, then washed with the de-ionized water, and dried carefully to obtain hydroxide modified CdS films (*M*-OH). Further, to obtain the Co_3O_4 and NiO nanoparticle modified CdS film, the *M*-OH film obtained in above step was subjected to the thermal treatment at 623K. This facilitated the conversion of *M*-OH into *M*-O over the CdS surface. Thus, modified CdS electrode exhibited surprisingly distinct PEC behavior in contrast to the bare CdS electrode.

2.3.4 MoS_2-MoO_3 nanostructures

MoS_2-MoO_3 nanostructures were synthesized by hydrothermal method [72]. For precursor preparation, 4×10^{-3} M of ammonium molybdate and 7×10^{-2} M of hydroxylamine hydrochloride was added to 50 ml of aqueous solution (deionized water). The above solution was stirred thoroughly. Another solution was prepared by dissolving 0.36 M of thiourea in 50 ml deionized water. The two solutions were mixed properly. The *p*H of the final solution was adjusted to 6 by dropwise addition of 2 M HCl. The above-prepared precursor was transferred into the Teflon container of autoclave and heated at 180°C for different time intervals *viz.* 10 hrs. 15 hrs. 24 hrs. 36 hrs. Finally, the obtained particles were washed with deionized water and acetone and were dried carefully. The MoS_2-MoO_3 nanostructures were attached to CdS surface by chemical impregnation at room temperature without the using any linking agent. The reaction time was optimized to 7 minute for all types of MoS_2-MoO_3 nanostructures.

2.3.5 Polyaniline

PANI was directly deposited over CdS surface by electrodeposition technique [73]. The electropolymerization of aniline involves formation of aniline cation radical by anodic oxidation on the electrode surface, which is considered as rate determining step. The oxidation of aniline monomer occurs at higher potential than the redox potential of PANI. The coupling of anilium radicals takes place followed by elimination of two protons and rearomatization that leads to the formation of the dimer. The aniline dimer and oligomers further oxidize on the anode to be attached with aniline. The chain propagation is achieved by coupling radical cation of the oligomer with anilium radical cation. Later, the length of the chain increases and PANI is formed. Typically, for electrodeposition of PANI on CdS, 0.1 M aniline and 0.1 M of Na_2SO_4 in aqueous solution was used as precursor. The pH of the precursor was adjusted to 3 by using 0.5 M H_2SO_4. The electrodeposition of PANI was carried out potentiodynamically on as deposited CdS films in a three-electrode system where graphite was used as counter electrode and SCE (standard calomel electrode) as reference electrode. The number of cycles was optimized to 3 cycles to get adherent coating at a scan rate of 50 mV/s in the potential window of -1 V to +1 V.

2.3.6. Polypyrrole

PPY was also deposited on CdS surface by electrodeposition. The polymerization of PPY also occurs *via* cation-radical mechanism in a similar way as described in earlier section. Initially pyrrole monomers are oxidized to cation radical at anode. Further the cation radical couple and forms a dimer with the elimination of two protons. The dimer is further oxidized into cation radical, which couples with cation radical of monomer to form trimer. Likewise, the polymer

chain length grows and polymerization takes place. Electrodeposition of PPY was performed by taking a 0.1 M pyrrole solution. Similar procedure was followed as as it was done for PANI.

Precise details related to variation of different parameters during experiments are mentioned in the respective section of results and discussion (*Chapter-3*).

2.4   Design and fabrication of photoanode and PEC cell

In this section, designs of different reactors feasible to use at lab scale are discussed and the electrode fabrication part is explained briefly. Based on the information available in literature, details of reactor design for this work have been discussed in the subsequent section.

2.4.1 Photoreactor design

Design of reactor is an important aspect of PEC cell. The appropriate design of reactor can improve the efficiency of PEC cell in following ways: (1) Increase in light collection by use of focused/concentrated sunlight; (2) Separation of products to avoid back reaction; (3) Minimize ohmic losses by putting anode and cathode as close as possible; (4) Reactor must be inert to the electrolyte and impervious to hydrogen so end product can be collected effectively. Different types of reactors have been designed and tested earlier for lab-scale hydrogen generation and for research purpose. Several types of reactors have been reported in literature [74], they are; single chamber reactors, reactor with ports, reactor with optical window, reactors with gas separation. There are also distinguishable difference with respect to lab-scale reactor and large-scale (commercial) reactor. For this dissertation, we have restricted discussion to the lab-scale reactor.

A simple lab scale reactor is constructed by suitable ports and quartz window. In the present work, a single compartment reactor is designed where sacrificial reagents were used to supress oxygen generation. We have used two type of reactors for experiments one with "horizontal" and another with "vertical" illumination. They are briefly explained in the following section.
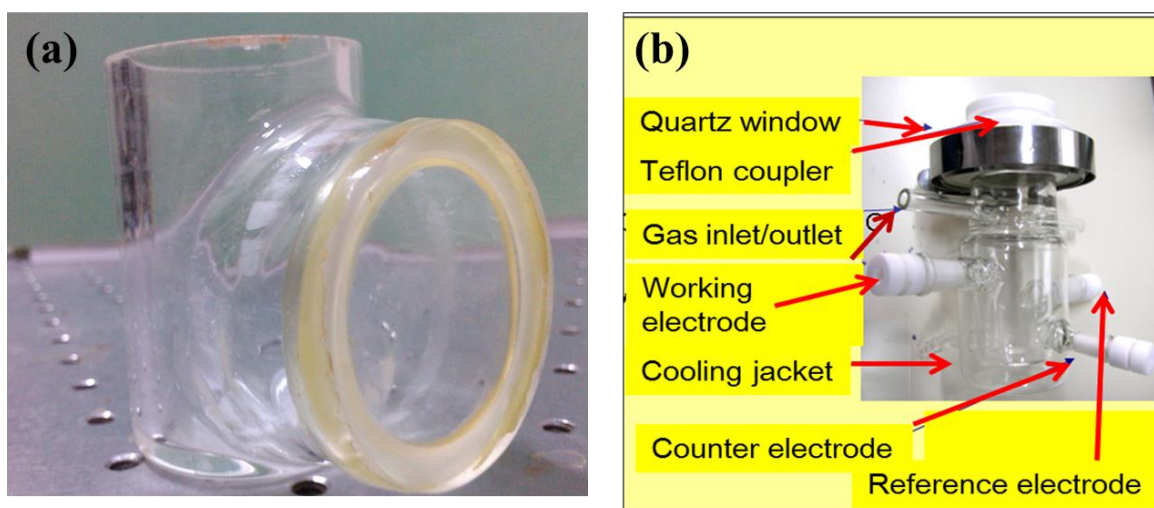
Figure 2.4.1 (a) Reactor cell for PEC measurements (horizontal illumination) (b) Reactor cell for PEC measurements (Vertical illumination).

For the horizontal illumination, a dedicated reactor was designed, fabricated, and used in present study. Figure 2.4.1 (a) shows the photograph of reactor. It is a cylindrical glass reactor (100 ml), which is provided with a side window made of quartz. The window is of diameter 45 mm. An airtight Teflon cover provided at the top, has hole to insert working, reference and counter electrodes. During the PEC experiment, the electrodes have been inserted vertically into the reactor that is filled with electrolyte (with effective volume of 75 ml) and the entire arrangement is interfaced with an electrochemical workstation and placed before the light source. The details of the light source are mentioned in *section 2.5.8*. The light is allowed to pass through the quartz window, and illuminates the electrodes placed vertically (either with back or front illumination) for PEC reaction.

For vertical illumination, a dedicated reactor was used with vertical illumination geometry. The cell used for this work is shown in Figure 2.4.1 (b). This design is desirable to utilize solar simulator light as source. It is consists of a Teflon cover with the quartz window at the top. It can be fitted with a coupler to the glass cell. This airtight cell has different ports provided at the sides to insert the electrodes inside the cell. In addition, the cell is provided with a cooling jacket and a gas inlet/outlet arrangement for gas detection using gas chromatography spectrometer. These two types of reactors were used during the investigation described in this dissertation.

2.4.2 Fabrication of electrode
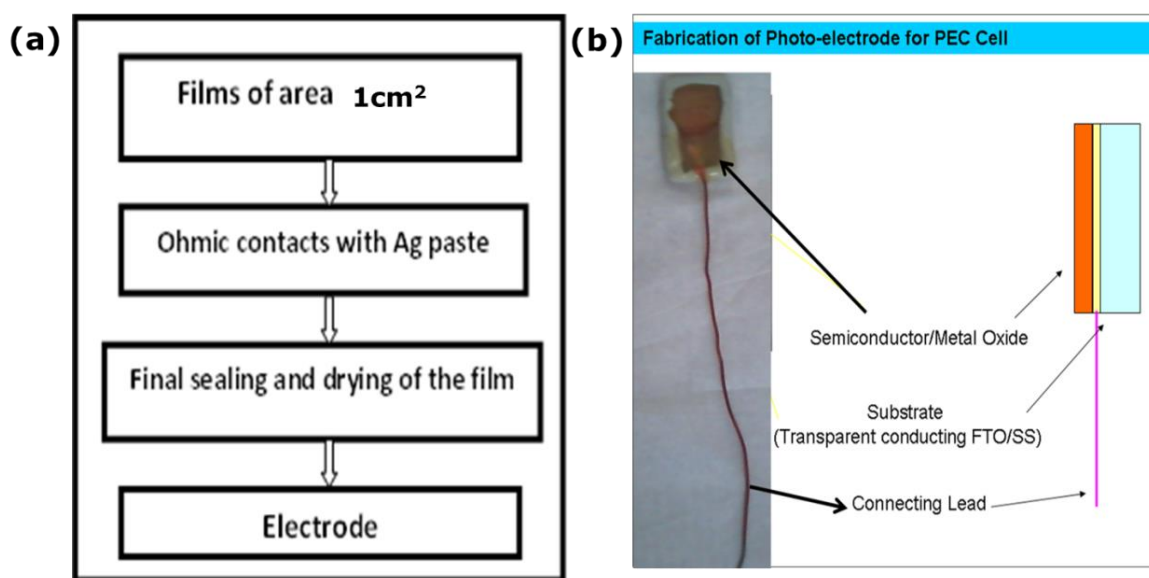
Figure 2.4.2 (a) Schematic showing the procedure for fabrication of electrodes. **(b)** Image of electrode fabricated for PEC measurements.

All the electrodes were fabricated according to the procedure described in this section and summarized in Figure 2.4.2 (a). The photoelectrodes were fabricated from as deposited films. Films of area 1 cm^2 were cut from the deposited films.

Silver paste is used to make an ohmic contact over the film surface. Thus, formed electrode assembly was finally sealed with a leak proof adhesive and dried. Figure 2.4.2 (b) shows a typical electrode fabricated for PEC measurements.

Throughout the work routine and similar procedure was adopted in order to have consistency of results, those were confirmed from their PEC characterization as described in *section 2.5*.

2.5   Physico-chemical characterization of nanoparticles and thin films

This section describes the different techniques used for characterization of modified and unmodified samples. The structural, optical, elemental detection, morphological and PEC properties of different samples have been studied. The principles and methods of characterization as well as sample preparation for characterization have been discussed in the subsequent section.

2.5.1 X-ray diffraction (XRD)

XRD is a widely used characterization technique for the determination of crystal structures of materials. The technique uses the Bragg's law of X-ray diffraction which states that when incoming X-rays diffracted constructively by the atoms in the crystal planes, the path difference between the rays diffracted by the successive atomic planes is directly proportional to the integer multiples of incident X-ray wavelength as shown in Figure 2.5.1. The powder X-ray diffractometer can be used to analyze thin film samples by means of a change in mechanical arrangement. One such arrangement is Grazing angle incidence X-ray diffractometer, where the angle between the incident X-ray beam and the thin film sample is adjusted to 0.5-1°. This arrangement exposes the film to X-rays more effectively than the substrate. X-ray diffraction

provides information such as the crystallographic structure, crystallite size and preferred orientation in a polycrystalline sample.

Bruker – D8 advanced X-ray diffractometer with Cu K$_\alpha$ radiation (λ = 1.54 Å) is used to examine the phase constitution of the films and powder used in this study. The scan is taken in the range of 2θ = 10-70° with an increment of 0.01° per second at the grazing angle of incidence. The as-deposited films and as synthesized powder were directly used for the XRD characterization. In case of films, grazing incidence XRD (GIXRD) is employed to examine the diffraction patterns. An angle of 0.5° is used for the grazing incidence XRD.
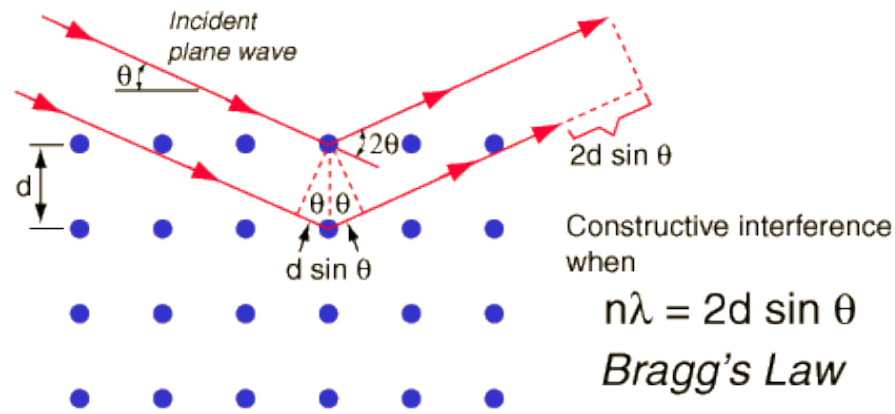
Figure 2.5.1 Schematic of Bragg's law (Ref 75).

In order to estimate the crystallite size, Debye Scherer's formula [75] was used as given by equation (2.2):

$$D = \frac{0.9\,\lambda}{\beta\cos\theta} \qquad\qquad (2.2)$$

Where, *D*- crystallite size, λ-wavelength, θ-diffraction angle and β-FWHM. In some part of this dissertation, Rigaku rapid d/Max Rapid 2 was used to record micro XRD patterns for different nanostructured film with a beam size of 100 μm at wide-angle X-ray scattering.

2.5.2. UV-Vis Spectrophotometry

The optical properties of semiconductors are generally studied by absorption measurements at room temperature with a UV/Visible/NIR absorption spectrometry. Optical bandgap (E_g) and absorption coefficient are well known related to photon energy by the following equation (2.3) [76]:

$$\alpha = \frac{K\ (h\nu - E_g)^{\frac{n}{2}}}{h\nu}\ \dots\dots\dots\dots\dots\dots(2.3)$$

Where K is constant, E_g is optical band gap, and n=1 for direct band gap material such as CdS. The band gap E_g is determined from the E vs. (αhv) 2 graph. The intercept on the energy axis obtained by extrapolating the tangent to the curve gives the value E_g. By measuring the absorbance of the materials vs. the wavelength of the incident radiation, one can calculate the absorption coefficient (provided thickness of the film is known) and hence, the bandgap of the material.
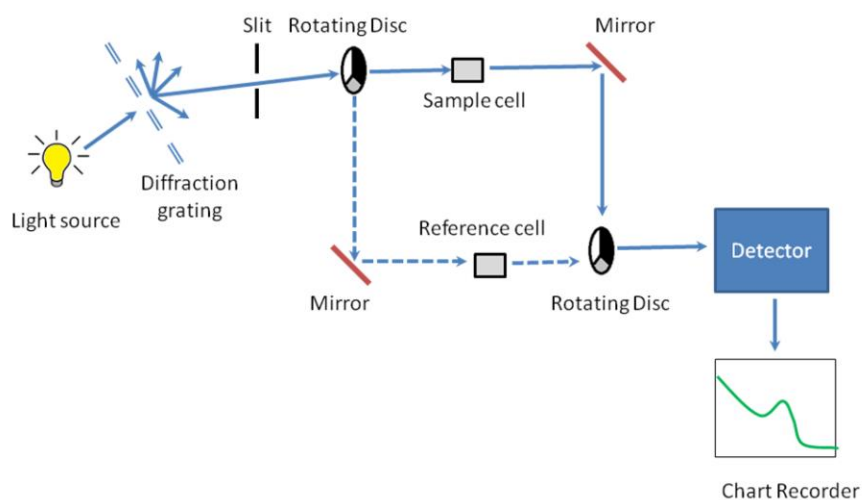
Figure 2.5.2 Schematic showing working details of UV-Vis spectrophotometry (Courtesy : *Physical Methods in Chemistry and Nano Science, 2009, Andrew R. Barron, Rice University*).

In general, an integrating sphere apparatus is used to record the transmittance spectra of the thin-films on any metal or metal coated glass substrate. The transmittance can then be converted to absorbance to determine the absorption coefficient. The simple schematic of working details of spectrometer can be seen in Figure 2.5.2.The optical properties were studied using Perkin-Elmer model lambda 650 spectrophotometer. The scan was taken in wavelength range of 200-800 nm.

2.5.3. Field Emission Scanning Electron Microscopy (FESEM)

FESEM provides the information about the samples based on the interaction of an accelerated high energetic electron beam with the matter (samples). The interaction results in the emission of secondary electrons, backscattered electrons, X-rays, etc. Knocking out of electrons from the samples by high energetic incident electrons occurs through the momentum transfer results in secondary electrons and without any momentum transfer leads to back scattered electrons. These emissions are then detected to analyze aspects such as surface morphology, particle size, cross-sectional morphology, composition, etc. of the samples. In general, secondary electrons and backscattered electrons provide the information about the morphological aspects and elemental contrast of the samples as shown in Figure 2.5.3. The analysis using the energy of emitted X-rays is usually known as energy dispersive X-ray spectroscopy (EDX or EDS) and provides the information about individual atomic composition of the samples since the energy of these X-rays depends directly on the atomic number of the atoms from which it is being emitted. EDX is a common tool to analyze the composition of samples qualitatively as well as quantitatively for atomic numbers above 10. It is also used as a local probe, for most samples, to detect the constituent elements since it spans an interaction volume of $\approx 1 \ \mu m^3$.

In the present study, a Hitachi – S4300SE/N field emission scanning electron microscope with an attached EDS (EDAX) detector has been used to study the morphology and composition of the samples. An accelerating voltage of 20 kV is used for the electron beam during the analysis. The working distance between the sample surface and electron beam is maintained in the range of 8 – 15 mm. For sample preparation, as deposited films on FTO and as synthesized nanoparticles are coated with gold prior to the analysis.
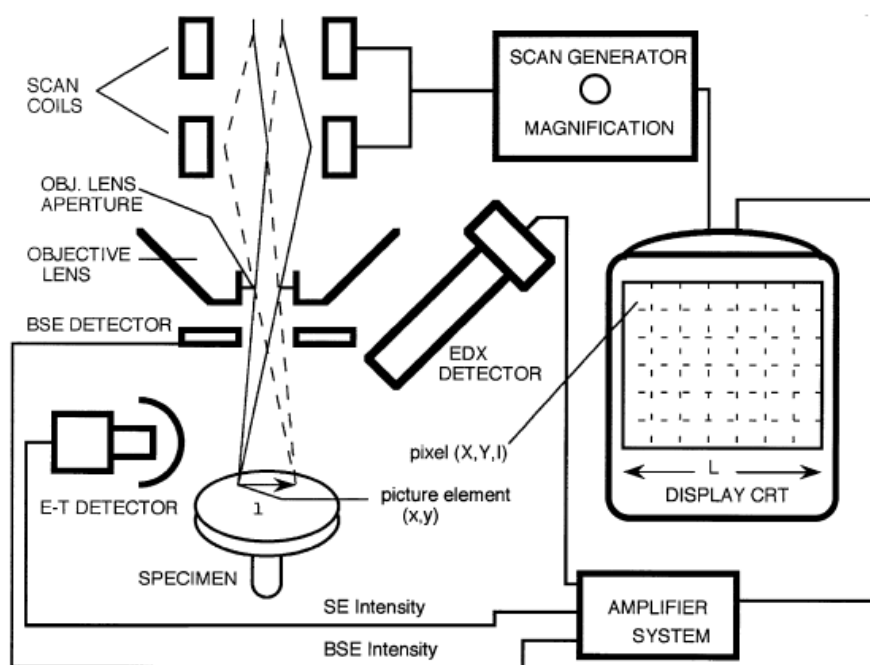
Figure 2.5.3 Schematic showing working principle of FESEM (Courtesy: *Characterization of Materials, E. N. Kauffman, 2003, Wiley Interscience*).

2.5.4 Transmission electron microscopy (TEM)

TEM is used to produce images from a sample by illuminating the sample with electrons (i.e. the electron beam) within a high vacuum, and by detecting the electrons that are transmitted through the sample as shown in Figure 2.5.4. It is an analytical tool allowing visualization and analysis of specimens in the realms of 1 nm. TEM reveals levels of detail and complexity inaccessible by light microscopy because it uses a focused beam of high energy electrons.
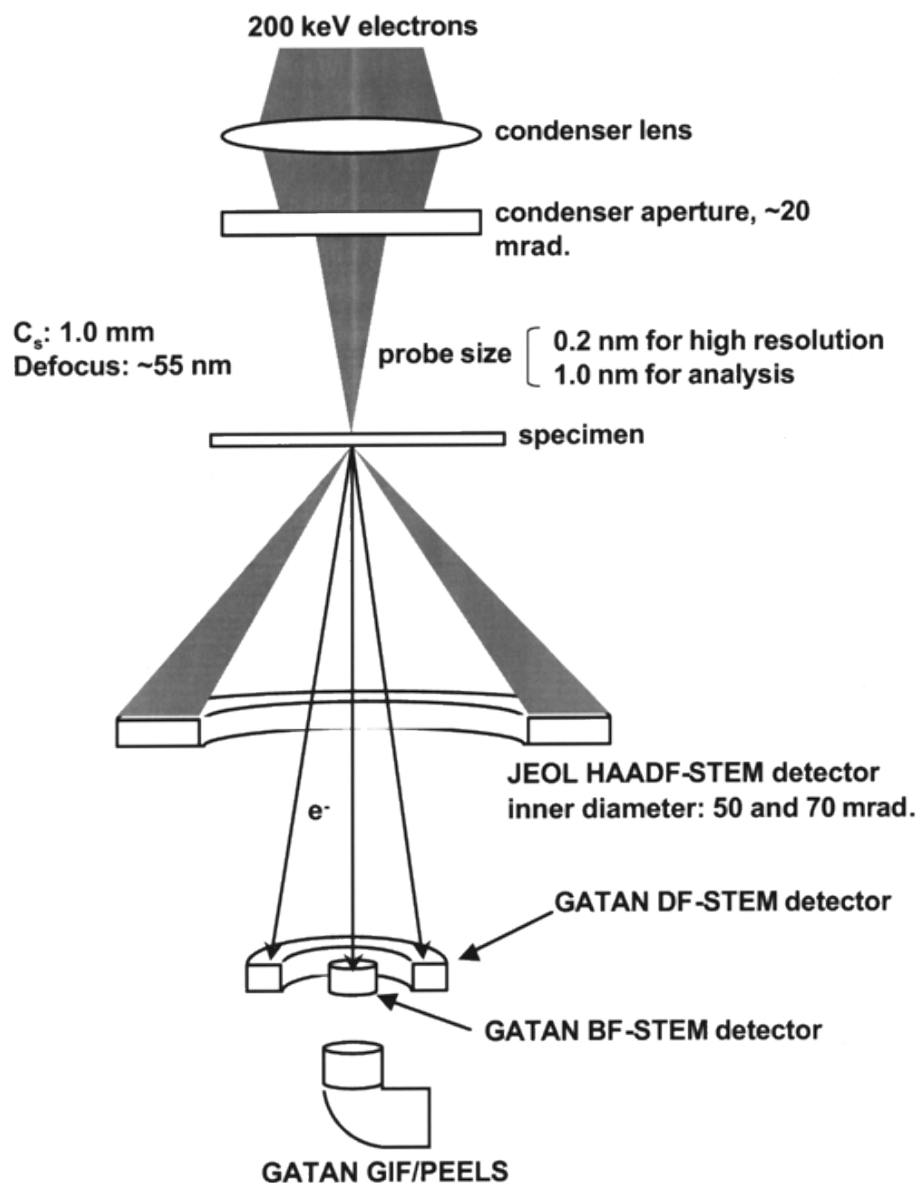
Figure 2.5.4 Schematic showing TEM microscope (Courtesy: *Santoshi et al, Envir. Sci. tech., 2013, 37, 786*).

It allows detailed micro-structural examination through high-resolution and high magnification imaging. It also enables the investigation of crystal structures, specimen orientations and chemical compositions of phases, precipitates and contaminants through diffraction pattern, X-ray and electron-energy analysis. Ultimately, using a TEM we can see the columns of atoms present in crystalline samples. FEI Tecnai G^2 transmission electron microscope with LaB_6 filament is used to record the HRTEM images of nanoparticles in the present study. An

accelerating voltage of 200 kV is used to energize the electrons. Samples were prepared by dispersing nanoparticles in ethanol. Ethanol suspension was finally dropped onto Cu grid for TEM analysis..

2.5.5 X-ray photoelectron spectroscopy (XPS)
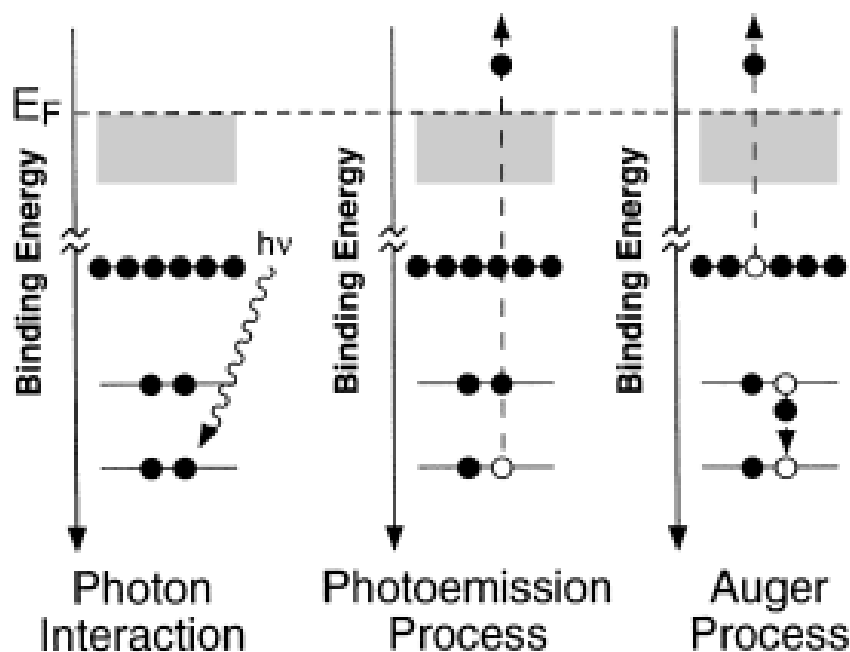
Figure 2.5.5 Schematic showing working principle of XPS (Courtesy : *Characterization of Materials, E. N. Kauffman, 2003, Wiley inerscience*).

XPS is a surface sensitive quantitative analysis technique for detecting elemental composition of compound. X-ray of particular wavelength (for Al K_α X-rays, E_{photon} = 1486.7 eV) is bombarded on the surface of sample and kinetic energy ($E_{kinetic}$) of emitted electron is measured. The binding energy of electrons is determined by the use of incident photon energy and kinetic energy of emitted electron ($E_{binding}$=E_{photon}-$E_{kinetic}$). Figure 2.5.5 shows working principle of XPS.

In present work, XPS (O-micron model) has been used for elemental and compositional analysis. The instrument has the capabilities of depth profiling by Ar ion etching, Imaging XPS, Auger photoelectron spectroscopy (static and scanning modes), sample heating (upto 100 ℃) and cooling (liquid N_2.). The technique being surface sensitive, it is very useful to characterize nanomaterials including, powders and thin films. As deposited films of area less than 1 cm^2 were used as sample for XPS analysis.

2.5.6 Fourier transform infrared spectroscopy (FTIR)
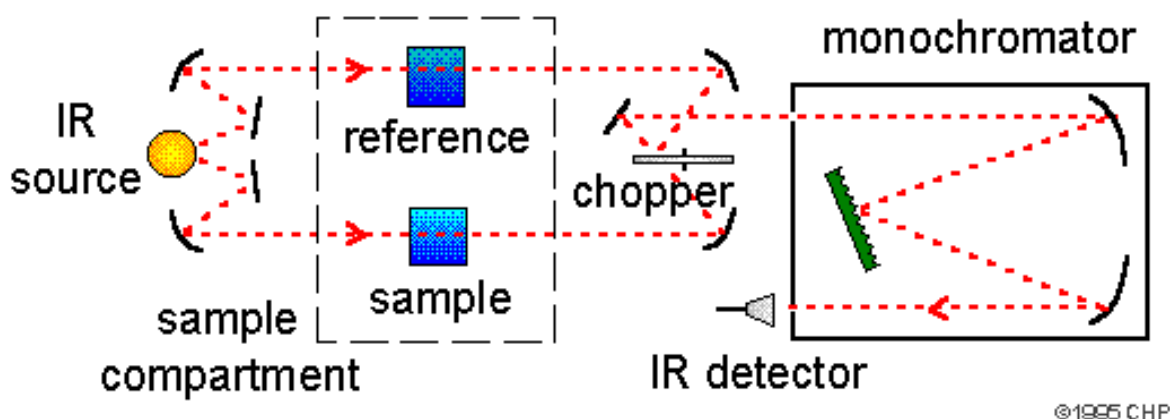
Figure 2.5.6 Schematic showing working principle of FTIR spectrometer (Courtesy : *Gaffney et al., 2012. Fourier Transform Infrared (FTIR) Spectroscopy. Characterization of Materials. 1–3*).

FTIR spectroscopy was used to detect various bonding and species present on the surface of material. Fourier transform infrared (FTIR) spectrum was recorded using a Spectrum GX Optica, Perkin Elmer, USA in the range of 4000 cm^{-1} to 500 cm^{-1}. FTIR spectrometers mostly constitute Michelson interferometer. It includes number beam splitter, number of mirrors that produces interference pattern at the detector as shown in Figure 2.5.6. For sample preparation, film on FTO was scratched to make 1 mg powder (as synthesized nanoparticles were used in case of

powder sample). This 1 mg of powder was mixed with 100 mg of KBr and transparent pellets were made to use as samples.

2.5.7 Raman Spectroscopy
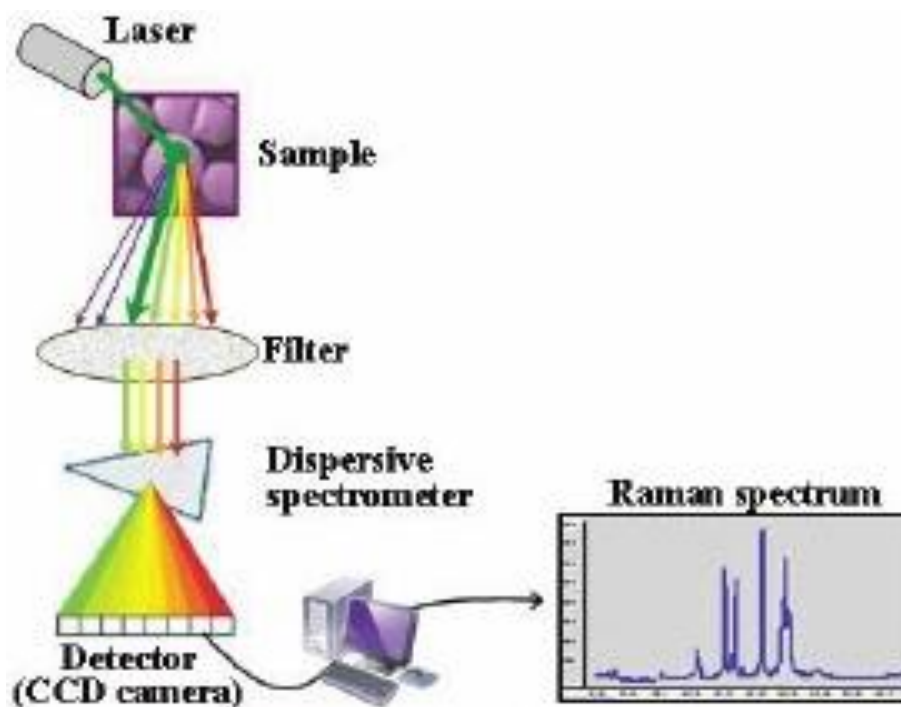
Figure 2.5.7 Schematic showing working principle of Raman spectrometer (*Salvas et al. Raman Spectroscopy to Analyze Intact Pharmaceutical Tablets: Factors Influencing MVPM-based PAT Methods, 2010, American pharmaceutical reviews*).

Raman spectroscopy is a technique based on the inelastic scattering of monochromatic light, usually from a laser source. Inelastic scattering means that the frequency of photons in monochromatic light changes upon interaction with a sample. Photons of the laser light are absorbed by the sample and then reemitted as shown in Figure 2.5.7. Frequency of the reemitted photons is shifted up or down in comparison with original monochromatic frequency, which is called the Raman effect. This shift provides information about vibrational, rotational and other

low frequency transitions in molecules. Raman spectroscopy can be used to study solid, liquid and gaseous samples. Raman scattering has been frequently used as a nondestructive, highly sensitive spectroscopic technique in the region of spectro-chemical analysis to investigate the structural characterization of a semiconductor compound.

Micro Raman provides phase identification; even traces of secondary phase can be detected as the polarization changes for different kinds of bonds that is detected in the Raman intensity. Raman spectra was recorded using Horiba Jobin Yvon; Labram Micro Raman Spectrometer in the range of 50 cm^{-1} to 4000 cm^{-1}. This Spectrometer has a resolution of 0.36 cm^{-1} and spot size of 1 micron. As deposited films of area less than 1 cm^2 were used as sample for Raman analysis.

2.5.8 Photoelectrochemical measurements

PEC measurements were carried out using two-electrode cell (or 3- electrode cell, wherever mentioned) with the photoanode as a working electrode and graphite (/platinum) as a counter electrode in a quartz PEC reactor. In case of 3-electrode cell, Ag/AgCl was used as reference electrode. The electrolyte was made using 0.01 M Na$_2$S & 0.02 M Na$_2$SO$_3$ to minimize the photo-corrosion. The solar simulator with AM 1.5 filter (Newport) having irradiance of 80mW/cm^2 was used as light source. In order to carry out the Incident-Photon-Current-Conversion Efficiency (IPCE) measurements, an Oriel monochromator capable of generating desired wavelengths (λ accurate up to ±2 nm) in the range of 200-900 nm was used. It was interfaced with gas chromatography (GC) equipment and an electrochemical set up (PARSTAT 2273). The schematic of PEC cell is shown in Figure 2.5.8.
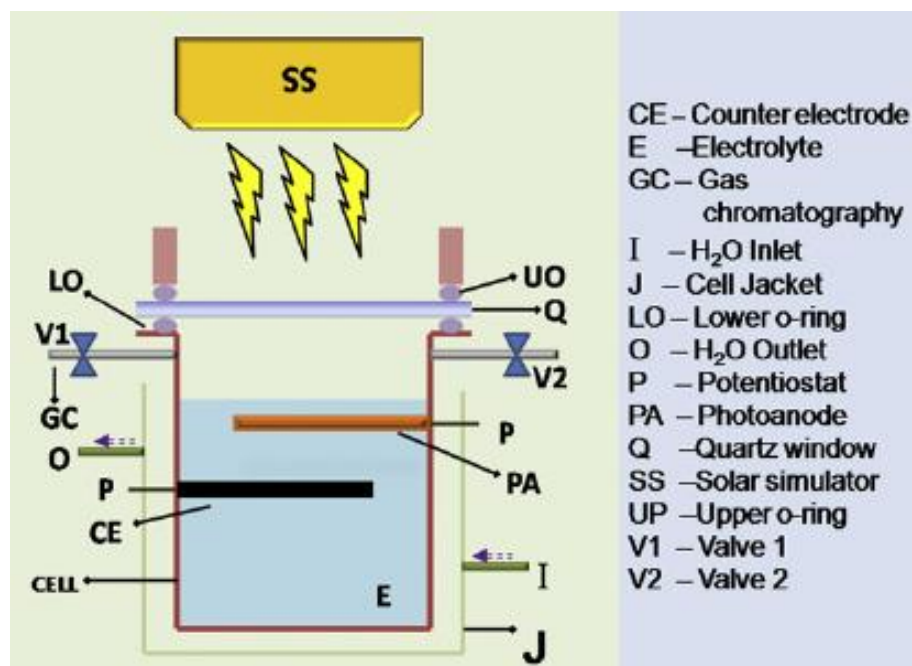
Figure 2.5.8 Image showing electrochemical workstation (Ref 62).

2.5.9 Gas chromatography (G.C.) Analysis

Quantitative detection of Hydrogen gas is important for this project. Shimadzu GC unit, GC-2010 plus model, was used in present work. Principle of gas G.C. is briefly given below.

Gas Chromatography is a physical method of separation of gases from a mixture after passing through a separating column having some absorbing material with the help of carrier gas. After separating the different constituents of the gas, it can be detected by using suitable detector. Nitrogen gas was used as carrier gas.

As shown in Figure 2.5.9 Gas Chromatograph has 3 parts:

1) Injection port:

Gas is injected in the gas chromatograph through injector port. This gas will be moved in with the help of carrier gas.

2) Column:

After Injection gas passes through column. In this part interaction between column and gas molecules takes place which decides the retention time of gas.

3) Detector:

Here TID (Thermal ionization detector) is used to detect gases. This detects gases based on thermal conductivity of gases.
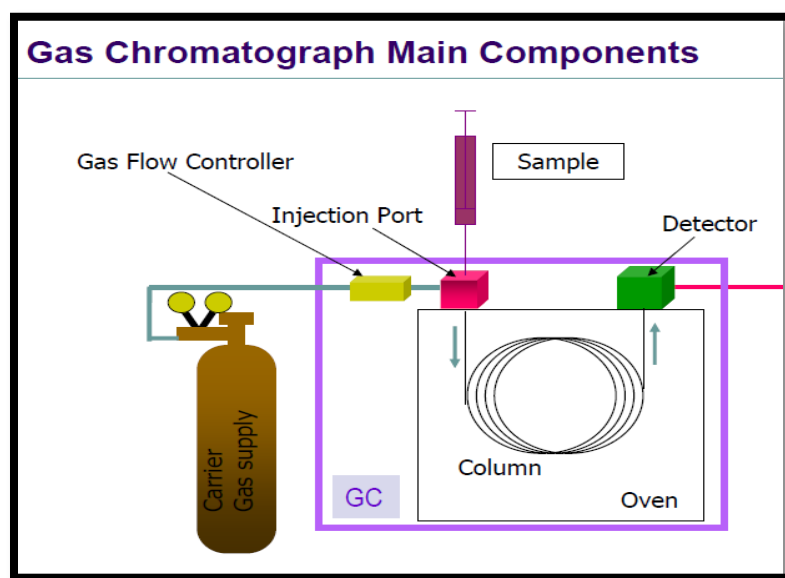
Figure 2.5.9 Image showing Gas chromatograph main components.

2.6 Efficiency calculations

This section explains the procedure for the calculation of different efficiencies required for the quantification of performance of PEC cell. This includes the calculation of incident photon to current conversion efficiency, solar to hydrogen conversion efficiency and power conversion

efficiency that are used throughout the dissertation for comparing the performance of PEC cell employing different modified electrodes.

2.6.1 Incident photon to current conversion efficiency (IPCE)

IPCE is one of the most important characterizations for PEC devices. It describes the photocurrent collected per incident photon flux as a function of illumination wavelength. IPCE was calculated for bare CdS and modified electrodes using the equation (2.4) [77]:

$$IPCE = \frac{1240 * J_{ph}}{P * \lambda}$$ ………………………… (2.4)

Where J_{ph} the photocurrent density in mAcm^{-2}, P is power of source in mWcm^{-2} and λ is wavelength in nm.

2.6.2 Solar to hydrogen conversion efficiency (STH)

STH (η_{STH}) was calculated for bare CdS and the most stable modified electrode at 0.2 V / SCE using following equation (2.5) [78]:

$$\eta_{STH} \ (\%) = \frac{(V_{rev} - V_{app}) * J_p}{I_0} * 100$$ ……………………….. (2.5)

Here V_{rev} is standard reversible potential *i.e.* 1.23 V, I_0 is power intensity of source *i.e.* 80 mWcm^{-2} and

$$V_{app} = V_{meas} - V_{oc}$$ ……………………………………… (2.6)

Where, V_{oc} is open circuit potential and V_{meas} is the potential at which photocurrent measurements are carried out with respect to a reference electrode (SCE).

2.6.3 Power conversion efficiency

Power conversion efficiency (η) was calculated using equation (2.7) [79]:

$$\eta = \frac{V_{oc} \times I_{sc} \times F.F.}{P_{input}} \times 100\% \text{.. (2.7)}$$

Where, V_{oc} and I_{sc} are the open circuit potential and short circuit current *respectively* and fill factor (F.F.) is given by equation (2.8):

$$F.F = \frac{V_m \times I_m}{V_{oc} \times I_{sc}} \text{..(2.8)}$$

Where, I_m and V_m are the current and voltage obtained at the maximum-power point on the photovoltaic power output curve, *respectively*.

The efficiency of PEC cell for all modified and unmodified CdS photoanodes were calculated throughout the dissertation using the above formula equation (2.4) to (2.8).

Chapter -3

RESULTS AND DISCUSSION

This chapter includes the complete details of results and discussion section pertaining to the work presented in this dissertation. Briefly it describes the optimization of *deposition parameters* of CdS attained while using the spray pyrolysis method to achieve the standard ***CdS photoanode*** (PART-I). This ***standard reference electrode*** is further subjected to various types of surface modifications using metal-oxide nanoparticles (PART-II), *co*-catalyst colloids (PART-III) and the conducting polymers (PART-IV) that are desirable to improve the photo-stability of CdS.

RESULTS AND DISCUSSION

PART- I

Optimization of CdS photoanodes

Outcome: Fabrication of large area nanorod like structured CdS photoanode for solar H_2 generation using spray pyrolysis technique, International Journal of Hydrogen energy, 2012, 36, 1; Photoelectrochemistry of nanostructured CdS photoanodes: High efficiency improvement from nano-architectures (*submitted to chemistry of materials*).

Motivation: PART-I describes the minute details of optimization method carried out during the CdS thin film deposition using spray pyrolysis technique. This part constitutes variation of different deposition parameters *viz.* flow rate (*section 3.1*), deposition time (*section 3.1*), and thickness of film (*section 3.2*). These parametric variations are desirable to obtain the nanostructured films. Subsequent to the deposition of CdS films, their complete characterization techniques are presented in the *section 3.1 and 3.2*.

3.1 Nano-structuring of CdS photoanode

In this work, nano-structuring [80] has been utilized to impart an efficiency improvement of CdS photoanode in PEC cells. In spray pyrolysis technique, by controlling the aerosol droplet size, its population and its impingement time, various nano-features *viz.* aligned nanorods, nanotubes and nanowires of CdS have been demonstrated for the first time. The growth mechanisms have been proposed to predict the temporal evolution of the nanostructures. The prominent nanoscale structures show improved optical properties in the visible range of solar spectrum. The structural studies validate the morphological differences of nanostructures in terms of their texture coefficient analysis. Electrochemical characterization has been carried out to understand the effect of nanostructuring on PEC performance of CdS photoanodes in sulphide (0.1 M Na_2S + 0.02 M Na_2SO_3) electrolyte at 0.2 V (vs. SCE) applied bias. The evolution of morphology from aligned rods to nano wire is responsible for improved photocurrent (3.5 times). The morphology CdS film can be tuned into nanotubes, nano-rose buds and nanorod bunches by doping Zn^{2+} ions in CdS lattice. Nano-structuring of doped CdS has shown enhanced performance of the photoanodes. The nanotube structured yielded highest photocurrent density of 1.6 mA/cm^2.

3.1.1 Morphological studies of nanostructured films

This section presents the change in film morphology with increase in the flow rate and deposition time. As shown in Figure 3.1.1, with an increase in the flow rate the morphology of the CdS film changes from aligned nanorods to porous protrudes and becomes dense with further increase in the flow rate. Thus, an increase in the flow rate leads to an increase in the solvent concentration of the aerosol, which in turn delays the precipitation process and hence forms a solid dense structure. These solid protrudes are transformed into mesh-like nanowires with further increasing the flow rate of precursor.
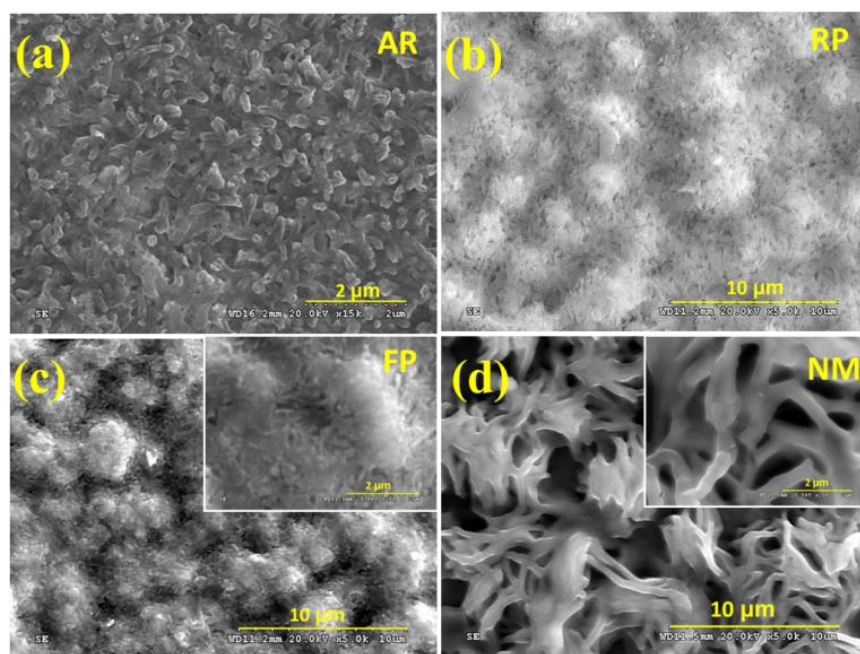
Figure 3.1.1 Change in the morphology of CdS films with variation in the flow rate as (a) 5 ml/min, (b) 6 ml/min, (c) 8 ml/min and (d) 9 ml/min, *respectively* during spray pyrolysis deposition. Inset shows magnified images of corresponding film.

Further, study has been carried out to reveal the effects of deposition time on morphology of CdS thin films. Figure 3.1.2 shows systematic evolution of nanowires with increase in the deposition time.
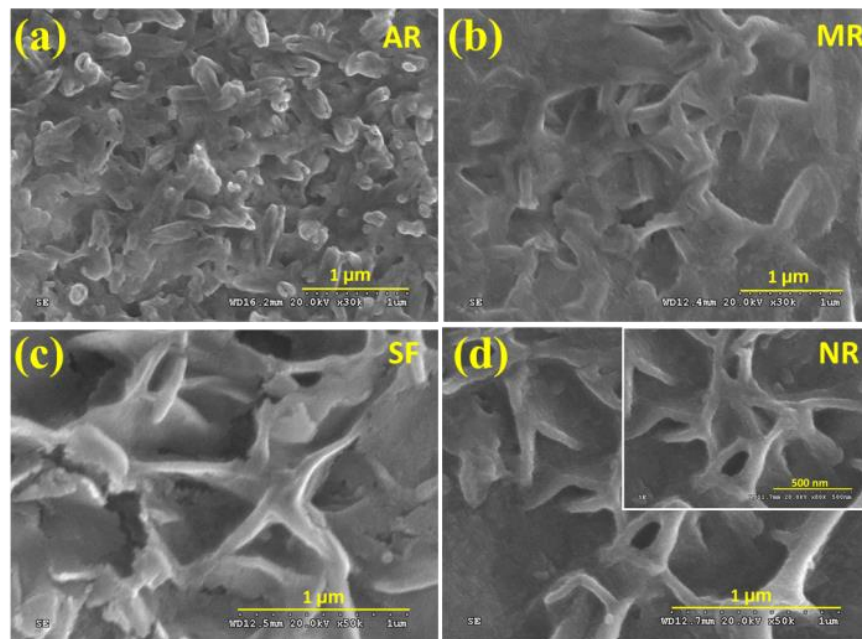
Figure 3.1.2 Change in the morphology of CdS films with the variation of the deposition time as (a) 1 min (b) 3 min (c) 4 min (d) 6 min, during spray pyrolysis deposition. Inset shows magnified images of corresponding film.

At lower deposition time and flow rate, aligned nanorods are observed as shown in Figure 3.1.1 (a) and 3.1.2 (a). As the deposition time increases the rods start merging into each other as shown in Figure 3.1.2 (b) and with further increase in the deposition time it is transformed into starfish like feature. These features acquire the shape of nanowires for 6 min of deposition time. From this study, it is also clear that by optimization of the flow rate and deposition time, *aligned nanorods* can be transformed into *nanowires* and *nanowire mesh* like feature. The growth mechanism of these nanostructures can be correlated with the parameters of spray pyrolysis and can be explained through Scheme 3.1.1. As a brief extension of this work, for the sake of completeness, we have studied the evolution of CdS nanostructures with incorporation of Zn^{2+} ions in CdS host lattice. This indicates that under favorable condition of dopant in the host crystal lattice, a structured morphology can be generated. Scheme 3.1.1 (a) clearly shows how

the spray pyrolysis technique grants access to tune the material property by change in deposition time, temperature, flow rate and nozzle to substrate distance, carrier gas *etc.* Scheme 3.1.1 (b) shows that with variation in deposition time and flow rate the various morphologies have evolved by using spray pyrolysis method.
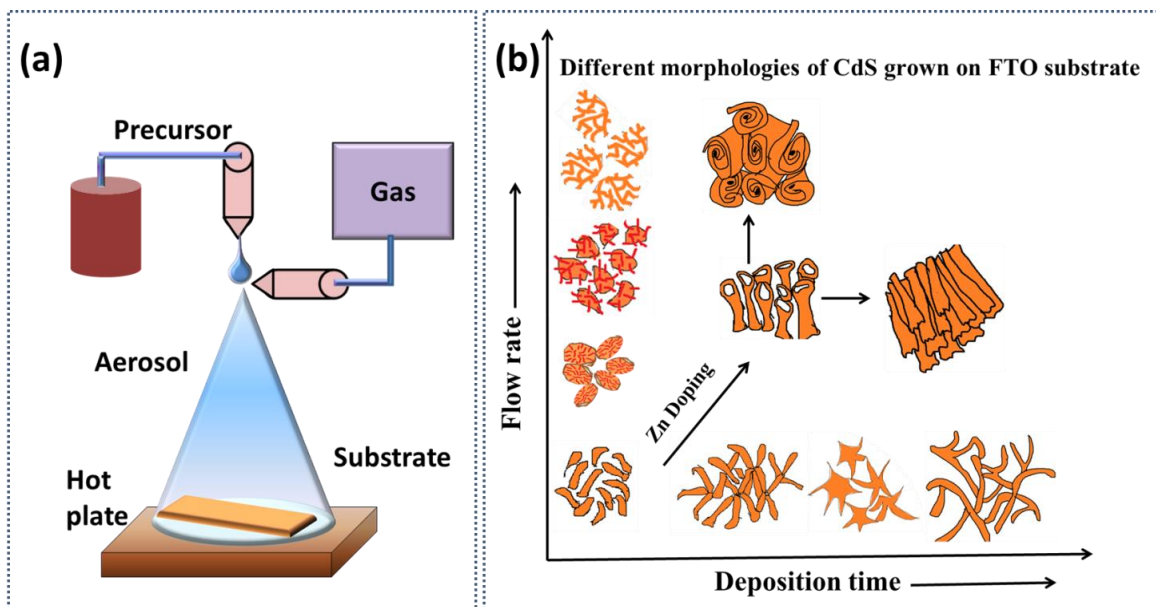
Scheme 3.1.1 (a) Schematic of spray pyrolysis deposition equipment and (b) Mechanism of formation of various nanostructures with change in flow rate, deposition time and doping Zn in CdS lattice. Further change in morphology of Zn doped CdS films with increase in flow rate and deposition time is shown.

Figure 3.1.3 (a) shows typical FESEM image of the Zn doped CdS thin films deposited at 5 ml/min (1 min deposition time). It displays the formation of nanotubes from aligned nanorods due to doping Zn^{2+} ions in CdS lattice under similar condition of the undoped counterpart. Figure 3.1.3 (b) shows the formation of rosebuds like features obtained at the higher flow rate of 9 ml/min and bundled rods like structures have been obtained with increase in deposition time as shown in Figure 3.1.3 (c).

Table 3.1.1 Effect of flow rate and deposition time of spray deposited CdS photoanodes on its morphology, V_{oc}, I_{sc} and J.

S.No.	Name	Flow rate (ml/min)	Deposition time (min)	Morphology	Absorption coefficient (cm^{-1}) at 550 nm	V_{OC} (V)	J_{SC} (mA/cm^2)	J (mA/cm^2) at 0.2 V/SCE
1	AR	5	1	Aligned nanorods	4.0	0.70	0.5	0.48
2	RP	6	1	Rough spherical protrudes	13.9	0.81	1.1	1.0
3	FP	8	1	Dense spherical protrudes	13.2	0.58	1.2	1.3
4	NM	9	1	Nanowire mesh	16.9	0.78	1.8	1.5
5	MR	5	3	Merged rods	6.0	0.95	0.6	0.67
6	SF	5	4	Star Fish	4.5	0.92	1.0	1.00
7	NW	5	6	Nanowires	5.9	0.96	1.3	1.20

This further confirms that increase in the flow rate yields *solid-structures*, whereas increase in the deposition time leads to the *wire* and *rod like* of morphologies. We have assigned suitable abbreviation for each CdS nanostructures with respective deposition parameters as summarized in Table 3.1.1 and Table 3.1.2. Figure 3.1.3 (d) shows the morphology of film that was quenched instead of slow cooling to room temperature. It is important to note that the name convention shown in column two (Table 3.1.1 and Table 3.1.2) has been used *throughout* in this section for the sake of understanding.

Table 3.1.2 Study of effect on morphology and PEC performance by variation in flow rate and deposition time of spray deposited Zn doped in CdS photoanodes

S.No.	Name	Flow rate (ml/min)	Deposition time (min)	Morphology	J (mA/cm^{-2}) at 0.2 V/SCE
1	NT	5	1	Nanotubes	1.0
2	RB	9	1	Rose buds	1.6
3	NRB	5	3 m	Nano rod bundles	1.2
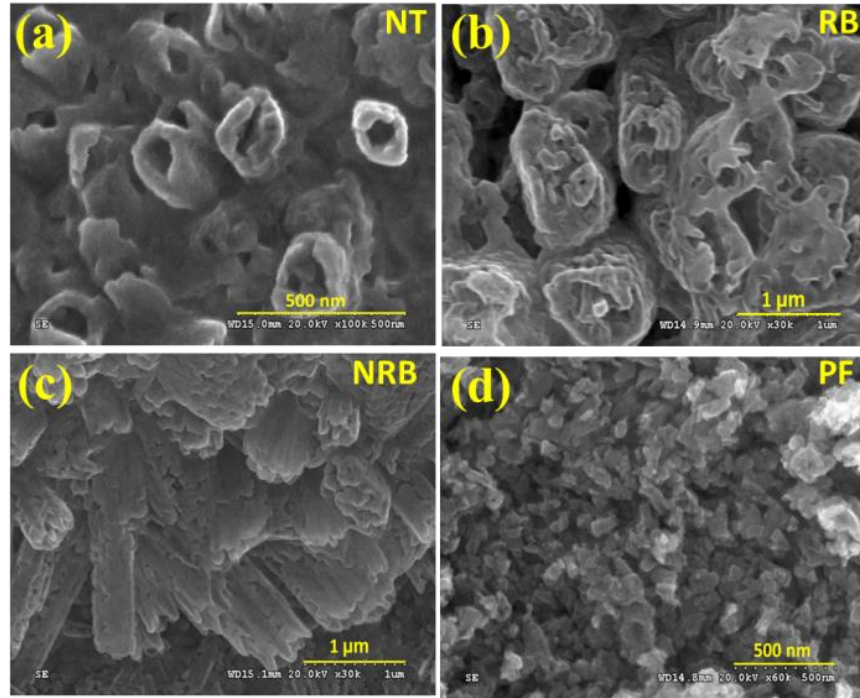
Figure 3.1.3 Variation in the morphology doped CdS films with the variation in the deposition time and flow rate of spray pyrolysis deposition (a) 1 min at 5ml/min (b) 1 min at 9 ml/min (c) 3 min at 5 ml/min (d) 1 min at 5ml/min quenched films

3.1.2 Structural and optical properties of nanostructured films

This section provides the correlation between film morphology with the structural and optical properties of the film. Figure 3.1.4 reveals the micro XRD pattern for the CdS thin film of different nanostructures. The peaks could be clearly assigned to the hexagonal wurtzite CdS (JCPDS No. 04-008-8223). All films has shown multidirectional growth indicating the polycrystalline nature. To identify the preferentially oriented of growth CdS film, their texture coefficient was calculated using equation (3.1.1) [81-82] :

$$TC(hkl) = \frac{I\,(hkl)}{I_0\,(hkl)} \left(\frac{1}{n} \sum \frac{I\,(hkl)}{I_0(hkl)} \right) \dots\dots\dots\dots\dots\dots\dots\dots\dots \text{(3.1.1)}$$

Where *TC (hkl)* is the texture coefficient of specific plane *(hkl)*, *I (hkl)* is the intensity of *(hkl)* plane measured from XRD pattern, I_0 *(hkl)* is the intensity of (*hkl*) plane taken directly from the JCPDS file and *n* is the number of peaks considered for calculating *TC(hkl)*. If *TC (hkl)* is greater than unity, it indicates the preferential growth of the grains in particular *(hkl)* direction. Here, *TC* is calculated considering seven planes *viz.* (100), (002), (101), (110), (103) and (112); it is as summarized in the Table 3.1.3. AR film has shown *TC*>1 for (002), (110), (103) and (112) planes which implies the existence of aligned nanorods like morphology, which are oriented in respective growth directions. NT film has shown *TC (002)* ≈ 2, which has shown preferential growth of nanotubes along *c*-axis and are, oriented perpendicular to the substrate. However, it is also observed for the NT films that *TC* >1 along (103) and (112) planes, which is because the nanotubes are not uniformly and perfectly vertically aligned. NW and NM have shown film growth along (002), (103) and (112) planes. This is consistent with the nanowire like morphology for both the films. However, in the case of NM films *TC* (103) >*TC* (002), this leads to a two-dimensional growth of wires in NM films and hence probably wire mesh feature is obtained. Whereas, in the case of NW, *TC (002)* is predominated over *TC (103)* thus generating a one-dimensional wire based nano-architectures. The above analysis supports a probabilistic mechanistic evolution of various nano-morphologies in CdS thin films during the film deposition.

In PEC cells, the generation, spatial separation and collection of electron holes pairs are important processes. The generation of charge carriers is effectively dependent on the absorption and capturing of incident solar radiation, is decided by the absorption length of the semiconducting material.
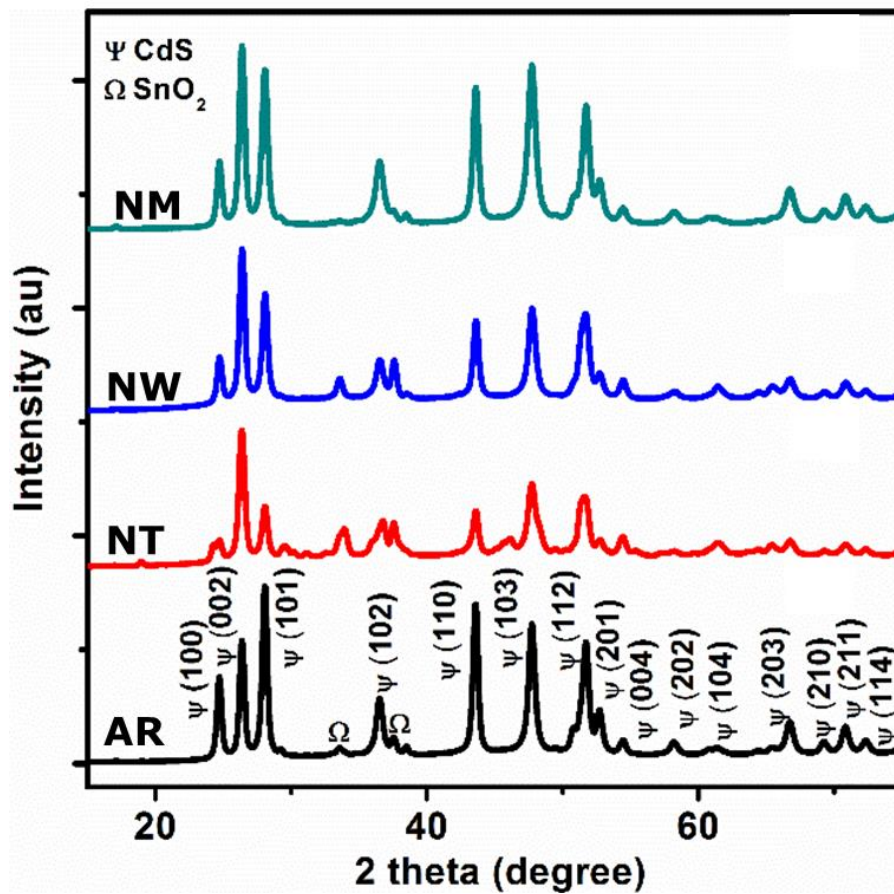
Figure 3.1.4 Micro XRD pattern of various nanostructured CdS thin film deposited by spray pyrolysis deposition technique.

Latter two phenomenons depend on how efficiently charges are transferred without the recombination losses, which ultimately relies on the diffusion length of the charge. For efficient charge separation and transfer processes, it is highly desirable to have a shorter absorption length than the diffusion length of the charges. Unfortunately, most relevant materials in PEC cells show mismatch between the desired absorption length and diffusion length of the charge carriers.
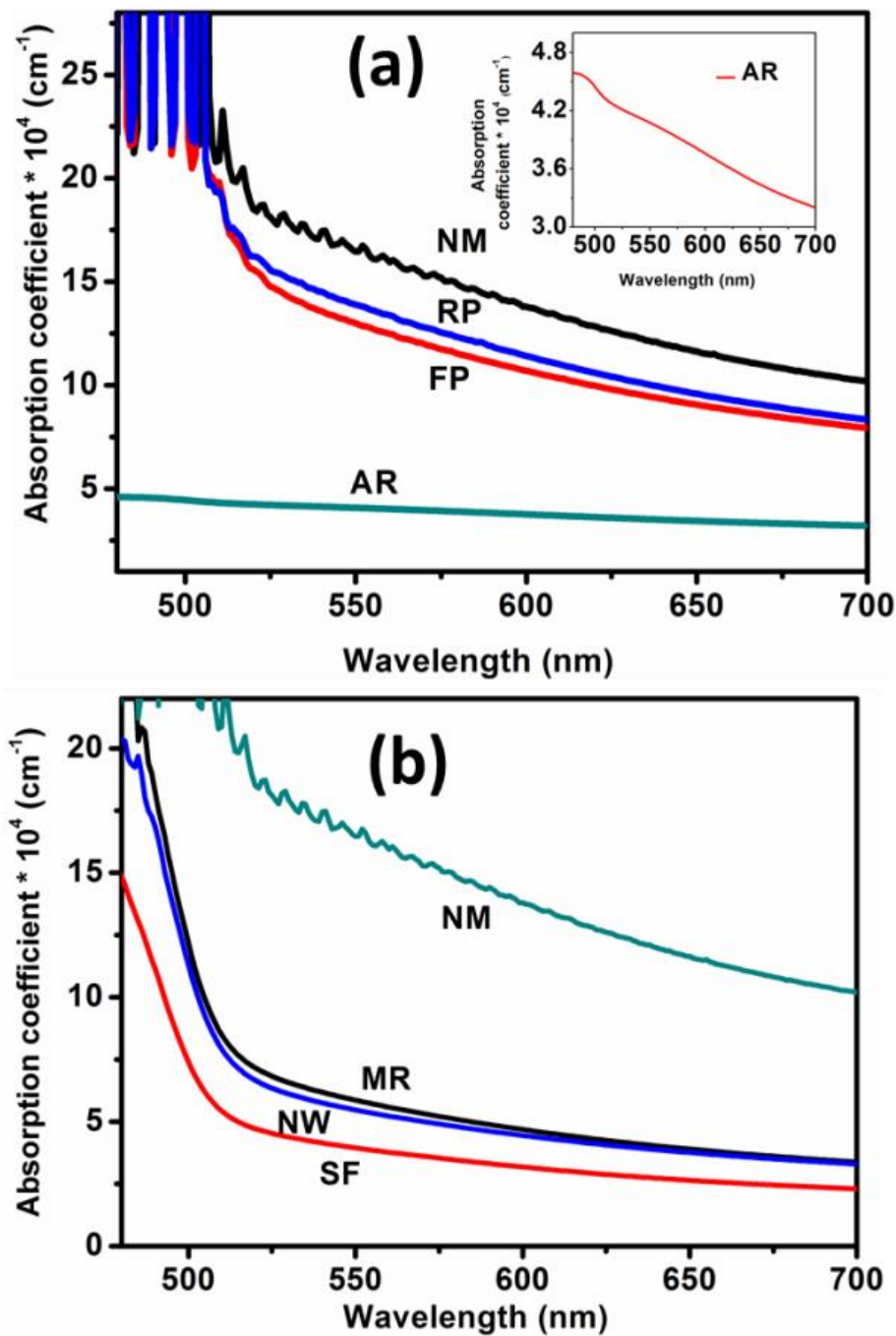
Figure 3.1.5 Absorption coefficient of CdS thin film with the variation in the (a) flow rate (inset shows absorption coefficient of AR) and (b) deposition time (NM is also added to compare) of spray pyrolysis deposition technique.

Nanostructuring is a potential technique capable of tuning the optical property, thus improving the light absorption to yield high operational efficiencies. Nanostructuring improves the optical

properties (band gap and absorption coefficient) of the semiconducting materials by controlling the "size" and "shape" of materials. Engineering a distinct nano-feature in a semiconducting material renders them a large surface area and nanoscale volumes to absorb maximum light, which also facilitates scattering of photons over nanostructure surface and ensures better utilization of incident light. Therefore, it is highly important to study the optical properties of various nanostructures of CdS deposited in this study. Figure 3.1.5 shows the absorption coefficient spectra with respect to wavelength calculated from UV-Vis spectrophotometry measurements. It is evident that with the evolution of different nanostructures the absorption coefficient increases.

Table 3.1.3 Calculated texture coefficient and crystallite size of respective nanostructures of CdS films.

Sample name	Texture coefficient (*hkl*)							Crystallite size (nm)
	(100)	(002)	(101)	(102)	(110)	(103)	(112)	
AR	0.60	1.07	0.80	0.92	1.51	1.45	1.45	19.0
NT	0.41	1.99	0.42	0.98	0.75	1.32	1.26	16.4
NW	0.42	1.68	0.61	0.78	0.93	1.20	1.32	19.1
NM	0.41	1.42	0.63	0.86	0.85	1.53	1.31	16.8

Film with nanowire mesh like structures (NM) has highest absorption coefficient (14.8 x 10^4 cm^{-1} at 550 nm) at all wavelength range. Nanowire (NW) has higher value of absorption coefficient with respect to the film deposited at different deposition time. Therefore, it is quite clear that nanostructuring induces a drastic improvement in the optical properties of semiconducting materials.

3.1.3. Photoelectrochemical performance of nanostructured films
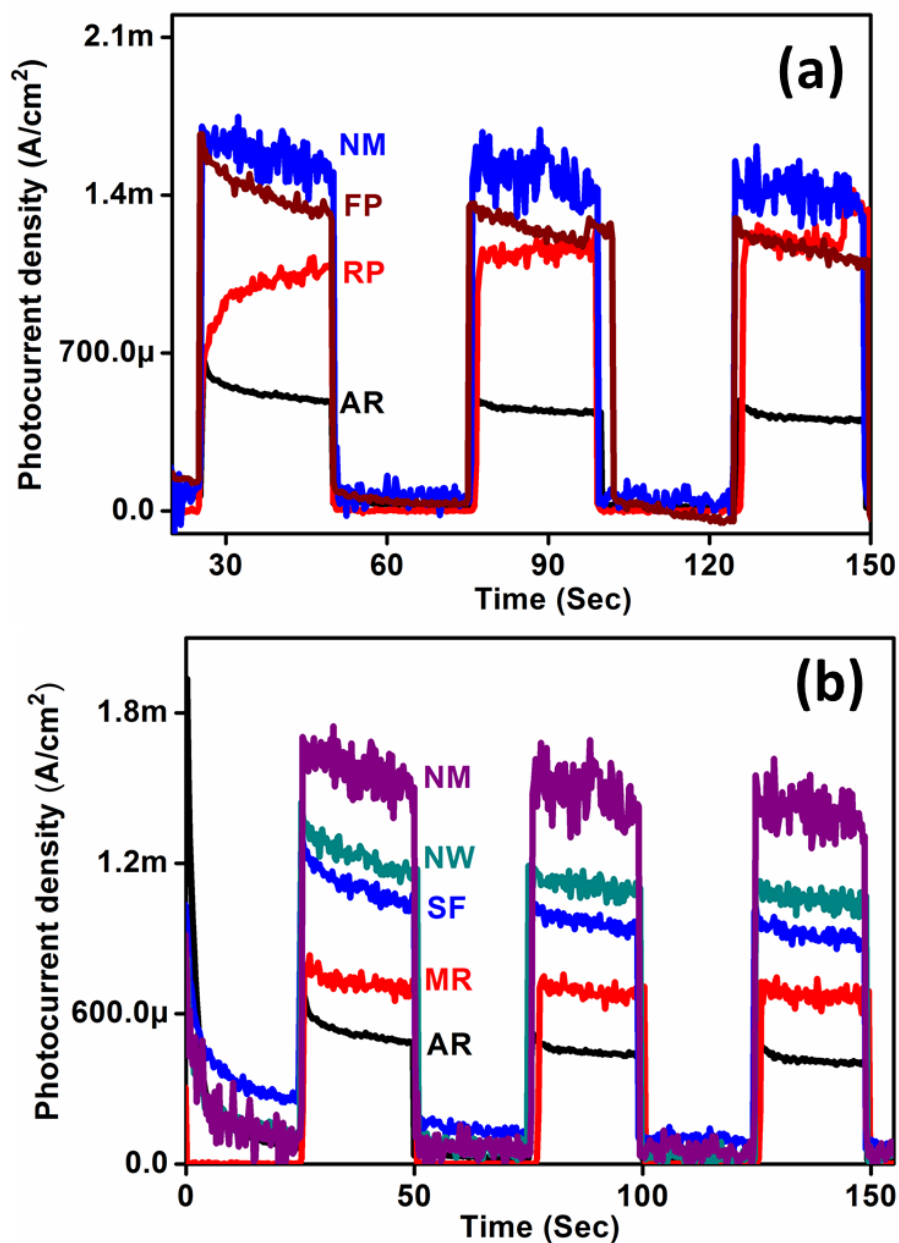
Figure 3.1.6. Chronoampereometric curves of CdS photoanodes deposited at different (a) flow rate and (b) deposition time of spray pyrolysis deposition technique

To understand the direct impact of nanostructuring on the improved electrical properties of CdS photoanodes, their PEC measurements were carried out. An electrolyte of Na_2S/Na_2SO_3 was

used to provide a necessary scavenging agent in order to curb the photocorrosion and to provide a rectifying contact for nanostructured CdS photoanodes.

The chronoampereometric measurements were carried out in a three-electrode system under 100 mW/cm^2 AM 1.5 solar simulator. As expected nanowire mesh like structures generates highest photocurrent density of 1.5 mA/cm^2 as shown in Figure 3.1.6 (a).
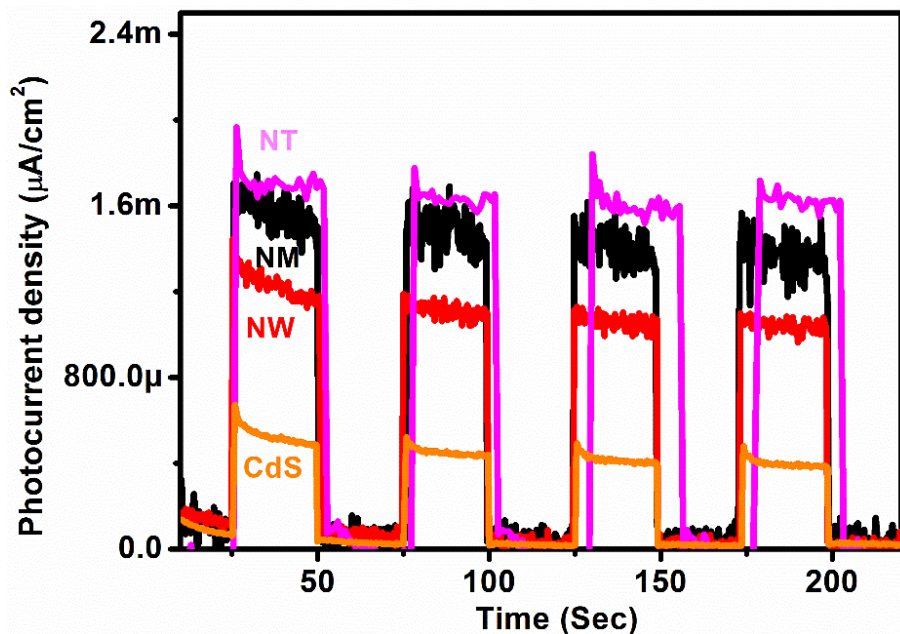
Figure 3.1.7 Chronoampereometric curve of doped (NT), undoped nanostructured CdS thin film.

Enhancement in photocurrent is observed for all the nanostructured films with the increase in flow rate. Similar results are obtained for the nanostructures formed with the increase in deposition time as shown in Figure 3.1.6 (b). The highest photocurrent density of 1.2 mA/cm^2 is achieved for nanowire film. The PEC performance of all nanostructured CdS thin film exhibits a clear correlation with the enhanced absorption coefficient, which explained the better performance of NM films. The conclusion drawn from above analyses is clearly demonstrated from Table 3.1.1. It can be noted that, the results are pertaining to undoped CdS electrodes.

It is known that introduction of a defect in certain crystal structure (*as hexagonal crystal of CdS and ZnO*) [83] facilitates the formation of nanostructures. This is clearly demonstrated in this work that Zn doped CdS results in nanotubes, rose bundles and nanorod bundles. The optical properties of the doped nanomaterials differ from corresponding host material, as dopants induce defect states in the host bandgap. Analogously, introduction of transition metal ions in cadmium sulphide enhances its electrical properties. It also enhances the chemical stability and renders a longer exciton lifetime. Zinc is an interesting element to substitute Cd site in the CdS lattice in view of their similar crystal structure and lattice parameters. The Zn doping in the CdS lattice improves the degree of crystallinity, shifts the conduction band position and improves the light absorption [84]. To realize the above-proposed facts we have studied the morphological evolution and effect of Zn doping on PEC performance of CdS photoanodes. Importance of Zn doping in CdS can be realized by the prominence of CdZnS in PEC research [85]. Doping of Zn in the CdS lattice induces further improvement in the photocurrent. As shown in Figure 3.1.7, the photocurrent density is improved to 1.6 mA/cm^2 after doping. The improvement in morphology and PEC performance of CdS thin films after Zn doping is tabulated in Table 3.1.2.

3.1.4   Summary of this section

The nanostructuring of CdS thin films has been demonstrated by making use of simple and cost effective spray pyrolysis deposition technique for the first time. Flow rate and deposition time have been controlled to obtain different nano-architects *viz.* aligned rods; nanowire and nanowire mesh of CdS on FTO substrate. Zn^{2+} incorporation in the lattice facilitates the formation of nanotubes, rose buds and bundled nanorod like structures. The growth mechanism has been deduced for the evolution of different nanostructures, which is further supported, by micro XRD

analysis and approximation of texture coefficient analysis that validates for film growth in preferential direction. The high absorption coefficient is achieved for film with more prominent nano features and large surface area. The evolution of morphology with increase in the flow rate from rods to nanowire has improved photocurrent by 3 times, thus yield highest photocurrent density of 1.5 mA/cm^2. Doping of Zn in CdS lattice enhanced PEC performance of NT photoanodes exhibiting a photocurrent density of 1.6 mA/cm^2. The study envisages the implication of nanotechnology in realizing an improved and efficient performance of CdS photoanodes. This is achieved by simple cost effective, economically viable and scalable spray pyrolysis deposition technique.

3.2 Optimization of CdS film thickness

This section includes the thickness optimization of CdS thin films using spray pyrolysis method. It has been found that optimized photoanode yields the Solar-to-Hydrogen conversion efficiency (STH) of 0.2 % under solar simulator (AM 1.5) with 80 mW/cm^2 irradiance. The 500 nm thick film exhibits uniformly distributed nano-rod feature and yields *3*-times more photocurrent as compared to bare CdS. Superior optical properties display a direct optical bandgap of 2.4 eV, and a high crystallinity that exhibits a hexagonal phase of CdS with space group *P63MC*. Nanostructured morphology is attributed to the superior performance of the film (photoelectrode) deposited under the optimized conditions.

3.2.1 Structural and optical properties of films

Based on thickness of CdS films deposited by varying number of cycles of deposition, films are named as shown in Table 3.2.1. Figure 3.2.1 shows XRD pattern for the films (A, B and C)

deposited at optimized temperature (350 ℃). All the films exhibit hexagonal crystal structure of CdS lattice that belongs to P*63MC* (SG no. 186) space group. There are no traces of any impurity phase of CdO are observed. The crystallinity is increased from A to C, with the increase in the net-deposited content on the substrate. The peak for FTO substrate peak (200) is appeared in all
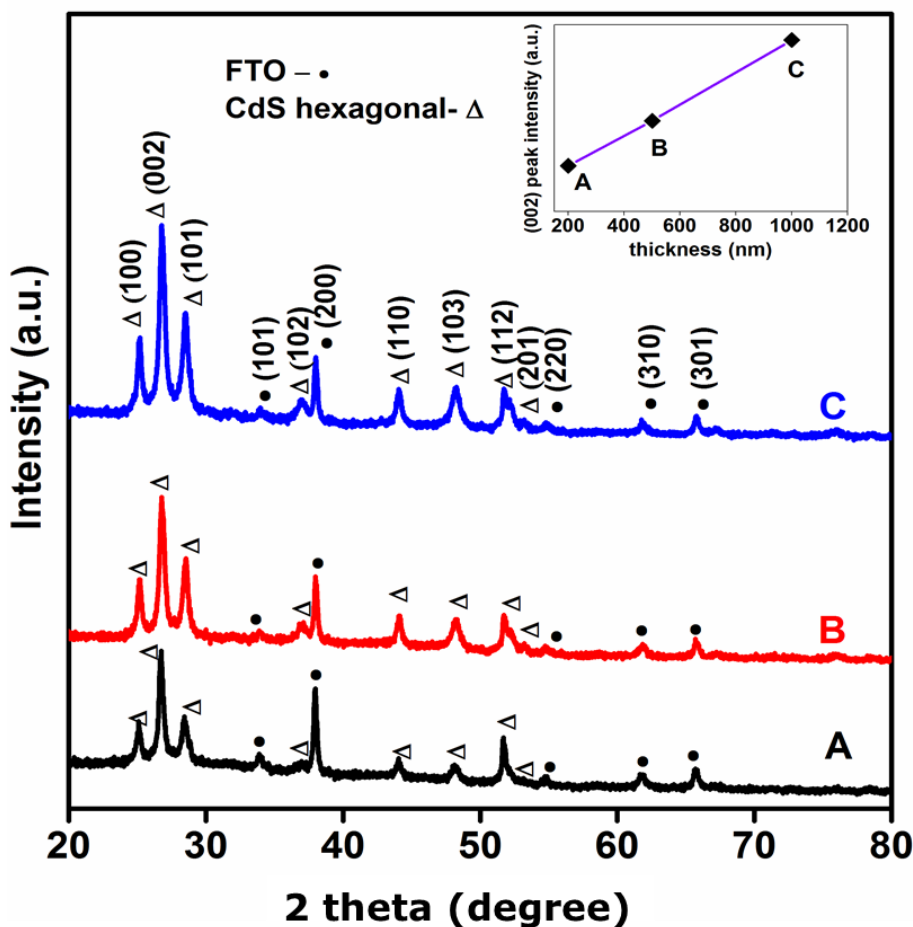
Figure 3.2.1 XRD patterns of CdS film deposited with different thickness *viz*. A (200 nm), B (500 nm) and C (1000 nm). Substrate (FTO) peaks are indicated by solid circle. Inset shows the change in (002) peak intensity with the increase in the film thickness from A to C.

samples. The inset of the Figure 3.2.1 displays the variation in (002) peak intensity with change in film thickness from A to C, which indicates the effect of film thickness on its crystallinity. On the contrary, the intensity of (200) peak of FTO is found to be decreased due to increase in the film thickness.

70

Table 3.2.1 Films deposited at 350 ˚C are named based on the deposition cycles and observed film thickness as characterized from cross-section measurements.

Film Name	No. of Deposition cycles	Thickness* (nm)
A	5	200
B	10	500
C	15	1000
*Results obtained from FESEM (cross-sectional studies)		
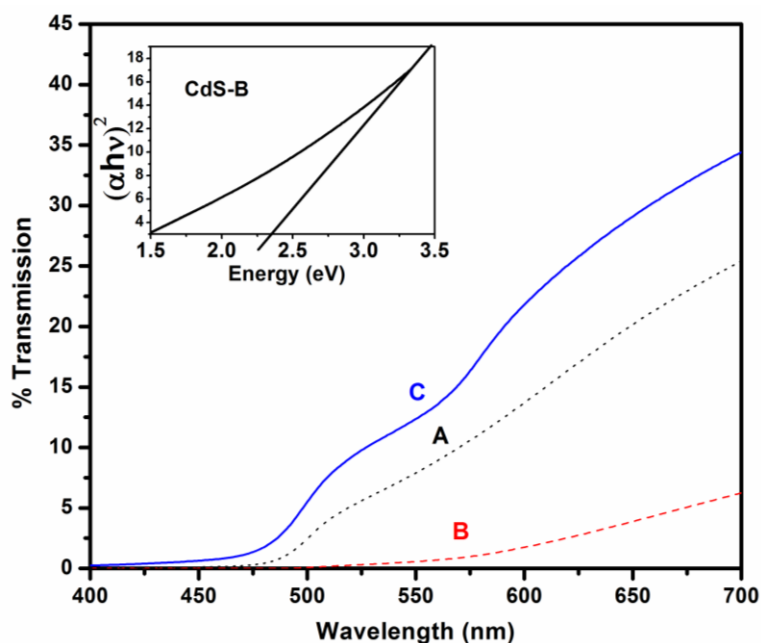
Figure 3.2.2 Transmission spectra of CdS films deposited for thickness of: A- 200nm, B-500nm and C-1000nm. Inset shows Tauc plot of CdS-B film that has been used for band gap estimation.

Figure 3.2.2 shows the optical transmission spectra for the CdS films A to C, indicating the absorption edge for film B at wavelength longer than 500nm. Film B exhibited very low transmission than film A and C, confirming its high absorptivity towards visible light photons. Films A and C display a systematic variation in transmission with increase in thickness from film

A to C. Band gap is estimated using Tauc plots analysis. Inset of Figure 3.2.2 shows Tauc plot for the typical film B revealing its direct bandgap as 2.4 eV, which is in accordance with the known reports [86, 87].
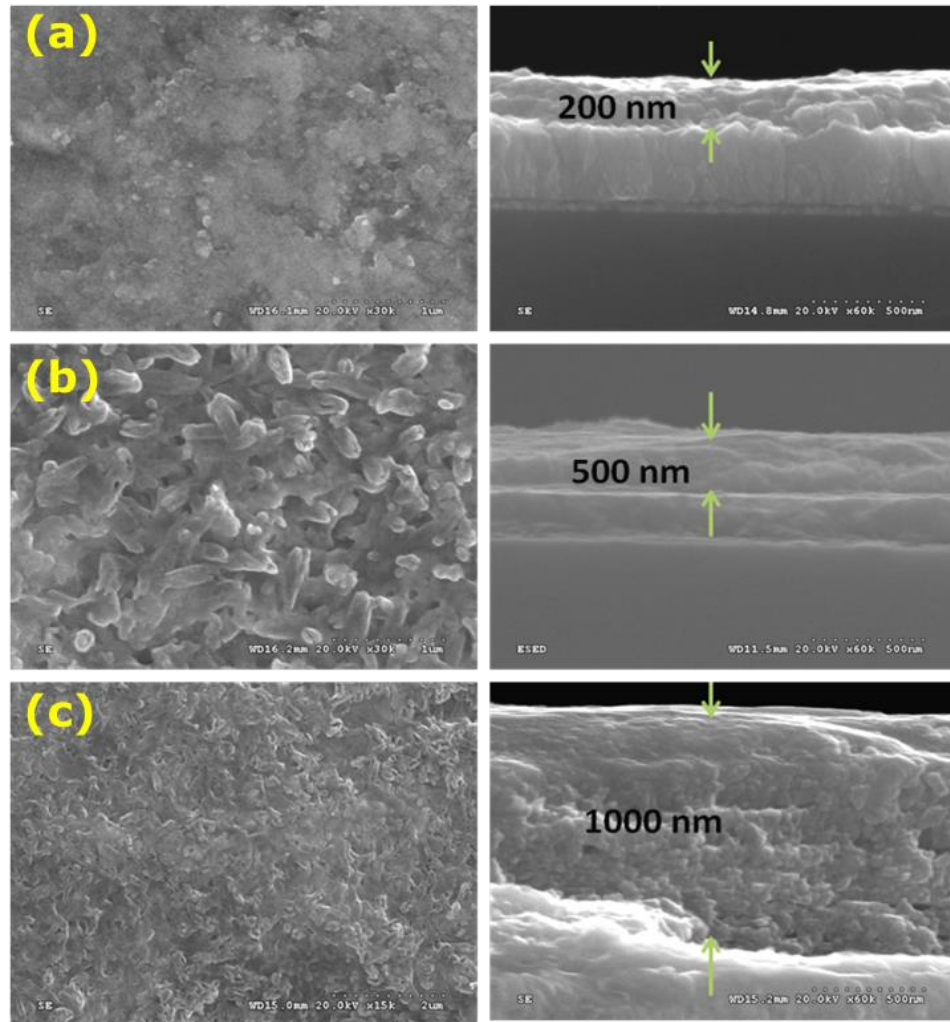
Figure 3.2.3 FESEM images showing morphology and film cross-section for the film thickness of, (a) 200 nm (Film-A), (b) 500 nm (Film-B), and (c) 1000 nm (Film-C).

In order to study the morphology of the films and to measure the film thickness, morphological and cross-sectional studies have been carried out. Figure 3.2.3 shows the surface morphology of the films A to C along with their respective cross-sectional view, exhibiting respective distinct features. Interestingly, the surface of film B exhibits certain aligned rod like nanostructure throughout the surface. On the other hand, the films with other thicknesses *viz.* film A and C display very smooth and highly rough surface, *respectively*. The film thickness have been calculated from the cross-sectional view and are found to be 200 nm, 500 nm and 1000 nm for film A, B and C *respectively*. In view of achieving rod like features, film B is investigated with special focus on it PEC property.

Elemental analysis of the films has been carried out using XPS. Typical XPS analysis is shown in Figure 3.2.4 for film B. As clearly seen in Figure 3.2.4 (a), the survey scan indicates the presence of Cd 3d and S 2p along with the remnant carbon. The region wise scan of S 2p and Cd 3d was shown in Figure 3.2.4 (b) and (c) *respectively*. A detail analysis using de-convolution of S 2p peak yields two peaks, one at B.E.~160.9 eV, and other at 162.2 eV. These peaks can be assigned to the S^{2-} of bulk S atoms [88] and to S^{2-} ions of surface S-atoms, *respectively*. Further, Figure 3.2.4 (c) displays the peaks of Cd $3d_{5/2}$ and Cd $3d_{3/2}$ centred at about 404.69 eV and 411.52 eV, validating the spin-orbit separation of 6.83eV. The doublet-separation can be attributed to the Cd^{2+} of Cd-S bond [88]. XPS results did not yield any other additional component, thus ruling out the existence of Cd-O over the film surface. This is in accordance with the XRD studies, which validates the absence of any oxide in the film. The XPS study clearly demonstrates that, the film consisting of a stoichiometric composition of CdS crystal structure is deposited using spray pyrolysis method.
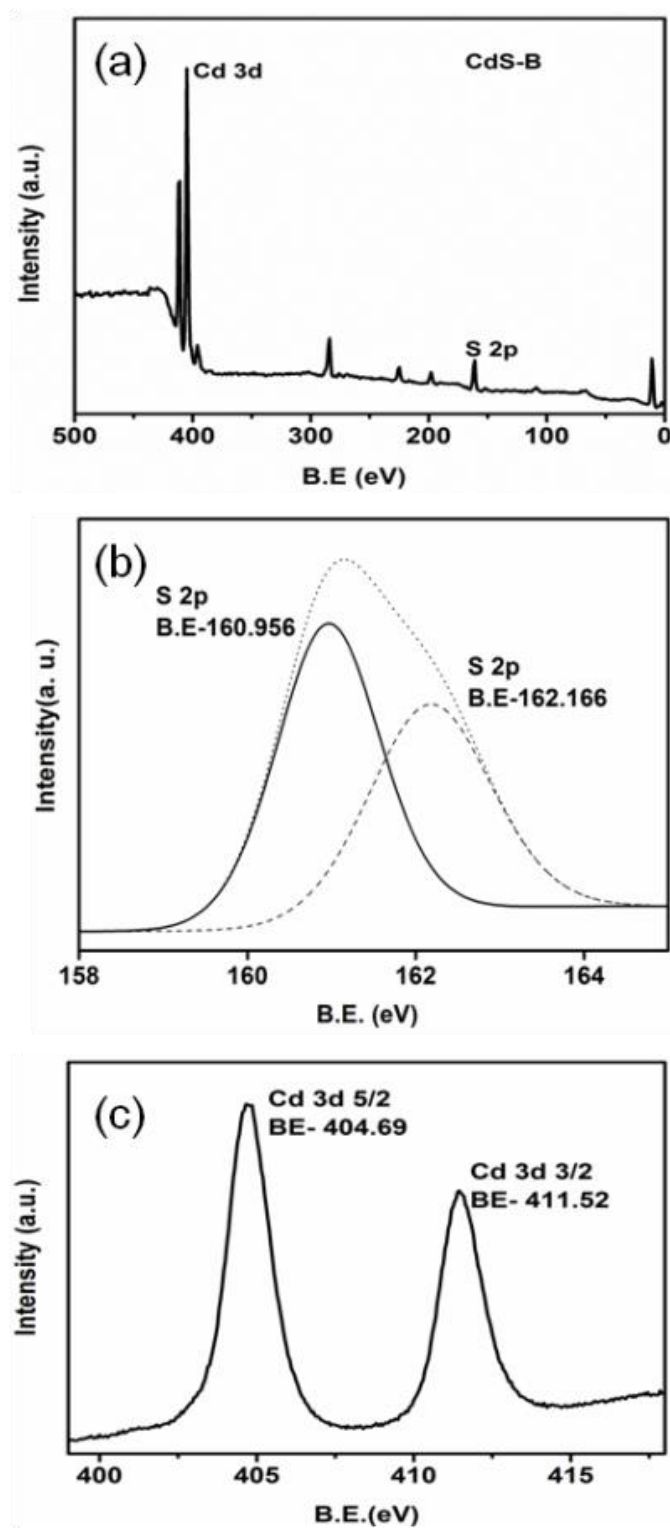
Figure 3.2.4 XPS spectrum of 500nm thick CdS film (Film-B) showing survey scan **(a)** and region wise scan for Cd 3d level **(b)** and S 1s level **(c)**.

3.2.2 Photoelectrochemical studies

PEC characterization is very important to identify and quantify the performance of a photoanode. Figure 3.2.5 (a) shows the graph of variation of photocurrent-density and quantitative solar (Solar simulator A.M.1.5) H_2 evolution from these photoanodes. Photocurrent variation and H_2 evolution display a concurrent trend in variation from film A to C, exhibiting maximum photocurrent generation and H_2 evolution from film-B. Ideally, the hydrogen generation is directly proportional to the photocurrent (J). The current is generated and the photo-induced electrons are available for the H_2 evolution reaction,which is given by the equation (3.2.1):

$$2H^+ + 2e^- \rightarrow H_2 \ (gas) \dots\dots\dots\dots\dots\dots\dots\dots\dots\dots\dots \ (3.2.1)$$
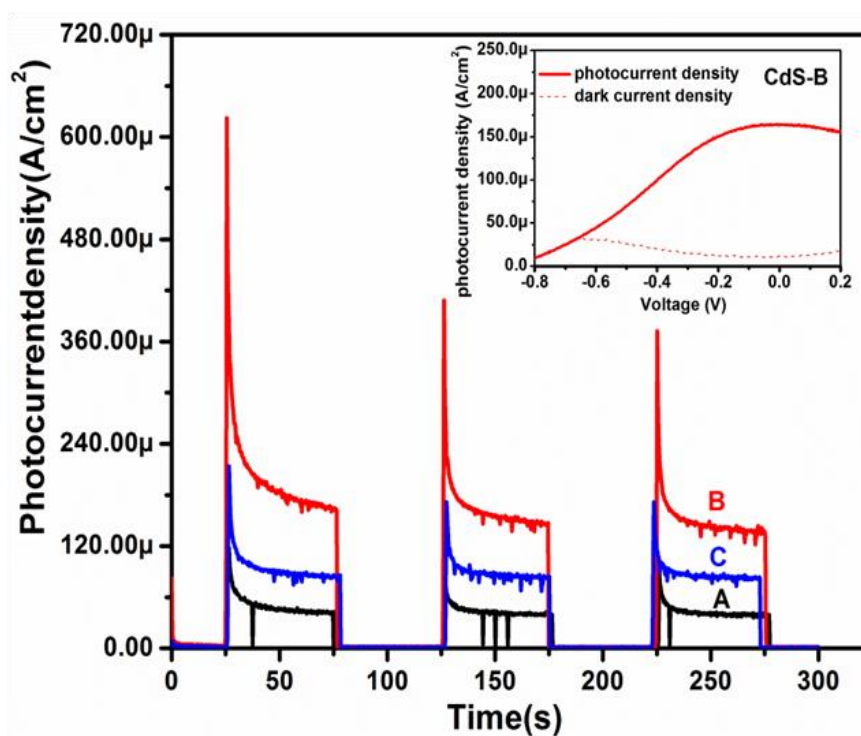
Figure 3.2.5 Plots showing variation of photocurrent and hydrogen generated in an electrolyte (0.01 M Na_2S + 0.02 M Na_2SO_3) at 0.2 V over CdS photoanodes (Inset shows the IV curve of CdS photoanode).

It indicates that during PEC reaction, the photogenerated electrons react with H^+ ions at the counter electrode to yield H_2 gas. Figure 3.2.5 (a) displays the transient photocurrents from respective photoanodes, displaying presence of strong photocurrents, film-B being the highest. In all cases the anodic current rises rapidly (~ms) when light is incident on the film, but decays to a much lower value (steady state) within a few tens of second. The shape of transient part is approximately exponential in nature having some time constant, which can be determined by the applied bias, incident light intensity and redox species present in the electrolyte. Such faster decay kinetics reveals the larger recombination rates in the photoanode. The steady state value is highest (137 μA/cm^2) in case of film-B indicating that film deposited at 350 ℃ yields better film in the form of nanostructured morphology. It is noteworthy that film-B displays maximum absorption thus contributing to its improved PEC performance.

The study presented in above *2 sections (3.1 and 3.2)* has enabled us to choose best suited, efficient CdS film for its utilization in the remaining part of study. We selected AR film (film B in *section 3.2*) as the reference in view of its ideal and balanced performance with respect to *efficiency* and *stability*.

3.2.4   Summary of this section

Adherent and uniform aligned nanorod structured CdS thin films are produced using spray pyrolysis deposition. The thickness of the film has been optimized to obtain adherent efficient CdS film. Film thickness of 500 nm has yield best PEC performance with solar-to-hydrogen (STH) efficiency of 0.2 %. Superior performance is attributed to the nanorod-structured morphology of the film. It is demonstrated that high quality film of CdS has been achieved to produce enhanced PEC performance, using a very simple economic film deposition method.

RESULTS AND DISCUSSION

PART- II

Modification of CdS surface using metal oxide nanoparticles

Motivation: The PART-II of Results and Discussions section includes the modification of CdS surface with stable metal oxides that acts as a protective coating and avoids direct exposure of CdS to electrolyte, as discussed in *section 1.3 of first chapter*. TiO_2 and Nb_2O_5 are best candidates for this task due to their similar photocatalytic properties and *eco-friendly* nature except the fact that, TiO_2 shows stability in whole pH range, whereas Nb_2O_5 shows stability in the pH range 0-12.2 [89]. Accordingly, in *section 3.3 and 3.4* we have discussed the work on the modification of CdS photoanode by TiO_2 and Nb_2O_5 nanoparticles.

At this point, it is important to note that valence bandedge of wide band gap metal oxide is more positive than CdS due to which holes transfer is restricted. This affects the efficiency of PEC cell. To overcome this hurdle it is proposed that *holes* transfer through metal oxide layer over CdS surface can only take place through tunnelling effect. For tunnelling effect to occur, the metal oxide layer thickness should be less than 20 nm and that is a difficult task. In view of the above discussion we have synthesized nanoparticles of TiO_2 and Nb_2O_5 (size in few nanometres) by chemical method and attached them to CdS by using linking agent. Use of linking agent assures the formation of few layers of metal oxide over CdS [90].

3.3. Metal oxide I: TiO$_2$ nanoparticles

CdS thin film is functionalized by TiO_2 nanoparticles to achieve the photostable anodes. For this, the surface of spray deposited CdS thin film was modified through bi-functional molecule mediated chemisorption of TiO_2 nanoparticles (NP). Consequently, a systematic control over efficiency and photoanode stability against corrosion has been investigated. Quantitative analysis of the photocorrosion of these photoanodes has further been studied using chronoampereometry,

78

XPS spectroscopy and induced coupled plasma spectroscopy. TiO_2 NP modified photoanodes has shown an enhanced efficiency and stability. For PEC systems, the stability factor ($\sum$) has been defined for the first time based on the time dependent chronoampereometry, which clearly demonstrates that $\sum_{modified} >> \sum_{bare}$. The modified photoanode has shown an improved IPCE of 22% than the bare CdS (~8 %) electrode. It gives an enhanced STH of0.7% with respect to bare CdS (0.2%) under AM 1.5G solar simulator, at 0.2 V/SCE. Improved stability for more than nine hrs. and enhanced efficiency is attributed to the controlled passivation of CdS surface through TiO_2 NP (5 nm), and inhibition of the charge recombination. Superior and stable performance of modified photoelectrode has been validated by higher and stable hydrogen evolution over modified electrode. Details pertaining to above discussion are as follows.

3.3.1 Structural, optical and morphological characterization of TiO_2 nanoparticles
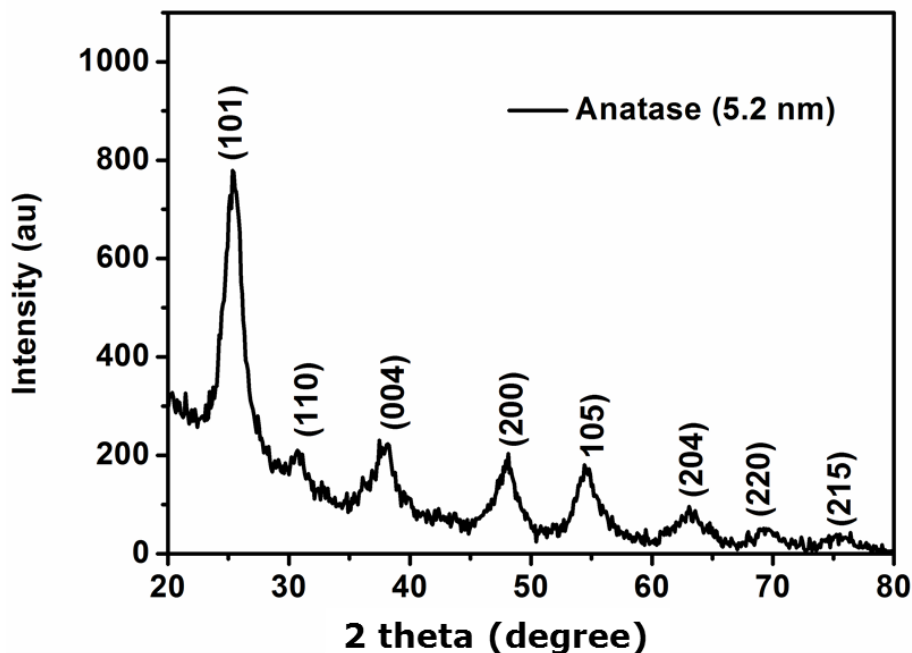
Figure 3.3.1 XRD pattern of TiO_2 nanoparticles.

TiO$_2$ NPs were synthesized according to the methodology described in experimental section (*chapter 2, section 2.3.1*). A detailed characterization has been explained in this section. Figure 3.3.1 shows the XRD pattern of as synthesized TiO$_2$ nanoparticles by hydrolysis method. The XRD pattern clearly reveals the formation of crystalline pure anatase phase of titania nanoparticles with preferential growth progressed in the (101) direction. The de-bye Scherer formula has been used to evaluate the particle size of nanocrystals. The average size of the nanoparticles is estimated to be 5.2 nm (with in the experimental errors).
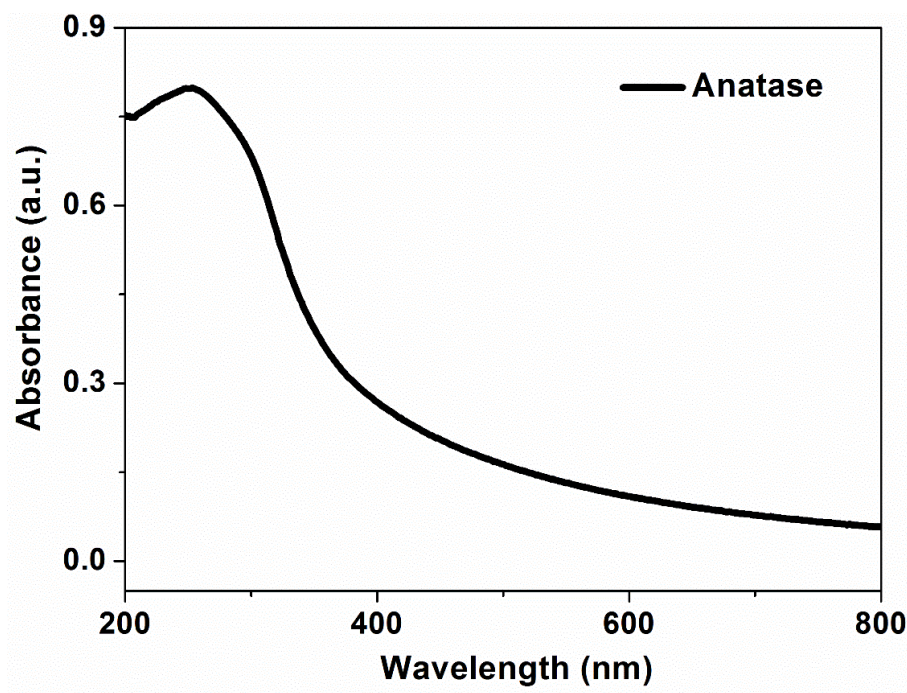
Figure 3.3.2 Absorption spectrum of TiO$_2$ nanoparticles.

To study the optical properties of titania nanoparticles, absorption spectra is recorded as shown in Figure 3.3.2. It can be easily observed that absorption edge of nanoparticles is appeared around 380 nm, which corresponds to the band gap of 3.2 eV (1240 /λ).
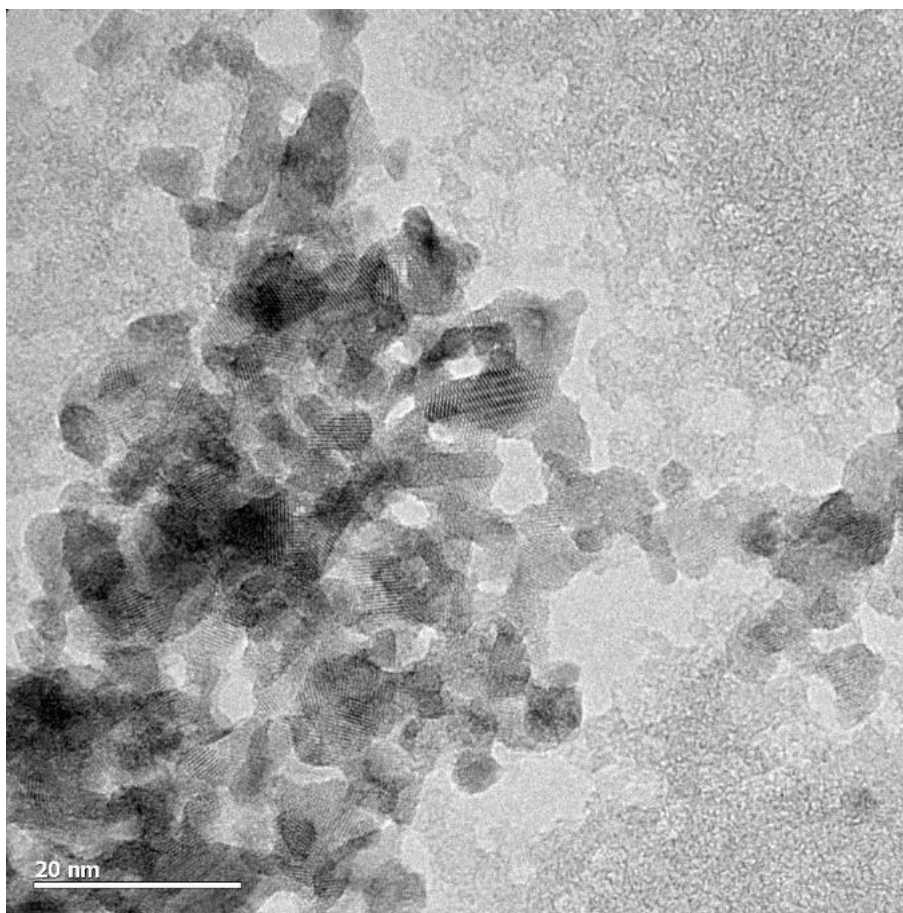
Figure 3.3.3 TEM image of TiO$_2$ nanoparticles.

Figure 3.3.3 shows the TEM image of anatase TiO$_2$ nanoparticles. It could be clearly seen formation of crystalline nanoparticles of average size 5.0 nm, which is also validated by crystalline size calculation using XRD pattern (within the experimental errors).

3.3.2   Characterization of TiO$_2$ nanoparticles functionalized CdS films

Based on the *TiO$_2$ nanoparticle treatment time* over the CdS surface, films are named as tabulated in Table 3.3.1. Figure 3.3.4 (a) shows the XRD pattern of the bare CdS and the

modified photoelectrodes. All the films exhibits hexagonal phase belongs to the P63MC (JCPDS file No. 00-006-0314) space group. The peaks appeared due to FTO substrate can be easily observed, which indicates the existence of thin film over FTO substrate at the background of the film.

Table 3.3.1 TiO_2 nanoparticle modified CdS films with different treatment time.

Time of treatment	CdS/NPT
3 minute	NPT-a
7 minute	NPT-b
15 minute	NPT-c
30 minute	NPT-d

Peaks related to TiO_2 are not found in the spectra. The crystallite size is calculated to be 22 nm, as estimated from de-bye Scherer equation (equation 2.2). The study indicates the formation of nanostructure film over CdS/TiO_2 film. These films are further used for the fabrication of modified electrode.

Figure 3.3.4 (b) shows the UV-Vis absorption spectra of bare CdS, CdS/TG and modified CdS thin films. Bare CdS and TG modified films show very similar behavior, whereas CdS/NPT shows a blue-shift in their absorption with respect to the bare film. The result of optical analysis is presented in Table 3.3.2. The study confirms that optical property of the CdS film remain unaffected after adsorption of TG. On the contrary, a small blue-shift in bandgap of other two modified samples is observed, which can be correlated to the existence of nano-sized TiO_2 in case of NPT treated CdS photoanodes [51].
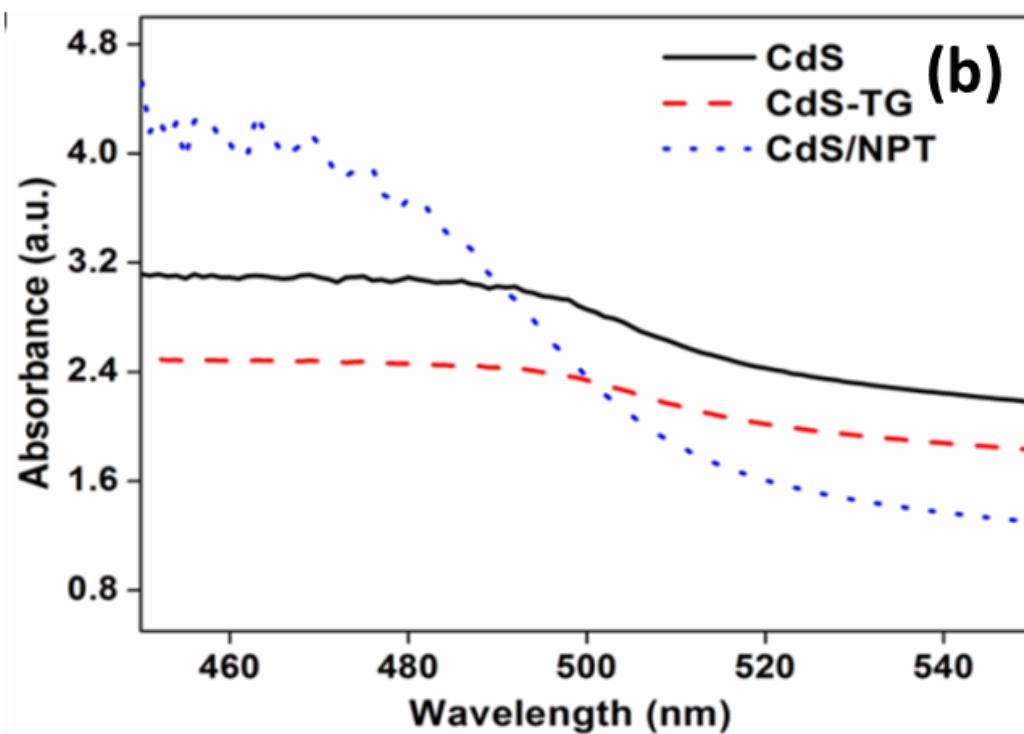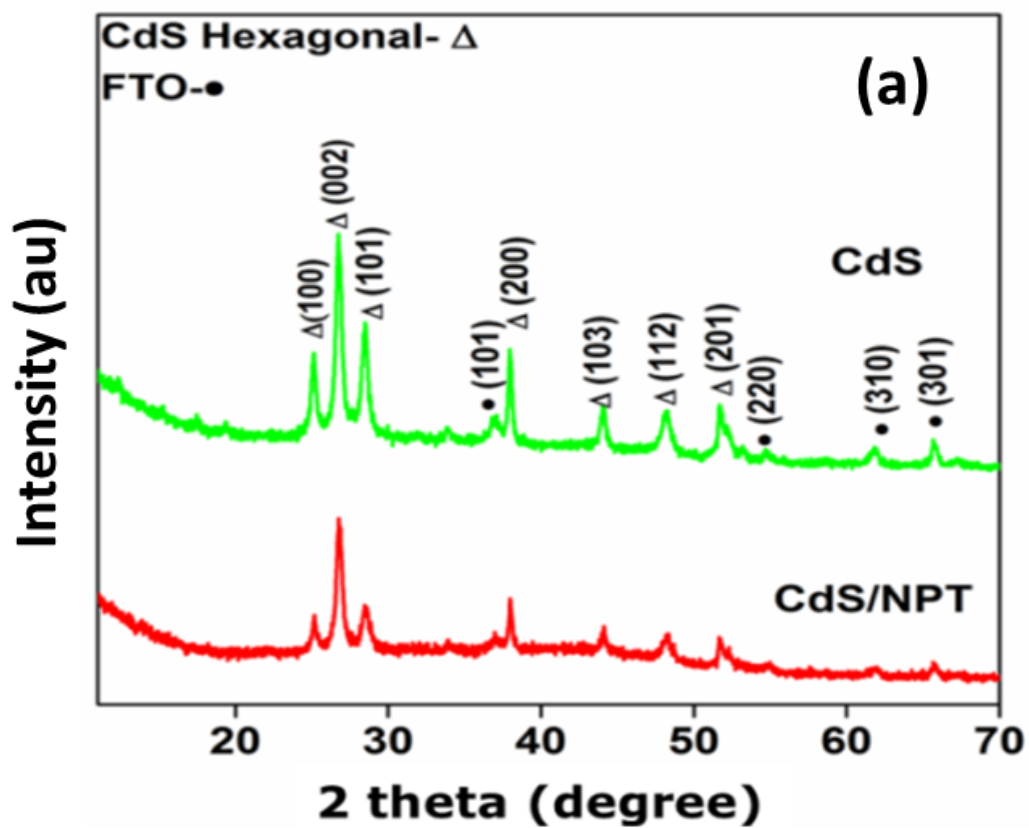
Figure 3.3.4 (a) XRD patterns and **(b)** Absorbance spectra for the comparison of bare CdS photoanodes with NPT modified CdS photoanodes and CdS/TG.
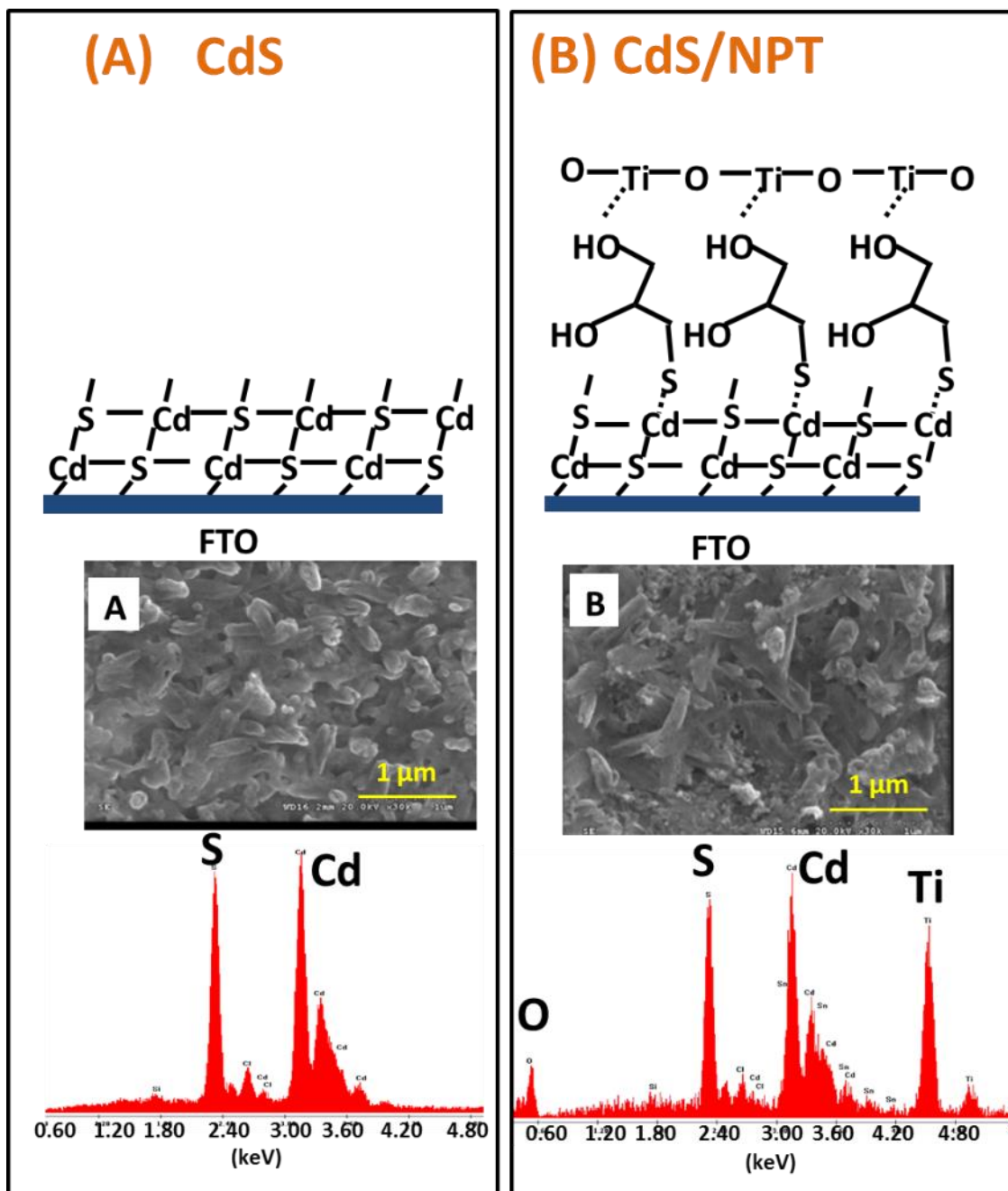
Figure 3.3.5 Schematic representation, EDS spectra and FESEM images of **(A)** bare CdS photoanode and **(B)** NPT modified CdS photoanode.

Figure 3.3.5 shows the schematic representation and surface morphologies of the bare and modified CdS films, along with their EDS spectra. Bare CdS film displays a nanostructured surface (Figure 3.3.5 (a)) consisting of randomly aligned rods throughout, which undergoes

filler-type morphology changes, upon the NPT treatment (as seen in the SEM of Figure 3.3.5 (b)). When TG (*i.e.* S--R--OH) comes into the vicinity of CdS film surface, the thiol groups strongly reacts with the substrate, and distort or fill-up the cavities near the rods yielding an asymmetrically scattered rods all over the CdS surface. The NPT treatment further leads to the linking of dangling hydroxyl ions of TG to that of interactive ions of NPT. Presence of NPT can be clearly seen in the form of spherical particles (white color) on the CdS surface as seen in Figure 3.3.5 (b). The detection of Ti in EDS further validates the existence of linked TiO_2 nanoparticles over the surface of CdS film. This adherent NPT remains over the film even after washing of film with solvent for several times.

Table 3.3.2 Absorption edge and Bandgap gap variation with the surface modification of CdS photoelectrode

Sample name	Absorption edge (nm)	Bandgap (eV)
CdS	496	2.50
CdS-TG	491	2.52
CdS-NPT	496	2.50

This is in agreement with the earlier report [91] that S-terminated CdS surface has affinity towards the thiol group, whereas TiO_2 towards the hydroxyl group of TG. This study demonstrates that we are able to achieve NPT modified nanostructured CdS films. In order to validate this model in a quantitative manner, we have further performed the XPS study for the sake of completeness. The film surface studies confirm to the proposed model as shown in Figure 3.3.6 (a) and support the results of above section. Surface studies clearly reveal the

existence of Ti and O in the modified films. Figure 3.3.6 (b) shows the XPS spectra of Ti in

CdS/TiO$_2$ films, which indicates the presence of Ti in IV oxidation state (TiO$_2$). XPS spectra of

O in CdS/TiO$_2$ gives two peaks, one at 529 eV corresponds to the presence of TiO$_2$ and other at

531.8 eV corresponds to the presence of hydroxides on the surface.
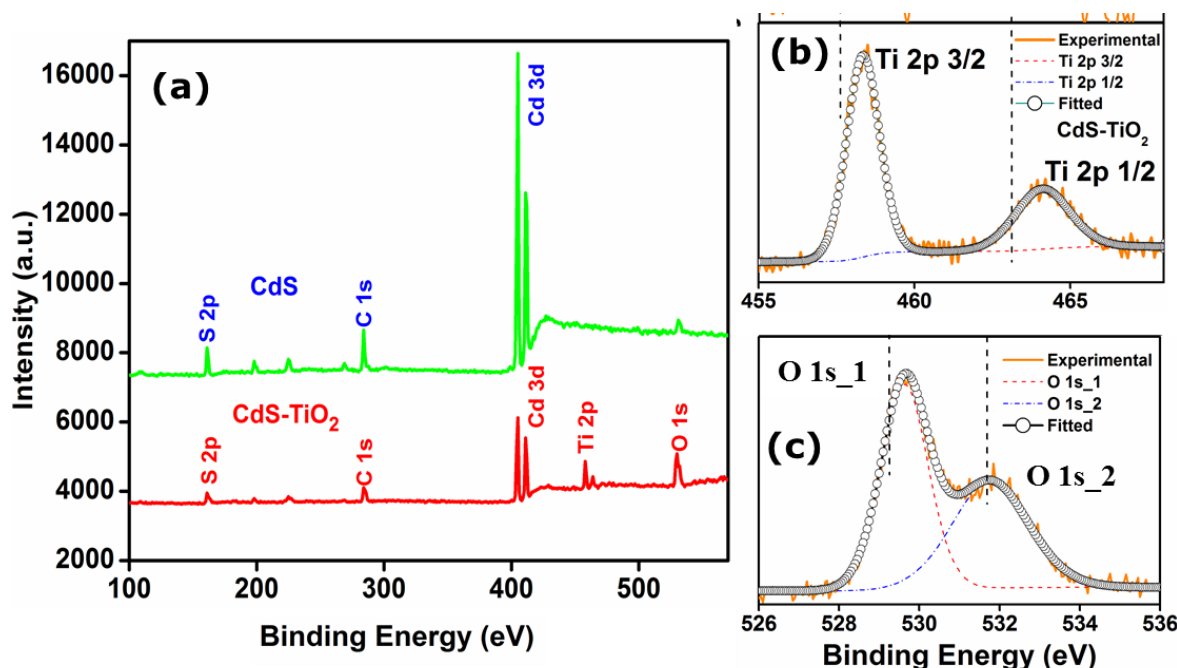
Figure 3.3.6 (a) XPS survey spectra of CdS and TiO$_2$ nanoparticles modified CdS photoelectrodes. XPS spectra of **(b)** Ti and **(c)** O in TiO$_2$ modified CdS films.

3.3.3 Photoelectrochemical characterization of TiO$_2$ nanoparticle functionalized CdS photoanode

The purpose of nanoparticle mediated surface modification of CdS is to achieve an improved

photoanode. Consequently, in order to investigate the PEC behavior of CdS and modified CdS

photoanodes, PEC characterization of respective photo-electrodes has been carried out. Figure

3.3.7 shows the comparative chronoampereometric curves for NPT modified CdS photo-

electrodes with respect to the bare CdS photoelectrode. An improvement in the efficiency with the adsorption of NPT on CdS surface is confirmed from the above studies.
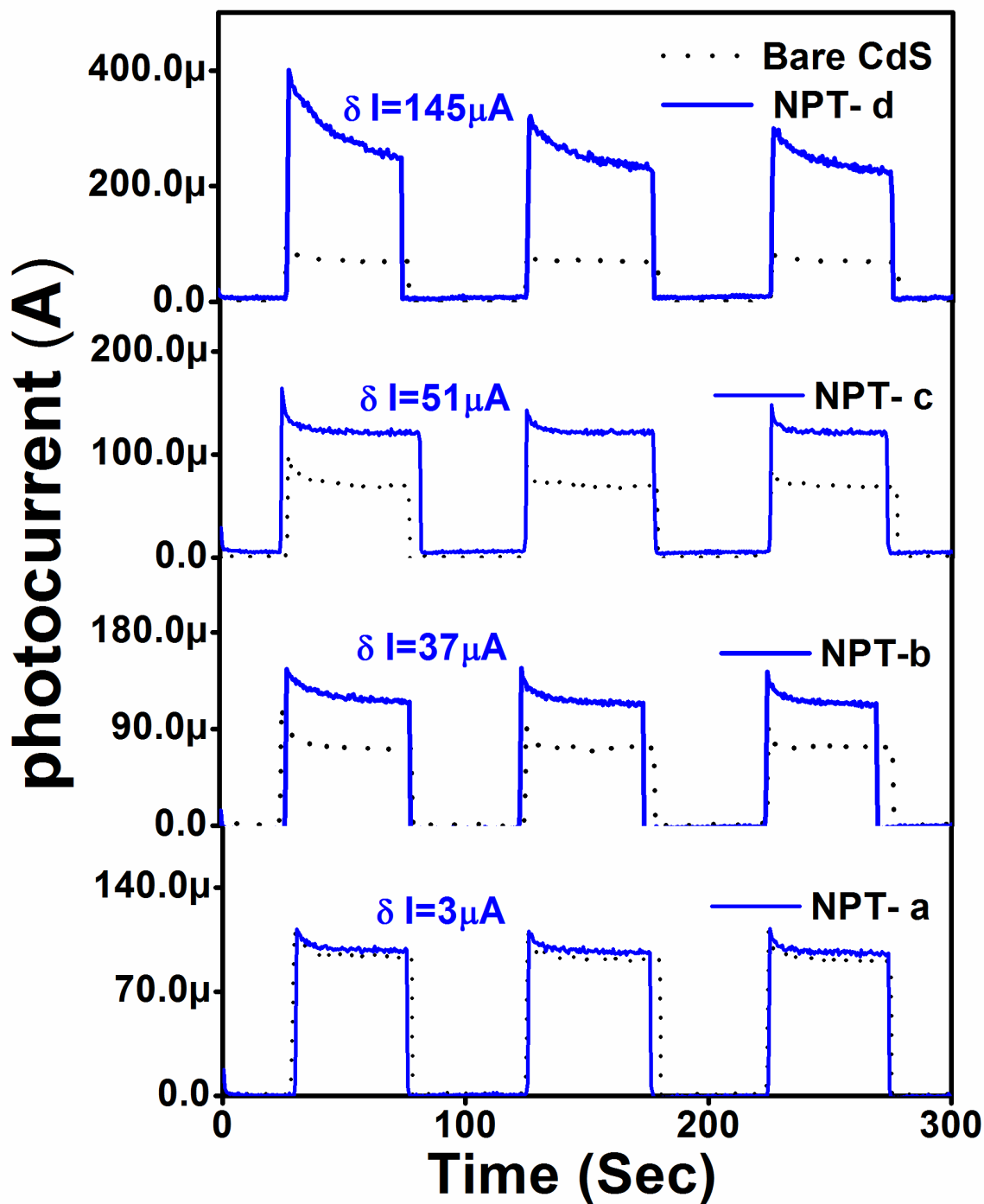
Figure 3.3.7 Comparative study of photocurrent variation with NPT treatment time for NPT photo-electrodes with respect to bare CdS, ($\delta I = I_{\text{Modified film}} - I_{\text{Bare CdS}}$).

Figure 3.3.7 shows the effect of surface modification of CdS photoanode with NPT on the PEC properties. It is clearly seen in case of NPT-d photoanode that the photocurrent increases by 3.7 times than that generated by the bare CdS photoanode. Above photocurrent improvement is evaluated using simple differential function of I as defined by δI ($\delta I = I_{\text{Modified film}} - I_{\text{Bare CdS}}$). The values of δI as shown in Figure 3.3.7 clearly indicates an enhancement in the photocurrent of modified photoelectrode with respect to the bare CdS photoelectrode. Similarly there is a systematic increase in the efficiency for NPT-a, NPT-b and NPT-c photoanodes. This enhancement in the efficiency with TiO_2 can be attributed to the reduction of density of surface states on CdS surface with the adsorption of NPT [92].

Electrochemical impedance spectroscopy has been carried out to understand the charge transfer mechanism between photoelectrode and electrolyte interfaces. All the measurements were performed in dark with an applied frequency of 10 kHz and ac small signal amplitude of 10 mV. Figure 3.3.8 shows the comparison of the Nyquist plots of CdS and NPT modified photo-electrodes. A semicircle in the Nyquist plot clearly depicts that the charge transfer process at the CdS/electrolyte interface is dominant and capacitive in nature [92]. The experimental data have been fitted using Z-View software. Figure 3.3.8 (d) shows an equivalent circuit deduced from the analysis of corresponding Nyquist plot.

In equivalent circuit, R_s represents an Ohmic resistance of electrolyte. R_t and C_t are the resistance and capacitance of the electrode electrolyte interface. It can be seen from the Figure 3.3.8 (a) that the diameter of the semicircle of Nyquist plot corresponding to the NPT modified photoelectrode has much greater value than that of the bare CdS photoelectrode. It is important to note the recombination time, which is equal to the product of resistance of the solid interface and the capacitance ($\tau_r = R_t \times C_t$) [92].
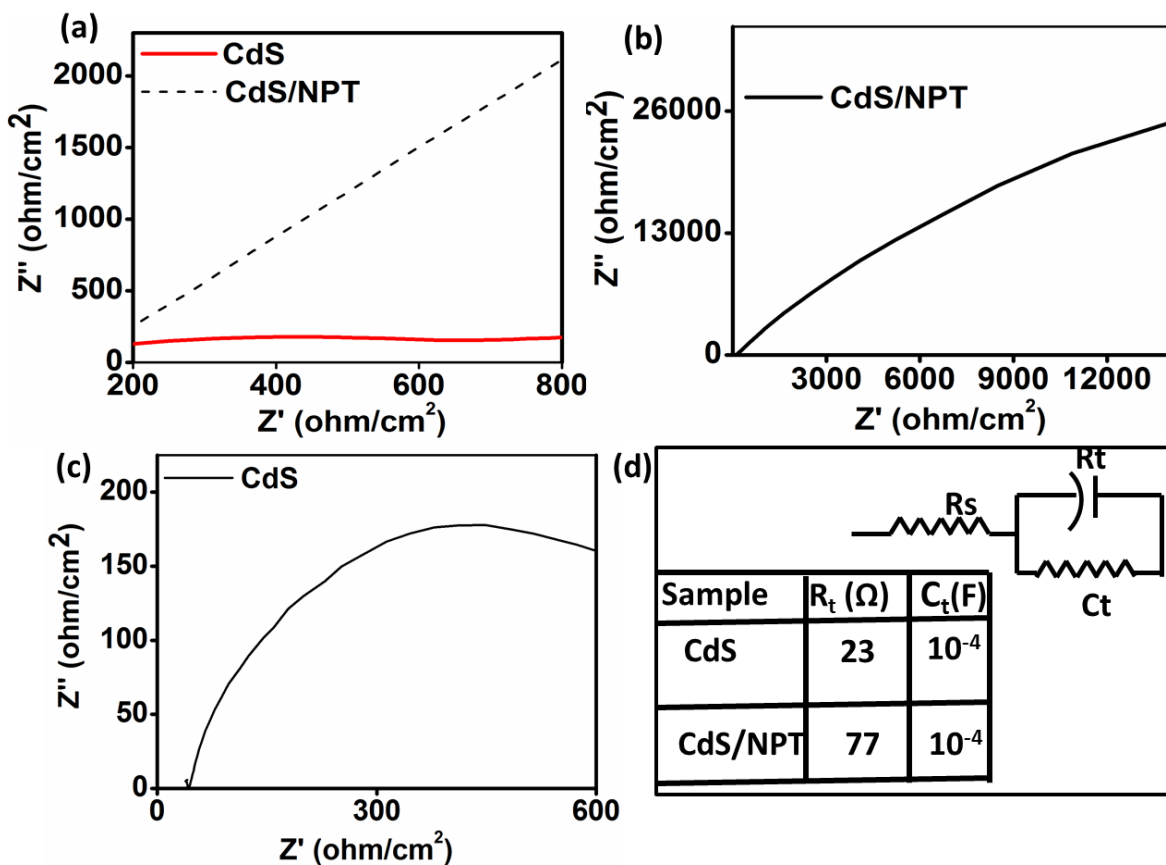
Figure 3.3.8 Electrochemical impedance studies of (a) bare CdS, NPT modified photoanode (b) only NPT modified photoanode (c) bare CdS photoanode (d) Equivalent circuit and corresponding values of charge transfer resistance and capacitance values.

The NPT modified photoanode has shown much higher recombination life time than the bare CdS, implying reduction in the recombination process of charge carriers in modified electrodes. Hence, these electrodes show an improved PEC performance.

Photoelectrochemical stability studies of NPT modified electrodes: Implementation of sustainable hydrogen energy for energy applications necessitates achieving a stable and an efficient photoanode. Stability remains one of the most important factors that controls life of a photoanode, and ultimately even of PEC cell. In general, stability depends on several physical, chemical and other factors [93]. Accordingly, in order to quantify the stability of a photoanode,

we have defined a new parameter ($\Sigma_{photoelectrode}$) which is function of several dependent parameters as described below in equation (3.3.1):

$$\Sigma_{photoelectrode} = \varphi(\text{physical}) \circ \varphi(\text{chemical}) \circ \varphi(\text{others}) \ldots (3.3.1)$$

Where, Σ *(physical)* - physical properties of electrodes correlated to stability *viz*. crystal structure, orientation, thickness, area, geometry.

Σ *(chemical) – pH* of electrolyte, electrolyte composition, concentration of electrolyte.

Σ *(others)* - temperature, time, stirring and photocurrent density.

It is imperative that stability is multiple-parameter dependent function involving various processes, and thus it is difficult to describe it quantitatively. However, in order to simplify its quantitative estimation in present study, we have considered the variation of *photocurrent with time* as a means to estimate the time-dependent stability of a photoanode; accordingly we propose "*photoanode-stability*" to be a simple function of photocurrent density and illumination time, assuming other parameters to be constant (equation 3.3.2):

$$\Sigma_{photoelectrode} \% = \frac{\Delta_{CdS} - \Delta_{mod\,ified}}{\Delta_{CdS}} * 100\%$$

$$\Rightarrow \begin{array}{l} \Delta_{mod\,ified} \to \Delta_{CdS}, \Sigma_{photoelectrode} \to 0 \\ \Delta_{mod\,ified} \to 0, \Sigma_{photoelectrode} \to 1 \end{array} \quad \ldots\ldots\ldots\ldots\ldots\ldots\ldots\ldots\ldots.. (3.3.2)$$

Where, $\Delta_{photoelectrode}$ is slope of "I *vs*. t" curve of the photoelectrode and can be presented by following equation (3.3.3):

$$\Delta = \frac{\partial I}{\partial t} = \frac{I(t_2) - I(t_1)}{t_2 - t_1} \quad \ldots\ldots\ldots\ldots\ldots\ldots\ldots\ldots. (3.3.3)$$

Where, $I(t_1)$ is photocurrent at time 't$_1$' and $I(t_2)$ is photocurrent at time 't$_2$'.

Slope of I-t curve of CdS (Δ_{CdS}) and modified photoanode ($\Delta_{modified}$) are calculated from Figure 3.3.9. Accordingly, Σ has been calculated for each modified photoanode with respect to bare CdS photoanode. If the decay in photocurrent of modified photoanode is similar to that of bare CdS, means it has poor stability factor. If there is no decay in photocurrent of modified photoanode until a specific time period then photoanode has 100 % stability upto that time interval. This is clearly expressed in equation (3.3.2) and the slope can be represented by equation (3.3.3)
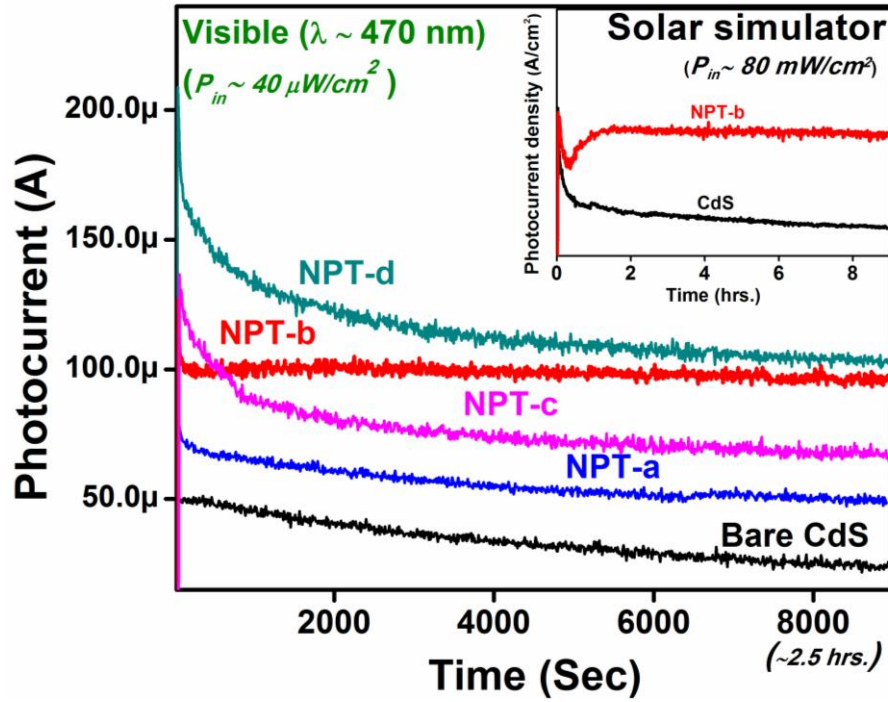
Figure 3.3.9. Chronoampereometry of bare CdS and NPT treated photoanodes for different adsorption time for 2.5 hrs. under 470 nm filter ($P_{in} \sim 40\mu W/cm^2$). Inset shows chronoampereometry of bare CdS and most stable electrode NPT-b under solar simulator ($P_{in} \sim 80 mW/cm^2$) for 9 hrs.

Mathematically slope is given by equation (3.3.4):

$$\Delta = \tan\psi \Rightarrow \begin{array}{l} \psi = 0 \approx stable\ photoelectrode \\ \psi = 45^0 \approx unstable\ photoelectrode \end{array} \quad \dots\dots\dots\dots\dots\dots\dots (3.3.4)$$

An ideal stable photoanode exhibits y=c behavior in *I vs. 't'* curve *i.e.* straight line with Δ=0. Deviation from ideal behavior leads to reduction in photocurrent, which shows deteriotion of photoanode due to photocorrosion process. On the basis of above proposed theory, we have taken *'I' vs. 't'* characteristics of all the NPT treated photoanode as shown in Figure 3.3.9. As can be seen in Figure 3.3.9 photoanode NPT-b has shown an improvement in the stability factor ($\Sigma_{mod\,ified}$) rather than bare CdS (Σ_{CdS}). It shows almost no reduction in photocurrent even for longer hrs. Variation in the stability factor with the modification of photoanode has been summarized in Table 3.3.3.

Table 3.3.3 Change in photocurrent and stability evaluation of bare CdS photoanode and NPT modified CdS photoanodes.

Thin films	ΔI = I (modified film) –I (bare CdS) (μA)	Δ	% Stability (for 2.5 hrs.)
CdS bare	0	0.00230	99.77
3 min dipping time	3	0.00190	99.81
7 min dipping time	37	0.00000	100
15 min dipping time	51	0.00063	99.93
30 min dipping time	145	0.00062	99.93

In Figure 3.3.9 we can observe the adherent NPT layers for NPT-b which corresponds to optimum adsorption and stable photocurrent but NPT-d shows delays equilibration of photocurrent. This is due to the fact that only few layers of NPT can be adhered to the CdS surface after getting linked to hydroxyl group of TG. During electrochemical measurement extra

TiO$_2$ layers comes out in the electrolyte with time until it reaches an optimum amount which can be adherent to CdS surface. This leads to reduction in current upto a specific duration of time and then it becomes stable. After studying the stability of different NPT modified electrodes under 470 nm filter for 2.5 hrs., further stability studies have been performed for the most stable electrode, *i.e.* NPT- b under AM 1.5 solar simulator for 9 hrs. as shown in **inset of** Figure 3.3.9. The above electrode is further found to be stable for 9 hrs. without any deteriotion in the electrode performance. Stability factor is calculated for NPT-b under solar simulator measurements for 9 hrs. as mentioned in Table 3.3.3 (NPT-b S).
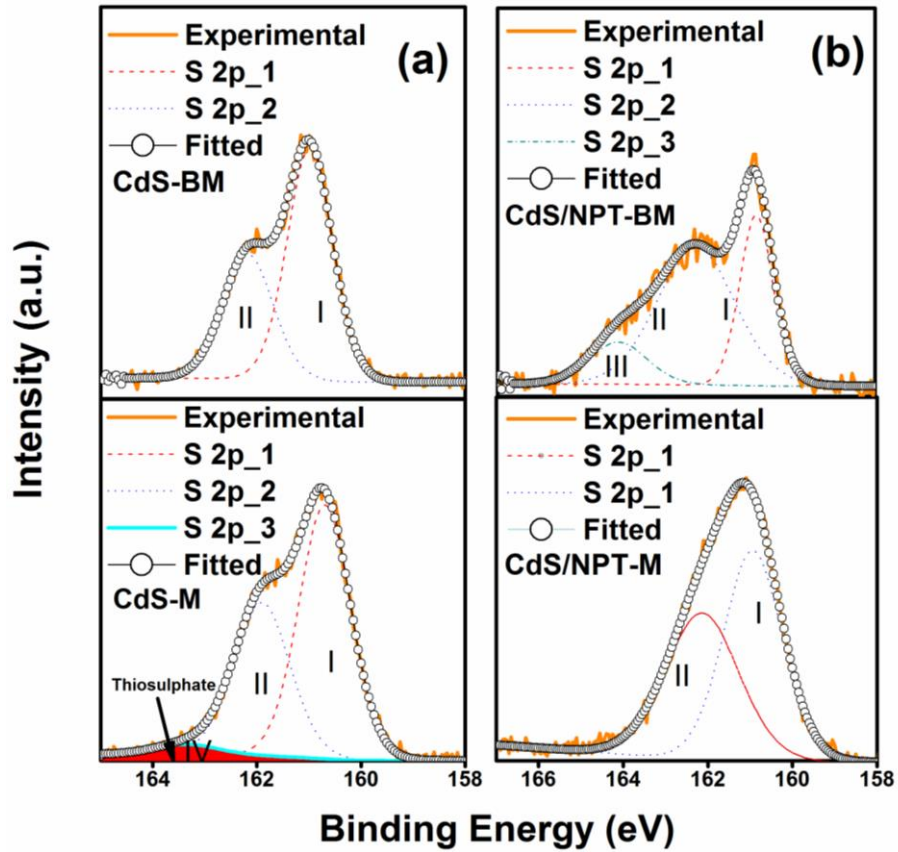
Figure 3.3.10 X-ray photoelectron spectroscopy of (a) CdS photoanode before (CdS-BM) and after (CdS-M) (b) CdS-NPT photoanode before (CdS/NPT-BM) and after (CdS/NPT-M) 2.5 hrs. of PEC measurement.

Quantitative analysis of elements in electrode and ions in electrolyte is carried out to further prove the suppression of photocorrosion. XPS is performed for the analysis of deterioration of photoelectrode by photocorrosion process.

In a PEC cell, hydrogen is produced by photoelectrons generated during illumination of photoelectrode given by reaction (equation 3.3.5):

$$2H^+ + 2e^- \rightarrow H_2 \dots\dots\dots\dots\dots\dots\dots\dots\dots\dots\dots\dots \text{ (3.3.5)}$$
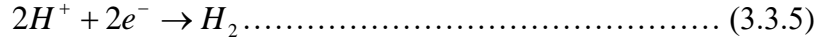
And holes generated are consumed to oxidize sulphide ions into elemental sulphur. This process is known as photocorrosion process as given by the reaction (equation 3.3.6) [94]:

$$S^{2-} + 2h^+ \rightarrow S \dots\dots\dots\dots\dots\dots\dots\dots\dots\dots \text{ (3.3.6)}$$
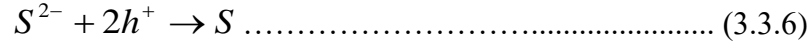
This elemental sulphur combines with sulphite ion present in electrolyte ($Na_2S + Na_2SO_3$) and forms thiosulphate ion as given by equation (3.3.7):

$$S + SO_3^{2-} \rightarrow S_2O_3^{2-} \dots\dots\dots\dots\dots\dots\dots\dots\dots\dots \text{ (3.3.7)}$$
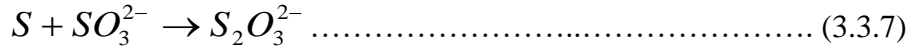
Therefore, the presence of thiosulphate on the electrode is the evidence of photocorrosion reaction occurring during illumination of photoelectrode.

Keeping this in view, XPS analysis is carried out for photoelectrode before and after 2.5 hrs. of PEC measurements. Figure 3.3.10 shows the region wise XPS spectra of sulphur in CdS and NPT coated CdS photoanodes before and after 2.5 hrs. of PEC measurements. As shown in Figure 3.3.10 (a) there is a thiosulphate peak observed at 163.3 eV after 2.5 hrs. of PEC measurements (highlighted with red colour in Figure 3.3.10 (a)) which is not seen before PEC measurements in XPS spectra. It clearly confirms photocorrosion reaction occurred during the measurements. Figure 3.3.10 (b) shows the XPS spectra of NPT modified CdS photoelectrode before and after 9 hrs. of PEC measurements. In Figure 3.3.10 (b) there is no thiosulphate peak

observed after 2.5 hrs. of PEC measurements. This clearly demonstrates the suppression of photocorrosion reaction in NPT modified films. There is a peak at 164.2 eV in CdS-NPT electrodes before measurements which corresponds to S of thio group present in thioglycerol which is absent in bare CdS as expected.

For further confirmation of inhibition of photocorrosion and to know the extent of film dissolution in the electrolyte, induced coupled plasma (ICP) elemental analysis has been performed. As already known during photocorrosion process, deterioration of CdS photoelectrode takes place because of which Cd^{2+} ions would be present in an electrolyte [65]. So concentration of Cd^{2+} ions in electrolyte has been investigated before and after 2.5 hrs. of PEC measurements. The detection of concentration of Cd ions in electrolyte is shown in Table 3.3.4. As expected, negligible concentration of Cd^{2+} is observed in electrolyte used for CdS-NPT photoanodes, rather than electrolyte tested for bare CdS photoanodes. Therefore, stability of CdS photoelectrode has much improved by the passivation of its surface by making use of nano-TiO$_2$ layer.

Table 3.3.4 ICP measurements of Cd^{2+}ion concentration of different CdS modified electrodes in electrolyte.

Sample name	Measurement time (hrs)	Concentration of Cd^{2+}ions (ppm)
Electrolyte	-	Not detected
CdS	0 (Before measurement)	Not detected
CdS	2.5 (After measurement)	0.0146
CdS-NPT	0 (Before measurement)	Not detected
CdS-NPT	2.5 (After measurement)	0.00819

These results demonstrated by above quantitative elemental analyses (Table 3.3.4) are inline with the estimated stability factor specially described in this study. Thus, the work clearly confirms the achievement of highly stable and efficient CdS photoelectrode attained by NPT modification.
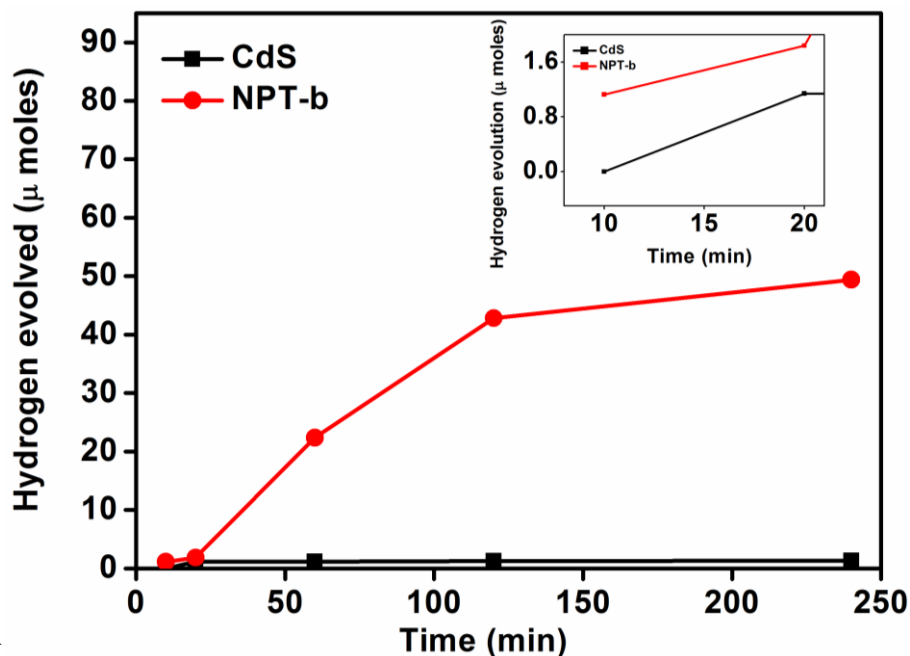
Figure 3.3.11 The evolved hydrogen with reaction time demonstrates that the modified photoanode (NPT-b) stably generates 25 times higher hydrogen gas under simulated solar radiation (AM 1.5) as compared to the unmodified CdS.

Stable and efficient hydrogen evolution from modified photoanode: Finally, in order to validate stability and efficiency of modified CdS photoanode with respect to hydrogen production, following studies has been carried out. Accordingly, accumulated hydrogen has been detected for bare CdS as well as for NPT-b electrodes at different time intervals. Expectedly, NPT-b has shown a very high hydrogen evolution than bare CdS. Figure 3.3.11 clearly demonstrates that the modified photoanode (NPT-b) stably generates 25 times higher hydrogen gas under simulated solar radiation (AM 1.5) as compared to the unmodified CdS. It is worth mentioning that during first 20 minutes, modified electrode generates noticingly much higher amount of hydrogen gas as

compared to the bare CdS electrode. However, for longer accumulation times, very high magnitude of hydrogen gas is being evolved. The comparison of the time dependent behavior of CdS and modified photoanode reveals that during the initial phase of PEC reaction, photocorrosion of the bare CdS is seemingly very less significant.

During later part of the PEC reaction both the photocorrosion and hydrogen productions are competitive processes, as correlated from the detected Cd/S and generated photocurrent as well as evolved hydrogen gas. Thus in the case of bare CdS, photocorrosion is found to be a dominating process as shown in earlier section (Figure 3.3.10 and Table 3.3.3). This leads to bare CdS yielding negligibly low hydrogen. In case of the modified photoanodes the photocorrosion is inhibited, and at the same time photocurrent generation is a dominating process as supported by the elemental analysis (Figure 3.3.10 and Table 3.3.4) and time dependent photocurrent measurement (Figure 3.3.10 and Table 3.3.3). Consequently, inline with our earlier discussion, reduced charge-recombination is the main parameter that is responsible for yielding the higher efficiency for modified photoanodes. This behavior is consistent even for longer time of PEC reaction. Hence, modified NPT-b comes out to be an efficient and a stable photoelectrode for hydrogen generation *via* cleavage of water molecule. This is one of the desired and important achievements for CdS photoelectrode, which has been specifically demonstrated, in present work.

3.3.4   Summary of this section

Very stable CdS photoanodes has been fabricated by spray pyrolysis film deposition technique. The modification of "*aligned rod-like nanostructured CdS*" bare electrodes by adsorption of TiO$_2$ (5 nm) nanoparticles yields 3.7 times enhanced photocurrent generation than bare CdS

97

electrode. The modified electrode generates 25 times more hydrogen gas than the bare CdS. An enhanced IPCE of 22 % is obtained for TiO_2 modified photoanode as compared to bare CdS (~8%). Modified photoanode has shown improved STH of 0.7 % than that of bare CdS (~0.2%). Enhancement in photocurrent displayed by *nanoparticle TiO₂ modified CdS photoanode* is attributed to the reduction in the electron-holes recombination process. Specifically, photochemical-stability is studied by quantitative elemental analysis using XPS and time dependent photocurrent. Stability factor ($\sum$) that has been defined for the first time, further which has been quantified for the bare and the modified electrodes. It is found that $\sum_{modified}$ (100 %) achieved is much better than $\sum_{CdS}$ (72%) when tested for a typical duration of 2.5 hrs. of PEC reaction time. Thus, obtained $\sum$-factor for modified electrode demonstrates an improved stability for nano-TiO_2 modified photoelectrode. Such high efficiency and stability is attributed to its passive behavior over photo-corrosive CdS surface.

3.4 Metal oxide II: Nb₂O₅ nanoparticles

This section describes the surface modification of CdS film with niobia nanoparticles *via* thioglycerol as organic linker. They are further used for fabrication of an efficient and a stable photoanode in PEC cell. In this part of study, we have attempted to study the particle size dependence on modification of CdS film and its PEC performance. As per the method described in experimental section (*chapter-2, section 2.3.2*), we synthesized three different sized (~3, ~6 and ~9 nm) *niobia nanoparticles* by hydrothermal synthesis approach. Further, we investigated the particle size dependent PEC performances of the *nanoparticle modified* CdS photoanode. FTIR and XPS confirm the formation of Nb_2O_5 nanoparticles those are prepared *via* decomposition of niobium *peroxo* complex during the hydrothermal reaction and reveals the

presence of surface OH⁻ group over niobia nanoparticles those impart high catalytic properties to a material. Nano-Nb_2O_5 modified photoanode displays 23-times higher power conversion efficiency than CdS. This modified structure increases the open circuit voltage (OCV) from 0.65 V to 0.77 V, which is attributed to the nano-Nb_2O_5 induced surface passivation effect over the bare CdS. Linking of nanoparticles on CdS surface, thus improves the photocorrosion stability of the CdS photoanode for even longer than 4 hrs. in contrast to tens of minutes for base CdS photoanode. The uniform coverage of CdS photoanode surface by niobia nanoparticles is thus found to be the controlling parameter for achieving a higher PEC performance and stability of the photoanode. This finding directed us to design an improved CdS photoanode for efficient and prolonged PEC hydrogen generation from PEC Cell.

Table 3.4.1 Table showing the values of observed V_{oc}, I_{sc}, and η of unmodified and niobia modified photoelectrodes.

Name of sample	Size of nanoparticle (nm)	V_{oc} (V)	I_{sc} ($\mu A/cm^2$)	η (%)
CdS		0.65	85	0.02
CdS/NP-1	3	0.70	417	0.10
CdS/NP-2	7	0.66	670	0.20
CdS/NP-3	9	0.77	830	0.28
CdS/BLK	bulk	0.94	506	0.03

3.4.1 Structural, optical properties and morphological characterization of Nb_2O_5 nanoparticles

Different films are named according to the size of nanoparticle as summarized in Table 3.4.1. Figure 3.4.1(a) shows the FTIR spectra of *as*-prepared niobia nanoparticles (NP-1) synthesized from the hydrothermal treatment of the *niobium peroxo complex*. There are two dips *viz.* observed in range of 3000 to 3600 cm⁻¹, which predominantly corresponds to the stretching
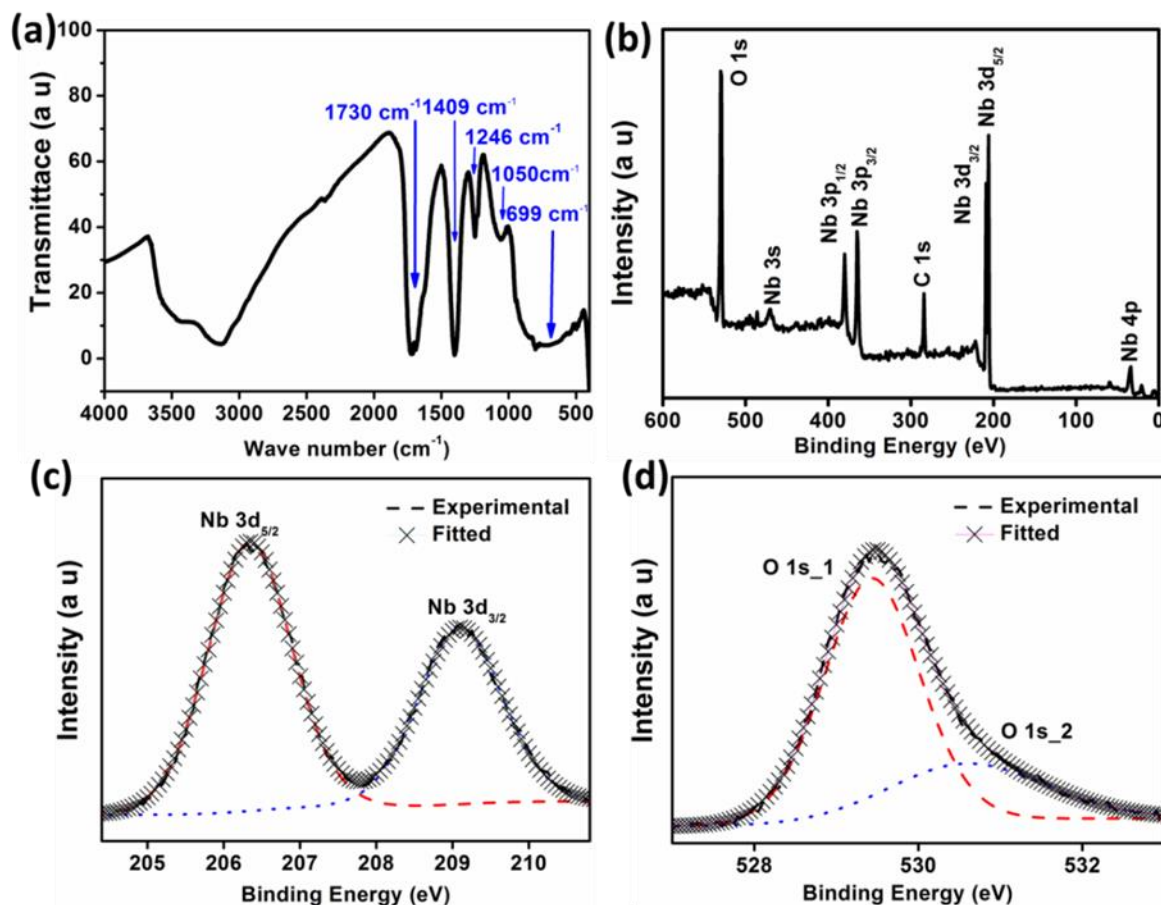
Figure 3.4.1 (a) FTIR spectrum of as prepared niobia nanoparticles (NP-1). XPS characterization of Nb_2O_5 nanoparticles (NP-1) in the form of **(b)** survey spectrum; and region-wise scan of Nb 3d **(c)** and O 1s **(d).** Dotted lines show de-convoluted component that can be superposed to simulate fitted curve.

mode of H-bonded O-H groups of the adsorbed water, and other due to N-H bond [95]. The peak at 1730 cm^{-1} is correlated to the bending mode of the carbonyl group [95]. The transmission peak at 1409 cm^{-1} appeared due to the stretching of the N-H bonds of NH_4^+ [70]. Peak at 1246 cm^{-1} corresponded to the C-O bond that can be related to the oxalate ions in the precursor [96]. Dip at 1050 cm^{-1} and 690 cm^{-1} corresponds to the stretching vibration of O-O bond belonging to –O-O-H (*peroxo*) group and Nb-O bond [96, 97], *respectively*. FTIR study clearly reveals that Nb^{5+} ions in acidic solution, reacted with H_2O_2 in aqueous solution to form *peroxo* niobic acid. This occurs *via* cleavage of *oxo* and *hydroxo* bridges in niobic acid precipitate and coordination of

peroxo group (O^{2-}) to Nb^{+5} ions. This demonstrates that the hydrothermal synthesis of niobia nanoparticles occurs *via* the decomposition of niobia *peroxo* complex.

Further oxidation state of Nb and O elements in niobia nanoparticles (NP-1) are investigated using XPS. Figure 3.4.1 (b) shows the survey spectrum of the Nb$_2$O$_5$ nanoparticles that indicates the existence of Nb, O along with some remnant carbon. The binding energy of Nb 3d$_{5/2}$ and Nb 3d$_{3/2}$ are 206.33 eV and 209.09 eV, *respectively* with spin orbit separation of 1.76 eV, which is characteristic of pentavalent Nb of Nb$_2$O$_5$ [54] (see Figure 3.4.1 (c)). After *de*-convoluting O 1s, it is found to exhibit two peaks, one at 529.42 eV (O 1s_1) which is attributed to oxygen in metal oxide, and another at 530.6 eV (O 1s_2) which corresponds to the -OH species (Figure *3.4.1* (d)). XPS analysis clearly demonstrates the formation of acidic Nb$_2$O$_5$ nanoparticles with surface -OH group. Acidic nature of nanoparticles is necessary to provide the good photocatalytic properties to the material.

Figure 3.4.2 (a), (b) and (c) show the TEM micrographs of Nb$_2$O$_5$ nanoparticles synthesized from 2, 6 and 9 hrs. of reaction time, *respectively*. As expected, increase in the size of nanoparticles is clearly observed with respect to the reaction time that facilitated the growth of the initially form nuclei. The TEM studies indicates that size of nanoparticle increases from 3 nm, to 7 nm and finally to 9 nm with increase in reaction time from 2 hrs. to 6 hrs. and finally to 9 hrs. The SAED pattern in the *inset* of respective Figure 3.4.2 (a) & (b) consists of the broad diffused rings, which are indicative of the small size of nanoparticles. Inset of Figure 3.4.2 (c) shows the SAED pattern consists of rings with many spots which is observed due to the presence of small particles at multiple orientations. The transformation of diffused rings to sharp featured rings clearly demonstrates an increase in the size and in the crystallinity of the nanoparticles with respect to increase in the reaction time.
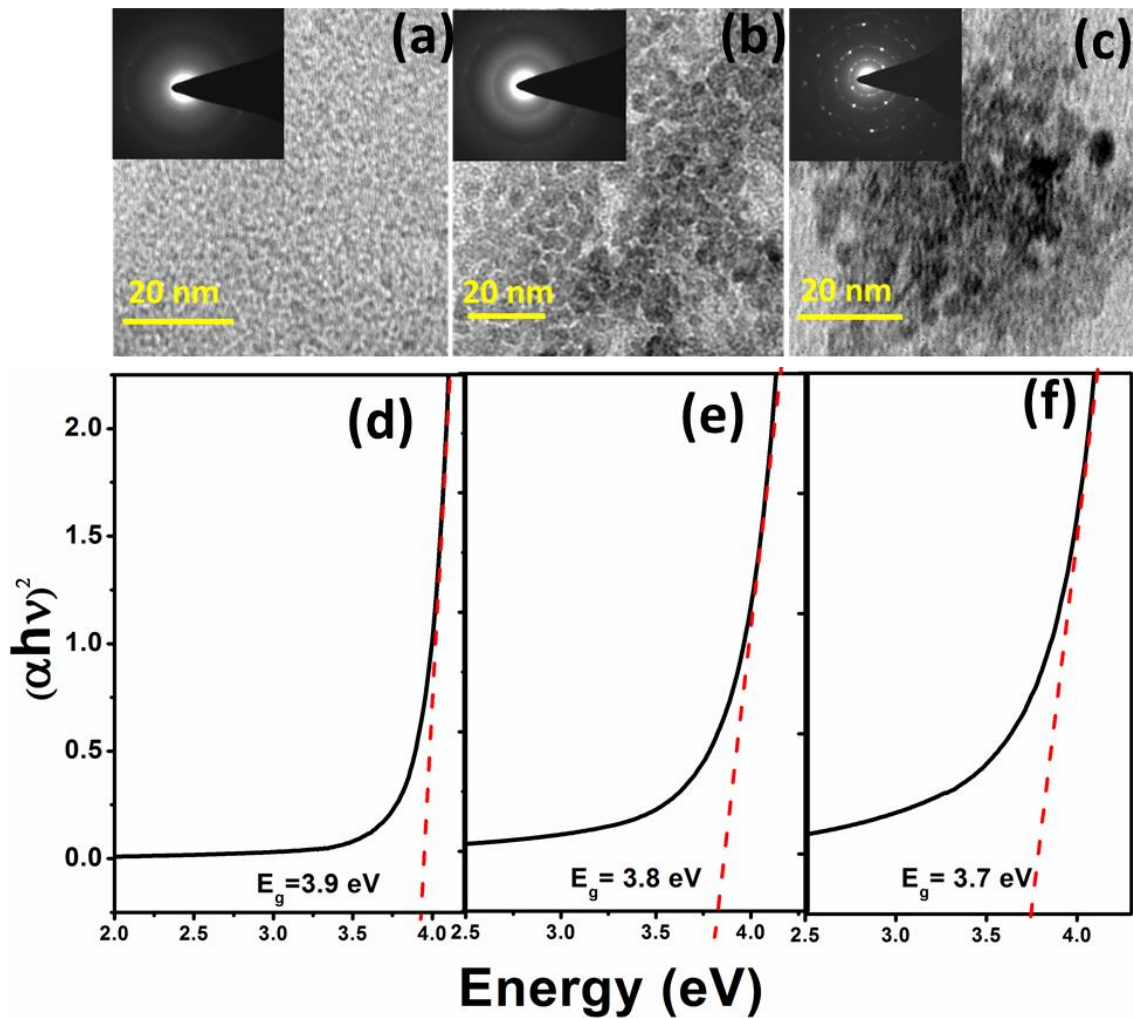
Figure 3.4.2 (a), (b) and (c) shows TEM images, along with the respective inset showing their SAED patterns for the respective nanoparticles synthesized by 2, 6 and 9 hrs. of reaction time, *respectively*. Corresponding absorption spectrum in **(d), (e) and (f)** indicate the expected variation in the band-gap of difference niobia nanoparticles synthesized in present study, *respectively* for 2. 6 and 9 hrs.

Bulk materials exhibit definite physical and optical properties those are independent of their size and dimensions. However, when the particle dimensions of the particles in the bulk system become less than the *Bohr-radius of exciton* for this material system, it induces a transition in the band-structure from a continuous energy-band to discrete energy levels. This size dependent electronic structure effect in turn alters the optical properties of the material. Consequently, with in the *confinement regime*, the quantum dot of material displays a larger bandgap than its bulk

counterpart. Generally, it is observed that there is a blue shift in the bandgap and photoluminescence excitation peak of the semiconductor nanoparticles with a decrease in the particle-size [92]. Thus, variation in particle size induces a change in the bandgap of the material. According to '*effective mass approximation*', the bandgap dependence of particle size in the quantum-confinement regime can be expressed by equation (3.4.1) [98]:

$$\Delta E \approx \frac{h^2\pi^2}{2R^2(\frac{1}{m_e}+\frac{1}{m_h})}$$ ……………………………………….. (3.4.1)

Where m_e and m_h are the effective mass of *electron* and *holes respectively*. This equation (3.4.1) clearly indicates that the bandgap can be tuned by tuning the particle-size. As shown in Figure 3.4.2 (d-f) experimental bandgap of the nanoparticles has been calculated using Tauc plots [70]. In line with the expectation of equation (3.4.1), we found that decrease in the particle size from NP-3 to NP-1 led to an increase in the bandgap from 3.7 eV to 3.9eV, and thus attributed to the quantum confinement effect [99].

3.4.2   Characterization of Nb_2O_5 nanoparticle functionalized CdS film

To understand the effect of chemical linking of niobia nanoparticles on the structural and optical properties of CdS photoanode, XRD and UV-Vis spectrophotometry have been carried out. From XRD pattern as shown in Figure 3.4.2 (a), it is clear that the existence of niobia nanoparticle over CdS surface doesn't alter XRD pattern of CdS. However, it reduces or shadows the diffracted intensity of the peaks of CdS. This is because these nanoparticles are nearly amorphous in nature (SAED Figure 3) and also since amount of niobia linked on CdS surface are too low and beyond the detection limit of XRD. The effect of nanoparticle modification on the optical properties of

CdS has been studied by using UV-Vis absorbance spectrophotometry. The absorption edge of modified CdS is blue shifted as compared to the bare CdS (Figure 3.4.2(b)). The blue shift is due to the effect of optical property of wide band-gap niobia nanoparticles (inset of Figure 3.4.2 (b)). The presence of these particles also screens the overall intensity that leads to the decrease in the absorption of modified CdS as compared to bare CdS absorption in visible range. To assure the presence of linking agent on the CdS surface XPS of modified film is carried out. A detail analysis using de-convolution of peaks indicates that S 2p can be fitted with three peaks, one at B.E. 162.7 eV, other at 164.74 eV and third being at 167.42 eV. These peaks could be attributed to the S related to CdS, thioglycerol [68] and sulphate moieties due to damaged free thiol, *respectively* [100, 101]. The presence of S related to thioglycerol clearly validates the presence of linking agent on CdS surface.

3.4.3 Photoelectrochemical characterization of Nb_2O_5 nanoparticle functionalized CdS photoanode

Effect of linking agent on the PEC performance of CdS photoanode: The modification of CdS photoanode with niobia nanoparticles (NP-3) was carried out by two different ways; one was by physisorption; which includes the physical adsorption of niobia nanoparticles over CdS photoanode by mere dipping the unmodified film in niobia nanoparticles dispersion [92].

Another method was chemisorption, which involved use of *bi*-functional molecules (organic linkers) for chemically linking two compounds with preferred functional groups [90, 102-103]. It is an efficient way of the adsorption of niobia nanoparticle on CdS photoanode surface. This is confirmed by the difference in photocurrent generation by such
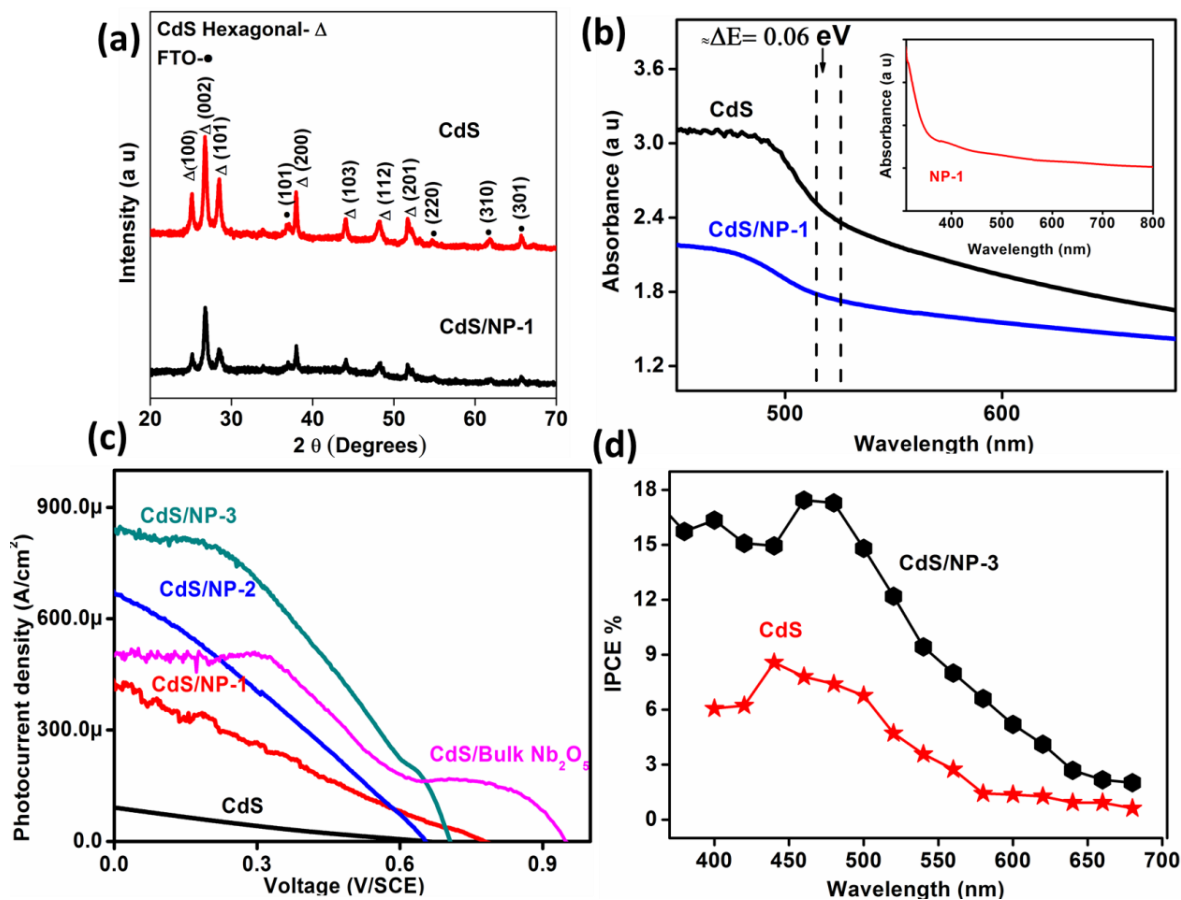
Figure 3.4.3 (a) XRD pattern of CdS films under study; (b) Absorbance spectra of niobia modified and bare CdS films (inset shows absorption spectrum of Nb$_2$O$_5$ nanoparticles); (c) I-V characteristics of various modified CdS films; (d) IPCE spectra of niobia modified and bare CdS films.

modified photoanode as shown in Figure 3.4.4. The chronoamperometric measurement clearly reveals that photocurrent density of later *i.e.* chemically linked photoanode (725 μA/cm^2) is much higher than former *i.e.* physically modified photoanode (429 μA/cm^2). The improved performance is attributed to the fact that the chemical linking promises uniform monolayer coverage of niobia nanoparticles over the available CdS surface. The monolayer coverage has been confirmed by elemental mapping of the surface during EDX analysis (Figure 3.4.5). The chemisorption technique utilizes affinity of CdS and Nb$_2$O$_5$ surfaces towards the thiol (R-SH) and hydroxyl (-OH) functional groups *respectively*, which has been used to form a hybrid

structure. In this chemical approach charge transport properties mainly depends on the length of *bi*-functional (linker) group [91]. Larger length of the *bi*-functional group causes hindrance to the transfer of electrons from one semiconductor to other semiconductor.
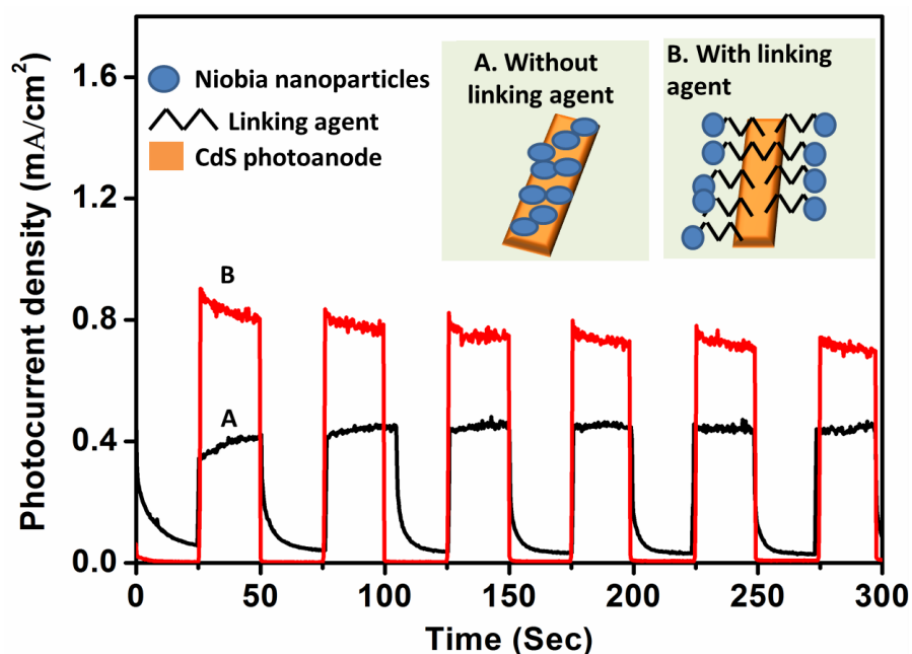
Figure 3.4.4 Effect of niobia nanoparticle (NP-3) modification over CdS with and without linking agent on their PEC performance.

The PEC measurements were carried out in a three-electrode glass cell having a transparent quartz window for photo-illumination. During PEC reaction, a junction is formed between the photoanode surface and electrolyte. Generally, during PEC reaction the electrolyte containing ionic pair of S^{2-} and SO_3^{2-} is used to resolve the inherent problem of Cd chalcogenide photo-dissolution in aqueous media. Figure 3.4.3 (c) shows the I-V curves of CdS and niobia nanoparticle modified photoanodes. It is quite evident from the I-V measurements that the CdS modified with niobia nanoparticle of size 9 nm has shown efficient PEC performance as compared to those modified by niobia particle of size 3 nm and 6 nm. For the sake of completeness, further CdS film was also modified by bulk Nb_2O_5 particles and PEC performance
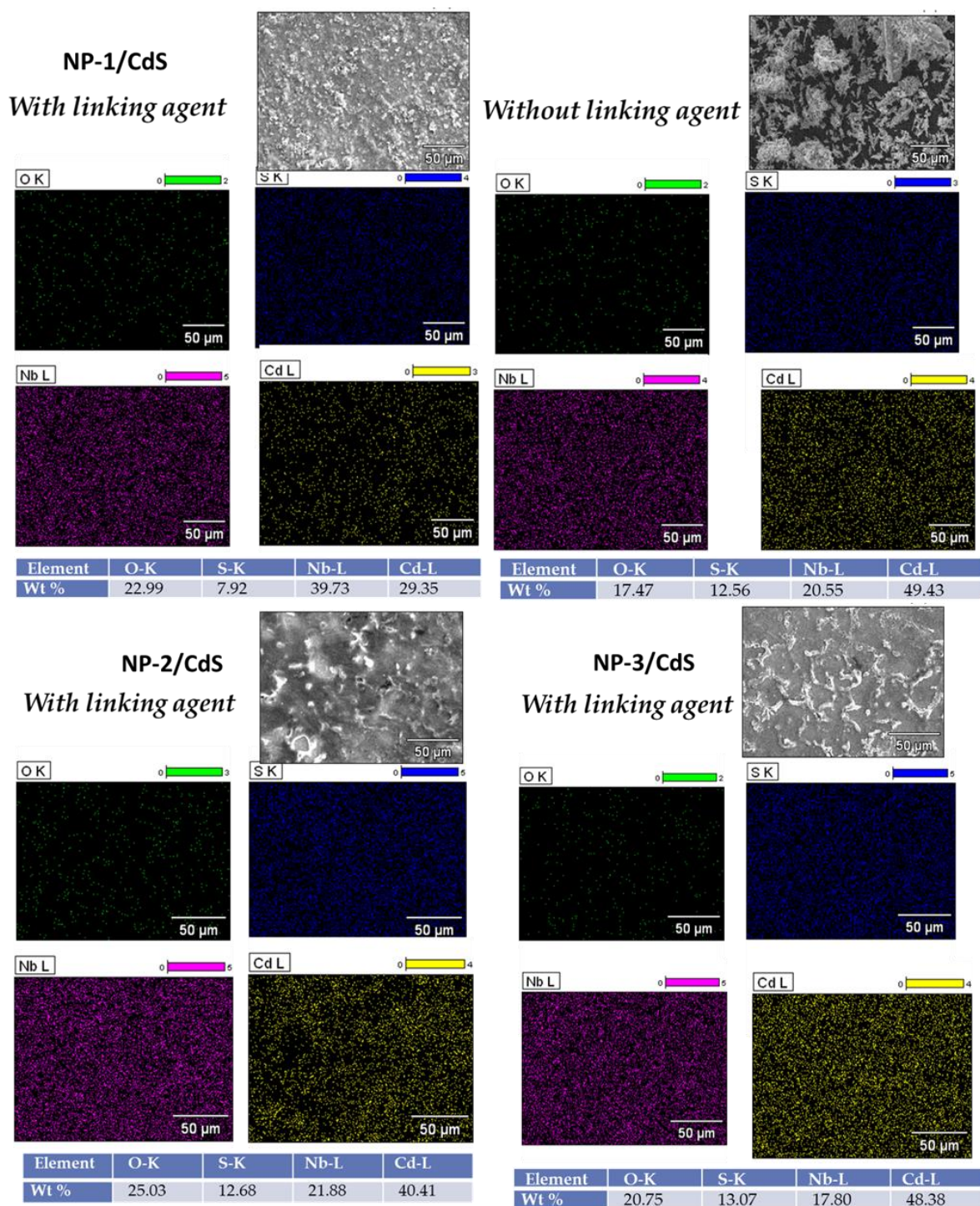
Figure 3.4.5 EDX analysis and elemental mapping of NP-1 modified CdS thin film with and without linking agent. EDX analysis of NP-2 and NP-3 modified films. Table shows respective atomic wt%.

The tables shown in the figure are:

NP-1/CdS With linking agent:

Element	O-K	S-K	Nb-L	Cd-L
Wt %	22.99	7.92	39.73	29.35

Without linking agent:

Element	O-K	S-K	Nb-L	Cd-L
Wt %	17.47	12.56	20.55	49.43

NP-2/CdS With linking agent:

Element	O-K	S-K	Nb-L	Cd-L
Wt %	25.03	12.68	21.88	40.41

NP-3/CdS With linking agent:

Element	O-K	S-K	Nb-L	Cd-L
Wt %	20.75	13.07	17.80	48.38

has been compared, it is found that the photocurrent of bulk particle modified film tremendously decreased with respect to nanoparticle modified film as shown in Figure 3.4.3 (c). There are

various factors those affect the PEC cell performance and are directly dependent on the physical and chemical properties of the semiconductor. Electron-holes recombination is one such crucial factor, which plays an important role. Recombination of photogenerated charge carriers at surface largely depends on the density of surface states in the semiconductor. Nanoparticle adsorption on the surface of CdS leads to the passivation of the surface-states, which in turn reduces the recombination process. This can also be deduced from the increased open circuit potential (V_{oc}) from 0.65 V to 0.77 V because of niobia modification of CdS photoanode. Another important point is that the film CdS/NP-1 shows higher V_{oc} compared to CdS/NP-2 and CdS/NP-3. It could be due to the better coverage of CdS surface with smaller nanoparticles. This is evident from the coverage of CdS surface, as evidenced by surface elemental mapping using EDX characterization (Figure 3.4.5). Although short circuit current (I_{sc}) is enhanced with the increase in the nanoparticle size used for the modification of CdS surface, however it could also be correlated to improvement in the particle crystallinity with respect to increase in the particle size. Variation in the efficiency (η), V_{oc} and I_{sc} of the niobia nanoparticle modified CdS photoanode with the change in the particle size are summarized in Table 3.4.1. This observation is inline with the improved PEC performance as confirmed by the comparison of IPCE spectra. Figure 3.4.3 (d) shows the IPCE spectra of CdS/NP-3 and unmodified CdS photoanode. CdS/NP-3 shows an IPCE of 18 % at 480 nm, which is more than double of the bare CdS photoanode (8 %). They exhibit a synchronous variation in V_{oc}, I_{sc} and efficiency with the increase in the niobia particle size.

Photoelectrochemical stability studies of Nb$_2$O$_5$ nanoparticle modified electrode: It is a well-known fact that Cd-chalcogenides are very prone to the photoanodic dissolution, consequently despite their tremendous potential as efficient photoanode, the hurdle has affected this class of

material for photoanode applications. Hence, to propel this class of material in a PEC cell, essentially it requires a long-lasting stability.
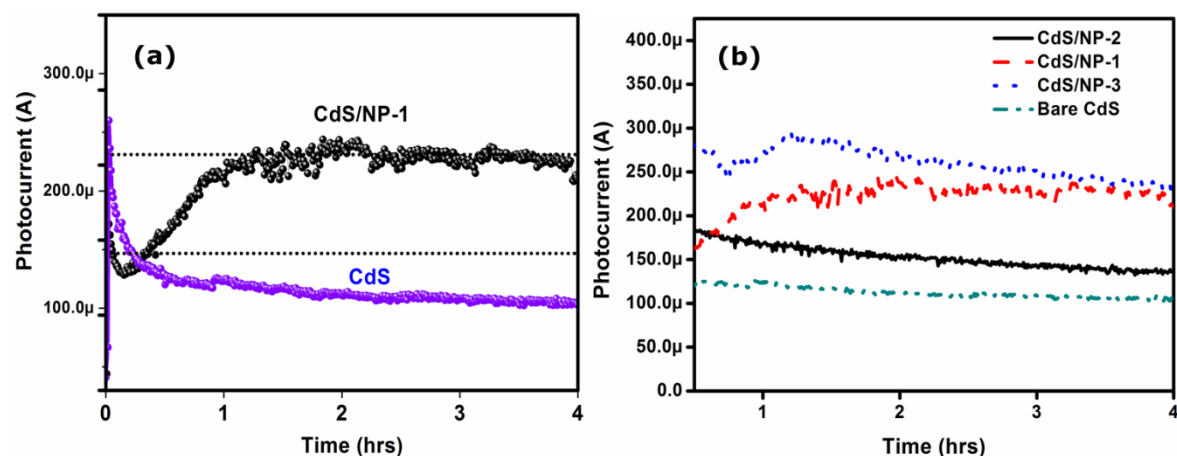
Figure 3.4.6 **(a)** Chronoamperometric curve for bare CdS and modified CdS photoanode (CdS/NP-3) recorded for the duration of 4 hrs. of PEC measurement as a measure of photocorrosion stability (b) Stability measurements of the CdS photoanode modified with different sized niobia nanoparticle, all overlaid in one graph.

Among some simpler remedies, electrolyte composition plays a *pivotal* role in PEC cell. Polysulphide electrolyte quenches the photocorrosion process by retarding photoanode polarization and curbing the surface ion-exchange process at electrode surface and electrolyte. As discussed above, another popular important method of metal oxide passivation can avoid the direct exposure of CdS surface to electrolyte [104]. In present work, we have employed both the options to curb the photo corrosion of CdS photoanode. However, it is important to detect the deterioration of the semiconductor electrode due to the photocorrosion. A prolonged chronoamperometric measurement is a well-known method to detect photocorrosion. Figure 3.4.6 (a) shows the chronoamperometric measurements of unmodified and modified CdS (CdS/NP-1) photoanodes for 4 hrs.

Noticeably, photocurrent generated due to illumination of the CdS photoanode decreased abruptly with time whereas CdS/NP-1 photoanode has shown remarkably a constant

photocurrent for 4 hrs. of measurement. The slope of chronoamperometric curve can be utilized to calculate stability factor, which can further be used to compare the stability of modified and bare CdS photoanode. The stability factor has been calculated using above formula [62] as given by equation (3.4.2):

$$\sum\nolimits_{photoelectrode} \% = \frac{\Delta_{CdS} - \Delta_{\mathrm{mod}\,ified}}{\Delta_{CdS}} * 100\% \dots\dots\dots\dots\dots\dots (3.4.2)$$

Where $\Delta_{photoelectrode}$ is slope of "I *vs.* t" curve of the photoelectrode, given by equation (3.4.3):

$$\Delta = \frac{\partial I}{\partial t} = \frac{I(t_2) - I(t_1)}{t_2 - t_1} \dots\dots\dots\dots\dots\dots\dots\dots\dots\dots (3.4.3)$$

Here, $I(t_1)$ is photocurrent at time 't$_1$' and $I(t_2)$ is photocurrent at time 't$_2$'.

The stability factor comes out to be 99.8 % for niobia-modified film for 4 hrs. of illumination time. The comparative study of stability of modified film with respect to the variation in nanoparticle size was also carried out and is shown in the Figure 3.4.6 (b).

Effect of particle size on CdS film coverage: The dependence of niobia nanoparticle size on the stability of modified CdS photoanodes can be correlated to the ease with which nanoparticles can form a uniform coverage over the CdS surface. This can be understood schematically from Figure 3.4.7, which reveals the size dependent coverage criteria of CdS surface. The coverage due to bigger sized nanoparticles is similar to the case-I in Figure 3.4.7. This indicated that such bigger size nanoparticles linked on CdS leave larger CdS surface exposed to electrolyte *via* bigger voids between the spherical particles, and hence has a probability of higher photocorrosion. While in case-II, *i.e.* smaller sized nanoparticles cover CdS surface uniformly and completely, thus electrolyte has comparatively lower penetration to the CdS substrate and

thus seized the photocorrosion to a greater extent. Thus above study demonstrates various aspects on the CdS stability, when it is modified by the nanoparticles of different sizes. The results of hydrogen evolved from niobia modified CdS photoanodes are mentioned in the *chapter 4.*

I. Nanoparticle of larger size　　　**II. Nanoparticle of smaller size**
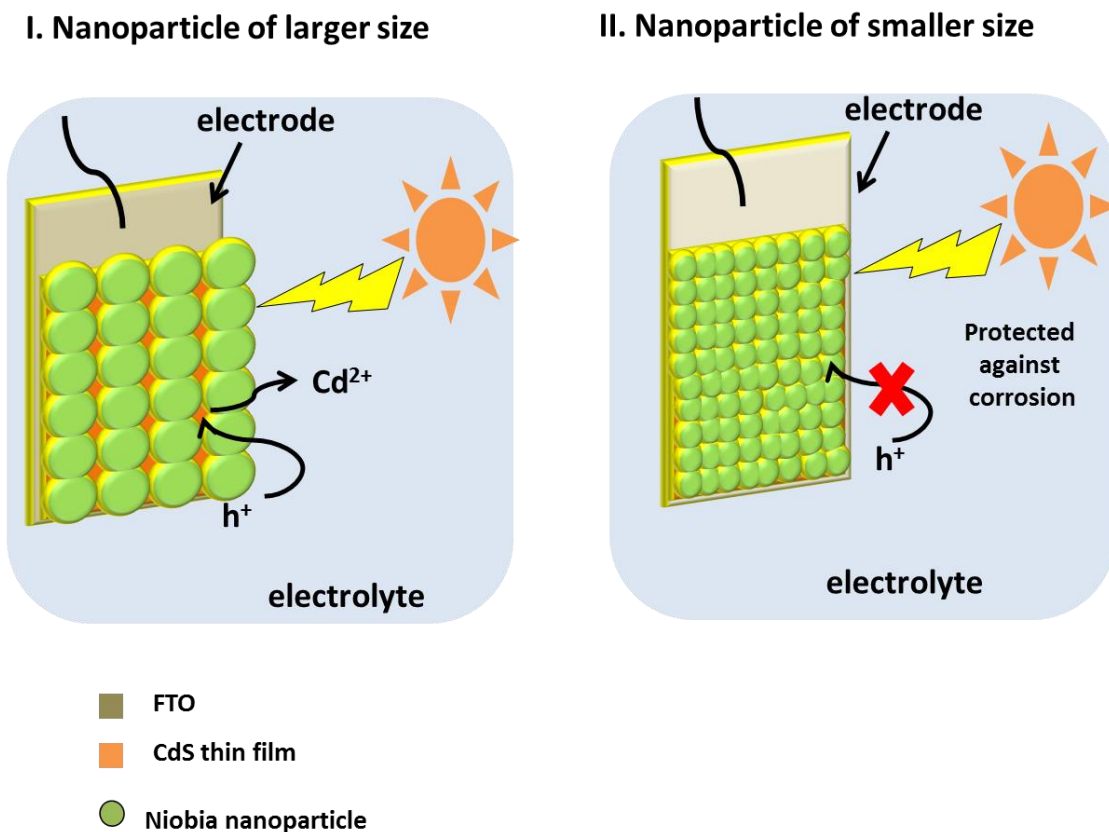
Figure 3.4.7 Schematic demonstrating the better adsorption of nanoparticles with smaller size leading to uniform coverage over CdS surface and hence curb photocorrosion better

3.4.4   Summary of this section

In this work, we describe the surface modification of CdS films by using niobia nanoparticles and effect of niobia particle size on the PEC efficiency and stability. Three different niobia nanoparticle sizes viz. 3 nm, 7 nm and 9 nm were prepared for the present study. We have mechanistically explained the hydrothermal formation of niobia nanoparticles those are prepared

by ammonia niobium oxalate precursor. The improved crystallinity of niobia nanoparticles with increase in the size led to an enhanced Isc of the modified films (size~ 9nm). The power conversion efficiency improved by 23 times for niobia modified CdS with respect to bare CdS. There is no decay in the photocurrent density is observed even after prolong (4 hrs.) chronoamperometric measurements. The enhanced efficiency is attributed to the passivation of CdS surface states induced due to niobia nanoparticles. The linking agent confirms a uniform nanoparticle adsorption, which assures better PEC performance, relative to the sample without linking agent. The present work encourages the use of "*different metal-oxide*" to improve the stability and efficiency desired for excellent photocatalytic and PEC material in CdS like chalcogenide systems.

RESULTS AND DISCUSSION

PART- III

Modification of CdS surface using co-catalysts

Motivation: The PART-III of Results and Discussions section insights the use of *co* –catalysts to modify CdS surface by using *transition metal hydroxides, oxides and sulphides*. The *co*-catalyst system reduces the barrier height for gas evolution reaction, which in turn lowers the overpotential at the interface and thus renders the stability to the chalcogenide electrode. As already discussed (*Chapter-1, Section 1.3*), in the absence of such *co*-catalysts holes participate in the anodic oxidation process of semiconductors to ultimately degrade it. Use of *co*-catalysts on CdS surface, increases the rate of oxygen evolution at photoanode surface that consumes holes (*Chapter-1, Section 1.3*) and thus the holes cannot participate in the photocorrosion reaction. Until now, enormous efforts have been put with respect to loading of Pt, Ru, RuO_2 and other inert-metals on CdS surface to content the problem of photo-corrosion in low-band gap materials. These chemically inert metals are however known to be very expensive and thus make such technology unfeasible. Nonetheless, there is a high demand of cost-effective *co*-catalyst that can improve the efficiency and stability of semiconducting photoanodes in a PEC cell. It is already reported that transition metal *viz.* Ni, Co (*section 3.3*) and Mo (*section 3.4)* based hydroxides, oxides and sulphide compounds show higher catalytic activity and stability [105]. These materials are eco-friendly, cost-effective and earth abundant materials. Keeping this in mind, we have selected Ni, Co related hydroxides and oxides; and Mo related sulphides and oxides, as suitable candidates for the CdS surface modification.

3.5 *Co*-catalyst system-I : Ni and Co related hydroxide and oxide

Metal M *(Ni, Co)* related *oxide* (***M***-O) and *hydroxide* (***M***-OH) harbours extra merit of low cost, high catalytic activity and high stability in aqueous media during PEC reaction. Here, Ni and Co related systems are presented together. This is because they exhibit very analogous role *viz.* oxygen evolving catalysts and their magnitude of catalytic activities. Though, Ni related

compounds show higher stability and lower overpotential [105] (overpotential is 0.45 V for Ni related compounds and 0.69 V for Co related). These earth abundant systems have been synthesized by simple chemical precipitation method as described in *chapter 2, section 2.3.3*. Geometrically hexagonal structure and well defined *micro rice* and *nano-sheets* like features are obtained for $Co(OH)_2$ and $Ni(OH)_2$ colloids, *respectively*. The standard reference CdS photoanode was then modified with as synthesized hydroxide colloids using chemical impregnation method. NiO and Co_3O_4 treated CdS photoanodes have been achieved by calcination of hydroxide-modified photoanodes at 350 °C. XPS has been used to validate the

3.5.1 Structural, optical and morphological properties of M: Ni,Co hydroxides
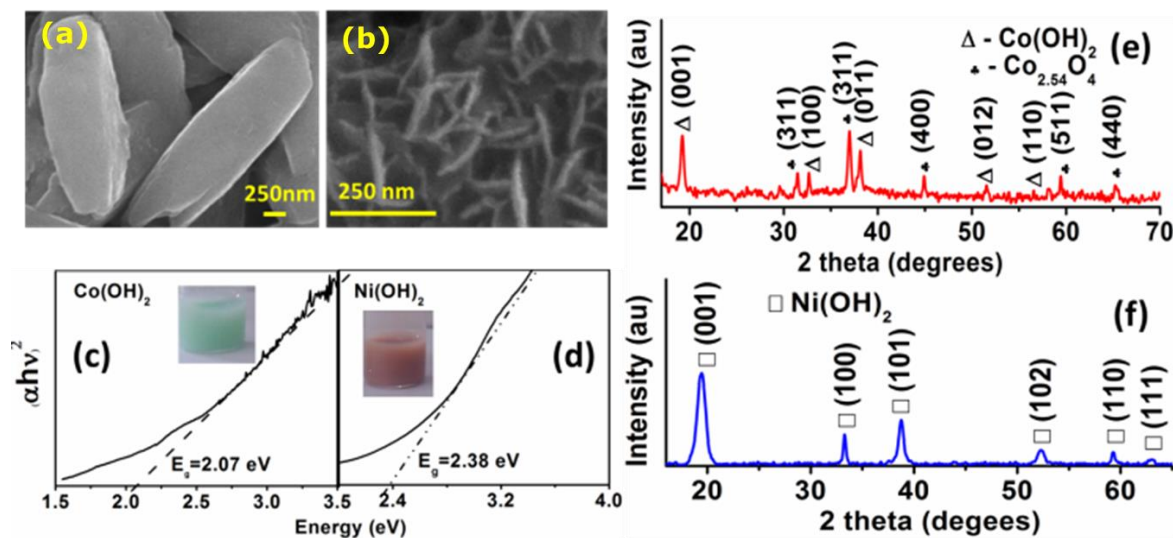
Figure 3.5.1 FESEM images of as prepared **(a)** $Co(OH)_2$ **(b)** $Ni(OH)_2$ *nano co-catalysts*; Respective Tauc plots of **(c)** $Co(OH)_2$ and **(d)** $Ni(OH)_2$ with *inset* showing the color of dispersion.; Respective XRD pattern of the *co*-catalyst particles (e) and (f).

presence of Ni-Co hydroxide and oxide on CdS surface. Various modifications exhibits significantly enhanced photocurrent, prolonged stability (> 8 h) to CdS, and facilitate impulsive

H$_2$ evolution. Nano-NiO modification yields three orders of higher H$_2$ evolution rate (2.5 mmol/hr) as compared to bare CdS.

The phase composition of as prepared colloids of *M*-OH has been analyzed by using XRD. The XRD pattern has shown mainly the existence of hexagonal crystal structure of Co(OH)$_2$ with preferential growth of rice along (001) orientation (Figure 3.5.1(e)). It also reveals that there is a *co*-existence of CoO and Co$_{2.5}$O$_4$ impurity phases. In case of Ni(OH)$_2$, the XRD pattern reveals existence of pure phase hexagonal structure of Ni(OH)$_2$ as shown in Figure 3.5.1(f). UV-Vis spectrophotometry has been used to understand and evaluate the optical properties of *M*-OH colloids. Its band gap is calculated by Tauc plot analysis by utilizing respective *M*-OH absorption spectrum [70]. The band-gap values of Ni(OH)$_2$ and Co(OH)$_2$ are found to be 2.3 eV and 2.07 eV (Figure 3.5.1(c) and (d)), *respectively*. FESEM images of Co(OH)$_2$ and Ni(OH)$_2$ colloids are shown in Figure 3.5.1. As prepared Co(OH)$_2$ colloid yields rice-shaped morphology as shown in Figure 3.5.1(a). It exhibits aspect ratio of ~3.1 at the observed length of 2.5 μm. In contrast Ni(OH)$_2$ exhibits the nano-sheet morphology with the dimension of around 200 nm as displayed in Figure 3.5.1(b).

It is important to mention that post calcination of hydroxide modified CdS films yields oxide films, which have been used as *oxide modified films* in the further studies.

3.5.2 Characterization of M: Ni, Co hydroxide and oxide functionalized CdS films

Figure 3.5.2 shows the absorption spectra of CdS films modified with Co(OH)$_2$, Co$_3$O$_4$, Ni(OH)$_2$ and NiO nanostructures. It can be clearly seen that modification yields no significant changes in the optical properties of CdS thin films
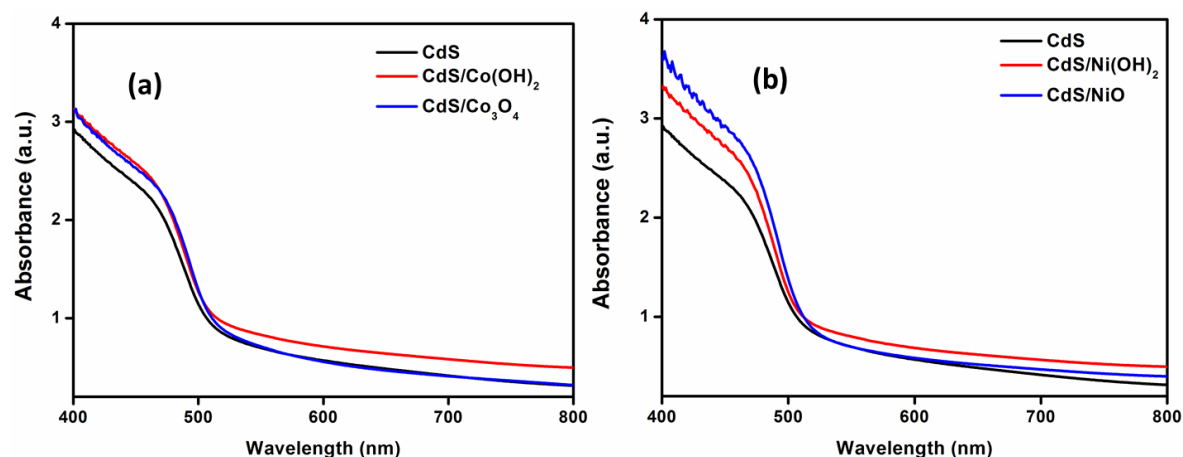
Figure 3.5.2 Absorption spectra of **(a)** $Co(OH)_2$ and Co_3O_4 modified CdS thin films and **(b)** $Ni(OH)_2$ and NiO modified CdS thin films.

Figure 3.5.2 reveals the transformation of CdS surface with different modification. As deposited films has aligned rods like features and as synthesized $Co(OH)_2$ collids forms rice like nanostructures. Upon modification presence of nanostructured $Co(OH)_2$ colloids could be seen on CdS surface (Figure 3.5.2 (b)). Film becomes rough on further heat treatment of $Co(OH)_2$ modified CdS films at 350 °C which leads to the formation of Co_3O_4 modified CdS films. Similar morphological evolution has been seen for $Ni(OH)_2$ and NiO modified CdS films. As synthesized $Ni(OH)_2$ has nanosheets like features and heat treatment at 350 °C yields NiO modified CdS films.
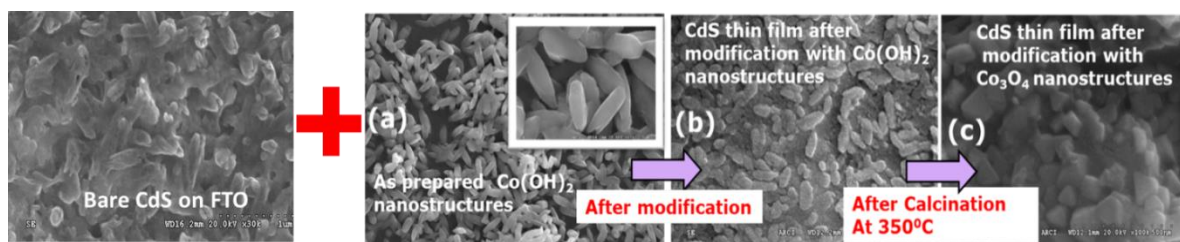
Figure 3.5.3 SEM of bare CdS on FTO (extreme left) **(a)** As synthesized $Co(OH)_2$ nano-rice structures; And CdS thin films modified with **(b)** $Co(OH)_2$ and (c) Co_3O_4.
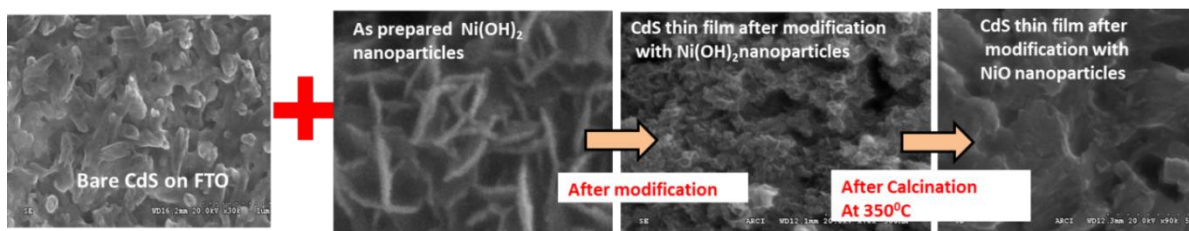
Figure 3.5.4 SEM of **(a)** As synthesized Ni(OH)$_2$ nano-sheets structures and CdS thin films modified with **(b)** Ni(OH)$_2$; (c) NiO.

Elemental characterization of M: Ni, Co hydroxide and oxide modified films: To analyse the chemical composition of modified CdS photoanode with Ni and Co related oxide and hydroxide,
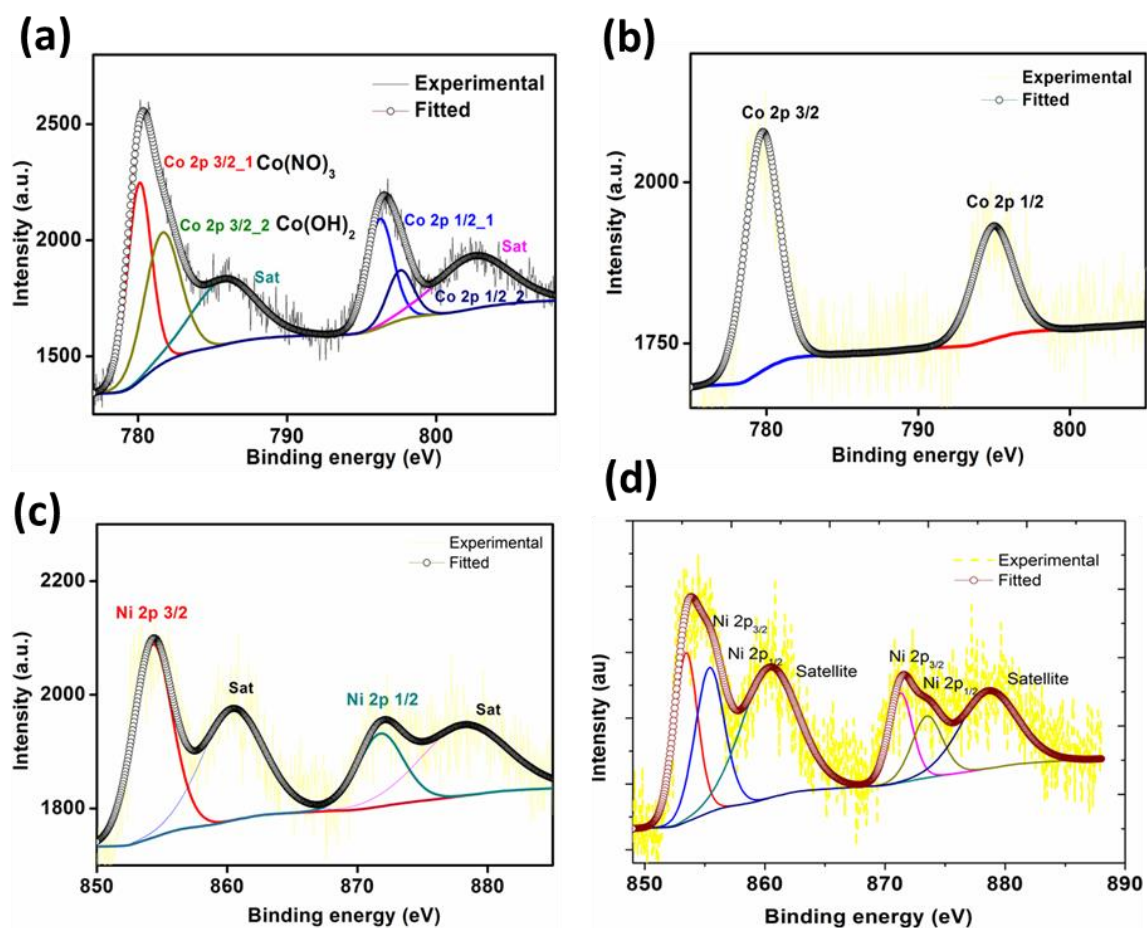
Figure 3.5.5 XPS spectra of Co (2p) in **(a)** Co(OH)$_2$ and **(b)** Co$_3$O$_4$ (c) Ni(OH)$_2$ and **(d)** NiO modified CdS thin films.

XPS has been carried out. The Co (2p) spectra of $Co(OH)_2$ modified CdS films has shown existence of Co 2p $_{3/2}$ at binding energy of 780.094 eV and 781.62 corresponding to $Co((OH)_2$ and $Co(NO_3)_2$, *respectively* (Figure 3.5.4(a)). The XPS spectra of Co_3O_4 modified CdS film has shown Co $2p_{3/2}$ peak at 779.73 eV which is attributed to Co of Co_3O_4 (Figure 3.5.4(b)). On the other hand Ni $2p_{3/2}$ peak of $Ni(OH)_2$ modified film has shown presence of Ni related to pure $Ni(OH)_2$ whereas NiO modified CdS film has shown the presence of NiO with Ni_2O_3 (Figure 3.5.4(c) and (d)).

3.5.3 Photoelectrochemical performance of M: Ni, Co hydroxide and oxide functionalized CdS photoanodes

The PEC measurements have been carried out in a *three*-electrode system. Liquid junction is formed between fabricated photoanode and electrolyte in a glass cell having transparent quartz window. Ionic pair of S^{2-} and SO_3^{2-} is used as electrolyte to resolve the inherent problem related to photo-dissolution of Cd-chalcogenides in an aqueous media during the PEC reaction .PEC performance of all the modified CdS photoanodes surprisingly improved with respect to the reference bare CdS electrode. Accordingly, NiO modified photoanode has shown highest photocurrent density of 1.2 mA/cm^2 as shown in Figure 3.5.5 (a), whereas bare CdS displays 0.5 mA/cm^2.

Further, IPCE spectrum has been recorded to understand the wavelength dependent PEC performance of modified CdS photoanode. All the modified electrodes has shown excitingly improved performance in the visible region as compared to the bare CdS photoanode with a maximum 18% IPCE for NiO modified CdS photoanode as shown in Figure 3.5.5 (b). The superior performance of Ni related electrode over Co related photoanode can be explained due to exceedingly better catalytic activity of Ni related *co*-catalysts [106]. Although, in both the cases

M-O related electrode performs better than *M*-OH, the fact is correlated with the calcination of

M-OH that yielded *M*-O *nano*-particles. This process induces a
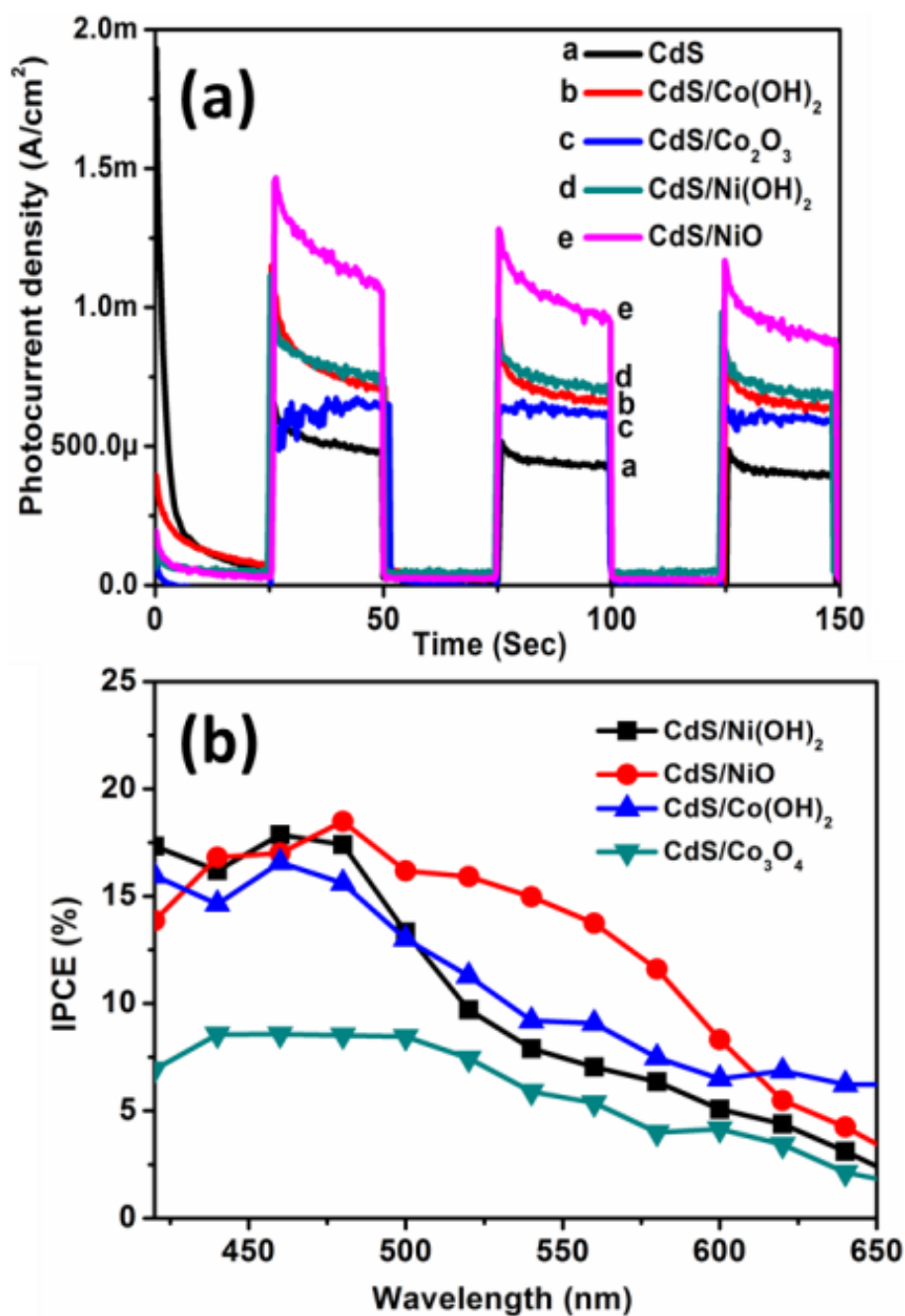
Figure 3.5.6 (a) Chronoampereometry curves of MOH and MO modified CdS photoanodes (b) IPCE spectra of of MOH and MO modified CdS photoanodes.

compact *nano*-junction formation between CdS/NiO *nano*-sheets or CdS/Co$_3$O$_4$ *nano* rice, which leads to an efficient transfer of holes at the interface. In addition, this step improves the electrode stability, and is a salient feature of this modified electrode.

Efficient hydrogen evolution from M: Ni, Co hydroxide and oxide modified photoanodes: Figure 3.5.6 (a) shows the rate of hydrogen evolution in a PEC cell using various modified CdS photoanodes. It is clearly seen that the amount of H$_2$ evolved in the PEC cell in presence of ***M*-OH** and ***M*-O** modified electrodes is impulsively higher than the bare CdS photoanode (1.17 μmoles/hr). NiO modified CdS photoanode induces a highest rate of H$_2$ evolution of 2.5 *milli*-mol/hr at counter electrode, thus illustrates efficient water oxidation and reduction kinetics at electrode/electrolyte interface.

Photoelectrochemical stability studies of M: Ni, Co hydroxide and oxide modified photoanodes: Another important aspect of this work is to impart stability [31, 62-63] to CdS photoanodes by surface modification *via **M*-O** and ***M*-OH** *co*-catalysts. Figure 3.5.6 (b) shows the effect of MO and MOH *co*-catalysts loading for the protection of CdS photoanodes against photocorrosion. It can be clearly seen in prolonged chronoamperometric measurements that in case of modified CdS photocurrent decrease less rapidly than bare CdS photoanodes. Consequently, this enhanced stability is attributed to efficient transfer of photogenerated holes from CdS surface and hence inhibiting electrode dissolution. As expected ***M*-O** modified films has shown better stability than ***M*-OH** modified films.

It is known that even semiconductors those exhibited sufficient band-gap and required band-edge positions for water-splitting have a poor efficiency of PEC cell due to lower reaction kinetics of hydrogen and oxygen evolution reaction. Due to such limitation, over-potential is developed at the interface and which is needed to be overcome to efficiently drive the reaction.
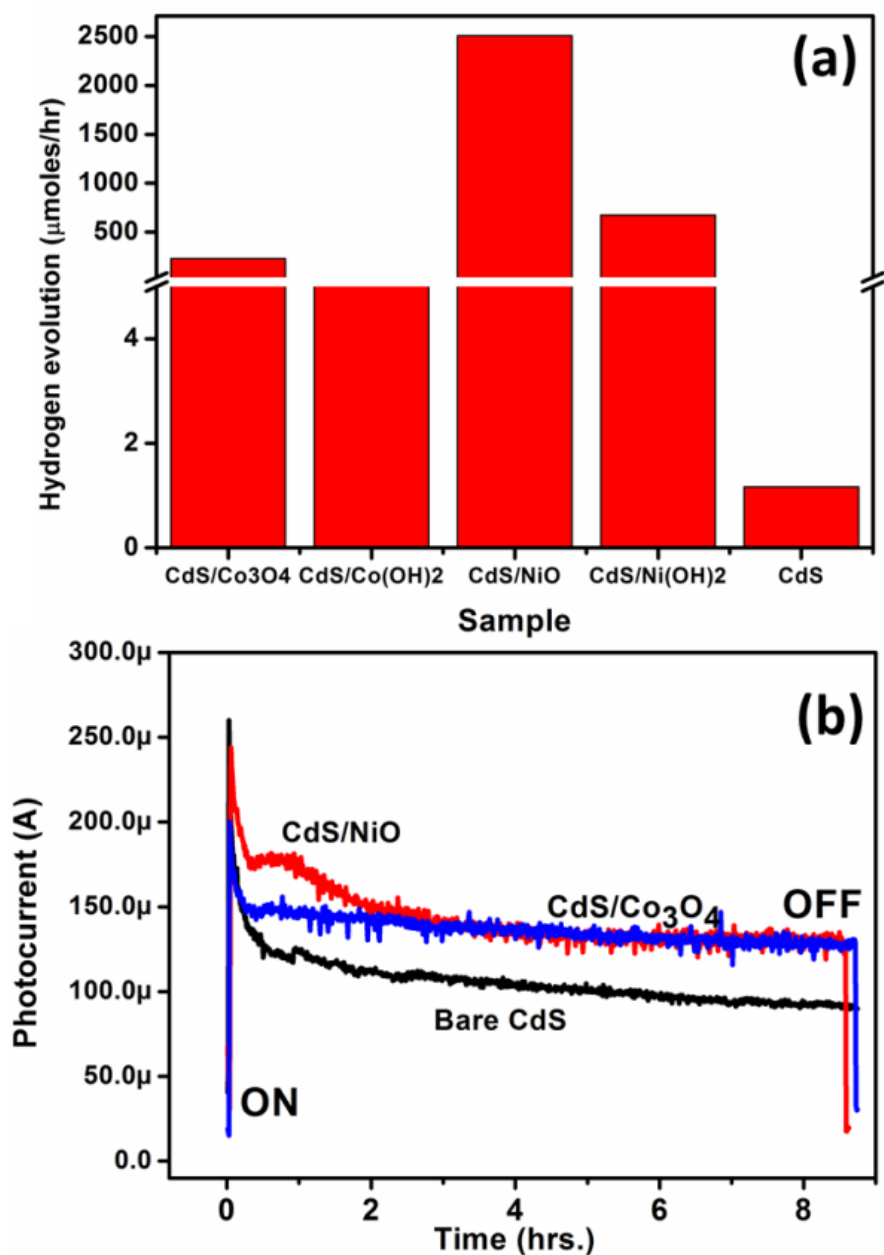
Figure 3.5.7 (a) Rate of hydrogen evolution in PEC cell for MOH and MO modified CdS photoanodes and **(b)** Stability measurements of MOH and MO modified CdS photoanodes.

The over-potential generally reduces the usable output voltage and thus hampers the PEC efficiency. To counter this loss, a *co*-catalyst is loaded on the semiconductor surface so as to improve the reaction kinetics. Optimally, this could be done by uniform and discontinuous
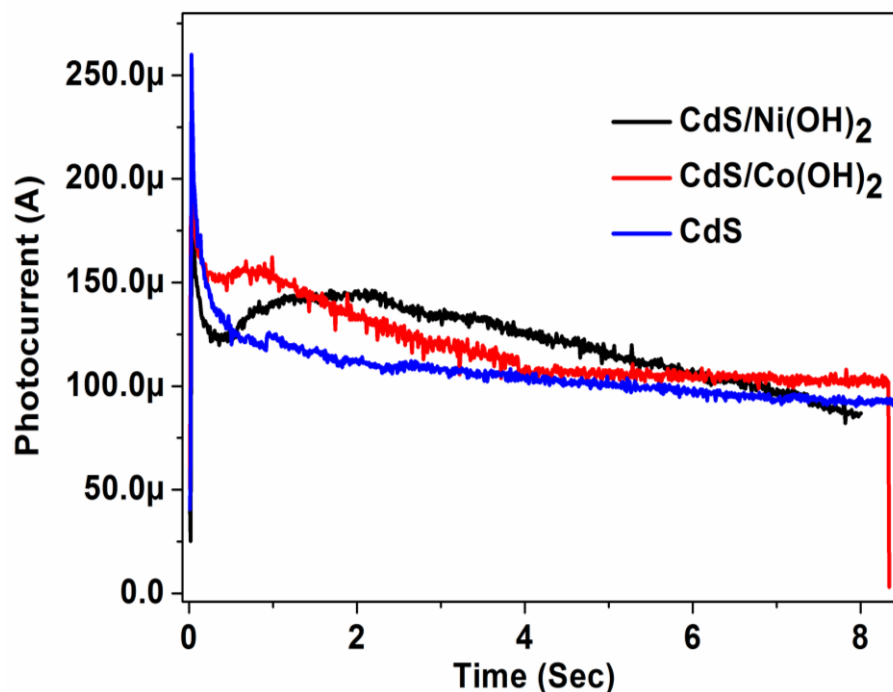
Figure 3.5.8 Comparision of time dependent choronoamperometric measurement of MOH modified CdS photoanodes.

deposition of *co*-catalyst particles on the semiconductor surface. Ideally, smaller sized particles of the dimensions smaller than the wavelength of incident photons [106] are expected to yield a maximum-voltage output *via* the *co*-catalyst configuration. This strategy assures that the distribution of *co*-catalyst remains optically transparent during PEC reaction, and thus does not affect the light absorption property of semiconductor in use. In this work, it can be clearly seen in the absorption spectra of the modified films, that the optical property of CdS does not undergo any observable change after the surface modification by *M*-OH and *M*-O *co*-catalysts. Therefore, these results effectively imply that a discontinuous and a uniform distribution of highly activity *co*-catalysts over CdS photoanode predominately yield sustainable hydrogen evolution.
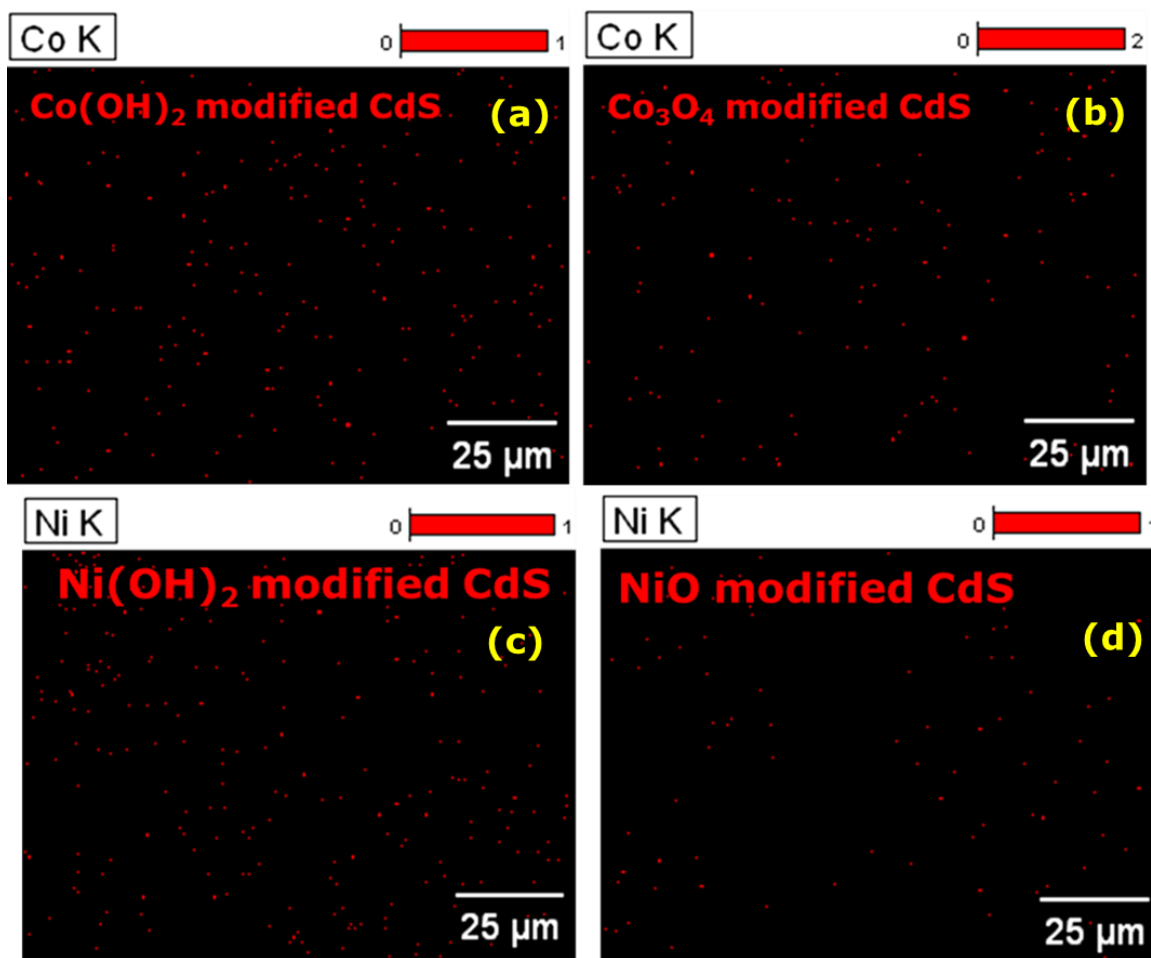
Figure 3.5.9. Elemental mapping of Co in **(a)** Co(OH)$_2$ and **(b)** Co$_3$O$_4$ modified CdS thin films by EDX analysis and elemental mapping of Ni in **(a)**Ni(OH)$_2$ and **(b)** NiO modified CdS thin films by EDX analysis.

Mechanism for superior performance of CdS/NiO system

NiO is a *p*-type semiconductor apt for facilitating the holes transfer due to high hole mobility [107]. With the control of interfacial properties at *p*-NiO and *n*-CdS interface, NiO is expected to form a *p-n* junction with *n*-type semiconductors, while also acts as an oxidation *co*-catalyst [108]. Formation of *p-n* at the interface leads to efficient charge separation and refrain the electron-hole recombination. Moreover, it lowers the overpotential due to excellent oxidizing catalytic capability of NiO.
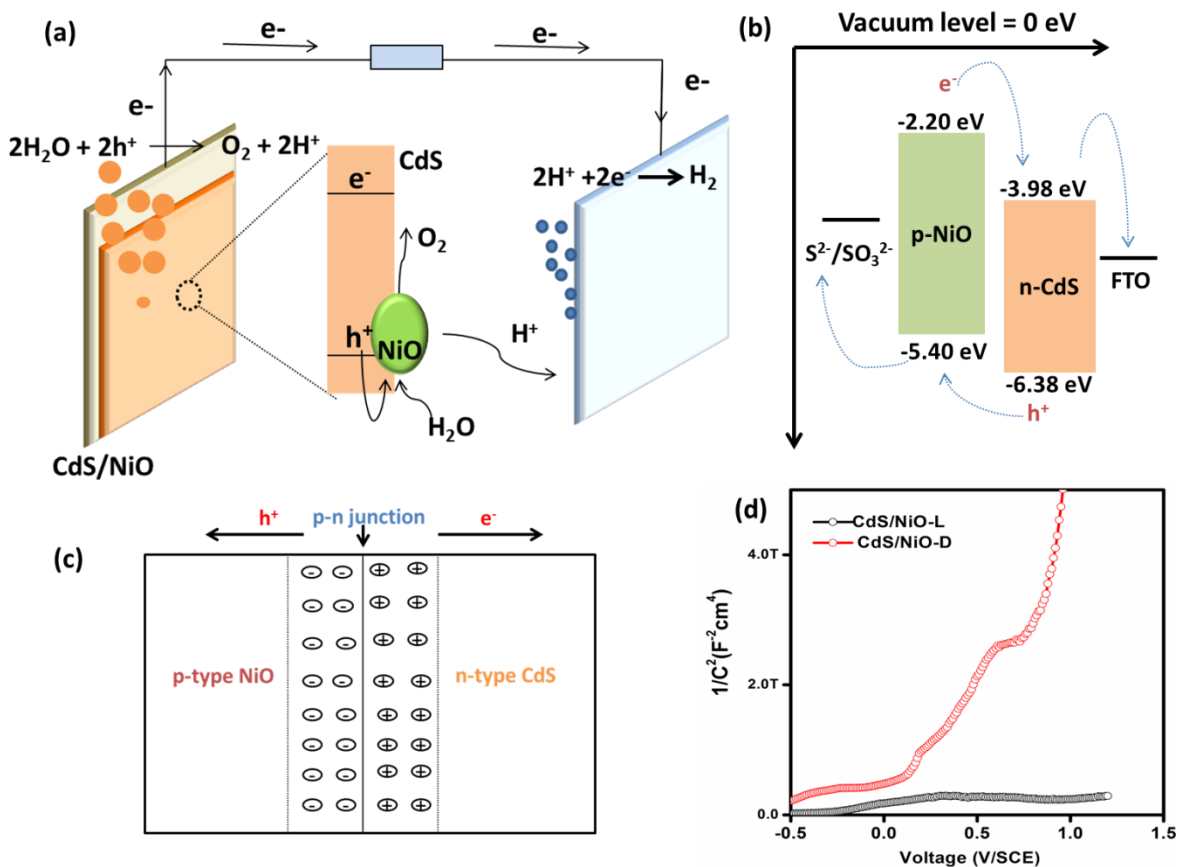
Figure 3.5.10. (a) Schematic presentation of mechanism of enhanced performance of NiO modified CdS photoanodes, **(b)** Band-energetics of *p*-NiO and *n*-CdS junction , **(c)** Schematic for charge transfer at *p-n* junction and **(d)** Mott-Schottky plots of CdS/NiO photoanodes in dark and light.

It is believed that NiO deposition enhances the photoelectrochemical properties of photoanode in two aspects (1) formation of *p-n* junction, which efficiently extracts the holes and separates the charge carriers that lead to improvement in photocurrent [109]. (2) NiO acts as a *co*-catalyst to reduce the barrier for oxygen evolution, which enhances the gas extraction [110]. Figure 3.5.10 (a) shows the schematic diagram showing reaction kinetics occurring at the CdS/NiO/electrolyte interface in a PEC cell. The NiO on CdS surface acts as an oxidation *co*-catalysts and improves the water splitting reaction following the mechanism equation (3.5.1-3.5.4) [111]:

$$CdS \xrightarrow{h\vartheta} e^- + h^+ \dots\dots\dots\dots\dots\dots\dots\dots \text{(3.5.1)}$$

$$M^n + H_2O + h^+ \rightarrow M^{n+1}(OH_{ad}^-) + H^+ \quad \dots\dots\dots\dots \text{(3.5.2)}$$

$$2M^{n+1}(OH_{ad}^-) \rightarrow M^{n+2}O + M^n + H_2O \dots\dots\dots\dots\dots \text{(3.5.3)}$$

$$2M^{n+2}O \rightarrow 2M^n + O_2 \dots\dots\dots\dots\dots\dots\dots \text{(3.5.4)}$$
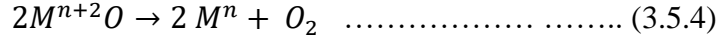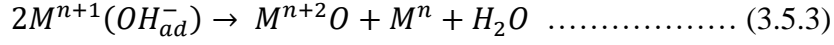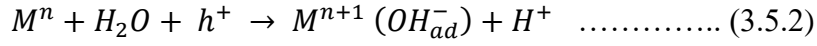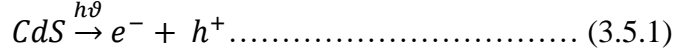
Where M^n is metal active sites of Ni, Co with valence state of n^+.

It is clear from above reactions that *co*-catalyst loaded semiconductor shows lower barrier potential for oxygen evolution reaction due to faster holes consumption. It is clearly shown in schematic that NiO on the surface of CdS facilitates the holes transfer, which combines with water molecules to drive oxygen evolution and produces H^+ ions. The electrons at counter electrode *via* external circuit reduce the H^+ ions to produce hydrogen gas. Thus, these catalysts indirectly enhance the rate of hydrogen evolution at counter electrode that can be clearly seen in Figure 3.5.10 (a). Unfortunately, we could not show oxygen evolution rate since sulphide electrolyte is used in above experiment as holes scavenger to avoid CdS photocorrosion. There are numerous reports showing stoichiometric hydrogen and oxygen evolution using NiO *co*-catalysts on different semiconductors [112,113, 114]. The above discussion illuminates the mechanism of NiO *co*-catalyst for high reaction kinetics.

Figure 3.5.10 (b) shows the band energetics at CdS/NiO interface. It can be easily deduced from the Figure that the band edge positions of CdS and NiO leads to moving of electrons in direction; NiO → CdS → FTO → counter elecrode → H^+ → hydrogen. It facilitates the holes transfer in reverse direction from CdS to S^{2-}/SO_3^{2-} *via* NiO [115]. The charge transfer mechanism in a *p-n* junction formed by *p*-NiO and *n*-CdS can be easily understood from Figure 3.5.10 (c) [115].

126

When *p*-type NiO is deposited on *n*-CdS surface, it forms a number of micro-junctions at the interface. For equilibrium of charges, an inner electric field is generated at the NiO/CdS interface. This field induces negative charge in NiO whereas positive charge in CdS. When the photoanode is illuminated electron-hole pairs are created in photoanode. In the presence of inner electric field, the holes move to the negative field and electron transfers to the positive field. This induces the separation of photogenerated charge carriers effectively and supresses the recombination process. Since CdS is an *n*-type semiconductor, it possesses high electron conductivity and *p*-type NiO facilitates high holes mobility, this leads to fast transport of separated charges at the surface of photoanode. This mechanism explains the enhanced photocurrent by the formation of *p-n* junction. Figure 3.5.10 (d) confirms the formation of *p-n* junction at *p*-NiO/*n*-CdS interface. It shows the Mott-Schottky curves of NiO/CdS in light and dark. The co-existence of positive and negative slopes in Mott-Schottky curve validates the presence of *p-n* junction [10].

Similar mechanism can be explained for already reported Co_3O_4 [116], $Co(OH)_2$ [117] and $Ni(OH)_2$ [119] modified CdS photoanode. Although NiO has much higher catalytic activity than other *co*-catalyst systems, its superior performance could also be attributed to its morphology. Co related *co*-catalysts synthesized here are of micron size rods but Ni *co*-catalysts shows distinct nanosheets. The nanostructuring of Ni related *co*-catalysts assures better PEC performance of modified CdS photoanodes, as reported earlier regarding the dramatic improved performance of nanosheets in catalytic applications [120].

3.5.4   Summary of this section

In conclusion, robust *co*-catalysts *viz.* $Co(OH)_2$, Co_3O_4, $Ni(OH)_2$ and NiO are loaded on the surface of CdS photoanode by simple chemical impregnation method. The $Co(OH)_2$ and

Ni(OH)$_2$ as synthesized colloids give nano-rice and nano-sheets like morphology, *respectively*. After modification CdS photoanode acquires superior properties with respect to photocurrent generation, hydrogen evolution and photo-stability. Highest hydrogen evolution rate and photocurrent density of 2.5 mmol/hr and 1.2 mA/cm^2, *respectively*, is achieved for NiO modified CdS photoanodes. Wavelength dependent PEC performance reveals maximum IPCE of 18%. This work motivates to improve the PEC performance of different semiconducting system by employing economic *co*-catalysts.

3.6 *Co*-catalyst system-II: MoS$_2$-MoO$_3$ nanostructures

Recently, MoS$_2$ has gained wide attention due to its high catalytic properties and high stability in aqueous media. The literature on HER shows, MoS$_2$ is an important catalyst as it displays low overpotential of 692 mV [121]. However, its large internal resistance in bulk structures leads to an inefficient catalysis. This limitation necessitates the study of MoS$_2$-MoO$_3$ hybrid structures [122]. It is important to mention that nanostructuring does effect the charge transport properties. Thus, present work focuses on the modification of CdS surface by nanostructured MoS$_2$-MoO$_3$ to achive an efficient and stable photoanode. The MoS$_2$-MoO$_3$ nanostructures were synthesized by hydrothermal method, in which the effect of reaction time on the morphology (as discussed in *chapter 2, section 2.3.4*) was investigated. The structural characterization reveals that as the synthesis time of hydrothermal method increases the fraction of MoS$_2$ phase increases in the MoS$_2$-MoO$_3$ nanostructures. With an increase in reaction time, the morphology of MoS$_2$-MoO$_3$ nanostructures transformed from nanorod bundles to the flakes and then to flower like structures. Accordingly bandgap shows a decrease from 2.40 eV to 1.73 eV. These MoS$_2$-MoO$_3$ nanostructures were used for surface modification of CdS films by chemical impregnation method. The modified CdS film with flower like nanostructures of MoS$_2$-MoO$_3$ composites has

128

shown highest PEC performance *i.e.* 3.8 times higher photocurrent as compared to bare CdS photoanodes. The stability of modified photoanodes is enhanced for more than 8 hrs. as compared to bare CdS.

3.6.1 Structural, optical and morphological characterization of MoS$_2$-MoO$_3$ nanostructures
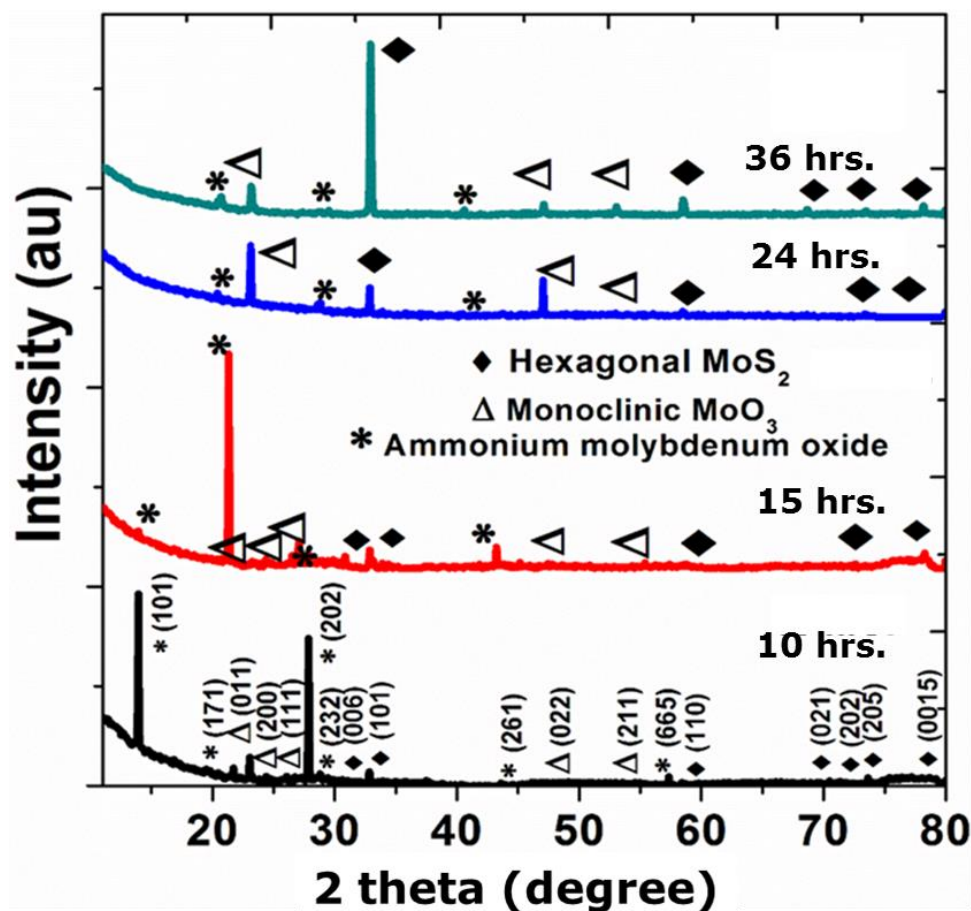
Figure 3.6.1 XRD pattern of MoS$_2$-MoO$_3$ nanostructures synthesized by varying the reaction time in hydrothermal method.

Figure 3.6.1 shows the XRD pattern of MoS$_2$-MoO$_3$ nanostructures synthesized at different reaction times during hydrothermal synthesis method. It is quite evident from the XRD pattern that for 10 hrs. of reaction the composite nanostructures dominantely exhibits monoclinic MoO$_3$ phase with structure showing preferential growth in (101) direction. It clearly shows that as the

reaction time increases the percentage of hexagonal MoS_2 phase increases and MoO_3 decreases. Ultimately at 36 hrs. of reaction time nanostructured composite has shown the formation of dominant MoS_2 phase, though an impurity phase of MoO_3 does exists.
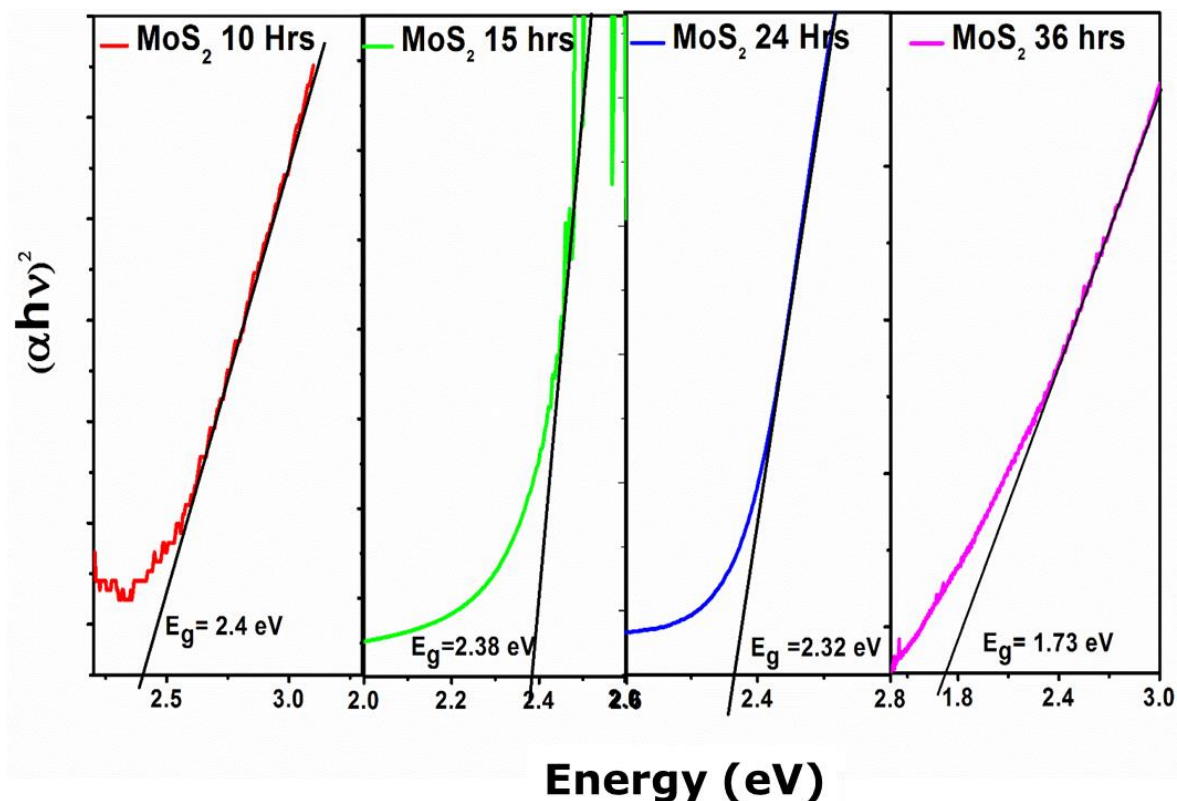
Figure 3.6.2 Tauc plots for MoS_2-MoO_3 nanostructures those synthesized by varying the reaction time in hydrothermal method.

Figure 3.6.2 shows the Tauc plots for MoS_2-MoO_3 nanostructures those are synthesized with respect to change in reaction time. It clearly shows that there is reduction in the bandgap as the reaction time increases from 10 hrs. to 36 hrs. This reduction in the bandgap is attributed to two factors. Firstly, with increase in reaction time, size of particles increases, which in turn minimize the quantum confinement thereby lowering the bandgap leading to bulk value. Secondly, there is effect of composition variation of MoS_2 (1.29 eV) and MoO_3 (3 eV). Structural characterization

reveals that there is increase in MoS_2 phase with increase in reaction time thus exhibits lower bandgap for 36 hrs. of reaction time
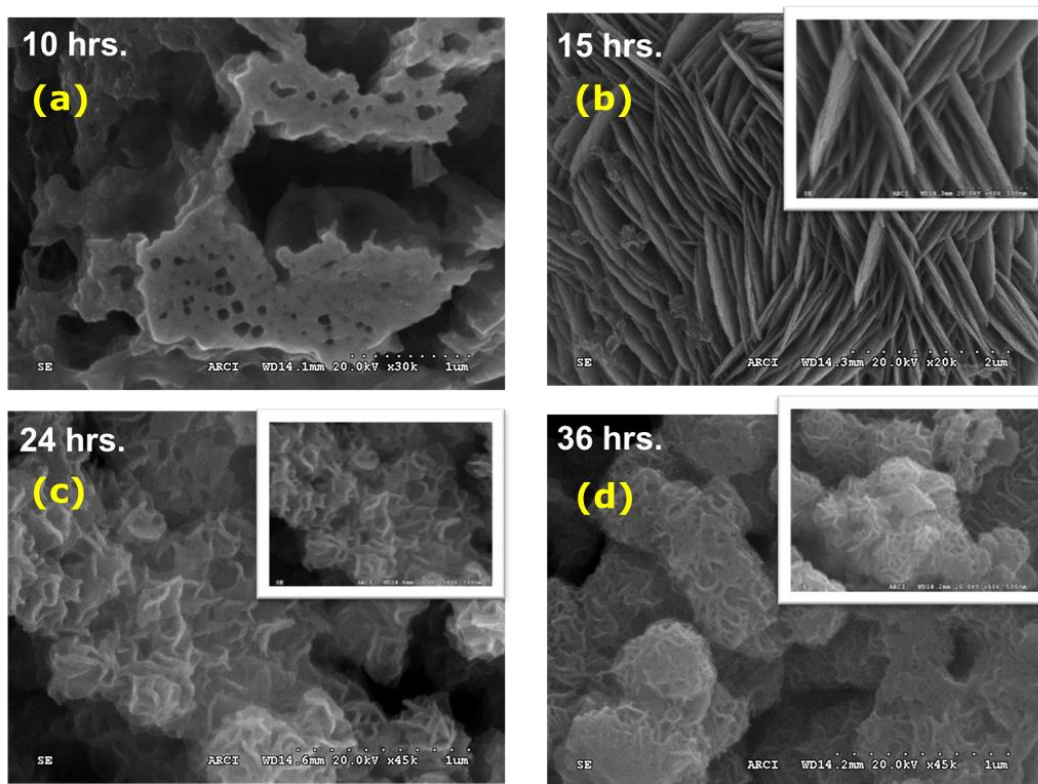
Figure 3.6.3 FESEM images of MoS_2-MoO_3 nanostructures synthesized for (a) 10 hrs. (b) 15 hrs. (c) 24 hrs. (d) 36 hrs. .of reaction time in hydrothermal method.

FESEM studies are carried out to understand the morphological evolution of composite with increase in the reaction time. It can be clearly seen from Figure 3.6.3 that the MoS_2-MoO_3 nanostructures synthesized at 10 hrs. of reaction time gives rod-bundle like morphology. With increase in the reaction time to 15 hrs., flake-like structures are formed and when the reaction time increased further to 24 hrs., flower like nanostructures formed.

3.6.2 Characterization of MoS₂-MoO₃ nanostructure functionalized CdS films

Different films are named according to synthesis time of nanoparticles and tabulated in Table 3.6.1
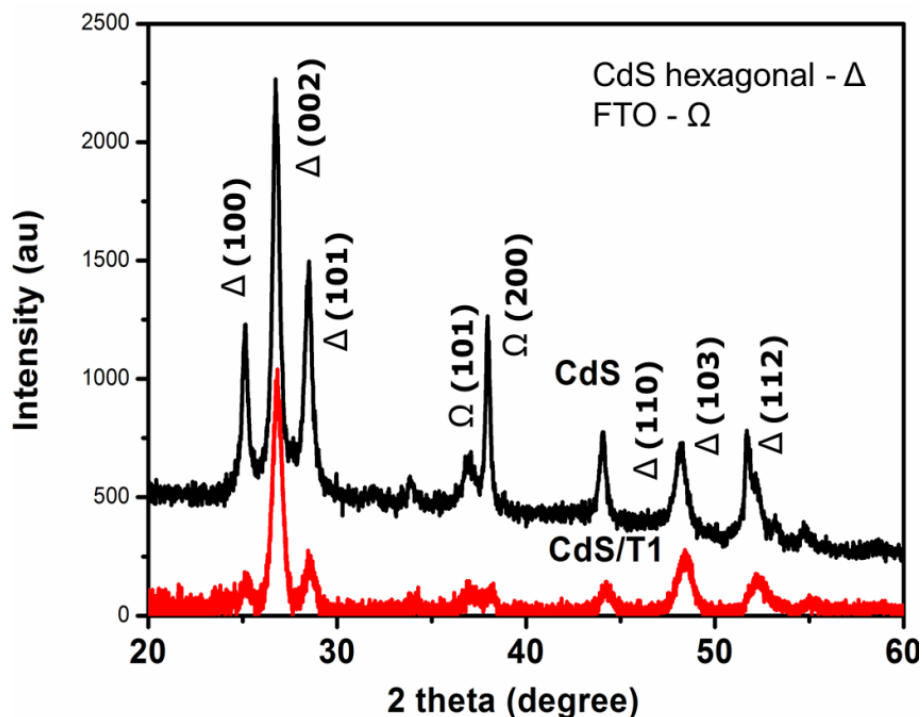
Figure 3.6.4. XRD pattern of bare and MoS₂-MoO₃ nanostructures (10 hrs. of reaction time) CdS thin films.

To understand the effect of functionalization of MoS_2-MoO_3 nanostructures over CdS surface, on the structural and optical properties of CdS photoanode, XRD and UV-Vis spectrophotometry has been carried out. XRD patterns as shown in Figure 3.6.4, shows that existence of Mo-composite does not alter XRD pattern of CdS. However, it shows decrease in the diffracted intensity of CdS XRD pattern.

Table 3.6.1. Table showing the names of respective modified films depending on the reaction time.

Name of sample	Hydrothermal reaction time (hrs)
CdS	0
CdS/T1	10
CdS/T2	15
CdS/T3	24
CdS/T4	36
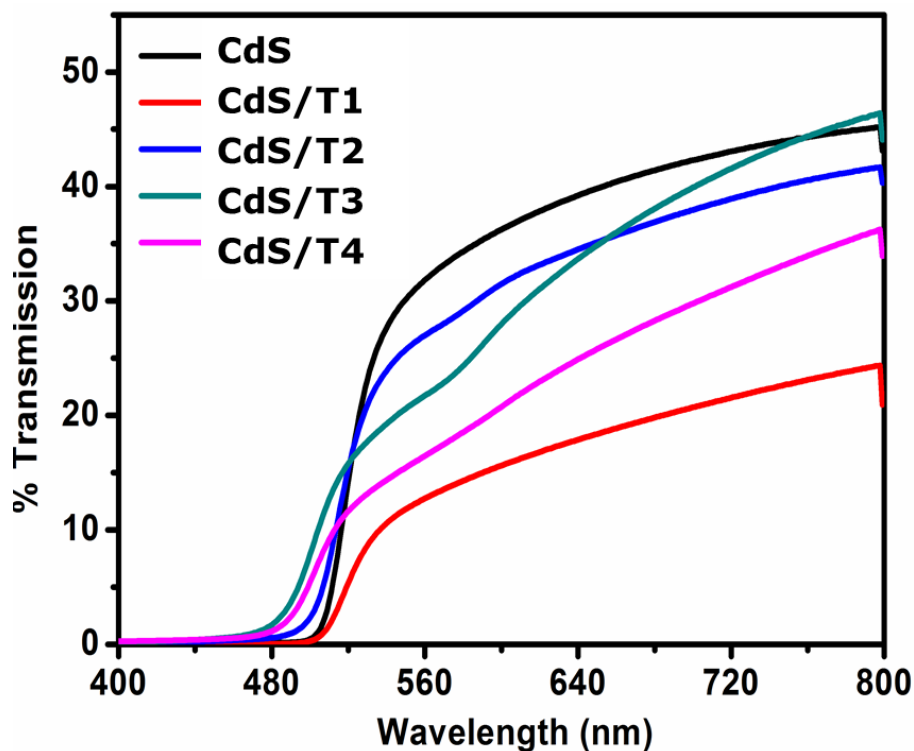
Figure 3.6.5 Transmission spectra of CdS thin films modified with MoS_2-MoO_3 nanostructures those are prepared by varying reaction time during hydrothermal synthesis.

Figure 3.6.5 shows the transmission spectra of CdS thin films modified with MoS_2-MoO_3 nanostructures. It is clear from the spectra that absorption of CdS films increases in the visible light range due to functionalization effect of MoS_2-MoO_3 nanostructures over CdS thin film. Although there is not much difference in the absorption edge of bare and modified CdS thin films.

3.6.3 Photoelectrochemical performance of MoS₂-MoO₃ nanostructure functionalized CdS photoanodes
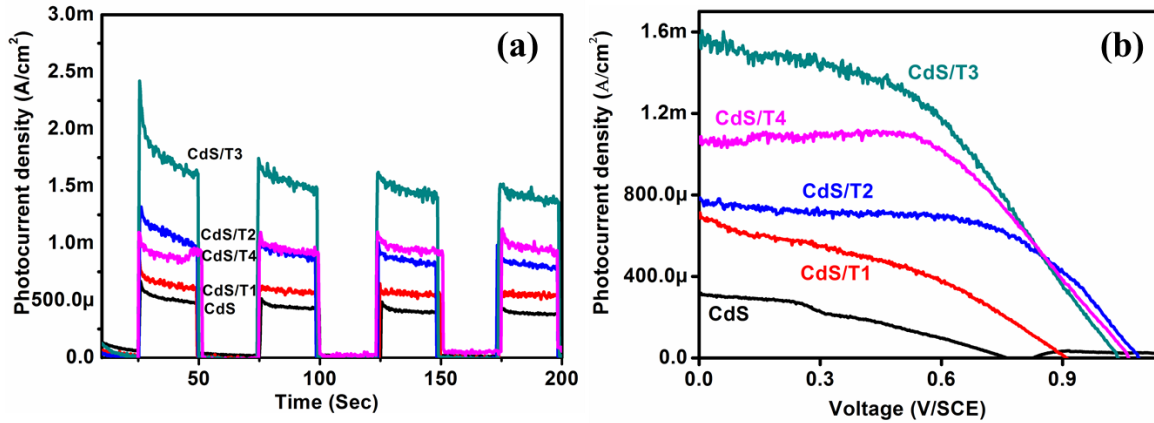
Figure 3.6.6 (a) Chronoampereometric curves and **(b)** I-V characteristics of CdS thin films modified with MoS₂-MoO₃ nanostructures by varying reaction time of hydrothermal method.

PEC characterization has been carried out to evaluate the effect of MoS_2-MoO_3 nanostructures functionalization over CdS surface. Figure 3.6.6 (a) shows the chronoampereometric curves for bare and MoS_2-MoO_3 functionalized CdS thin films for the samples shown in Table 3.6.1. The bare CdS has shown photocurrent of 350 $\mu A/cm^2$, whereas CdS/T3 photoanode has shown highest photocurrent of 1.5 mA/cm^2 at an applied bias of 0.2 V/SCE. This indicates that modification leads to 3-fold photocurrent enhancement as compared to bare CdS. Similar results are indicated by I-V characteristics of unmodified and modified films as shown in Figure 3.6.6 (b). The results of in-depth PEC characterization are summarized in Table 3.6.2 in terms of values V_{oc}, I_{sc}.

Results clearly reveal that the modified photoanodes shows improved performance than bare CdS photoanodes. This could be attributed to the improved charge transfer processes due to formation of heterojunction [123, 124], which facilitates electron and holes transfer at interface

and hence reduce their recombination process. Further, the better performance of CdS/T3 could be assigned to flower like nanostructure morphology of MoS_2-MoO_3 composite. It is expected that in contrast of planar surfaces, flower based morphology yield larger surface area and thus more area available for PEC reaction.
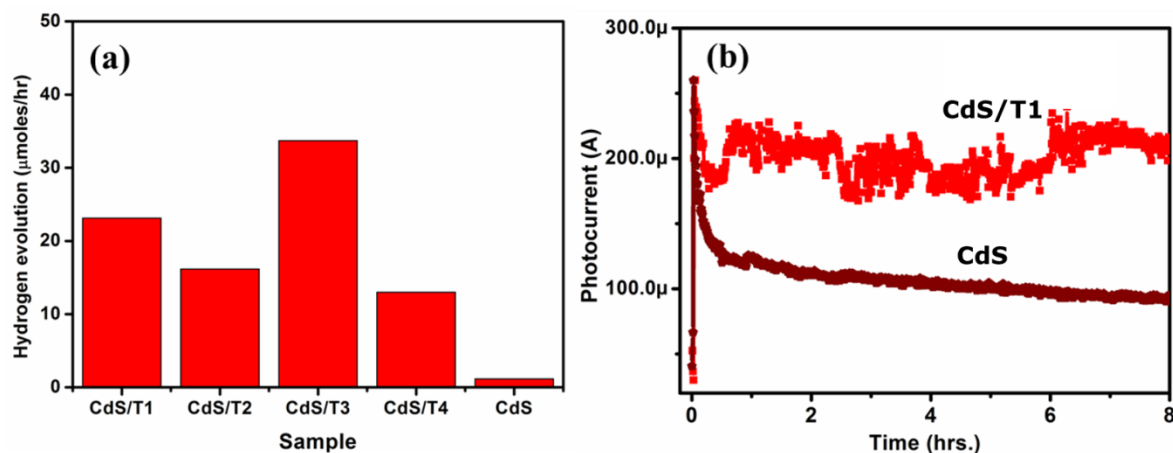
Figure 3.6.7 (a) PEC hydrogen evolution over MoS_2-MoO_3 nanostructures modified CdS thin films and **(b)** long hour chronoampereometric curve of CdS/T1.

Accordingly, above analysis indicates that MoS_2-MoO_3 modified CdS photoanodes acts as a potential candidate for PEC hydrogen generation. It could be clearly seen from the Figure 3.6.7 (a) that CdS/T3 has shown highest hydrogen evolution rate of 35 μmol/hr which is very higher than CdS/T1, CdS/T2 and CdS/T4 (23, 16, 12 μmol/hr, *respectively*) and unmodified CdS film.

Figure 3.6.7 (b) shows chronoampereometric curves of MoS_2-MoO_3 nanostructure modified CdS photoanodes acquired for longer time. As it can be clearly observed from the Figure 3.6.7 that photocurrent of CdS decreases with time whereas CdS/T1 has shown stable photocurrent until 8 hrs. of PEC measurements. Stability measurements have been carried out for all modified photoanodes but only CdS/T1 has shown enhanced stability (Figure 3.6.8).
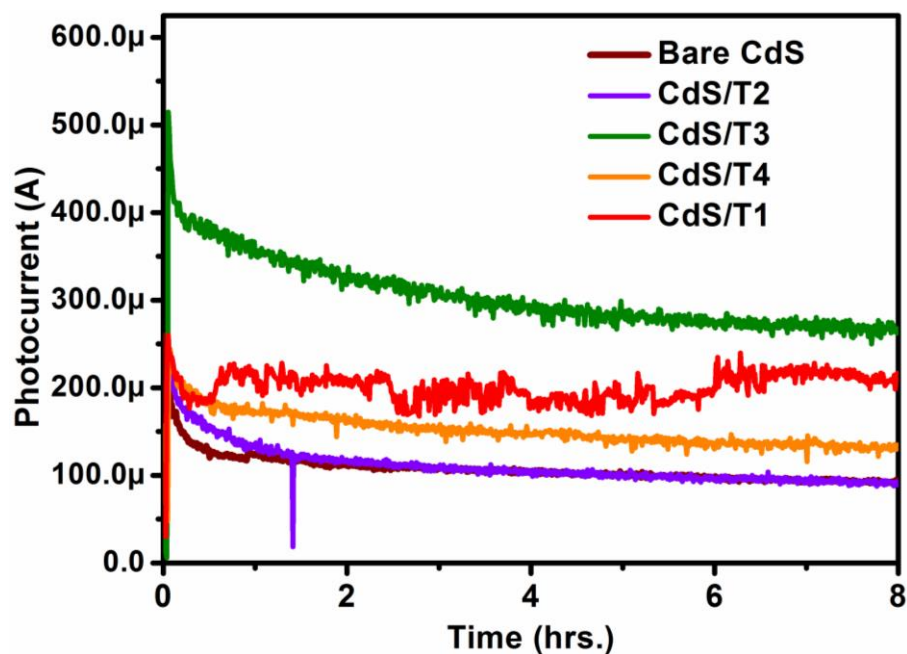
Figure 3.6.8 Chronoampereometric measurement of different MoS_2-MoO_3 nanostructures modified CdS thin films

for longer time.

Table 3.6.2 Summary of results deduced from I-V plots for MoS_2-MoO_3 modified CdS photoanodes.

Name of Sample	V_{oc} (V)	I_{sc} (mA)	η (%)	STH (%)
CdS	0.73	0.15	0.03	0.2
CdS/T1	0.90	0.68	0.23	0.75
CdS/T2	1.08	0.79	0.46	1.13
CdS/T3	1.03	1.07	0.71	1.90
CdS/T4	1.06	1.56	0.69	1.57

3.6.4 Summary of this section

In this work, we describe the functionalization of CdS surface by different MoS_2-MoO_3 nanostructures using simple chemical impregnation method. Prior to modification, three different nanostructures *viz.* bundled nanorods, nanoflakes and flower like nanostructures of MoS_2-MoO_3 are synthesized by varying the hydrothermal reaction time. The MoS_2 phase in the composite nanostructure increases with an increase in the hydrothermal reaction time, accordingly bandgap decreased in consonance with MoS_2 phase fraction. Modified CdS photoanode has shown three-fold increase in the photocurrent and similar improvement in hydrogen evolution rate. The CdS thin film modified with MoS_2-MoO_3 nanostructures with 24 hrs. of reaction time has shown highest short circuit current of 1.5 mA/cm^2 . The best PEC performance of these modified photoanode is attributed to the composition and the morphology of films. The stability of modified photoanode is found to be improved upto 8 hrs. Present work encourages the use of different Mo related compounds to improve the stability and efficiency desired for excellent photocatalytic and PEC material like CdS.

RESULTS AND DISCUSSION

PART- IV

Modification of CdS surface using conducting polymers

Motivation: The PART-IV of Results and Discussions section demonstrates the use of conducting polymer to passivate the surface of CdS against photoanodic decomposition. Polymers are regarded as stable systems to inhibit the photocorrosion process in PEC cell. In past, many low band gap photoanodes are known to be stabilized by utilizing polymer coatings (*Chapter-1, Section 1.3*). The stability problem is contented as the polymers on the surface isolates the semiconductor from electrolyte. It acts as a protective coating over the semiconductor surface. The conducting polymer coating over the semiconductor surface is also known to improve the efficiency of photoanodes. The conducting polymers exhibit valence bandedge position more negative than the semiconductor, which mediates an efficient hole transfer at the interface. This process reduces electron and holes recombination at the interface and increases the photocurrent. In the present work PANI (*section 3.7*) and PPY (*section 3.8*) are chosen for stabilizing CdS surface, they are electrodeposited on CdS surface due to following factors: (1) the oxidative polymerization potentials of pyrrole and aniline are lower than other conducting polymers; (2) the electropolymerization of pyrrole and aniline can be performed in acidic aqueous solutions, while other conducting polymers requires non-aqueous solution; (3) the electrical conductivity of as deposited polymer is higher for PPY and PANI; (4) PPY and PANI are *eco-friendly* conducting polymers [125].

3.7   Polymer -I: Polyaniline

The present work focuses on the modification of a spray deposited nanostructured CdS thin films by PANI using electro-polymerization method as described in *chapter 2, section 2.3.5*. PANI coated CdS thin films have been characterized by using XRD, RAMAN, FTIR. Electro-polymerized PANI on FTO gives a bandgap of 2.0 eV. Optimization of deposition parameters *viz.* applied field, concentration of monomer and *p*H of precursor has been performed to obtain a

uniform and an adherent coating over CdS and FTO. The optical properties of PANI/CdS are not affected by the modification of CdS surface. This ensures that there exists a thin coating of PANI over CdS. The photocurrent of CdS/PANI is found to be enhanced by 2.2 times as compared to the bare CdS. The stability of the CdS thin films could not be improved as the CdS film was peeling off after long hour measurements.

3.7.1 Structural, optical and morphological characterization of polyaniline coated CdS film
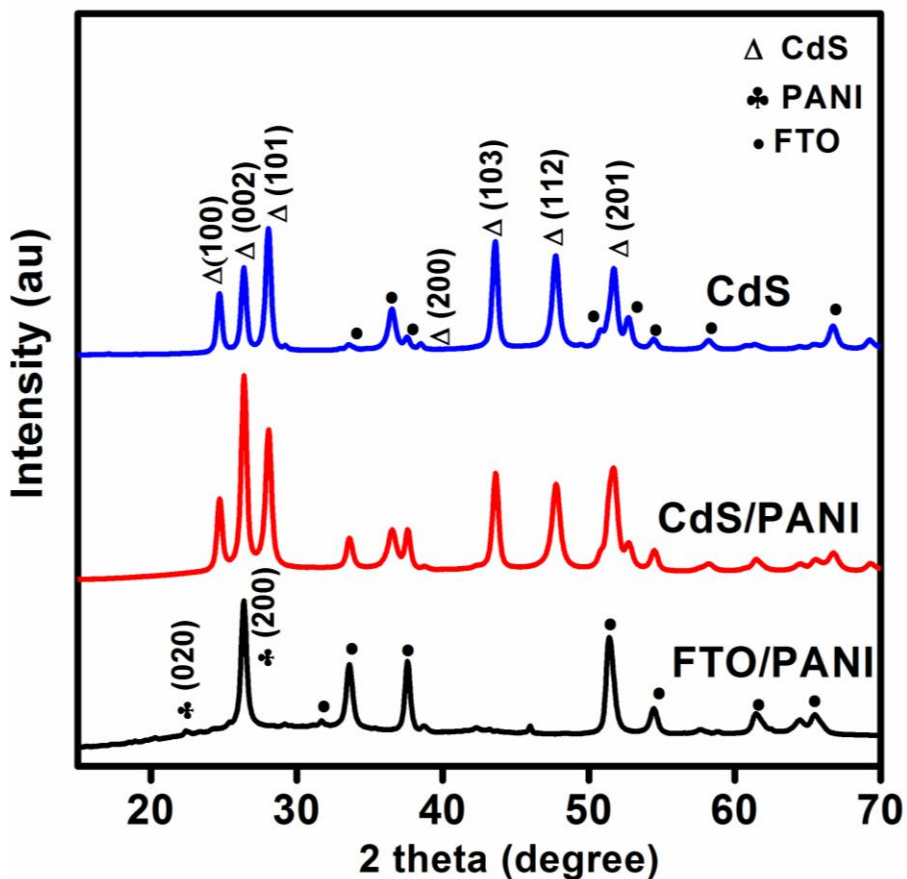
Figure 3.7.1 Micro-XRD pattern of bare, PANI modified CdS film and FTO.

Figure 3.7.1 shows the micro-XRD pattern of CdS, CdS/PANI and FTO/PANI films. The XRD pattern of PANI clearly shows the existence of two characterstic peaks of PANI at 22.50° and

26.44°. The characterstic peaks of PANI appear at 15.30°, 20.40° and 26.80° which correspond to (011), (020) and (200) crystal planes, *respectively* [126]. Coincidently (002) peak of hexagonal CdS appears at 26.40°. When PANI is electrodeposited on the surface of CdS, the diffraction peak of CdS at 26.44° overlaps with strong and sharp peak of PANI, which inturn enhances the intensity of peak at 26.40° in PANI/CdS films. The XRD pattern indicates no other peak pertaining to any impurity other than the substrate (FTO). The XRD results indicate the formation of an uniform crystalline outer layer of PANI over CdS and FTO.
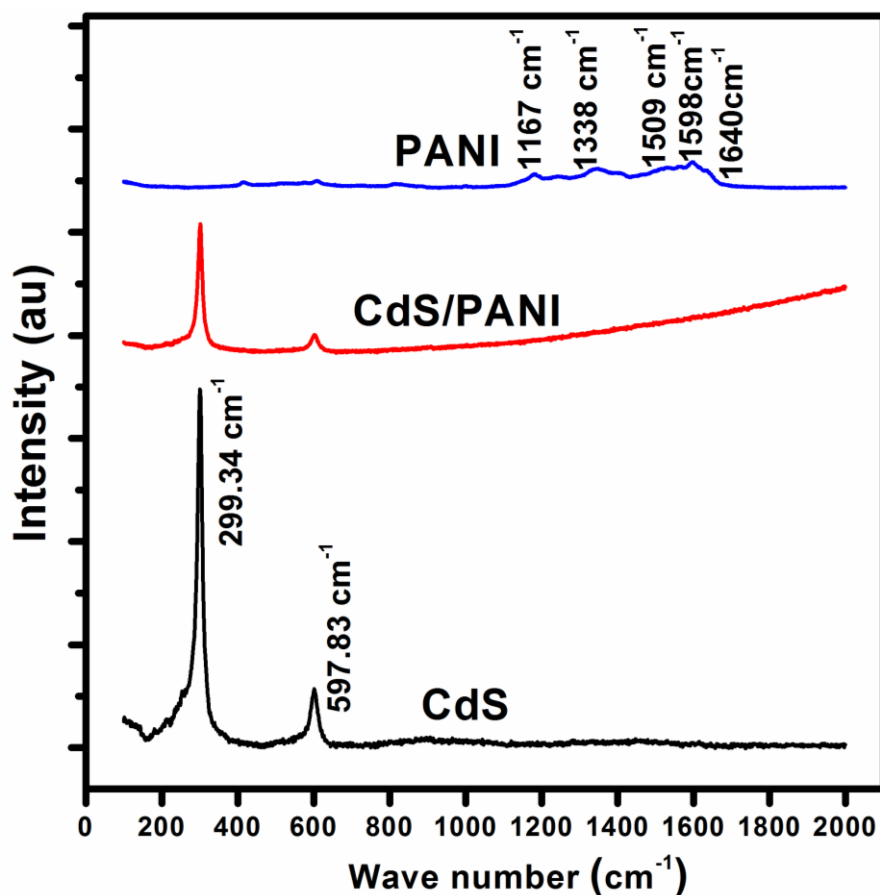
Figure 3.7.2 Raman spectra of bare, PANI modified CdS film and FTO.

Raman studies were conducted to examine the CdS, CdS/PANI and FTO/PANI films for validating the existence of polymer related functional group as shown in Figure 3.7.2. The Figure clearly reveals the presence of all the characteristic bands of pure PANI. The band at 1167 cm^{-1}

corresponds to the C-H bending vibration of quinoid/benzoid ring. The 1339 cm^{-1} band is assigned to the C-N[+] vibration of delocalized polaronic structure. The band at 1509 cm^{-1} indicates the presence of C=N stretching of the quinoid ring. The band at 1598 cm^{-1} is attributed to stretching vibration of benzoid ring. The bands at 1389 cm^{-1} and 1640 cm^{-1} correspond to vibration of delocalized polarons in the polymeric conformation [127]. The Raman spectra of CdS with characteristic peaks at 299.34 cm^{-1} and 597.83 cm^{-1} corresponds to fundamental band and overtone of longitudinal optical phonon mode of CdS, *respectively* [128].

It can be clearly seen from the Figure 3.7.2 that CdS/PANI shows all peaks corresponding to CdS and a hump after 1400 cm^{-1}, which is the range where PANI displays its characteristic bands.
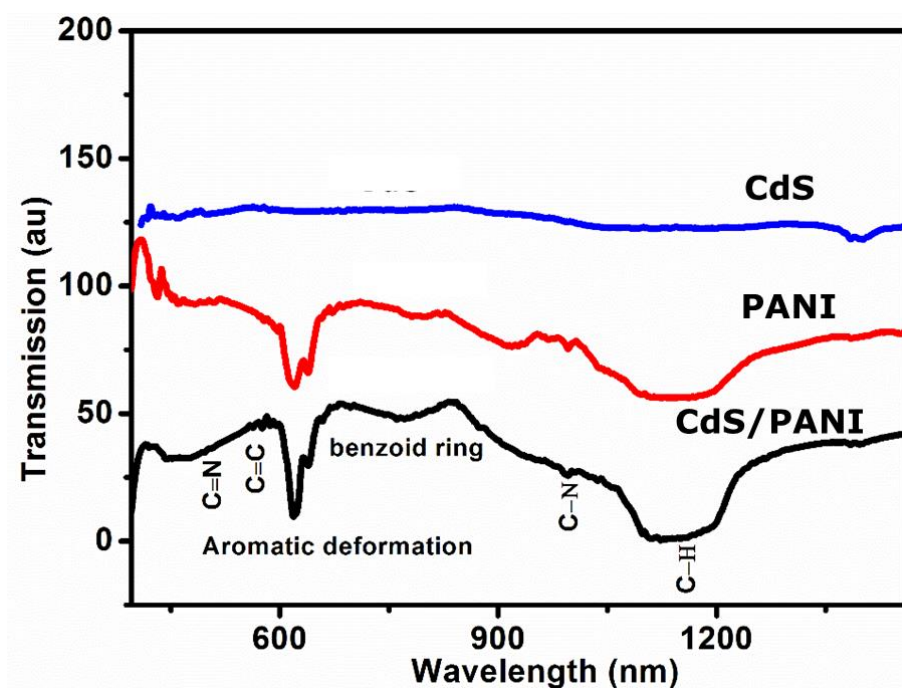
Figure 3.7.3 FTIR spectra of bare and PANI modified CdS film.

Figure 3.7.3 shows the FTIR spectra of bare CdS and PANI electrodeposited on FTO and CdS. FTIR spectra of FTO/PANI clearly validates the formation of PANI. The transmission peak in the range of 490 cm^{-1} to 570 cm^{-1} are related to the vibration of C=N and C=C vibrations in PANI units. The peaks at 1000 cm^{-1} and 1150 cm^{-1} assures the presence of C-N and C-H bonds in the PANI. This spectrum clearly validates the formation of PANI on CdS surface [129]. This is in line with earlier characterization.
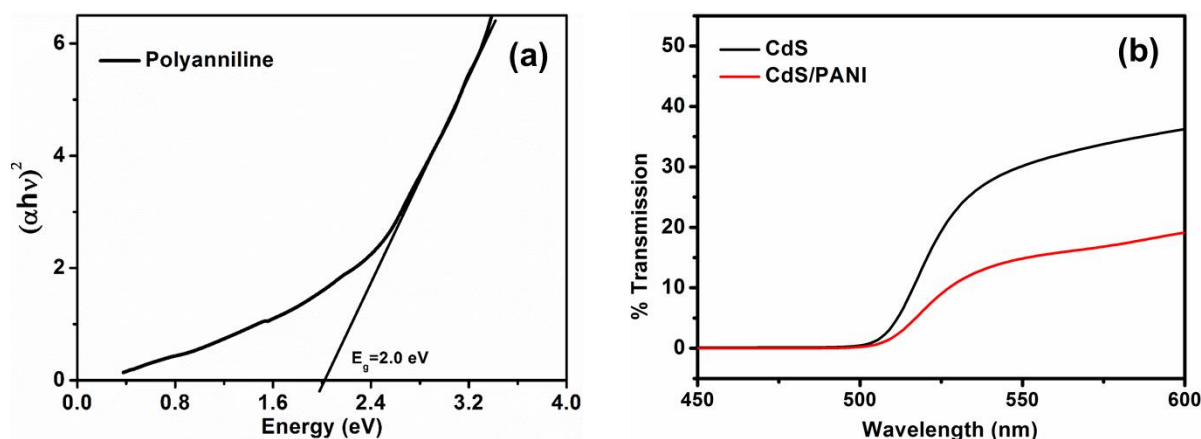
Figure 3.7.4 (a) Tauc plots of FTO/PANI and **(b)** Transmission spectra of bare and PANI modified CdS film.

The optical characteristics of as deposited PANI on FTO and CdS has been analysed by using UV-Vis spectrophotometry. Figure 3.7.4 (a) shows the Tauc plots of PANI films electrodeposited on FTO. The bandgap of FTO/PANI is found to be 2 eV, which corresponds to the wavelength of 620 nm. Therefore, FTO/PANI electrodeposited in this work is capable of absorbing visible light photons of solar spectrum. Figure 3.7.4 (b) shows transmission spectra of CdS and CdS/PANI films. It can be clearly understood from transmission spectra that absorption edge of CdS is not altered with PANI modification, however absorption in visible range is remarkably enhanced.
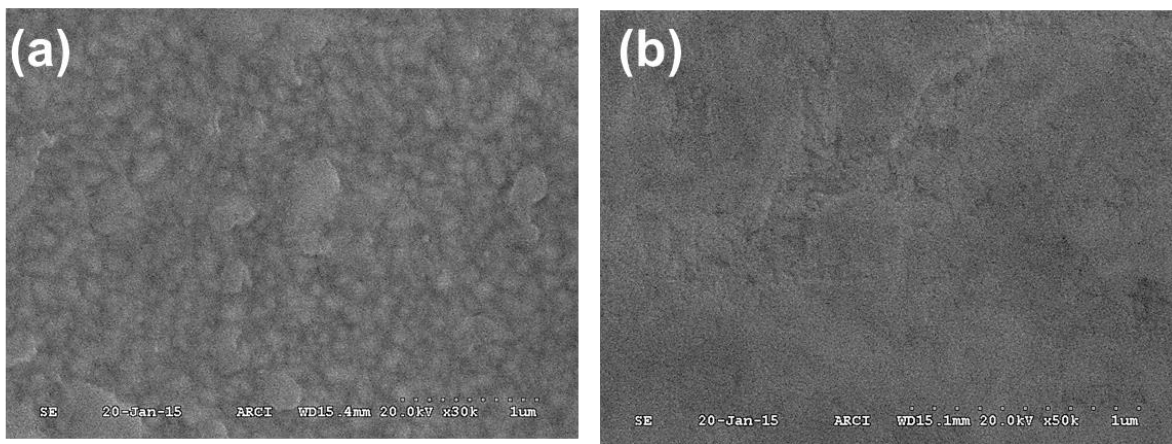
Figure 3.7.5 FESEM images of bare and PANI modified CdS film**.**

Figure 3.7.5 (a) shows the FESEM image of electrodeposited FTO/PANI film. The as deposited PANI film on FTO appears to be uniform and constitutes of nanosized grain. However, no distinctive features have been observed. Similarly, FESEM image of CdS/PANI film has shown the formation of thin PANI coating over CdS surface.

3.7.2 Photoelectrochemical performance of Polyaniline coated CdS photoanodes
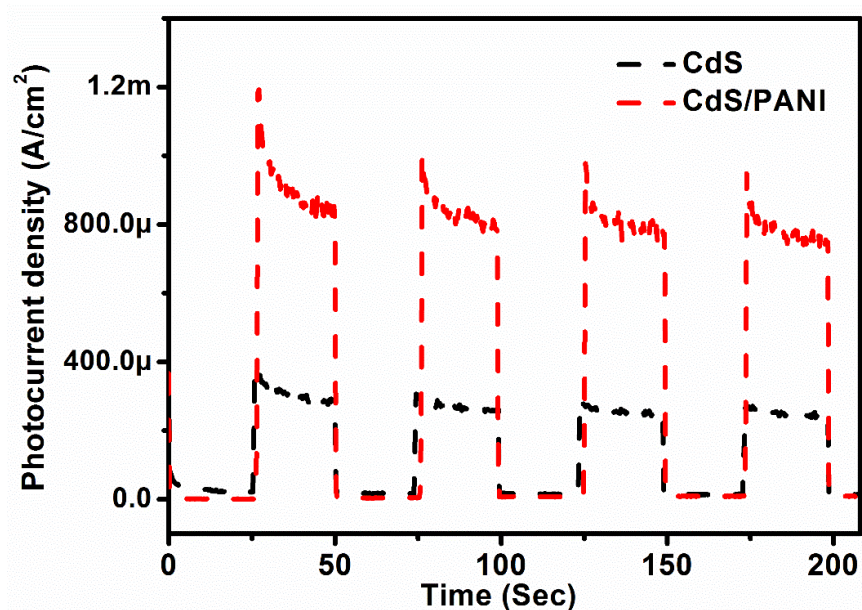
Figure 3.7.6 Chronoampereometric curves of bare and PANI modified CdS film.

For the demonstration of direct impact of polymer coating on improved electrical properties of CdS photoanodes, PEC measurements have been carried out. An electrolyte of Na_2S/Na_2SO_3 is used to provide necessary scavenging agents in order to content the photocorrosion and to provide the rectifying contacts for the nanostructured CdS photoanodes. The chronoampereometric measurement has been carried out in a three-electrode system under 100 mW/cm^2 AM 1.5 solar simulator. Figure 3.7.6 shows the chronoampereometric curves for bare and PANI modifies CdS photoanodes. It is evident from the Figure that surface modification of CdS photoanode with PANI increases the photocurrent by 3.19 times as compared to bare CdS. Bare CdS yields photocurrent of 250 $\mu A/cm^2$, whereas CdS/PANI gives photocurrent of 770 $\mu A/cm^2$. An enhanced PEC performance after polymer modification is attributed to an improved charge transfer process that occurs at the interface due to polymer coating [130].
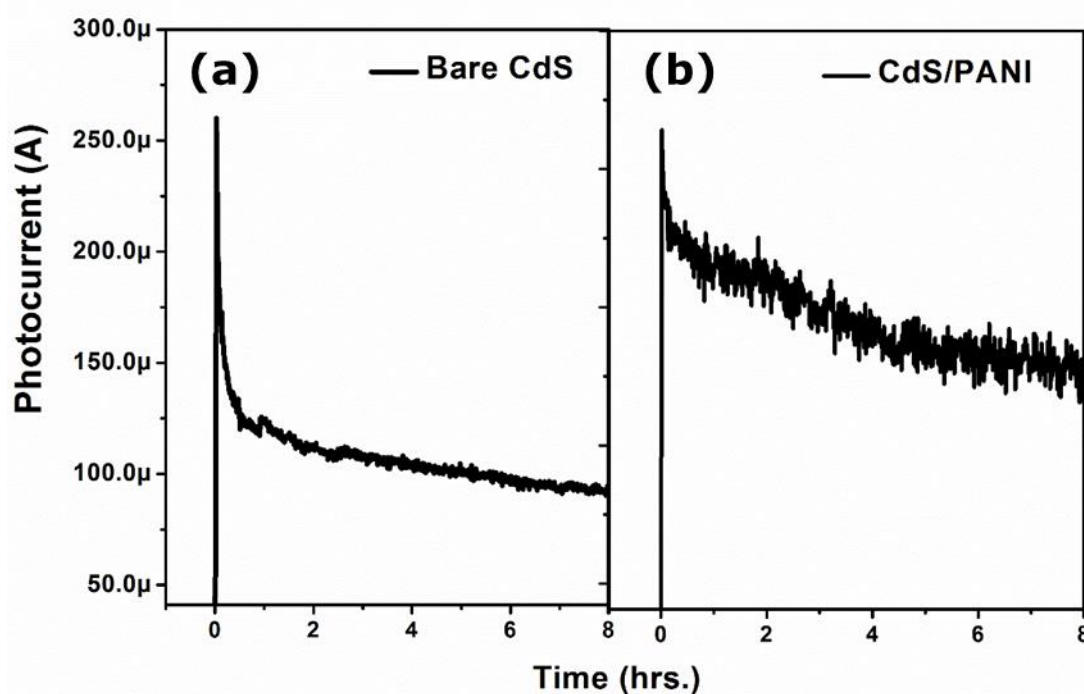
Figure 3.7.7 Long hour chronoampereometric curves of (a) bare and PANI modified CdS.

Figure 3.7.7 shows chronoampereometric measurements for CdS and CdS/PANI for long hour PEC measurements. The desired stability is not seen for PANI modified CdS photoanode. This can be explained due to the fact that for long time chronoampereometric measurements, the modified film is found to be peeled off from the surface. Indicating less adherence of the film probably due to (1) application of electric field during electro-polymerization, or (2) exposure of the film to highly acidic conditions during polymerization and extremely basic conditions during long hour PEC measurements.

3.7.3   Summary of this section

In this work, the surface of CdS thin film has been modified with PANI coating. The PANI is electrodeposited on the FTO and CdS surface by electrodeposition method. The existence of PANI on the bare FTO and on the surface of CdS is validated by XRD, RAMAN, FTIR spectroscopy. The bandgap of as deposited PANI has been estimated using Tauc plot and is found to be 2 eV. Absorbance of CdS thin film is enhanced in the visible light range due to modification by PANI, although absorption edge is not altered by the polymer coating over CdS surface. The morphological studies have shown the formation of uniform and thin polymer coating over CdS. The PEC characterization demonstrates an enhanced photocurrent of PANI modified CdS photoanodes by 3.2 times to that of bare CdS photoanodes. This validates the viability of these photoanodes in a PEC cell. The stability of modified films could not be improved due to peeling off CdS films in case of long hour PEC measurements.

3.8   Polymer-II: Polypyrrole

In this part of dissertation, fabrication and characterization of PPY coated CdS photoanode is reported for the efficient PEC water splitting. PPY was coated on CdS thin film by electro-

polymerization method as mentioned in *chapter 2, section 2.3.6*. Optimization of deposition parameters *viz.* applied field, concentration of monomer and pH of precursor has been performed to obtain uniform and adherent coating. The bandgap of as synthesized PPY on FTO is estimated to be 1.7 eV. FTIR, XRD, RAMAN, validates the formation of PPY over CdS surface. The PPY coating doesn't affect the structural and optical properties of CdS photoanode. The PEC performance of PPY/CdS is higher (1.8 times) as compared to bare CdS photoanodes. Although stability of CdS photoanodes could not be improved as films peeled off with higher exposure to electrolyte.

3.8.1 Structural, optical and morphological characterization of polypyrrole coated CdS films
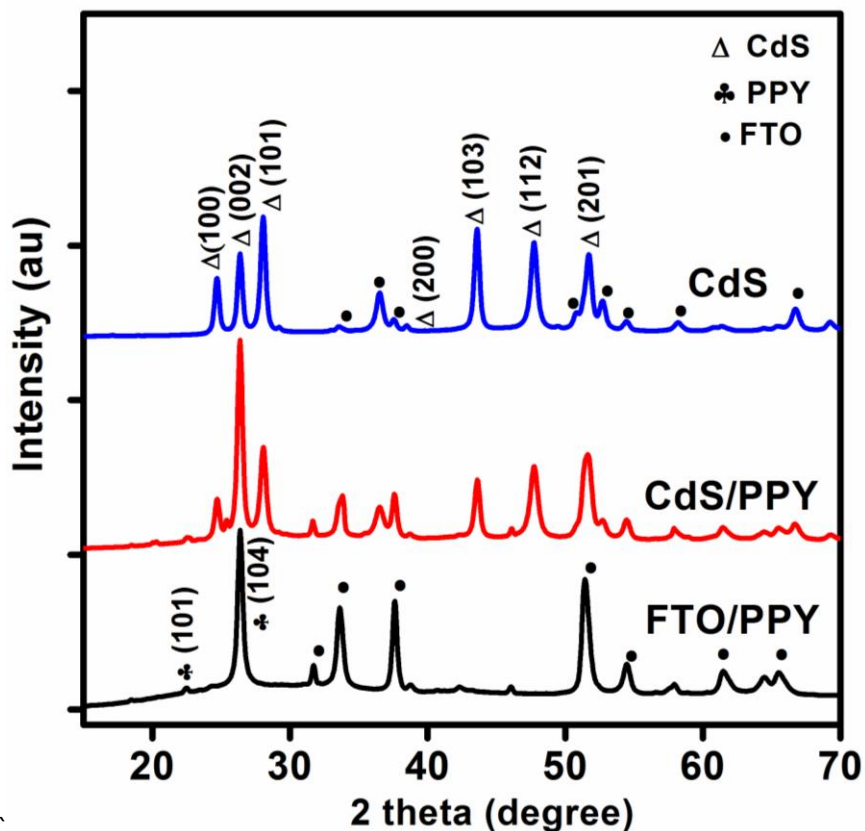
Figure 3.8.1 Micro-XRD pattern of bare, PPY modified CdS films and FTO.

Figure 3.8.1 shows the micro-XRD pattern of of CdS, FTO/PPY and CdS/PPY films. The characteristic peaks of PPY appear at 20° and 26° corresponding to 'd' spacing of 0.448 nm and 0.342 nm, *respectively*. The peaks at 26° and 20° arise from PPY chain close to interplanar Van der Waal's distance for aromatic ring and π-π* interaction of aromatic rings, *respectively* [131]. The sharp peak of PPY at 26° overlaps with the (002) diffraction peak of CdS and attributes to the presence of intense peak in CdS/PPY films. The XRD results confirm the presence of crystalline PPY layer on CdS.
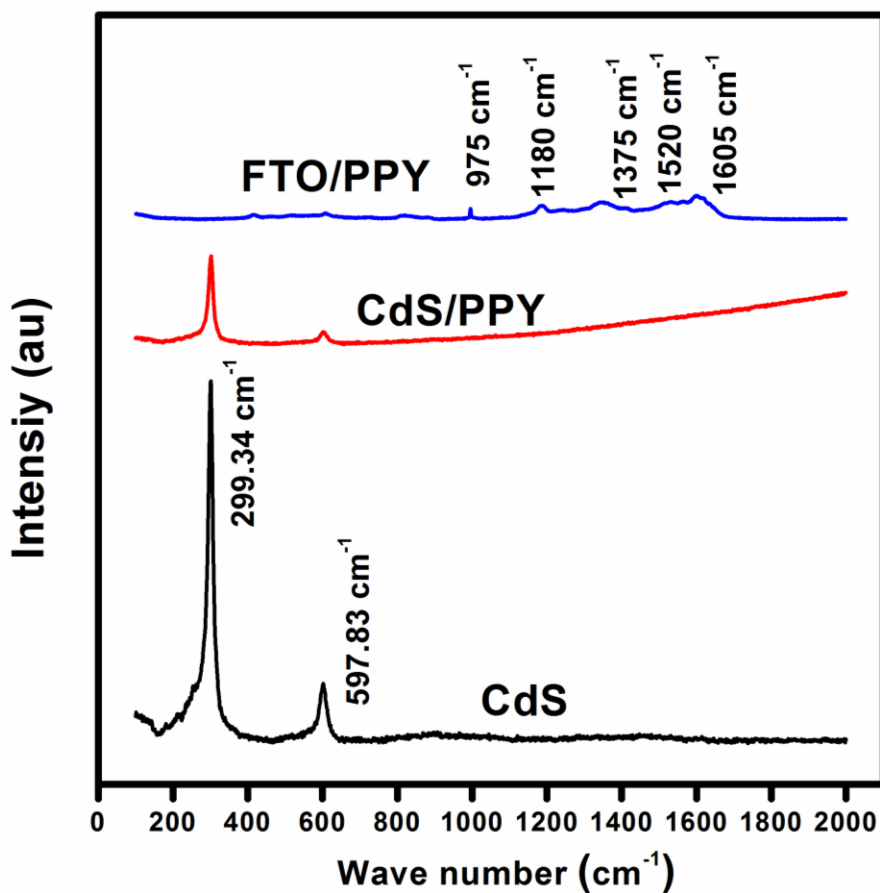
Figure 3.8.2 Raman spectra of bare, PPY modified CdS films and FTO.

Figure 3.8.2 shows the Raman spectra of CdS, CdS/PPY and FTO/PPY films. In Raman spectra of PPY, the band at 975 cm^{-1} is assigned to ring deformation associated with dication and radical cation . The band at 1375 cm^{-1} is due to inplane bending vibrations of N-H and C-H bonds. The peak at 1520 cm^{-1} is due to benzoid band of C=C and 1602 cm^{-1} belongs to quinoid band. The inplane vibration modes in the range of 1580-1605 cm^{-1} are due to C-C, C=C and N-H bonds in the PPY [132-134]. The CdS/PPY spectrum clearly shows the presence of CdS characteristic peaks and hump in spectrum after 1400 cm^{-1} which is attributed to the bands of PPY.
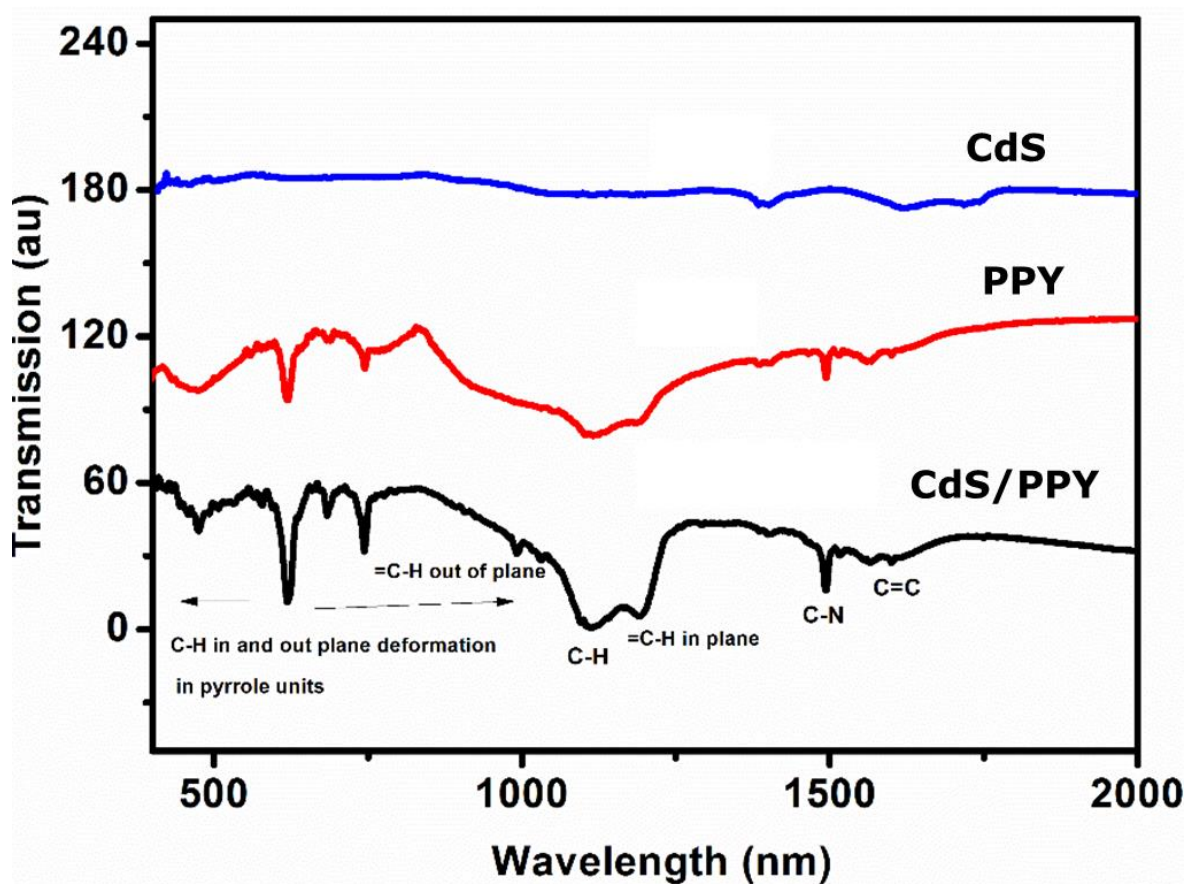
Figure 3.8.3 FTIR spectra of bare, PPY modified CdS films and FTO.

Figure 3.8.3 shows the FTIR spectra of bare CdS and PPY electrodeposited on FTO and CdS. FTIR spectra of FTO/PPY clearly validates the formation of PPY. The transmission peak in the range of 400 cm^{-1} to 750 cm^{-1} is related to C-H in and out of plane vibrations in pyrrole units. The peaks corresponding to 1115 cm^{-1} and 1192 cm^{-1} are appeared due to C-H bond and C=H bonds, *respectively*. The peaks at 1498cm^{-1} and 1563cm^{-1} assure the presence of C-N and C=C bonds in PPY [135].
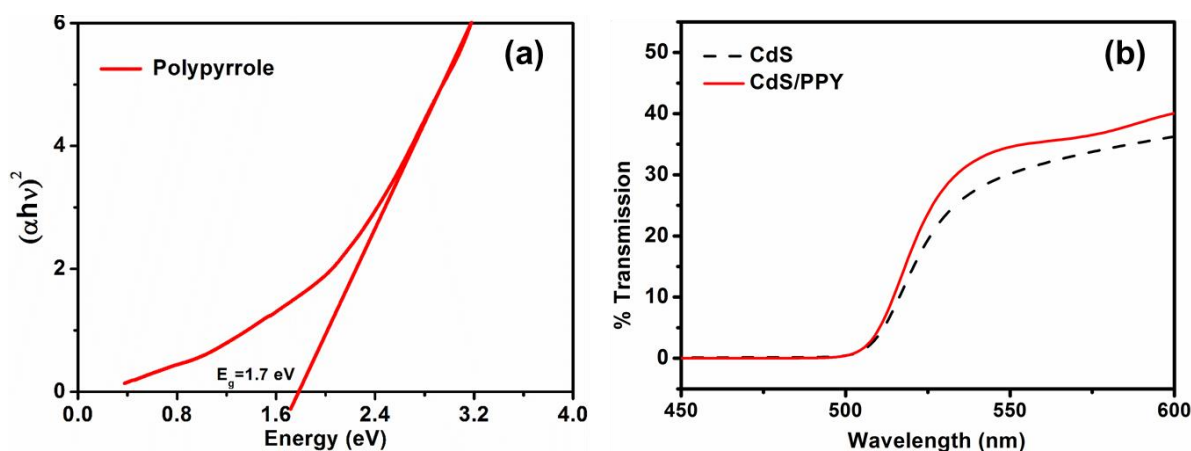
Figure 3.8.4 (a) Tauc plots of (a) bare and (b) PPY modified CdS photoanodes.

Optical properties of as deposited PPY on FTO and CdS are studied by recording transmission spectra. Figure 3.8.4 (a) shows the tauc plots of PPY films electrodeposited on FTO. The bandgap of FTO/PPY is estimated to be 1.7 eV, which corresponds to the wavelength of 729 nm. Therefore, FTO/PPY electrodeposited in this work is capable of absorbing visible part of solar spectrum. Figure 3.8.4 (b) shows transmission spectra of CdS and CdS/PPY films. It can be clearly seen from transmission spectra that optical properties of CdS are not altered with modification of PPY.

Figure 3.8.5 (a) shows the FESEM images of electrodeposited FTO/PPY films. The as deposited PPY film on FTO appears to be uniform and nanosized. However, no distinctive nano-features

are observed. Similarly, FESEM image of CdS/PPY film has shown formation of dense PPY coating over CdS surface.
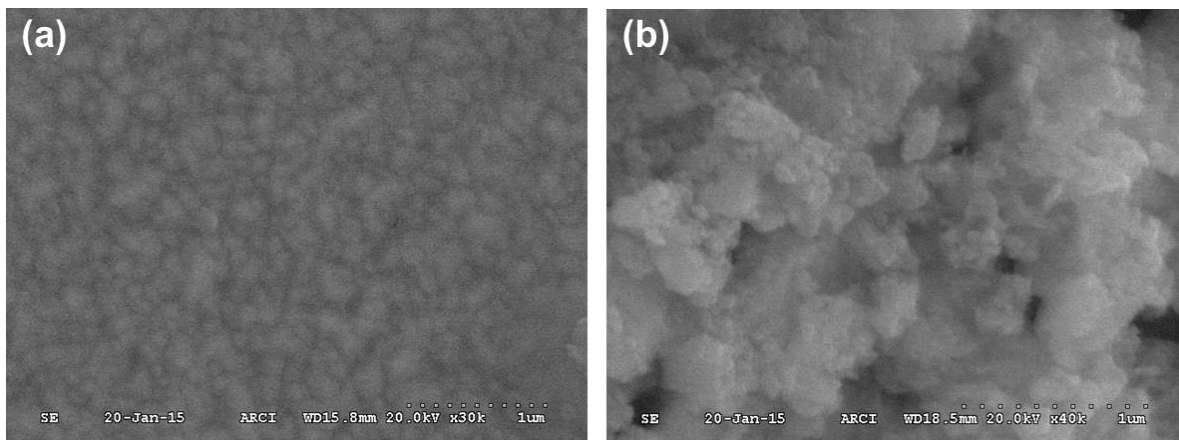
Figure 3.8.5 FESEM images of (a) PPY and (b) PPY modified CdS photoanodes.

3.8.2 Photoelectrochemical performance of polypyrrole coated CdS films
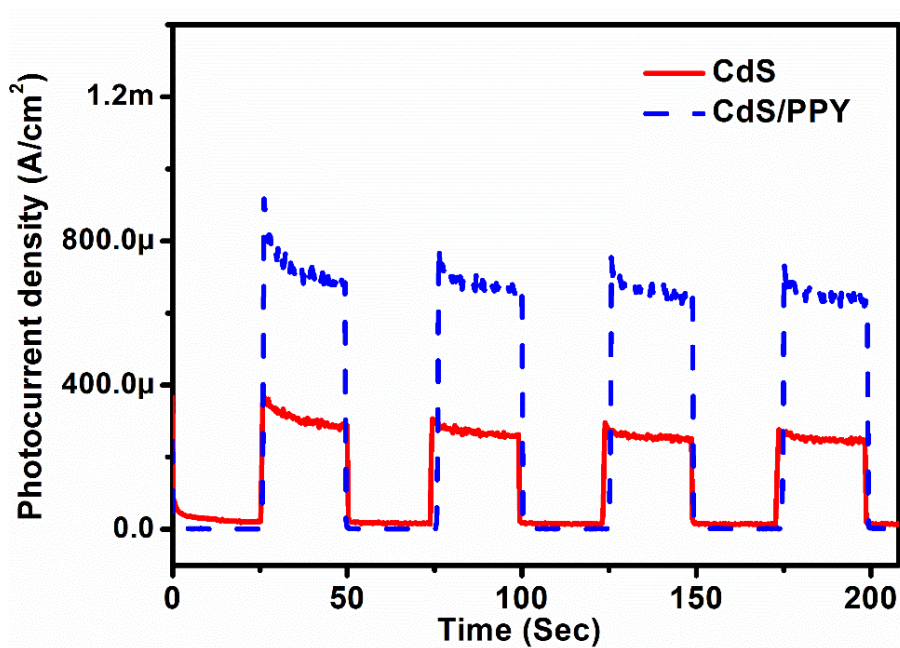
Figure 3.8.6 Chronoampereometric curves of bare and PPY modified CdS photoanodes.

To visualize the direct impact of polymer coating on improved electrical properties of CdS photoanodes, PEC measurements has been carried out. An electrolyte of Na_2S/Na_2SO_3 is used to provide necessary scavenging agents in order to curb photocorrosion and to provide rectifying contacts for nanostructured CdS photoanodes. The chronoampereometric measurements has been carried out in a three-electrode system under 100 mW/cm^2 AM 1.5 solar simulator. Figure 3.8.6 shows the chronoampereometric curves for bare and PPY modified CdS photoanodes. It is quite clear from the Figure that surface modification of CdS photoanode with PPY enhances the photocurrent by the factor of 2.6. Bare CdS yields photocurrent of 250 µA/cm^2, whereas CdS/PPY gives photocurrent of 650 µA/cm^2. The enhanced PEC performance after polymer modification is attributed to the improved charge transfer process at the interface [136].
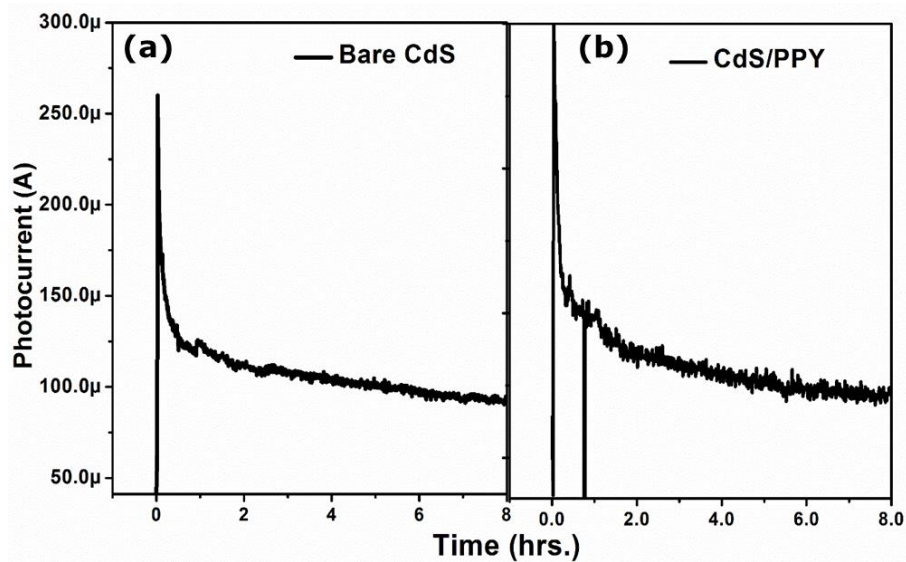
Figure 3.8.7 Long hour chronoampereometric curves of (a) bare and (b) PPY modified CdS photoanodes.

Figure 3.8.7 shows the results obtained from prolong chronoampereometric measurements for CdS and CdS/PPY. The desired stability is not seen for PPY modified CdS photoanodes. This

could be explained due to the fact that for prolong chronoampereometric measurements the modified films are found to be peeled off from the surface.

3.8.3 Summary of this section

In the present section, we have modified the surface of CdS thin film with PPY coating. The PPY has been deposited on FTO and CdS surface by electropolymerization method. The formation of PPY on various substrates is validated by FTIR, XRD and RAMAN, spectroscopy. Tauc plot reveals that as deposited PPY films possess a bandgap of 1.7 eV. Optical properties of CdS are not altered by the polymer coating over CdS surface. The morphological studies has shown the formation of uniform and dense coating over CdS. The PEC characterization of modified and unmodified CdS photoanodes is carried out to validate the viability of this photoanode in PEC cell. The photocurrent of PPY modified CdS films is found to be enhanced by a factor of 2.6. The stability of modified films could not be improved due to peeling off of films for long hour PEC measurements.

Chapter -4

CONCLUSIONS

In the previous chapters, in-depth analysis of the structural, optical, PEC properties of bare and modified CdS photoanodes has been described. This chapter concludes with the comparison of the results obtained from the study for different photoanodes with respect to their performance *viz.* photocurrent density, stability, IPCE and STH.
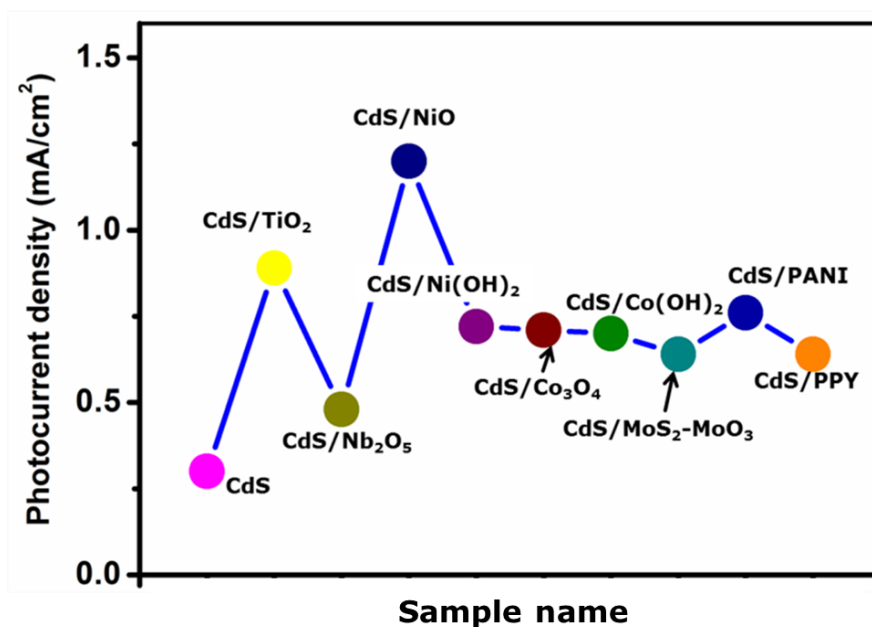
Figure 4.1. Photocurrent density of bare and modified CdS photoanodes at 0.2 V/SCE under AM1.5 solar simulator. Photocurrent shown here are for the film that shows stable PEC performance (Nb_2O_5 and nanostructure MoS_2-MoO_3 modified CdS films that shows higher photocurrent are not included in this graph as they are not stable).

Figure 4.1 shows the graph of photocurrent density with respect to different photoanodes where photocurrent variation is studied for the biasing voltage of 0.2 V/SCE. Photocurrent included in

this section is taken only for the most stable photoanode that is discussed in *chapter 3*. Figure 4.1 clearly demonstrates that *co*-catalyst modified photoanode shows higher photocurrent density than the polymer and metal-oxide modified CdS photoanodes. Accordingly, nanostructured NiO modified CdS photoanode show highest photocurrent density of 1.2 mA/cm^2 at 0.2 V/SCE. It is important to note that MoS_2-MoO_3 and Nb_2O_5 modified CdS photoanode show highest photo current density of 1.5 mA/cm^2 and 0.73 mA/cm^2, *respectively* but it is not included in Figure 4.1 as they are not stable (*see chapter 3, section 3.4, 3.6*). On contrary, the polymer modified photoanodes show least improvement that seems to be due to lower integrity of polymer with the semiconductor electrode. The detailed study of PEC performance of metal-oxide (*section 3.3, 3.4*), *co*-catalysts (*section 3.5, 3.6*) and polymer (*section 3.7, 3.8*) modified CdS photoanode is given in *chapter-3*. The present discussion clearly suggests that the modified CdS electrodes perform efficiently under solar radiation.

Further in order to analyse the wavelength dependent performance of the photoelectrodes, it is important to understand their IPCE behaviour. IPCE is defined as the photocurrent collected per incident photon-flux as a function of illumination wavelength. Figure 4.2 shows the results of IPCE measurements of bare and modified CdS photoanodes at 470 nm (*green region*). The IPCE results are inline with the results of respective photocurrent density mesurements described in above section for different modified photoanodes. The electrode modified by nanostructured TiO_2 modified photoanodes show the highest IPCE of 22 % that is three times higher than the bare CdS photoanode (8 %). In general, the IPCE spectrum of a photoactive material is known to account for three important phenomena namely; *photon absorption*, *charge transport* and *charge transfer* at the interface. So, an improved IPCE of nanostructured TiO_2 modified photoanodes

could be attributed to its *enhanced absorption* and the *charge transport porperties* as compare to the other modified photoanodes.
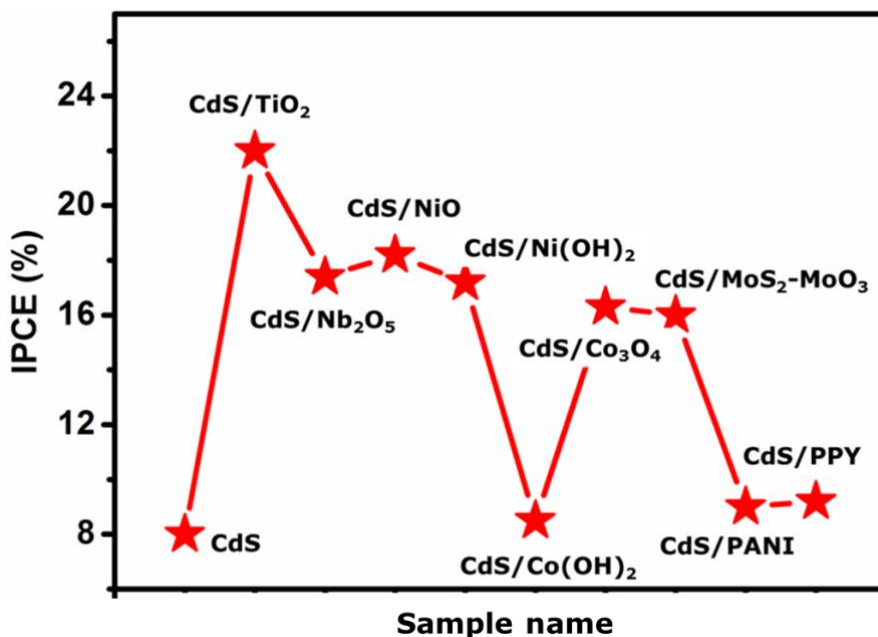
Figure 4.2. IPCE of bare and modified CdS photoanodes at 0.2 V/SCE under monochromatic wavelength of 470 nm.

The focus of the present systematic study is to produce hydrogen by utilization of solar radiation. Following section indicates the outcome of various systems studied, those are described in earlier respective sections (*chapter 3*). Figure 4.3 shows the STH efficiency of the bare and various other modified CdS photoanodes. It can be noted that the STH efficiency is calculated using the photocurrent generated at the optimum biasing volage as mentioned in the *section 2.5.2 of chapter 2*. Clearly STH reveals that it is a funtion of photocurrent density (Figure 4.1) and thus analogously the NiO modified CdS photoanode show highest STH (1.1 %) value among all the electrodes. All the modified electrodes shows much higher value of STH than the bare CdS (0.2 %).
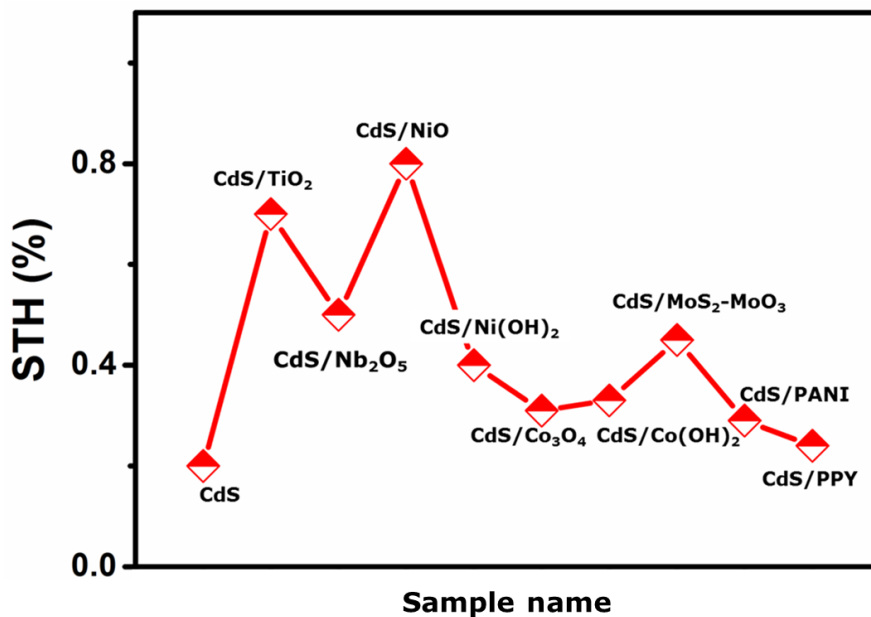
Figure 4.3. Variation of STH value with respect to the bare and modified CdS photoanode at 0.2 V/SCE under AM1.5 solar simulator.

PEC performance based on the STH efficiency results and photocurrent density graph are directly correlated, as the simulated solar radiation has been used as light source in these characterization. On the contrary, the trend of variation in IPCE (value at $\lambda \sim 470nm$) and STH result are bound to exhibit the differences in view of the difference in optical response of the material at different wavelengths.

Figure 4.4 shows the hydrogen evolution measurements of bare and modified CdS system. It is quite evident from the Figure that NiO modified photoanodes shows highest rate of hydrogen evolution rate of 2500 µmol/hr as compared to CdS (1.7 µmol/hr). This high rate of hydrogen evolution is attributed to higher catalytic activity of Ni related *co*-catalysts as discussed in *chapter 3 (section 3.5).*
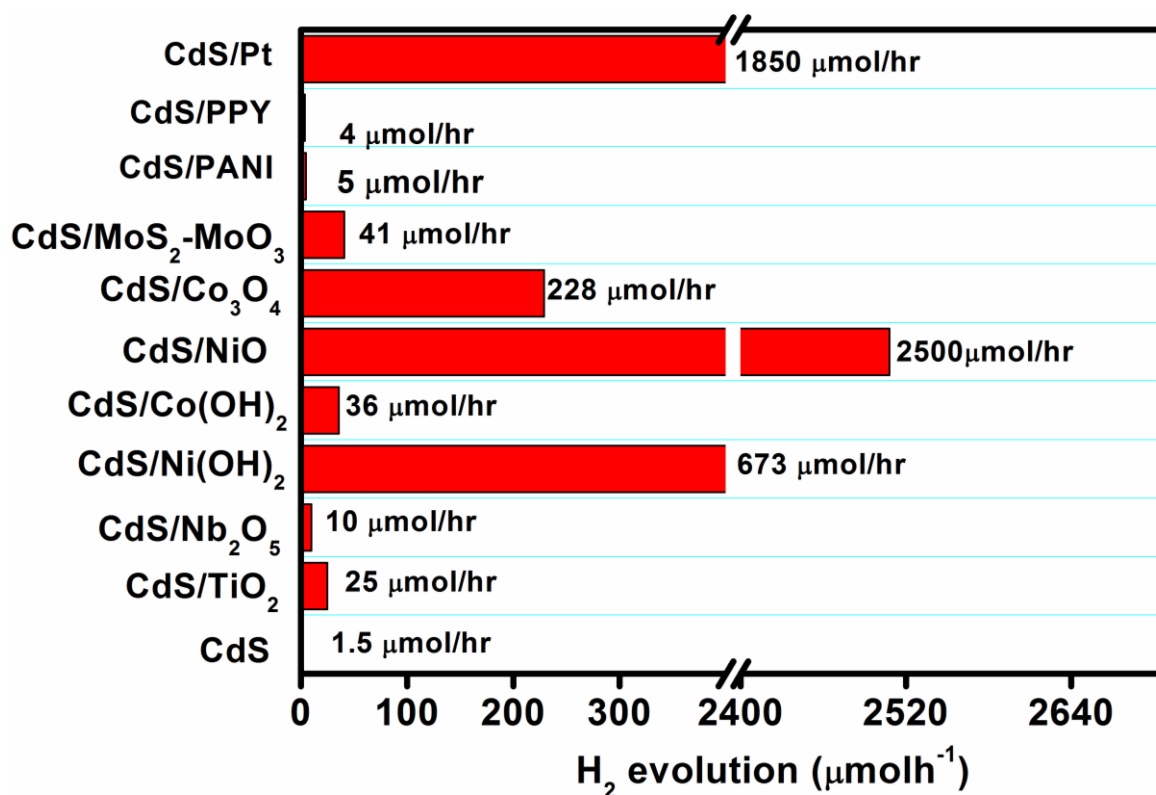
Figure 4.4 Rate of H_2 evolution of bare and modified CdS photoanodes at 0.2 V/SCE under AM1.5 solar simulator.

CdS is a well-known photocatalytic material, which on loading with co-catalytically active Ni particles improves the rate of gas evolution over CdS surface. This study also includes hydrogen evolution from platinum loaded CdS (1850 µmol/hr), which surprisingly shows the rate of hydrogen evolution lower than Ni related *co*-catalyst. All *co*-catalysts modified photoanodes shows the higher hydrogen evolution than metal oxide and polymer modified photoanodes. This could be correlated to reduced overpotential at the junction due to the use of *co*-catalysts on the CdS surface. It can be noted that inspite of the systematic study on efficiency; the main objective of the work is to improve the photostability of the photoanode.
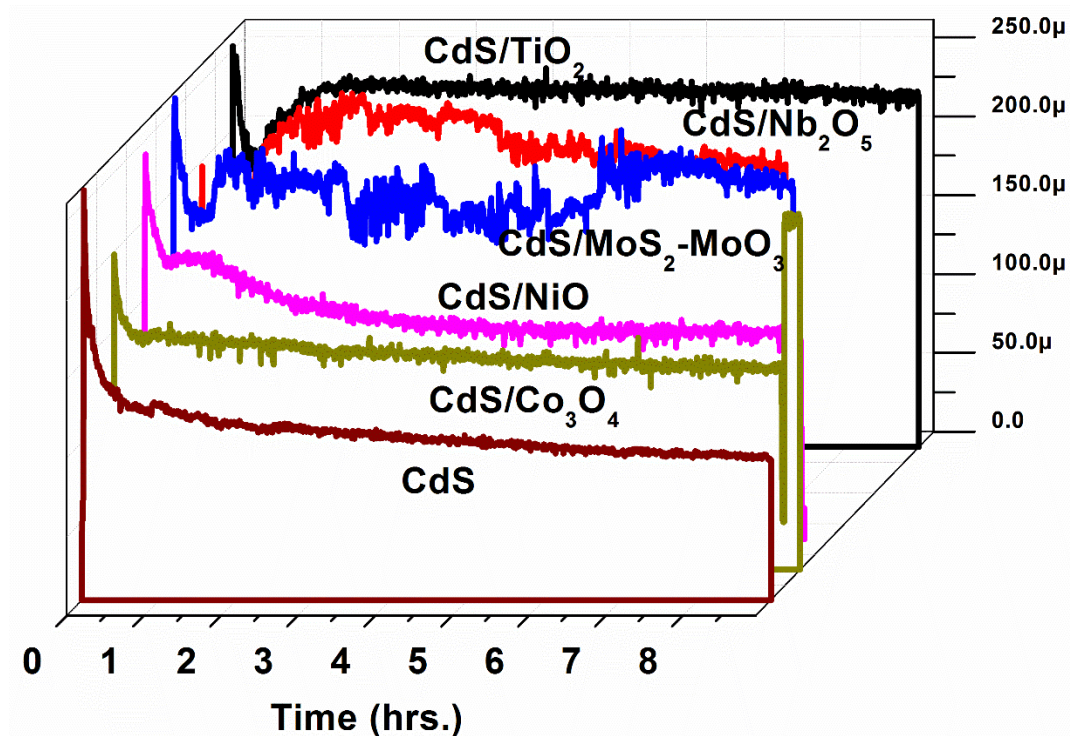
Figure 4.5. Prolong chronoampereometric measurements of bare and modified CdS photoanodes at 0.2 V/SCE under AM1.5 solar simulator to check stability.

It is important to state that electrode photostability, which is one of the most important focus of this study has been analysed in depth as described in *chapter 3, section 3.3*. The following paragraph highlights the electrode stability performance for various photoanodes studied during this work. Accordingly, prolong chronoamperometric measurements (*Chapter 3, section 3.3*) are displayed in Figure 4.5.

It shows the chronoampereometry curves of bare and modified CdS photoanodes for longer time of PEC reaction *i.e.* ≥9 hrs. It is evident from the Figure that metal-oxides based electrodes show the best stability among all the modified electrodes. Importantly CdS/TiO$_2$ based photoanode show absolutely no decay in the photocurrent, during the 9 hrs. of PEC measurement. Similar metal-oxide system *i.e.* Nb$_2$O$_5$ modified CdS photoanode show significant stability until 4 hrs. of

PEC measurement but the photocurrent decays later due to increase in pH of electrolyte above 12 (Nb_2O_5 is stable only in pH range (0-12)).

Table 4.1 Comparison of photostability with respect to slope of chronoampereometric curve and conclusions derived accordingly (*chapter 3, section 3.3*).

Strategy to curb photocorrosion	System name	Slope of 9 hrs chronoampereometric curve	Summary
-	CdS	12.7	
Metal –oxide	CdS/TiO$_2$	0	Most stable
	CdS/Nb$_2$O$_5$	5.5	
Co-catalysts	CdS/MoS$_2$-MoO$_3$	2.2	Moderately stable
	CdS/NiO	6.7	
	CdS/Ni(OH)$_2$	11.5	
	CdS/Co$_3$O$_4$	8.0	
	CdS/Co(OH)$_2$	8.75	
Conducting polymers	CdS/PANI	34.5	Very poor stability (slope is much greater than CdS)
	CdS/PPY	25.3	

From practical point of view, it may be necessitated to re-adjust the pH for stable operation of PEC cell. In other case of MoS$_2$-MoO$_3$ nanostructure modified photoanode, it does show a

constant photocurrent until 6 hrs. with some fluctuations in current value in-between. In case *co-catalyst* based *metal-oxides* like Ni and Co oxide modified photoanode, they acts as important candidate those exhibits dual benefits towards improvement of CdS PEC performance. However, the stability of Ni-Co hydroxide and polymer modified CdS photoanodes (*Chapter 3, section 3.5, 3.7, 3.8*) is not compared in Figure 4.5 due to their poor performance (it is summarized in Table 4.1). It is important to note that polymer modified photoanodes lacked adhesion and was peeling-off from the substrate after 30 minutes of PEC measurements. Table 4.1 shows the slope of chronoampereometric curves of different modifies photoanodes. Lesser the slope of curve more (as compared to CdS) is the stability of photoanode. It is obvious from the Table 4.1 that metal-oxide modified photoanodes shows highest stability, *co*-catalysts shows moderate stability and polymer modified photoanodes are having poor stability. It could be attributed to peeling off of polymer modified CdS films from the substrate during PEC measurements.

FUTURE SCOPE

The present dissertation is a compiled work highlighting the ways in which the performance of CdS photoanodes can be improved in efficiency and mainly the stability aspect. However, tremendous efforts are devoted to obtain an efficient and stable CdS photoanode. Still, there is a lot of scope to enhance the performance of CdS photoanodes in a PEC cell. There is huge demand of exploring doped metal oxide whose valence bandedge is lower than CdS. This technique could improve the charge transfer properties at interface and stability of PEC cell. Further, new techniques for modification of CdS surface with conducting polymers can be carried out so that peeling off film could be avoided. With the recent advances, the efficiency of

PEC cell can be further improved with the use of metal sulphide counter electrodes with CdS as working electrode. Hence, PEC research demands further improvement in various aspects *viz.* efficiency, stability *etc.* to visualize CdS photoanodes as competent photoanode.

References

[1] M. Graetzel, Inorg. Chem., 2005, 44, 6841.

[2] M. Gratzel, Nature, 2001,414, 338.

[3] E. Becquerel, Compt. Rend 1839, 9, 561.

[4] W. H. Brattain, C G B. Garret, Bull syst Tech, 1955, 34, 129.

[5] R. William J Chem phys 1960, 32, 1505.

[6] H. Gerischer J Phys chem. 1960, 26, 223.

[7] S R. Morrison Surf Sci 1969, 15, 363.

[8] R. Memming J Electrochem soc 1969, 116, 785.

[9] P J. Boddy J Electroanal Chem1965, 10, 119.

[10] A. Fujishima, K. Honda, Nature 1972, 238, 37.

[11] H Gobrecht R Kuhnkris, T. Tausend J Electrochem,1959, 63, 541.

[12] O. Khaselev, J. A. Turner, Science, 1998, 280, 425.

[13] G. Peharz, F. Dimroth, U. Wittstadt, Int. J. Hydrogen Energy, 2007, 32, 3248.

[14] M. G. Walter, E. L. Warren, J. R. McKone, S. W. Boettcher, Q. Mi, E. A. Santori , N. S. Lewis, Chem. Rev., 2010, 110, 6446.

[15] K. Rajeshwar, S. Licht, , A. Bard, , Eds. Wiley-VCH: Weinheim, Germany, 2002, 6.

[16] J. N. Arthur , Ann. Rev. Phys. Chernm. 1978, 29, 189.

[17] R. N. Dominey, N. S. Lewis, J. A. Bruce, D. C. Bookbinder, M. S. Wrighton, J. Am. Chem. Soc., 1982, 104, 467.

[18] R. Memming, Electrochim. Acta 1980, *25,* 77.

[19] B. Miller , A. Heller, Nature, 1976, 262, 680.

[20] V. Lionel , John Wiley & Sons (Asia) Pte Ltd, Singapore, 2009.

 [21] R. N. Dominey, N. S. Lewis, J. A. Bruce, D. C. Bookbinder and M. S. Wrighton, J. Am. Chem. Soc., 1982, 104, 467–482.

[22] G. Hodes, Nature 1980, 285, 29.

 [23] H. Gerischer, "Semiconductor Electrochemistry" in Physical Chemistry, An Advanced Treatise,edited by H. Eyring, D. Henderson, and W. Jost Academic, New York, 1970, Vol. IXA

[24] D. Meissner, C. Benndorf , R. Memming, Appl. Surf. Sci. 1987, 27, 423.

[25] Gerischer H, Physical chemistry, (eds), A H Erying, D Hendersonand W Jost, 1960, 9.

[26] A . J. Bard, , M . S. Wrighton, J. Electrochem. Soc., 1977, 124, 1706.

[27] Shiyou Chen, Lin-Wang Wang, Chem. Mater. 2012, 24, 3659.

[28] M. Tomkiewicz, In Semiconductor Liquid-Junction Solar Cells, Proceedings of Conference on Electrochemistry and Physics of Semiconductor-Liquid Interfaces Under Illumination, Airlie, Va., ed. A. Heller.Electrochem. Soc., Princeton, NJ, 1977, 92.

[29] C. D. Lokhande, Solar Cells, 1987, 22, 133.

[30] D. Cahen, Y. Mirovsky, J. Phys. Chem., 1985, 89, 2818.

[31] A. Pareek, N. Y. Hebalkar, P. H. Borse, RSC Adv., 2013, 3, 19905.

[32] A. Fujishima , E. Sugiyama , K. Honda, Bull Chem Soc Japan 1971, 44, 304.

[33] N. Serpone, E. Pelizzetti, Wiley, Photocatalysis: fundamentals and applications, 1989, ISBN: 978-0-471-62603-9.

[34] H. Gerischer ,J. Gobrecht , Ber Bunsenges Phys Chem 1976, 80, 327.

[35] H. Minoura, M. Tsljiki, Electrochimica Acta, 1978, 23, 1377.

[36] T. Inoue, T. Watanabe, A. Fujishima, K. Honda, K. Kohayakawa, J. Electrochem. Soc., 1977, 719.

[37] G. Hodes, J. Manassen,Solar Energy Mater., 1981, 4, 373.

[38] A. K. Mesmaeker, A. M. Decoster, J. Nasielski, Sol. Energy Mater. 1981, 4, 203.

[39] J. R. Wilson, Su-Moon Park, J. Electrochem. Soc.,1982, 129, 149.

[40] S. Licht, G. Hodes, J. Manassen, Inorg. Chem. 1986, 25, 2486.

[41] C.D. Lokhande, S.H. Pawar, Solid State Comm., 1984, 49, 765.

[42] J. Yang, D. Wang, H. Han, C. Li, Acc. Chem. Res., 2013, 46, 1900.

[43] K. Kalyanasundaram, E. Borgarello, D. Duonghong, M. Graetzel, 1981, 20, 987.

[44] D. Meissner, R. Memming, B. Kastening, Chem. Phys. Lett., 1986, 127, 419.

[45] D. Meissner,R. Memming, B. Kastening, J. Phys. Chem.1988, 92, 3476.

[46] K. Rajeshwar, M. Kaneko, A. Yamada, Rommel N. Noufi, J. Phys. Chem. 1985, 89, 806.

[47] M.S. Wrighton, R.C. Austin, A.B. Bocarsly, J.M. Bolts, O. Haas, K.D. Legg, L. Nadjo, M.C. Palazzotto,   J Am Chem Soc, 1978, 100, 1602.

[48] R. Noufi , A. J. Nozik , J. White , L. F. Warren , J Electrochem Soc, 1982, 129, 2261.

[49] R. Noufi , D. Tench , L. F. Warren, J Electrochem Soc, 1981, 128. 2596.

[50] N.A. Mancini, A. Pennisi, F. Simone, Sol.Energy Mater., 1987, 16, 205.

[51] H. Zhang, Y. Zhu, J. Phys. Chem. C, 2010, 114, 5822.

[52] W. Lee, H. J. Son, D. K. Lee, B. S. Kim, H. Kima, K. Kimc, M. J. Ko, Syn. Metals, 2013, 165, 60.

[53] A. J. Frank, K. Honda, J. Phys. Chem. 1982, 86,1933.

[54] Y.H. Hsieh, C.P. Huang, Colloids Surf., 1991, 53, 275.

[55] A. Henglein, Ber. Bunsenges. Phys. Chem., 1982, 86, 301.

[56] Rommel N. Noufi, Paul A. Kohl, James W. Rogers, Jr., John M. White, Allen J. Bard, J. Electrochem. Soc., 1979, 126, 949.

[57] R. Tenne, N. Miller, Y. Mirovsky and D. Lando, J. Electrochem. Soc, 1983, 130, 852.

[58] M. E. Rincon, M. Sanchez, J. RuizGarcia, J. Electrochem. Soc.,1998, 145, 3535.

[59] G. Campet, J.P. Manaud, C. Puprichitkun, Z.W. Sun, P. Salvador, Active and Passive Elec. Comp., 1989, 13, 175.

[60] P. A. Kohl, S. N. Frank, A. J. Bard, J. Electrochem. Soc, 1977, 124, 225.

[61] A. Sh. Aliev, M. N. Mamedov, M. T. Abbasov, Inorganic Materials, 2009, 45, 965.

[62] A. Pareek, R. Purbia, P. Paik, N. Y. Hebalkar, H. G. Kim, P.   H. Borse, Int. J. Hydrogen Energy, 2014, 39, 4170.

[63] A. Pareek, P. Paik, P.H. Borse, Langmuir, 2014, 30, 15540.

[64] M. Seol, J. W. Jang, S. Cho, J. S. Lee, K. Yong, Chem. Mater. 2013, 25, 184.

[65] X. Yan, G. Liu, L. Wang, Y. Wang, X. Zhu, J. Zou, G. Q. Lu, J. Mater. Res., 2010, 25, 182.

[66] K. Yu, X. Lin, G. Lu, Z. Wen, C. Yuan, J. Chen, RSC Adv., 2012, 2, 7843.

[67] R. Krishnakumar, V. Subramanian, Y. Ramaprakash, A.S. Lakshamanan, Mater. Chem. Phys. 1987, 15, 385.

 [68] A. Pareek, R. Dom, P. H. Borse, Int. J. Hydrogen Energy, 2013, 38, 36.

[69] P. H. Borse, L. S. Kankate, F. Dassenoy, W. Wogel, J. Urban, S. K. Kulkarni, J. Mater. Sci. Mater. Elect. 2002, 13, 553.

[70] E. R Liete, C. Vila, J. Bettini, E. Longo, J. Phy. Chem. C., 2006, 110, 18088.

[71] M. Liao , J. Feng , W. Luo , Z. Wang , J. Zhang , Z. Li, T. Yu , Z. Zou, Adv. Funct. Mater. 2012, 22, 3066.

[72] G. Tang, J. Sun, C. Wei, K. Wu, X. Ji, S. Lu, H. Tang, Mater. Lett., 2012, 86, 9.

[73] M. M Gvozdenovi,, B. Z. Jugovi, J. S.Stevanovi, T. L. Trišovi, B. N. Grgur, (2011). Electrochemical polymerization of aniline. In E. Schab-Balcerzak (Ed.), Electropolymerization (pp. 77–96). Rijeka, Croatia: InTech.

[74] L. J. Minggu, W. R. W. Daud, M. B. Kassim, Inter. J. Hydrogen Energy 2010, 35, 5233.

[75] B. D. Culity , Elements of X-ray Diffraction, 2 nd ed. (Addison-Wesley Publishing Compay, Inc., Reading, MA, 1978)

[76] E.Bacaksiz, M. Tomakin, M. Altunbas, M. Parlak, T. Colakoglu, Phys. B 2008, 403, 3740.

[77] Z Chen, T F Jaramillo, T G Deutsch, A K Shwarsctein, A J Forman, N Gaillard, R Garland, K Takanabe, C Heske, M Sunkara, W E McFarland, K Domen, Eric L Miller, J A Turner, H N Dinh., J. Mater. Res., 2010, 25, 3.

[78] S Kumari, C Tripathi, A.P Singh, D Chauhan, R Shrivastav., S Dass, V R. Satsangi, Curr. Sci. 2006, 91, 1062.

[79] A.A. Yadav, E.U. Masumdar, Sol. Energy, 2010, 84, 1445.

[80] F. Wang, R. Tang, H. Yu, P.C. Gibbons, W.E. Buhro, Chem. Mater. 2008, 20, 3656.

[81] R. Dom, H. G.Kim, P. H. Borse, Cryst. Eng. Comm., 2014, 16, 2432.

[82] K. S. Rao, K.V. Madhuri, S. Uthanna, O.M. Hussain, C. Julien, Mater. Sci. Eng. B, 2003, 100, 79.

[83] M. C. Baykul, N. Orhan, Thin Sol. Film, 2010, 518, 1925.

[84] W. Wang, I. Germanenko, M. S. El-Shall, Chem. Mater., 2002, 14 3028.

[85] N. Gaewdang, T. Gaewdang, Mater. Lett., 2005, 59, 3577.

[86] J. B. Mooney, S. B. Radding, Annu Rev, Mater. Sci., 1982, 12, 81.

[87] A.A. Yadav, E.U. Masumdar, J. Alloys Compd., 2011, 509, 5394.

[88] S.K. Kulkarni, U. Winkler, N. Deshmukh, P. H. Borse, R. Fink, E Umbach., Appl. surf. Sci., 2001, 169-170, 438.

[89] D. E. Scaife, Sol. Energy, 1980, 25, 41.

[90] I. Robel, V. Subramanian, M. Kuno, P.V. Kamat, J. Am. Chem. Soc. 2006, 128, 2385.

[91] P. V. Kamat, K. Tvrdy, D. R. Barker, J. G. Radich., Chem Rev., 2010, 110, 6664.

[92] M. Zhong, J. Shi, F. Xiong, W. Zhang, C. Li., Sol. Energy 2012, 86, 756.

[93] G. Hodes, J. Manassen., J. Electrochem. Soc., 1981, 128, 2325.

[94] J. S. Jang, D. J. Ham, N. Lakshmi, W. Y. Choi, J. S. Lee, Appl. Catal., A General, 2008, 346, 149.

[95] I. Ichinose, M. Terasaki, H. Katsuki, J. Ceram. Soc. Jpn. 1996, 104, 715.

[96] K. Nakamato, in: Infrared and Raman Spectra of Inorganic and Coordination Compounds, Wiley, New York, 1986, p. 105.

 [97] Z Wang, J. Hou, C. Yang, S. Jia, K. Huang, H. Zhu, Phys. Chem. Chem. Phys.2013, 15, 3249.

[98] M.V Ramakrishna, R.A Friesner, J. Chems. Phys. 1991, 95, 8309.

[99] Y. Wang, N. Heron, J. Phys. Chem. 1991, 95, 525.

 [100] Aslam M.; Mulla, I. S.; Vijayamohanan, K., Langmuir 2001, 17, 7487.

[101] S. Pethkar, M. Aslam, I. S. Mulla, P. Ganeshan, K. Vijayamohanan, J. Mater. Chem 2001, 11, 1710.

 [102] A. Kongkanand, K. Tvrdy, K. Takechi, M. Kuno, P. V. Kamat., J. Am. Chem. Soc. 2008, 130, 4007.

[103] R. S. Dibbell, D. F. Watson, J. Phys. Chem. C, 2009, 113, 3139.

[104] G. Campet, J. P. Manaud, C. Puprichutkun, Z. W. Sun, Active and Passive Elec. Comp. 1989, 13, 175.

[105] M. H. Miles, Y. H. Huang, S. Srinivasan, J. Electrochem. Soc., 1978, 125, 1931.

[106] M. G. Walter, E. L. Warren, J. R. McKone, S. W. Boettcher, Q. Mi, E. A. Santori, N. S. Lewis, Chem. Rev. 2010, 110, 6446.

[107] K.X. Steirer, J.P. Chesin, N.E. Widjonarko, J.J. Berry, A. Miedaner, D.S. Ginley, D.C. Olson, Org. Electron., 2010,11,1414.

[108] L. Ren, Y. P. Zeng, D. Jiang, Sol. State Sci., 2010, 12, 138.

[109] W. Fan, C. Zhang, H. Bai, X. Yu, W. Shi, Eur. J. Inorg. Chem. 2014, 3608.

[110] S. Xie, T. Zhai, Y. Zhu, W. Li, R. Qiu, Y. Tong , X. Lu, Inter. J. Hydrogen Energy 3 9, 2 0 1 4, 4 8 2 0.

[111] K. Sun, X. Pang, S. Shen, X. Qian, J. S. Cheung, D. Wang, Nano Lett. , 2013, 13, 2064.

[112] M. Higashi, K. Domen, R. Abe, J. Am. Chem. Soc. 2012, 134, 6968.

[113] R. Abe, M. Higashi, K. Domen, J. Am. Chem. Soc. 2010, 132, 11828.

[114] C. Ding, J. Shi, D. Wang, Z. Wang, N. Wang, G. Liu, F. Xionga, Can Li, Phys.Chem. Chem. Phys., 2013,15, 4589.

[115] Y. Li, X. Zhang , S. Jiang, H. Dai , X. Sun , Y. Li, Sol. Energy Mater. Sol. Cells, 2015, 132, 40.

[116] J. Li, F. Meng, S. Suri, W. Ding, F. Huang, N. Wu, Chem. Commun., 2012, 48, 8213.

[117] O. Yehezkeli , D. R. B. de Oliveira, J. N. Cha, Small, 2014, 11, 668.

[118] J. Yuan, J. Wen, Q. Gao, S. Chen, J. Li, X. Li, Y. Fang, Dalton Trans., 2015, 44, 1680.

[119] J. Ran, J. Yu, M. Jaroniec, Green Chem., 2011, 13, 2708.

[120] D. Voiry, M. Salehi, Rafael Silva, T. Fujita, M. Chen, T. Asefa, V. B. Shenoy, G. Eda, M. Chhowalla, Nano Lett., 2013, 13, 6222.

[121] J. Yang, H. S. Shin, J. Mater. Chem. A, 2014, 2, 5979.

[122] Z. Chen, D. Cummins, B. N. Reinecke, E. Clark, M. K. Sunkara, and T. F. Jaramillo, Nano Lett. 2011, 11, 4168.

[123] K. S. Rao, K.V. Madhuri, S. Uthanna, O. M. Hussain, C. Julien, Mater. Sci. Eng. B, 2003, 100, 79.

[124] Y. Liu, Y. X. Yu, W. D. Zhang, J. Phys. Chem. C, 2013, 117, 12949.

[125] J. Leger, M. Berggren, S. Carter, Iontronics :Ionic Carriers in Organic Electronic Materials and Devices, (CRC press, Taylor & Francis Group, 6000 Broken Sound Parkway NW, Suite 300, 2011)

[126] S. B. Kondawar, M. D. Deshpande, S. P. Agrawal, Inter. J. Comp. Mater. 2012, 2, 32.

[127] L. Wang, Q. Yao, H. Bi, F. Huang, Q. Wanga, L. Chen, J. Mater. Chem. A, 2015, 3, 7086.

[128] Z. Dai, J. Zhang, J. Bao, X. Huang, X. Mo, J. Mater. Chem., 2007, 17, 1087.

[129] A. Subathira, Rm. Meyyappan, Recent Res. Sci. Tech. 2010, 2, 124.

[130] Y. Huang, Y. Chen, C. Hu, B. Zhang, T. Shen, X. Chen, M. Q. Zhang, J. Mater. Chem., 2012, 22, 10999.

[131] K. Cheah, M. Forsyth, V. T. Tryuong, Syn. Met., 1998, 94, 215

[132] F. A. Beleze, A. J. G. Zarbin, J. Braz. Chem. Soc., 2001, 12, 542.

[133] P. P. Jeeju, S. J. Varma, P. A. F. Xavier, A. M. Sajimol, S. Jayalekshmi, Mater. Chem. Phys., 2012, 134, 803.

[134] B. Zhang, Y. Xu, Y. Zheng, L. Dai, M. Zhang, J. Yang, Y. Chen, X. Chen, J. Zhou, Nano. Res. Lett. 2011, 6, 431

[135] M. A. Chougulea, S. G. Pawara, P. R. Godsea, R. N. Mulika, S. Senb,V. B. Patila, Soft Nanosci. Lett., 2011, 1, 6.

[136] S. Zhang, Q. Chen, Y. Wang, L. Guo, Inter. J. Hydrogen Energy, 2012, 37, 13030.

Curriculum vitae

ACADEMIC QUALIFICATIONS

Master's : Master of Science in Physics, Devi Ahilya Vishwa Vidhyalaya, Indore, India, during 2008 – 2010. **CGPA: 8.34/10.00 (Percentage: 78.17 %)**

Bachelor's : B. Sc. Ed. (Bachelor of Science and Bachelor of Education), Regional Institute of Education, Ajmer, India, during 2004 – 2008. **Percentage: 74 %**.

Schooling : Senior Secondary School, Atomic Energy Central School, Rawatbhata, India, 2002 – 2004, Percentage: 83%.
Higher Secondary School, Atomic Energy Central School, Rawatbhata, India, 2002, Percentage: 77%

RESEARCH EXPERIENCE
- ✓ Presently I have been working on the topic "Stability improvement studies on Cd-chalcogenide photoelectrodes for photoelectrochemical cell" at International Advanced Research Centre for powder metallurgy and new materials (ARCI), Hydreabad , India, under the supervision of Dr. P. H Borse, since September, 2010.
  I registered for PhD in Hyderabad Central University under the guidance of Dr. Pradip Paik in Aug 2011 as an external student of ARCI.
- ✓ Completed Master's project on "Excitation of surface plasma waves by relativistic electron beam in a cylindrical plasma column" from Devi Ahilya Vishwa Vidhyalaya, Indore, India under the supervision of Dr. Y Choyal, during 2009-10
- ✓ Completed summer project on "To study the thermosphere ionosphere system using 630 nm airglow photometry" from Physical research laboratory (PRL), Ahmedabad, India, under the supervision of Dr. Debey Chakraborty, during May-June 2009

PUBLICATIONS
- ✓ Fabrication of large area photoanode of nanostructure CdS by spray pyrolysis for solar water splitting
  Authors: Alka Pareek, Rekha Dom, P.H. Borse
  Status: Published in International Journal of Hydrogen energy, 2013, Vol. 36, Issue 1, Pages- 36-44
- ✓ Fabrication of a highly efficient and stable nano-modified photoanode for solar H_2 generation
  Authors: Alka Pareek, Neha Y Hebalkar, P.H. Borse
  Status: Published in RSC Adv, 2013, Vol-3, Pages 19905-19908.

- ✓ Stabilizing effect in nano-titania functionalized CdS photoanode for sustained hydrogen generation
  Authors: Alka Pareek , Rahul Purbia, Pradip Paik, H.G. Kim, Neha Y Hebalkar, P.H. Borse
  Status: Published in International Journal of Hydrogen Energy, 2014, Vol. 39, 4170-4180.
- ✓ Characterization of nano-titania modified CdS /polysulphide electrolyte interface by utilizing electrochemical impedance spectroscopy
  Authors: Alka Pareek, Pradip Paik, P.H. Borse
  Status: Published electroanalysis, 2014, 26, 2403

- ✓ Nanoniobia Modification of CdS Photoanode for an Efficient and
  Stable Photoelectrochemical Cell
  Authors: Alka Pareek, Pradip Paik, P.H. Borse
  Status: Accepted Langmuir, dx.doi.org/10.1021/la503713t.
- ✓ Photoelectrectrochemical characterization of metal-semiconductor nanoparticle modified nanostructured CdS photoelectroded
  Status: Published in Proceedings to Fifth ISEAC Triennial International
  Conference on Advances and Recent Trends in Electrochemistry
  Authors: Alka Pareek, P.H. Borse
- ✓ Electrochemical characterization of Ag-loaded nano-titania modified CdS /polysulphide electrolyte interface
  Authors: Alka Pareek, Pradip Paik, P.H. Borse
  Status: Proceedings ICEE- 2014
- ✓ Characterization of nano-titania modified CdS /polysulphide electrolyte interface by utilizing electrochemical impedance spectroscopy
  Authors: Alka Pareek, Pradip Paik, P.H. Borse
  Status: Proceedings in Eleventh ISEAC, International discussion meet on electrochemistry and its applications, ISEAC DM -2014.
- ✓ 2 Manuscripts to be communicated in chemical communication and Solar energy and 3 manuscripts under preparation

AWARDS

- ✓ Best oral presentation award at ISEAC DM-2014, Radisson blu, Amritsar Punjab

- ✓ Best oral presentation award at ICEE-2014, JNTU, Hyderabad, Telangana

TECHNICAL SKILLS
- ✓ Spray pyrolysis deposition, Dip coating, Spin coating, Chemical bath deposition, Electrodeposition and Doctor Blade method for thin film deposition.

- ✓ Chemical, Hydrolysis and Hydrothermal method for nanoparticle synthesis.

- ✓ UV-Vis-NIR Optical Absorption Spectroscopy (Bandgap measurements), X-ray Diffraction, Photoelectrochemical (PEC) Characterization, Gas Chromatography, Impedance spectroscopy and PEC cell efficiency measurements.

CONFERENCES

- ✓ International Conference on Nanoscience and Technology (ICONSAT 2010)

    Poster presentation: Nanostructuring of cadmium sulphide thin film for energy application

- ✓ Fifth ISEAC Triennial International Conference on Advances and Recent Trends in. Electrochemistry (ELAC- 2013)

    Poster presentation: Photoelectrochemical characterization of coupled metal-semiconductor nanoparticles on nanostructured CdS thin films

- ✓ International union of Materials Research Society (IUMRS ICA-2013)

    Oral Presentation: Stability improvement of CdS photoanode by control over adsorbed titania nanoparticle phase

- ✓ 11 ISEAC DM-2014, organised by BARC

    Oral presentation: Characterization of nano-titania modified CdS /polysulphide electrolyte interface by utilizing electrochemical impedance spectroscopy

- ✓ International conference on energy and environment (ICEE-2014)

    Oral presentation: Electrochemical characterization of Ag-loaded nano-titania modified CdS /polysulphide electrolyte interface